Constraining rapid climate transitions in the North Atlantic using tephrochronology.

Griggs, Adam James

Constraining Rapid Climatic Transitions in the North Atlantic using Tephrochronology

Adam James Griggs

Swansea University
Prifysgol Abertawe

Thesis submitted to Swansea University in fulfilment of the requirements for the degree of Doctor of Philosophy

Department of Geography, College of Science

Swansea University

2015

ProQuest LLC.
789 East Eisenhower Parkway
P.O. Box 1346
Ann Arbor, MI 48106 – 1346

10 December 2015

Abstract

Abrupt climatic transitions that characterise the Late Pleistocene are recognised in a number of palaeoarchives, yet little has advanced our understanding of the causal mechanisms. High-resolution atmospheric changes are best represented in the Greenland ice-core records and North Atlantic marine sediments preserve a sequence of oceanic responses during these rapid events. An understanding of forcing mechanisms, however, is currently hampered by chronological uncertainties and an inability to integrate proxy records from these different realms. Tephrochronology is one of the few techniques that offer the potential to establish independent and precise tie-points between marine and ice-core records.

Four marine sequences are explored to assess the potential of utilising tephra and cryptotephra deposits as time-synchronous marker horizons during Marine Isotope Stage 2 and 3. Tephras preserved in the marine environment are subjected to a range of secondary transportation and depositional processes, such as iceberg rafting and bioturbation, as well as primary airfall. Using a range of diagnostic indicators, a protocol is proposed to i) assess the processes controlling tephra deposition ii) to inform isochron placement and iii) to identify primary deposits that can act as valuable marker horizons. Moreover, a pioneering application of thin-section and X-ray microtomography analyses are presented to assist in the assessment of post-depositional processes. These techniques highlight some of the complexities of marine tephrochronology and the possibilities they offer for fully resolving depositional integrity.

Through application of this protocol, ten primary tephra deposits are identified and together form a marine tephrochronological framework for the North East Atlantic region. Four deposits are new discoveries and augment the volcanic event stratigraphy and enhance the number of isochrons available for synchronisation. Geochemical characterisation and stratigraphical analysis are employed to assess the presence of coeval marine and ice-core horizons. Two ice-marine tie-lines, FMAZ II and NAAZ II, have been successfully utilised to identify the relative timing of climatic events and highlight the potential of synchronising records. Some of the challenges of correlating marine deposits to the Greenland ice-cores are explored, and recommendations are made for future applications of marine tephrochronology.

DECLARATION

This work has not previously been accepted in substance for any degree and is not being concurrently submitted in candidature for any degree.

Signed ..... (candidate)

Date 16/12/15

STATEMENT 1

This thesis is the result of my own investigations, except where otherwise stated. Where correction services have been used, the extent and nature of the correction is clearly marked in a footnote(s).

Other sources are acknowledged by footnotes giving explicit references. A bibliography is appended.

Signed ..... (candidate)

Date 16/12/15

STATEMENT 2

I hereby give consent for my thesis, if accepted, to be available for photocopying and for inter-library loan, and for the title and summary to be made available to outside organisations.

Signed ..... (candidate)

Date 16/12/15

Publications arising from this study

The following papers have been published or have been submitted as a direct result of this study. Some sections of chapters are quoted verbatim from Griggs et al. (2014) and Griggs et al. (submitted):

Griggs, A.J., Davies, S.M., Abbott, P.M., Rasmussen, T.L., Palmer, A.P., 2014. Optimising the use of marine tephrochronology in the North Atlantic: a detailed investigation of the Faroe Marine Ash Zones II, III and IV. Quaternary Science Reviews, 106, 122-139.

Griggs, A.J., Davies, S.M., Abbott, P.M., Coleman, M., Palmer, A.P., Rasmussen, T.L., Johnston, R., in press. Visualising tephra sedimentation processes in the marine environment; the potential of X-ray microtomography. Geochemistry, Geophysics, Geosystems.

Acknowledgements

Firstly, I would like to express sincere thanks to **Professor Siwan Davies** for her supervision, constant support, endless enthusiasm and for inspiring me in Quaternary Science. Thank you for providing me with numerous opportunities to explore different research avenues and present at international conferences. I would also like to say thank you to my second supervisor **Dr Peter Abbott** who has been brilliant and incredibly helpful throughout my PhD, supporting me through written and laboratory research. It has been a privilege to have had two fantastic supervisors.

Thank you to **Dr Richard Johnston** and **Dr Mark Coleman** from the Department of Engineering for your enthusiasm in helping develop X-ray microtomography to assist in tephra visualisation. Thank you also to **Dr Adrian Palmer** from Royal Holloway, University of London, for assisting in thin-section preparation and providing help with sedimentological interpretations. Thank you also to **Gareth James** and **Jonathan Woodman-Ralph** for your help and laughter in the labs.

Thank you to **Professor Ian Hall** from Cardiff University for providing me with access to marine core MD04-2829CQ. Thanks to **Professor Tine Rasmussen** from the University of Trømso for providing me with access to marine core JM11-19PC and help with depositional interpretatons. Thank you to **Dr Trond Dokken** from Bergen University for access to marine core MD95-2010. Thank you also to **Dr Frederique Eynaud** from the University of Bordeaux for access to marine core MD99-2281. I am grateful for the assistance of **Dr Chris Hayward** with the use of the electron microprobe at the Tephrochronology Analytical Unit, University of Edinburgh. Thank you also to **Dr Nick Pearce** for generating the trace element LA-ICP-MS data at Aberystwyth University

This study forms part of the Tephra constraints on Rapid Climate Events (TRACE) project and the research leading to these results has received funding from the European Research Council under the European Union's Seventh Framework Programme (FP7/2007-2013)/ERC grant agreement n° [259253]. This work was additionally supported in part by the Engineering and Physical Sciences Research Council (ESPRC) [grant number EP/I00145X/1]. Thank you to the QRA for the Postgraduate Research Award for thin-section preparation at Royal Holloway, University of London.

Finally, I would like to thank my wonderful family for their support, motivation and humour over the course of my PhD. I would also like to thank my wife-to-be; Melanie Rhodes, her family, menagerie and the Winkle for always keeping me smiling.

Table of Contents

Table of Figures

List of Tables

Abbreviations

μCT	X-ray microtomography
2D	Two-dimension
3D	Three-dimension
AMOC	Atlantic Meridional Overturning Circulation
BIIS	British-Irish Ice Sheet
DO	Dansgaard-Oeschger
EPMA	Electron micro-probe analysis
FMAZ	Faroe Marine Ash Zone
GISP	Greenland Ice Sheet Project
GI	Greenland interstadial
GS	Greenland stadial
gdw	Grams dry weight
GRIP	Greenland Ice Core Project
HCl	Hydrochloric acid
H	Heinrich event
INTIMATE	Integrating ice-core, marine and terrestrial records
IRD	Ice-rafted debris
LA-ICP-MS	Laser-ablation inductively coupled mass-spectrometry
LGM	Last Glacial Maximum
MIS	Marine isotope stage
NAAZ	North Atlantic Ash Zone
NADW	North Atlantic deep water
NEADW	Northeastern Atlantic Deepwater
NEEM	North Greenland Eemian Ice Drilling
NGRIP	North Greenland Ice Core project
NPS	N. pachyderma (sinistral)
NSDW	Norwegian Sea Deep Water
NSOW	Nordic Seas Overflow Water
PF	Polar front
RB	Rosemary Bank
RHY	Rhyolitic
RP	Rockall Plateau
RT	Rockall Trough
SAF	Sub-Arctic front
SC	Similarity coefficient
SPT	Sodium polytungstate
SST	Sea-surface temperature
TB	Tholeiitic basalt
TRACE	Tephra constraints on rapid climate events
WDS	Wavelength dispersive
Z	Atomic number

Chapter 1 Introduction

1.1 Synchronisation of disparate climatic archives

The shape of modern Quaternary Science has evolved considerably over the past decade, but little has advanced our understanding of the mechanisms driving abrupt climatic shifts punctuating the last glacial period (Alley et al., 1993; Lowe 2001; Hemming 2004; Clement and Peterson, 2008). The most dramatic insights into the behaviour of the climate system have been detailed in ice and sediment cores in the North Atlantic (Dansgaard et al., 1982; Bond et al., 1992; Alley et al., 1993). Transitions in climate state occurred over decadal timescales and were matched with large scale reorganisations in the ocean-atmosphere system (Steffenson et al., 2008). These excursions are known as Dansgaard-Oeschger (D-O) events; recurring roughly every 1500 years (Bond et al., 1997), manifesting as abrupt warming over Greenland, followed by a gradual return to stadial conditions (Dansgaard et al., 1982). Annually-resolved Greenland ice-core records detail the best stratigraphically uncompromised chronometer for the complex sequence of D-O events (Rasmussen et al., 2008, 2013, 2014). Bond et al. (1992) demonstrated that D-O events in Greenland are closely matched by changes in sea-surface temperatures (SST) recorded in North Atlantic marine sediments. This suggests linkage between oceanic and atmospheric processes. Triggers are thought to reside in the deep ocean i.e. disruption to the thermohaline circulation, and alternative hypotheses suggest abrupt transitions are initiated through changes in atmospheric dynamics (see section 2.1.2) (Broecker, 2003; Clement and Peterson 2008; Barker et al., 2015). Additionally, a large number of records from around the world detail evidence of similar short-lived climatic oscillations (Wang et al., 2001; Blaauw et al., 2009; Nakagawa et al., 2012; Lane et al., 2013). As such, a key challenge of palaeoclimatic research is to determine the causal mechanisms of these abrupt events.

To fully understand the regional expression and mechanisms driving rapid changes, precise correlations are required between the ice, marine and terrestrial realms to assess the relative timing of their impacts (Blockley et al., 2012; Brauer et al., 2014; Blockley et al., 2014; Davies, 2010). However, long-standing chronological issues have plagued the integration of disparate records, largely due to inherent dating difficulties such as those associated with radiocarbon dating (Muscheler et al., 2008, 2014; Davies et al., 2012). To avoid these issues, records are frequently tuned and wiggle matched based upon common patterns in the data-sets, which is not climatically independent and likely to mask any leads and lags that may be present in the system (Blauuw, 2012; Lane et al., 2013; Rach et al., 2014; Blockley et al., 2014) (Fig 1.1a,b). At present, tephrochronology offers high potential for the precise and independent correlation of disparate sequences (Lowe et al., 2001; Turney et al., 2004; Blockley et al., 2007; Davies et al., 2012; Lane et al., 2014) (Fig 1.1c).

Tephrochronology is based upon the utilisation of isochrons defined by volcanic ash (Thorarinsson, 1944). The instantaneous deposition of tephra following a specific eruption forms time-synchronous marker horizons and permits the correlation of separate deposits formed at the same time (Lowe, 2011). This technique has been revolutionised over the past decade through the identification of cryptotephras that increase the number and distribution of known and previously undiscovered tephra deposits (Dugmore, 1989; Turney et al., 2004; Pyne O'Donnell et al., 2012; Davies et al., 2014). In the quest for resolving causal mechanisms of D-O events, the most valuable tephra deposits are those that can be traced between the Greenland ice-cores and North Atlantic marine archives. This permits synchronisation of records that preserve atmospheric (ice) and oceanic changes (marine sediments) associated with these rapid events. Additionally, ages can be imported through the transfer of the GICC05 ice-core age into records containing equivalent tephra horizons, which can then be included in chronological models (Svensson et al., 2008; Davies et al., 2012). Tephrochronology offers much promise for the creation of independent time-scales and an insight into leads and lags within the ocean-atmosphere system (Brauer et al., 2014). TRACE (Tephra constraints on Rapid Climate Events) - a five-year project funded the European Research Council, aims to utilise cryptotephrochronology to precisely correlate the Greenland ice-cores with North Atlantic marine records.

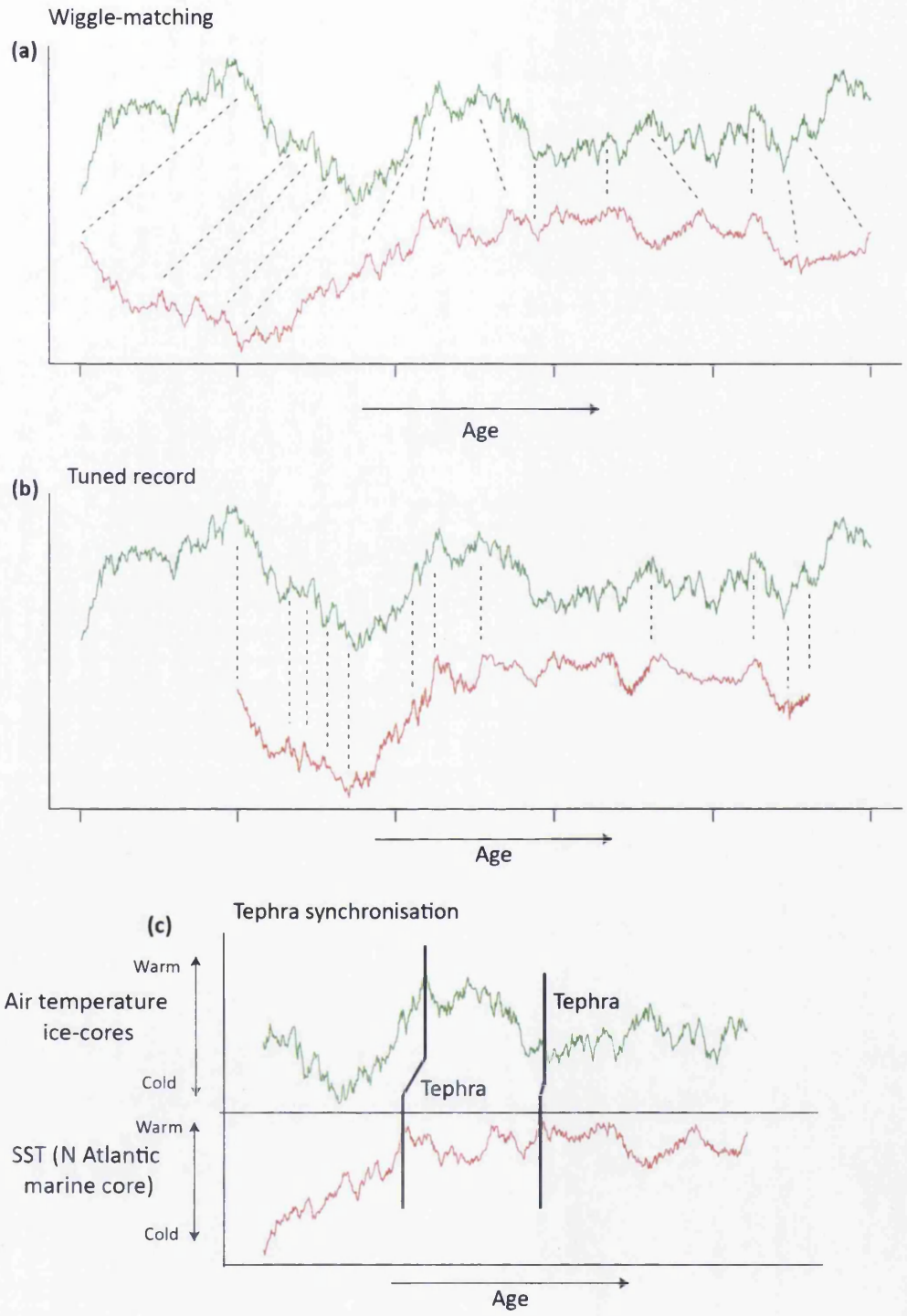

Figure 1.1 Schematic representation of tuning procedures after Blaauw, (2012). (a) Similar features within two time-series are identified (tie-points indicated by dashed lines). (b) Tie-points deduced in (a) are then aligned to the red series based upon tuning. (c) Schematic representation of TRACE synchronisation goals. The same data series are synchronised based upon the occurrence of common tephra horizons between the marine and ice realms.

This investigation forms part of the TRACE project and aims to exploit tephra isochrons found within these records to constrain phasing relationships between oceanic and atmospheric systems during the last glacial period (Fig 1.1c).

To date, the potential of tephrochronology to synchronise common tephra horizons between ice and marine environments has been demonstrated by the detection of the Faroe Marine Ash Zones (FMAZ) II (Wastegård et al., 2006; Davies et al., 2008) and the North Atlantic Ash Zone (NAAZ) II (Austin et al., 2004). Furthermore, Abbott and Davies (2012) summarise the potential of tracing cryptotephras within the Greenland ice-cores and new discoveries in Greenland ice, detected as part of the TRACE project, have greatly increased the number of horizons available for cross-correlations (Bourne et al., 2013, 2015). However, very few studies have explored the potential of tracing cryptotephras in North Atlantic marine sequences. Previous marine studies have focused on coarse grained or clearly visible horizons, and cryptotephra content within marine sediment has been largely overlooked (Ruddiman and Glover, 1972; Haflidason et al., 2000; Rasmussen et al., 2003). Recent cryptotephra investigations during MIS (marine isotope stage) 4 and 5 have demonstrated the potential of undertaking cryptotephra investigations (Brendryen et al., 2010; Brendryen et al., 2011; Abbott et al., 2011, 2013, 2014; Davies et al., 2014). The MIS 2 and 3 periods, however, are yet to be explored. This investigation will examine MIS 2 and 3 deposits to provide the foundations for a tephrochronological framework for the North Atlantic.

The high-eruptive frequency of Icelandic volcanic systems during the last glacial period, as shown by the cryptotephras in the ice cores, indicates the potential for widespread tephra dispersal into the marine environment (Bourne et al., 2015). However, a key challenge for the marine environment is the identification of tephra and cryptotephra deposits that originate from primary depositional processes and are unaffected by any secondary transport or depositional processes e.g. iceberg rafting and bioturbation (e.g. Davies et al., 2014; Griggs et al., 2014). In order to fully exploit tephra tie-lines, it is essential to first assess the depositional integrity of the tephra; an issue which is currently confounded by the complexity of processes that control deposition in the oceans (Austin et al., 2004; Brendryen et al., 2010; Abbott et al., 2011). As such, stratigraphic displacement of a deposit may lead to chronological uncertainties and erroneous use of tie-points, which has important

ramifications for establishing the relative timing of climatic signals preserved within palaeosequences (e.g. Davies et al., 2014). The complexity of processes operating on tephra and cryptotephra deposits cannot be fully unravelled using existing stratigraphic techniques. Resolving depositional integrity represents a crucial step in utilising tephrochronology to meet the TRACE synchronisation goals.

1.2 Aims and Objectives: Extending the tephra framework

A tephrochronological framework is constructed by combining precise and robust methods of geochemical characterisation with an assessment of stratigraphic integrity (Davies et al., 2012; Blockley et al., 2014). This includes the importance of; a) employing robust geochemical acquisition of individual glass shards; b) resolving sedimentation, transportation and dispersion processes, and; c) systematic data comparison exercises to determine likely correlations. These form the central themes of the thesis in order optimise the use of tephrochronology to meet the TRACE synchronisation goals. The general aims of the project are:

1. To assess the cryptotephra content within four marine cores in the NE Atlantic region spanning 16-55 ka, i.e. during MIS 2 and 3;
2. To geochemically fingerprint each marine tephra deposit to determine its volcanic origin and to assess the stratigraphic integrity of each deposit;
3. To develop a protocol for assessing the stratigraphic and depositional integrity of marine tephra deposits;
4. To assess the viability of utilising innovative sedimentological visualisation techniques for improving isochron placement in palaeosequences;

5. To develop and improve the MIS 2 and 3 North Atlantic marine tephrochronological framework and to assess potential correlations to other published tephra horizons in the ice-cores and other marine records;

6. To assess phasing relationships in the atmospheric and oceanic systems during the last glacial period

Chapter 2 Literature review

2.1 Abrupt climate change

2.1.1 Dansgaard Oeschger events; what are they?

Throughout the last glacial period the North Atlantic has experienced twenty five abrupt climatic fluctuations, known as Dansgaard-Oeschger (D-O) events, during which oceanic and atmospheric conditions alternated between warm (interstadial) and cold (stadial) episodes (Dansgaard et al., 1982; NGRIP Members, 2004; Rasmussen et al., 2014). Ice core records in Greenland have been instrumental in the examination of past abrupt climate change, offering unparalleled temporal resolution of D-O events in comparison to other sedimentary archives (Alley et al., 1999; Steffensen et al., 2008). As such, $\delta^{18}O$ records from ice-core records indicate initial rapid warming occurred within only a few decades (Steffensen et al., 2008; Thomas et al., 2009), typically in the range of 6-16°C (Dansgaard et al., 1992; Huber at al., 2006; Landais et al., 2004; Kindler et al., 2014). Interstadials, which vary in duration from centuries to millennia, were followed by a slow cooling trend over several centuries and a final rapid drop into cold stadial conditions (Huber et al., 2006). The most abrupt transitions are best reflected in the deuterium excess values, where the record indicates a sustained shift in the position of prevailing air masses occurring within only three years at the end of GS-1 (Greenland stadial) (Steffenson et al., 2008).

Alternating patterns of interstadials and stadials are reflected in a diverse range of palaeoarchives (Voelker and workshop participants, 2002; Brauer et al., 2008). The first marine evidence for abrupt climate changes during the last glacial period came from high accumulation rate sediment cores in the subpolar North Atlantic and were suggested to correlate to the events shown in the ice-cores (Bond et al., 1992,

Clement and Peterson, 2008). Sea surface temperatures (SSTs) reconstructed from planktonic foraminifera followed similar patterns to those seen in the ice with SST changes of ~5°C, however, the transitions appeared smoother than the ice cores (Bond et al., 1992). Additionally, thick, discrete, carbonate rich sedimentary deposits within marine cores are thought to have been deposited by discharges of debris-laden icebergs into the North Atlantic during some D-O events (Hemmings, 2004). These ice-rafted debris (IRD) layers are termed 'Heinrich' layers and represent a 'Heinrich' event (Heinrich, 1988). Heinrich events are thought to mark the final abrupt and extreme minimum of six interspersed D-O cycles throughout the last glacial (Hemmings, 2004). Heinrich events may be time-transgressive (Stanford et al., 2011) and the presence of IRD alone is not evidence for a D-O event in the marine record, despite its associated occurrence (Hemmings, 2004). Rasmussen et al. (2014) argue the Greenland ice-core records constitute the most comprehensive, well-resolved archive of D-O scale climate variability and it is in these records that D-O events should be defined and named. Much value is to be gained from unique proxy evidence recorded in the marine realm, which details oceanic changes during D-O cycles (Fig 2.1c). This information is crucial for integration with atmospheric changes recorded in the ice and is central to the TRACE synchronisation goals. Only when independent synchronisation is facilitated can the existence of leads and lags in the climate system be tested.

2.1.2 What caused D-O events?

Understanding the forcing mechanisms behind abrupt climate change still remains an elusive goal for palaeoclimate researchers (Blockley et al., 2012; Brauer et al., 2014). At present, the favoured paradigm for explaining abrupt climate change is a re-organisation in the North Atlantic deep-water ocean circulation (NADW). This is thought to be a result of freshwater input and its impact on heat transport to regions following disruption to the meridional overturning circulation of the North Atlantic (AMOC) (Bond et al., 1992; Alley et al., 1999; Broecker, 2003; Knutti et al., 2004; Clement and Peterson, 2008). Recent palaeoceanographic investigations have suggested iceberg discharge and freshwater input may be a consequence of stadial conditions rather than the cause (Barker et al., 2015). Barker et al. (2015) indicate

rapid transitions to stadial conditions may be a consequence of nonlinear responses to more gradual cooling across the North Atlantic.

The alternative view to an oceanic trigger in the North Atlantic focuses on the coupled ocean-atmosphere system originating in the tropics (Clement and Peterson, 2008). As tropical convective systems constitute the dominant element in the climate system, the trigger most likely resides in the El Nino-La Nina regions, and small changes in the tropics have the potential to alter the radiation budget of the planet, hydrological cycle, and NADW (Clement and Peterson, 2008, Cane and Clement, 1999). Ivanochoko et al. (2005) have argued that changes in strength and structure of tropical convective systems throughout the tropics may be sufficient to modulate terrestrial emissions of methane, providing a plausible mechanism for amplifying and perpetuating millennial scale variability. The forcing mechanism originating in the tropics points toward an atmospheric trigger of abrupt climate change.

Although there is strong marine evidence detailing re-organisations in the NADW and AMOC during D-O events, no unequivocal evidence exists to confirm whether they constitute the primary trigger, or amplify the forcing as a result of atmospheric changes initiated elsewhere (Broecker, 2003). This is partly due to the three dimensional nature of the deep ocean, which renders it inherently complex to reconstruct. If the trigger does reside in the oceans, the reorganisations must have perturbed tropical dynamics, which in turn drove global atmospheric changes (Broecker, 2003). The key to addressing this critical question is to resolve whether atmospheric signals recorded in proxy archives predate the changes in ocean circulation; a goal currently confounded by geochronological issues (Blaauw, 2012, Blockley et al., 2012) and spatio-temporal dependant expressions of D-O variability (Rasmussen et al., 2014).

2.2 The evolving paradigm; were D-O events asynchronous?

D-O event variability is expressed in numerous proxy records, ranging from evidence recorded in the ice and ocean, to lake and cave records across the globe

(Fig 2.1) (Bond et al., 1992; NGRIP members, 2004; Wang et al., 2001; Nakagawa et al., 2012; Blaauw et al., 2010; Lane et al., 2013). Diatom evidence from palaeolake Les Échets in France reveals a number of D-O like events during the last glacial period (Fig 2.1b). The oxygen isotope record from speleothems in Hulu Cave, China, has been dated using uranium-thorium and suggest a strong resemblance to rapid fluctuations recorded in the Greenland GISP2 isotopic record (Wang et al., 2001) (Fig 2.1a). Although fluctuations recorded in the ice were most likely related to the structure and age of millennial-scale events in other archives, it may not be the case that records registered the same climatic signal at the same time (Van Andel, 2005; Rohling, 2009; Blaauw 2012; Rasmussen et al., 2014). Interactions between ocean and atmospheric responses propagate in complex ways, which is likely to have produced a variety of regional and global manifestations of D-O behaviour (Rasmussen et al., 2014). Regional disparities in climate change are likely to span multi-decadal scales. Extremely precise and independent integration of different records from different regions is essential for detecting leads and lags in the climate system (Brauer et al., 2014). Traditional approaches have tuned records through wiggle match alignment to abrupt transitions recorded in the ice-cores (Wang et al., 2001; Shackleton et al., 2000; Skinner, 2008), which assumes artificial synchroneity (Hibbert et al., 2010; Austin and Hibbert 2012; Blauuw 2012) and neglects the effect of different temporal proxy responses (Brauer et al., 2014). This prevents an assessment of phasing relationships that may exist within the climate system.

The application of radiocarbon dating to date marine and terrestrial sediments is common but in this context its use is limited. The duration of transition is shorter than the precision of the dating technique, within errors of uncertainty (Blaauw, 2012). Given that abrupt climatic transitions are thought to have occurred within a few decades, the technique is not suitable for pinpointing proxy changes to the required precision. This is further complicated by uncertain marine reservoir offset ages for marine records (i.e. Muscheler et al., 2008). An independent tool to line up records with annual precision is required and can now be achieved through the use of time synchronous horizons of volcanic ash and the technique of tephrochronology, which does not assume co-variance of a climate signal (Davies et al., 2012).

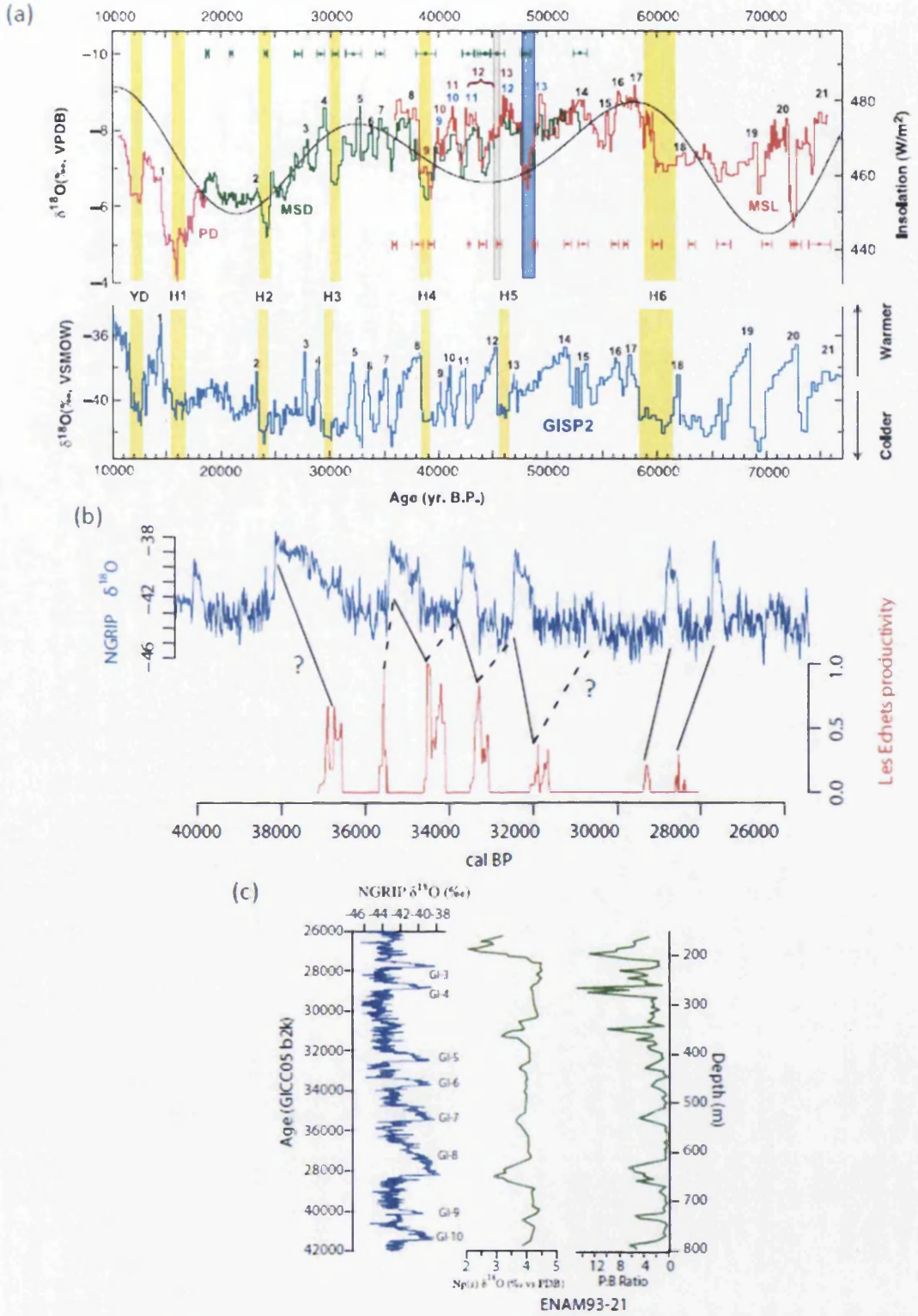

Figure 2.1 (a) ^{18}O Hulu Cave stalagmite record compared to GISP2 (Wang et al., 2001). ^{230}Th ages and errors are colour coded by stalagmite. Numbers of interstadials have been wiggle-matched to the GISP2 ice-core. Heinrich events are depicted by the vertical bars. The brown and blue bars indicate two possible correlations to H5. (b) Tuning of the productivity of lake core Les Échets against the ^{18}O NGRIP record (Blaauw et al., 2010). Black lines show proposed aligning of events and dotted lines show alternative tuning. (c) *N.pachyderma* sin. proxy record of ENAM93-21 marine record compared with NGRIP after Rasmussen et al. (2003) and Abbott and Davies (2012).

Tephrochronology is regarded as one of the key techniques for providing time-synchronous marker horizons to establish independent and precise tie-points between disparate palaeoarchives (e.g. Haflidason et al., 2000; Lowe et al., 2008; Davies et al., 2010; Abbott and Davies 2012). Lane et al. (2013) demonstrated that synchronising two high-resolution records using a tephra horizon indicated the onset of climatic amelioration during the Younger Dryas was abrupt, but time-transgressive across Europe. Examining the timing and rate of climatic propagation across the region can test various hypotheses regarding forcing mechanisms. This highlights the powerful approach of combining tephra isochrons within annually resolved records. If ice-cores and marine records can be successfully synchronised using tephra horizons, this may create opportunities to decouple ocean-atmosphere response to abrupt climate shifts (Blockley et al., 2012; Davies et al., 2012). This forms the central motivation for conducting marine tephra investigations presented within the study.

2.3 Tephrochronology

2.3.1 Principles of tephrochronology

Tephra is explosively erupted, pyroclastic products from volcanic eruptions (Thorarinsson, 1944). It encompasses all volcanological grain sizes; ash (<2 mm in diameter), lapilli (2-64 m), or blocks/bombs (>64 mm) (Fisher, 1961). Owing to the long distances from active volcanoes, tephra is studied in ash size fragments (Sparks, 1981; Haflidason et al., 2000). The subsequent deposition of tephra in ice sheets (e.g. Zielinski et al., 1996; Mortensen et al., 2005; Davies et al., 2008; Abbott et al., 2012; Abbott and Davies 2012; Bourne et al., 2013, 2015), lacustrine environments (e.g. Pyne O'Donnell et al., 2008), terrestrial sequences (e.g. Dugmore et al., 1992; Wastegård, 2002; Blockley et al., 2007) and marine environments (e.g. Rasmussen et al., 2003; Wastegård et al., 2006; Abbott et al., 2011), provide excellent palaeoclimatic archives from which to reconstruct a variety of Quaternary processes (Haflidason et al., 2000).

The fundamental prerequisite underpinning the use of tephrochronology is that tephra is deposited and preserved rapidly into sequences following an eruption, and its stratigraphic position at each site relates to the timing of the event (Lowe, 2011). Tephra isochrons provide stratigraphic tie-lines between records, which permit precise inter-site correlation and integration of unique proxy records (Lowe, 2011, Davies et al., 2012; Lane et al., 2013). If the tephra can be dated in one sequence by radiocarbon dating of the host sediment, then its age can be transferred to other occurrences of that horizon i.e. tephrochronology (Lowe, 2011). High precision ages can be applied if the tephra occurs within annually banded sequences such as ice-cores (Mortensen et al., 2005; Davies et al., 2008; Davies et al., 2010) or varved sediments (Blockley et al., 2007; Nakagawa et al., 2012; Lane et al., 2013). Even if the age of tephra is uncertain, the horizon can still act as a stratigraphically fixed tie point i.e. tephrostratigraphy (Lowe, 2011).

In order for tephras to be correlated between palaeoarchives, it is essential that each horizon is uniquely characterised through geochemical fingerprinting (Turney et al., 2004) (see section 2.3.3). Traditionally, if the site were proximal to the eruption site, visible properties of the tephra deposits i.e. shard morphology, grain size, colour and texture were deemed sufficiently diagnostic (Mangerud et al., 1984; Turney et al., 2004). The Laacher See tephra has highly vesicular shards, whereas the Vedde Ash is commonly described as being 'butterfly' shaped, with a cuspate and platy morphology (Mangerud et al., 1984). Numerous eruption events can occur from the same volcanic centre and produce similar morphological characteristics, making visual observations insufficiently diagnostic for pinpointing individual eruption events (Turney et al., 2004). In an ideal scenario, eruptions exhibit unique geochemical fingerprints and it is essential that comprehensive laboratory examinations of tephras are conducted to characterise the geochemistry of juvenile glass shards (see section 2.3.3) (Davies et al., 2002; Lowe et al., 2008). Robust major and trace element geochemical fingerprinting is an essential step for establishing tephra linkages between sequences (Davies et al., 2012).

Traditionally, records of tephra deposits and associated horizons were derived solely from visible layers of ash, usually due to the exceptionally high concentration of shards in sedimentary sequences and proximity to the eruption centre (Mangerud et al., 1984). Although some visible layers of ash have been discovered distally from

their volcanic source, i.e. Vedde Ash found in Norway (Birks et al., 1996) and the FMAZ II in the North Atlantic (Wastegård et al., 2006), the scope of tephrochronology was predominantly limited to proximal localities or areas where conditions favoured intensified shard accumulation (Turney et al., 2004). Persson (1966) initially identified several cryptotephras in a Swedish peat bog and the adoption of this approach increased when cryptotephras were found within a number of peat sequences (Dugmore, 1989). This allowed tephrochronolgical frameworks to be developed over larger areas than previously obtainable by extending the limits of eruptions by up to 2500 km (Blockley et al., 2007). Consequently, distal tephra studies offer a significant potential for providing wide ranging time-stratigraphic tie-lines and offer a comprehensive archive for reconstructing volcanic eruption histories (Davies et al., 2005; Blockley et al., 2007; Lowe et al., 2008; Davies et al., 2012).

2.3.2 Cryptotephrochonology

A marked change in tephra extraction techniques facilitated the first discovery of distal tephras shards; cryptotephras are typically fine grained (<100 μm in diameter) and/or occur in exceptionally low concentrations. Cryptotephras are defined as horizons that contain volcanic material in such low concentrations that they are not visible upon visual core inspection (Turney et al., 1997). The detection of cryptotephras using density separation techniques within terrestrial, marine and ice-core records is revolutionising the way palaeoenvironmental archives are dated and compared (e.g. Lowe et al., 2001; Wulf et al., 2004; Mortensen et al., 2005; Lane et al., 2011; Wulf et al., 2012; Davies et al., 2010; Abbott and Davies 2012; Davies et al., 2014; Lane et al 2014). Cryptotephra investigations have now been undertaken within a wide-range of different time-intervals (Wastegård et al., 2005; Hibbert et al., 2014), greatly increasing the area over which a diverse number of sediment sequences can be synchronised (e.g. Blockley et al., 2007, Pyne O'Donnell et al., 2012). For example, the Vedde Ash has been traced in Continental Europe (Turney et al., 2006) as far east as Russia (Wastegård et al., 2000) and Slovenia (Lane et al., 2011), south into the Netherlands (Davies et al., 2005) and most southerly in Switzerland (Blockley et al., 2007).

The application of cryptotephrochronology has been adopted to address a plethora of palaeoenvironmental and archaeological questions (e.g. Blockley et al., 2007; Lane et al., 2011; Lane et al., 2014). Distal occurrences have been utilised to augment volcanic history and dispersal compilations derived from the proximal realm (e.g. Larsen et al., 1999, Óladóttir et al., 2011). Deposits have additionally been used for improving chronological models (Brauer et al., 2014) and assessing landscape development (e.g. Dugmore and Newton, 2012). Many researchers' goal is the adoption of cryptotephrochronology in the quest for constraining rapid climatic events and assessing synchroneity between different components of the climate system (Lowe et al., 2008; Davies, 2015). This requires the construction of a comprehensive framework of volcanic events recorded in the Greenland ice-cores and marine sequences. Geochemical signatures, stratigraphic positioning and age estimates are essential building blocks for these frameworks (Lowe et al., 2008, Blockey et al., 2012; Davies et al., 2012; Blockley et al., 2014) (i.e. Fig 2.2). Before updating any framework, tephra discovery requires a careful assessment of origin and ruling out secondary deposition, which may introduce unwanted complexities to the stratigraphical position of the tephra deposit.

2.3.3 Geochemical fingerprinting

2.3.3.1 Major element analysis

Major element geochemical fingerprinting is an essential step for establishing correlations between sequences (Davies et al., 2012). Electron probe microanalysis (EPMA) has been routinely applied to acquire the geochemical composition of tephra deposits (Hunt and Hill, 1993; Hayward, 2012). Wavelength dispersive spectrometry is the preferred method of analysis which provides characterisation of ten major element oxides. An important progress made in EPMA analysis has been the optimisation of operating conditions to permit cryptotephra shards as small as 10 μm to be successfully analysed (Hayward, 2012).

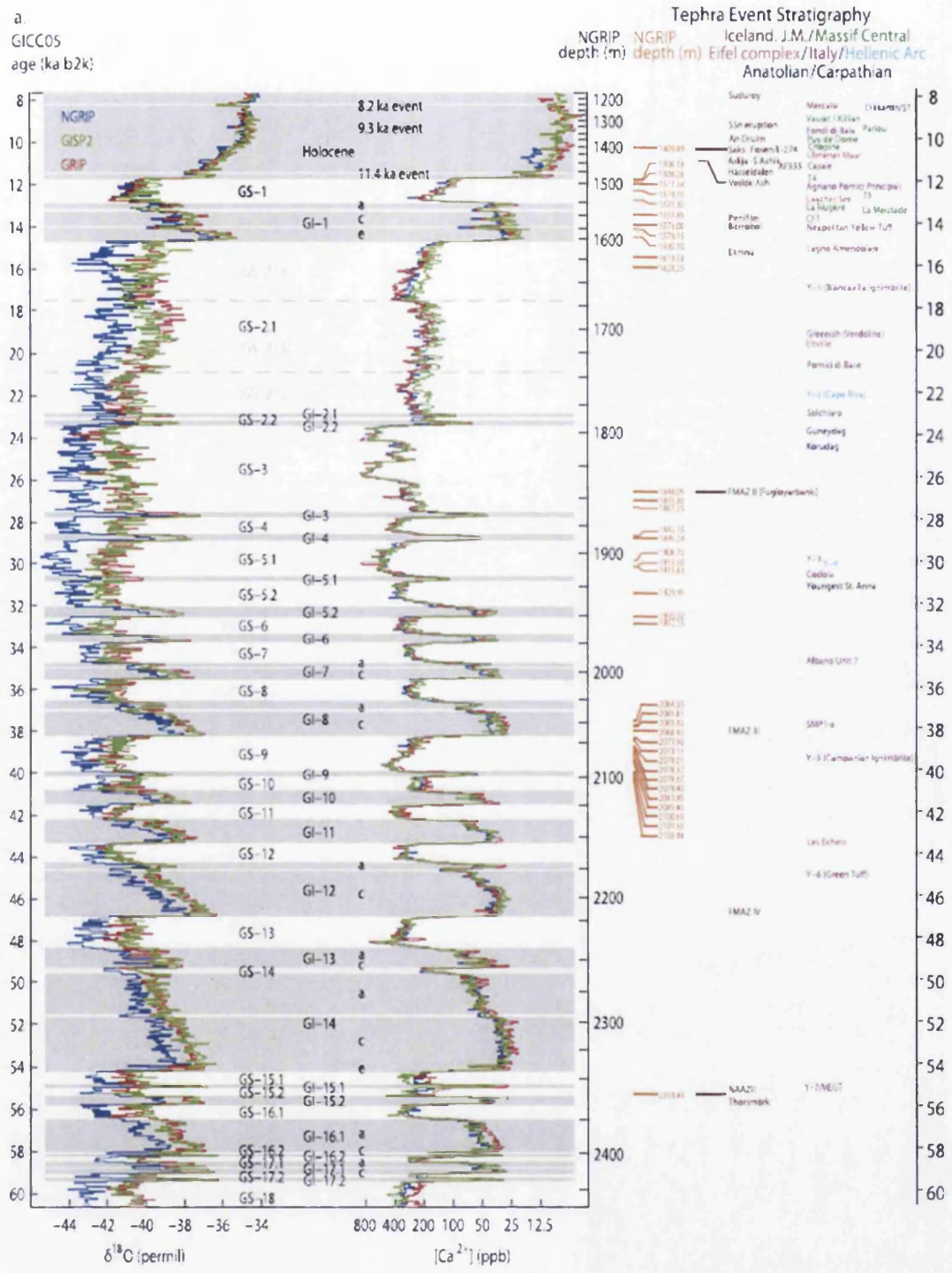

Figure 2.2 The INTIMATE event stratigraphy and corresponding tephrostratigraphical framework for European volcanic records after Blockley et al. (2014). Tephra located within the ice-core record are shown against NGRIP (orange lines) and are reported in Mortensen et al. (2005), Davies et al. (2010) and Bourne et al. (2013). Key tephras from other North Atlantic and continental European volcanic centres are shown.

Internationally accepted reference glasses i.e. Lipari and BCR2G are routinely used, providing a check on analytical quality (Kuehn et al., 2011). Reporting of secondary standards is crucial for the intercomparison of datasets (Kuehn et al., 2011; Davies et al., 2012). Reference standards analysed during EPMA conducted in this investigation are reported in the appendix.

Following EPMA, comparative compositional analysis of proximal and distal deposits is performed to establish volcanic provenance. The majority of Pleistocene proximal records are discontinuous but available volcanic histories provide a valuable assessment of source origin (Larsen et al., 1999). One of the most challenging issues in geochemical analysis is the discovery of several tephras of similar age that have repeated similar geochemical signatures (e.g. Bourne et al., 2013). Employing these deposits is difficult, especially if the potential correlative proxy record contains only one component of these deposits (Bourne et al., 2013; Davies, 2015). Trace element analysis may be necessary in addition to major elements to provide a diagnostic and more robust method of geochemical fingerprinting.

2.3.3.2 Trace element analysis

An advancing analytical approach in tephrochronology is the use of laser ablation inductively-coupled mass spectrometry (LA-ICP-MS) to provide data for thirty petrogenetically significant minor and trace elements (Pearce et al., 1999; 2007). Developments in laser technologies have enabled more controlled ablation of glass-shards and offer the possibility of analysing shards in the 10-20 μm range (Pearce 2010; Abbott et al., 2013; Pearce et al., 2014). Subtle variations in trace elements can retain the signature of different evolutionary phases of an eruptive event (Abbott et al., 2014) and demonstrate that miscorrelations may arise if major elements are used in isolation (Davies et al., 2012, 2014; Bramham-Law et al. 2013). Trace-element signatures of Katla rhyolites that are close in age proved indistinguishable, supporting common origins rather than aiding discrimination (Lane et al., 2011). Much is to be gained from future trace element work to expand the search for unique geochemical fingerprints. Trace element analysis clearly provides an important discriminatory tool for establishing tephra correlations and potential correlatives

must be characterised through 'side by side' microprobe analysis to minimise changes arising from different analytical periods (Pearce et al., 2014).

2.4 Taphonomical assessment

Understanding the stratigraphical distribution of a cryptotephra deposit is key to determining the exact timing of deposition and defining the precise occurrence of the isochron (Davies et al., 2012). The environment of deposition helps govern the degree of dissemination of the distal tephra concentration zone and preservation following site-specific sedimentation processes (Pyne-O'Donnell 2008; Lowe, 2011). Some tephras occur as a single, thin, laterally continuous horizon, whereas others may be discontinuous and dispersed through a sequence up to ten decimetres in thickness (Lowe, 2011). Usually, the point of maximum shard concentration is accepted as the isochron, but a variety of taphonomic and re-working processes can affect the primary depositional signal (Austin et al., 2004). Incorrect positioning of the tephra isochron may lead to erroneous age transfer and inappropriate comparison of climatic information derived from the proxy data. It is therefore essential that the stratigraphical and depositional integrity are thoroughly assessed. This is an issue particularly prevalent in the ocean due to the complexity of processes that transport tephra to the water surface and subsequently within the ocean system (e.g. Austin et al., 2004; Brendryen et al., 2010; Abbott et al., 2011; Griggs et al., 2014; Davies et al., 2014).

2.4.1 Marine tephrochronology: unravelling depositional processes

A shift in recent years has seen an increase in the search for cryptotephras within marine sequences, particularly during MIS 4 and 5 and the Lateglacial (Brendryen et al., 2010; Bourne et al., 2010; Abbott et al., 2011, 2013, 2014; Davies et al., 2014; Jennings et al., 2014). Although macroscopic deposits have been reported for many years (Haflidason et al., 2000; Rasmussen et al., 2003; Wastegård et al., 2006) it is only recently that fine-grained shards have been investigated to expand the potential

for synchronising distal tephra occurrences. Not only have these studies identified previously unknown volcanic events, but have facilitated tephra correlations between cores (Davies et al., 2014). Successful construction of a tephrochronological framework requires a challenging assessment of the integrity of cryptotephra deposits present within marine sequences. Unlike ice-core and terrestrial environments where tephra arrives predominantly by wind dispersal, the marine realm includes additional deposition mechanisms.

The regional dispersal and localised deposition of tephra in North Atlantic marine sequences is the product of several processes occurring aerially and internally within the ocean system, in turn influencing their applicability as isochronous horizons (Brendryen et al., 2010). Tephra shards in the ocean are subject to both secondary transport and depositional processes (Fig. 2.3), which potentially introduces stratigraphic and chronological uncertainties. These are particularly relevant for cryptotephra deposits that are comprised of a low concentration of glass particles and are more susceptible to re-working. Bioturbation may displace or blur the lower contact of the tephra horizon by drawing material down through the profile, reducing the tephra concentration at the peak of deposition. It may also move material upwards through the sequences, again decreasing the concentration of the tephra peak (Ruddiman and Glover 1972; Bromley 1986; McCave 1988; Todd et al., 2014; Cassidy et al., 2014). Direct sedimentological analysis of tephra and cryptotephra deposits, allied to rigorous geochemical fingerprinting and down-core shard concentration profiles can provide important diagnostic evidence for the mode of tephra delivery to the seabed. The main modes of tephra delivery from eruption to ocean water surface and through the water column are presented below (Fig 2.3).

2.4.1.1 Primary airfall

Following an eruption, tephra is ejected into the atmosphere and primary ash fall deposits are expected to contain a well-sorted distribution. Size and density-related processes determine transport of ash through the atmosphere (Sparks, 1981). A primary airfall deposit will most likely contain a greater concentration of fine-grained tephra particles as the distance from source increases. Primary airfall deposits are typically characterised by a homogeneous geochemical population,

representing a single eruption, or multiple homogeneous populations, from very closely timed eruptions (Brendryen et al., 2010).

2.4.1.2 Iceberg rafting

Following an eruptive event, an important transport pathway is the proximal deposition of tephra onto ice-sheets that undergo calving and rafting to distal locations (Fig 2.3) (Brendryen et al., 2010). This process can deliver larger material to a distal depositional site than would typically be associated with primary atmospheric fallout. Iceberg rafting is dependant on the time taken for the iceberg to calve from the ice-sheet into the ocean. It is likely to contain an amalgamation of material sourced from a number of eruptions and different volcanic centres (Ruddiman and Glover, 1972; Lackschewitz and Wallrabe-Adams, 1997; Brendryen et al., 2010). Tephra delivered via iceberg rafting is expected to be characterised by a poorly sorted size distribution and a heterogeneous geochemical signature (Brendryen et al., 2010; Abbott et al., 2011). The identification of co-varying IRD in the sequence is further criterion for identifying iceberg rafting events (Lackschewitz and Wallrabe-Adams, 1997; Davies et al., 2014). Iceberg rafting is likely to compromise the integrity of a tephra horizon by causing significant temporal delay between eruption and subsequent deposition into a sedimentary sequence, potentially by several millennia (Brendryen et al., 2010). It has been suggested that studying iceberg rafted tephra deposits could aid in the reconstruction of glacial ocean surface circulation patterns (Kuhs et al., 2014).

2.4.1.3 Sea-ice rafting

Another potentially important transport mechanism is deposition of tephra onto sea-ice, which can cause time lags of years to decades (Brendryen et al., 2010). Although sea-ice persisted in the North Atlantic during the last glacial, modelling estimates this was limited to the central Arctic Ocean and areas under the influence of the East Greenland Current. This suggests that sea-ice production was typically seasonal, particularly in the Nordic Seas (Stärz et al., 2012).

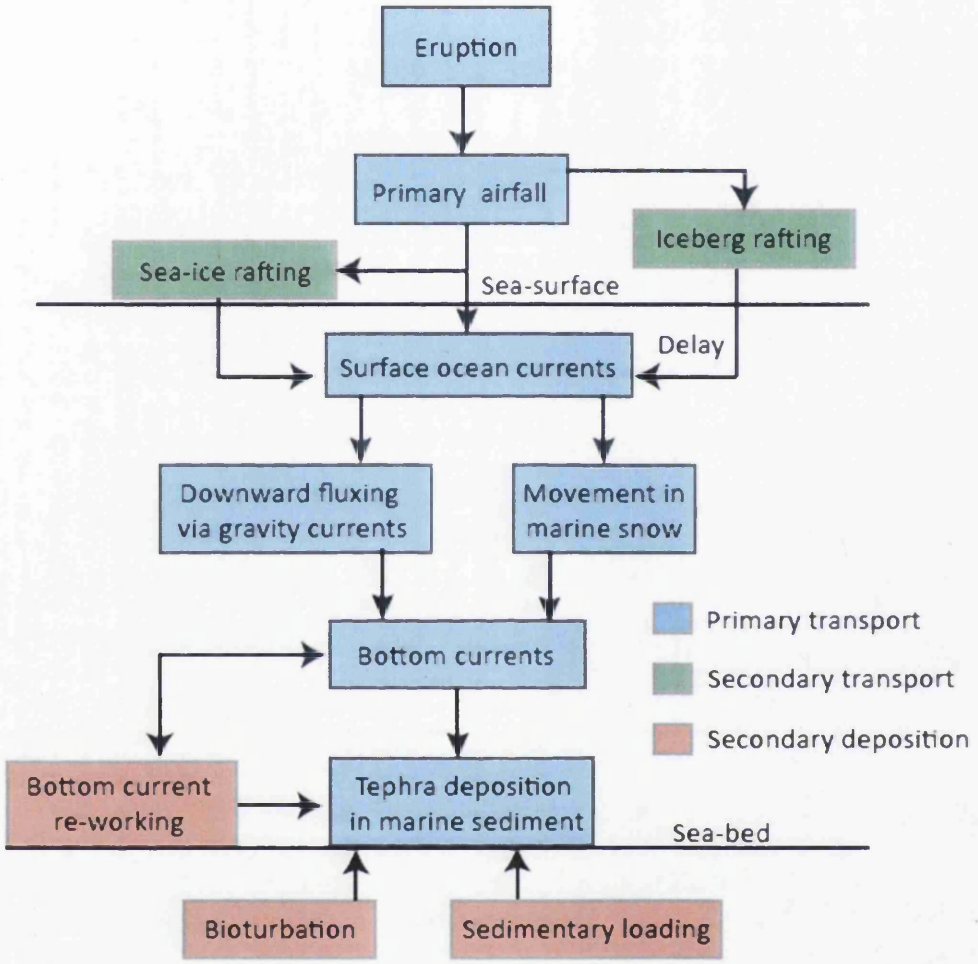

Figure 2.3 Schematic summary of the main processes that can influence the transport and deposition of tephra in the marine environment.

This prevents the accumulation of multiple eruptions and sea-ice rafted deposits are likely to have a homogenous geochemical signature (e.g. Austin et al., 2004). Austin et al. (2004) interpreted that homogeneous geochemistry and coarser shard sizes of the NAAZ II in MD95-2006, were indicative of initial airfall deposition and subsequent transport to the core site by sea-ice. However, coarser shard sizes are not always a diagnostic indicator of sea-ice rafting, as fine-grained glass shards can also be transported long distances on sea-ice. Whilst this mechanism can increase regional dispersal of tephra, it is unlikely to affect the integrity of deposits as an isochron, as the temporal lag is far shorter than the sampling resolution of marine sequences. As this mechanism does not involve calving from ice sheets, the deposit is unlikely to be associated with a coeval IRD signal.

2.4.1.4 Ocean Currents

Following tephra deposition onto the ocean surface by means of wind, iceberg rafting or sea-ice rafting, glass shards will move from the surface down to the seabed (Wallrabe-Adams and Lackschewitz, 2003). Laboratory experiments demonstrate that vertical density currents generated by ash loading allow the movement of particles to overcome strong density gradients in the ocean and transport ash one to three orders of magnitude faster than is possible by Stokes Law (Carey, 1997; Manville and Wilson, 2004). Wallrabe-Adams and Lackschewitz (2003) hypothesised that glass particles could be transported laterally over a relatively large distance (20-55 km) during the sinking process. However, rapid settling of ash particles implies that transport through the water column would not affect the chronological integrity of the deposit. Although residence time in the water column can be affected by turbulence and salinity boundaries (Manville and Wilson, 2004), this is unlikely to keep a shard in suspension for more than a few days to weeks, since tephra is likely to fall through the water column within marine snow (Fig 2.3). Wiesner et al. (1995) demonstrated that the vertical oceanic settling velocities into deep-water sediment traps in the South China Sea were >2 cm/s following the paroxysmal phase of the Pinatubo eruption in 1991.

One process that may disturb tephra following deposition is redistribution and erosion by bottom currents. Michels (2000) calculated that geostrophic bottom

current velocities may range from 25 to 36 cm/s in the Nordic Seas during storm events. This could influence spatial distribution of tephra, resulting in distinct variations in horizon thickness and glass shard concentration in nearby cores (Wallrabe-Adams and Lackschewitz, 2003). An increase in bottom currents during interstadials and storm events may remobilise material from previously deposited eruptions. Any bottom-current induced erosion is likely to mobilise tephra material and produce an upward gradational distribution or tail-off in shard concentration (e.g. Abbott et al., 2013, 2014). For cryptotephra deposits, an upward tail in concentration from a main peak would be expected to have a corresponding homogeneous geochemical signature throughout the deposit. However, material from older eruptions may become remobilised and transported from one site to another, resulting in the deposition of material sourced from a number of different events. This reinforces the need for careful scrutinisation of cryptotephra shard concentration profiles together with an assessment of geochemical results from several intervals within these deposits (Abbott et al. 2014; Davies et al., 2014).

2.4.1.5 Post-depositional re-working

Following deposition of tephra onto the seabed it is susceptible to bioturbation, as well as being reworked by bottom currents (Abbott et al., 2011). Characteristic sedimentological evidence of bioturbation includes a gradational upper contact that is spread over several centimetres, introducing a number of stratigraphical uncertainties (Manville and Wilson, 2004; Lowe, 2011, Todd et al., 2014). Low concentrations of shards below the peak are also considered to be a signature of bioturbation, although this is unlikely to affect position of the peak in shard concentration (Ruddiman and Glover, 1972). Remobilisation of material can occur as a result of turbidity currents, and present-day tephrostratigraphic techniques are not sufficient to isolate the complex interplay of post-depositional processes and pinpoint the modification mechanisms at work.

2.4.1.6 Exploring micro-sedimentological features

Two-dimensional (2D) investigations, such as thin section analysis, reveal many micro-sedimentological features in a range of sedimentary environments (e.g. Harris, 1998; Kemp, 1999; Paulsen et al., 2003; Atkins, 2004; Payne et al., 2006; Menzies and Brand, 2007; Kooistra and Pulleman, 2010). Recent investigations by Matthews et al. (2011a) examined the potential of micromorphology to identify 2D micro-sedimentological structures within tephra deposits from a marine core in the Southern Adriatic. This work identified features associated with turbidite deposition, bioturbation and additional micro-scale evidence of gravitational loading and resedimentation. Micromorphological analysis of sediment structures has the potential to provide additional supporting evidence for understanding the taphonomic processes associated with tephra deposition.

Exciting new studies have demonstrated the potential of applying three-dimensional (3D) techniques such as X-ray microtomography (μCT) to Quaternary sediments, providing greater insight into sedimentological processes (Kilfeather and van der Meer, 2008; Tarplee et al., 2011; Bendle et al., 2015). The ability to examine the 3D internal architecture of tephra deposits within cores is currently untested but may permit visualisation of a range of sedimentary features, facilitating examination of sediment/tephra interface through several planes of the core. This may improve stratigraphic accuracy of the tephra isochron, whilst supporting the interpretation of marine sedimentary processes. When combined with detailed analysis of the tephra geochemistry, shard distribution and particle size analysis, this approach should provide a more precise assignment of tephra in the marine environment.

High resolution μCT is a non-destructive method for imaging internal structures in three dimensions at micron-scale spatial resolution, based upon the fundamental principle that x-ray attenuation is a function of X-ray energy and the density and atomic number (Z) of scanned material (Landis and Keane, 2010; Cnudde and Boone, 2013). A series of radiographs are compiled to create 3D representations that can be computationally manipulated to perform a wide array of visualisation tasks (Ketcham and Carlson, 2001). Successful geological applications of μCT include the study of the pore geometry of carbonate reservoirs (Purcell et al., 2006), rock fluid analysis (Wennberg et al., 2009), glacigenic deformation structures (Tarplee et al., 2011) and proximal volcanic textures (Polacci et al., 2006). As tephra shards and their host sedimentological matrix fall within known density ranges (Turney, 1998;

Blockley et al., 2005) they should exhibit different X-ray absorption properties, allowing the detection and isolation of tephra in a marine core through the use of μCT techniques. However, the contrast between these materials is very small, with quartz (2.65 g/cm^3) and heavy minerals exhibiting similar densities to basaltic tephra (>2.5 g/cm^3). This may cause an overlap between the sediment and tephra reconstructions but, if this contrast can be detected, it should be possible to deconvolve the two phases using histograms of density variations (see section 3.10).

2.5 North Atlantic tephrochronological framework for MIS 2 and 3: current status

2.5.1 North Atlantic marine framework

Tephra deposits in North Atlantic marine sediments, retrieved mainly from the IRD belt, were originally described by Bramlette and Bradley (1941) and later by Ruddiman and Glover (1972). They named these Late Pleistocene horizons the NAAZ I, II and III. Investigations in the Faroes region during the past decade have identified three new tephra deposits; FMAZ II, III and IV (Rasmussen et al., 2003; Wastegård et al., 2006; Wastegård and Rasmussen, 2014). Five ash zones, 'V1-V5' spanning MIS 2-3 have additionally been discovered in numerous cores from the Reykjanes Ridge (Lackschewitz and Wallrabe-Adams, 1997). Tephra deposits covering this interval have also been detected in the Iceland Sea (Voelker et al., 2000). These tephras form the current marine tephrochronological framework for MIS 3 (Fig 2.6). This work has mainly focused on visible horizons or coarse-grained tephra shards, >150 μm in diameter, and may have failed to detect additional deposits present in low concentrations within finer fractions. The identification of coarser tephra shards in isolation may preferentially target material that has been susceptible to secondary deposition. As such, the low number of horizons detected in this interval may be a reflection of the limited number of cryptotephra studies employed during MIS 3, rather than the relative absence of tephra deposits. The following section outlines these previously discovered tephra deposits within the marine environment during MIS 2 and 3 (16-55 ka) and discusses their integrity and

integration within a marine tephra framework (Fig 2.6). The location of individual cores referred throughout the thesis is presented in Figure 2.4.

2.5.1.1 NAAZ II

The NAAZ II forms a complex ash zone that has been discovered extensively within the marine environment throughout the North Atlantic, rendering it a significant marker horizon during DO-15 and MIS 3 (Ruddiman and Glover, 1972; Kvamme et al., 1989; Lackschewitz and Wallrabe-Adams, 1997; Haflidasson et al., 2000; Austin et al., 2004; Wastegård et al., 2006; Brendryen et al., 2011) (Fig 2.7). A detailed geochemical characterisation of this horizon was originally performed by Kvamme (1989) and Lacasse et al. (1996), who recognised that the ash zone represents the products of multiple Icelandic volcanic eruptions, with one rhyolitic (II-RHY-1) and four mixed and dispersed basaltic components (the transitional alkali basaltic II-TAB-1, and the tholeiitic II-THOL-1, II-THOL-2, II-THOL-3). These are thought to have been deposited by a combination of ice-rafting and primary deposition with subsequent transportation via sea-ice (Austin et al., 2004). The II-RHY-1 component is the most widespread of the NAAZ II in marine cores across the North Atlantic (Fig 2.5), whereas the basaltic components are more irregularly dispersed (Wastegård et al., 2006; Brendryen et al., 2011). The II-THOL-2 component dominates cores from the Reykjanes Ridge (Lackschewitz and Wallrabe-Adams, 1997; Haflidasson et al., 2000).

This may be attributed to eruption dynamics; rhyolitic material is injected higher into the atmosphere than material of basaltic eruptions due to the greater explosivity of Icelandic silicic eruptions than phreatomagmatic basaltic eruptions (Larsen and Eiríksson, 2008). It may also reflect different modes of tephra transport and re-working. The rhyolitic component has been correlated to its geochemically related proximal deposit; the Thorsmörk ignimbrite, sourced from the Tindfjallajökull volcanic system in Iceland and dated to 54.5 ± 2 ka b2k, using argon-argon dating (Storey and Stecher, 2009).

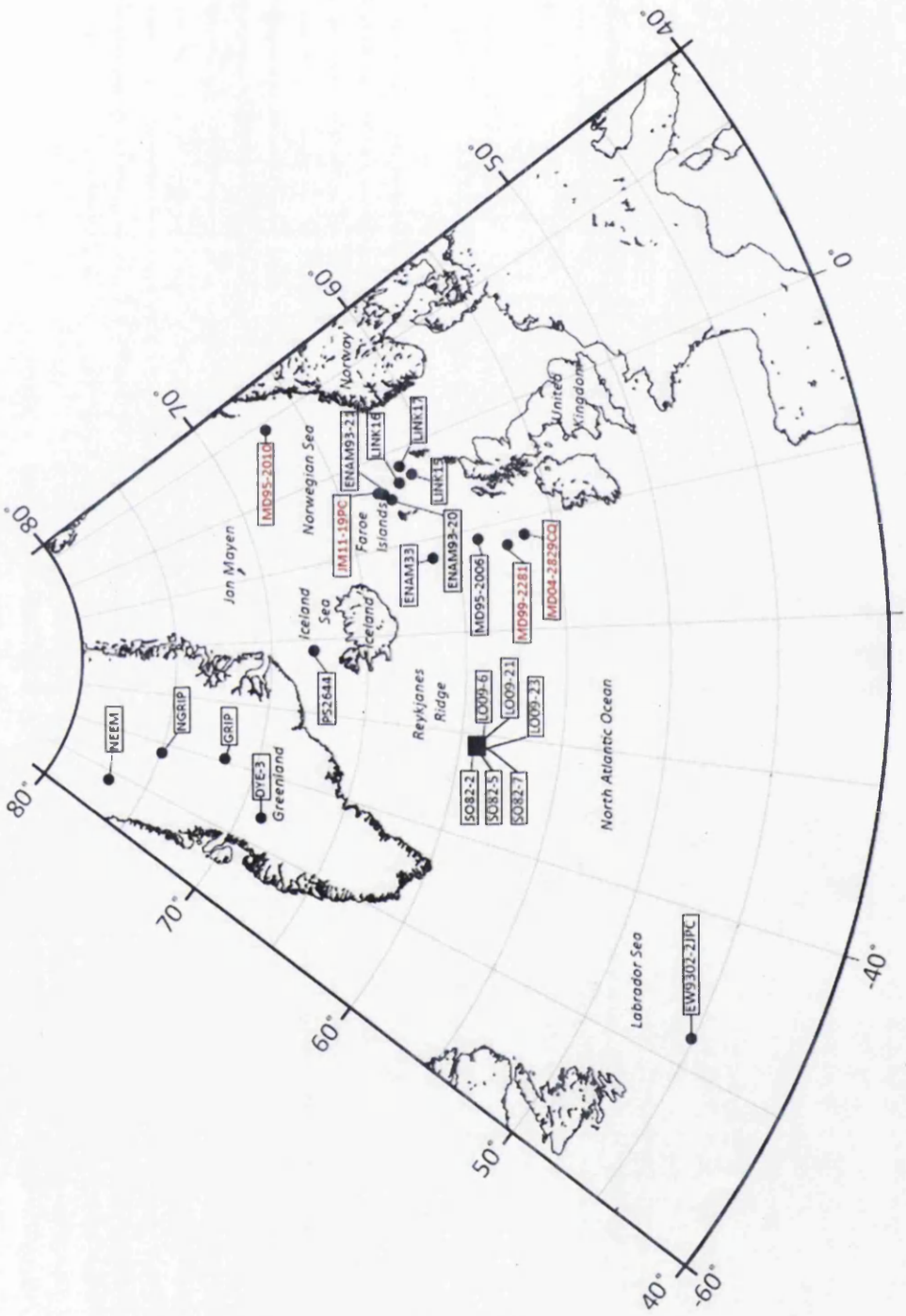

Figure 2.4 Location map of coring sites for North Atlantic marine and ice-core sequences referred to in the thesis.

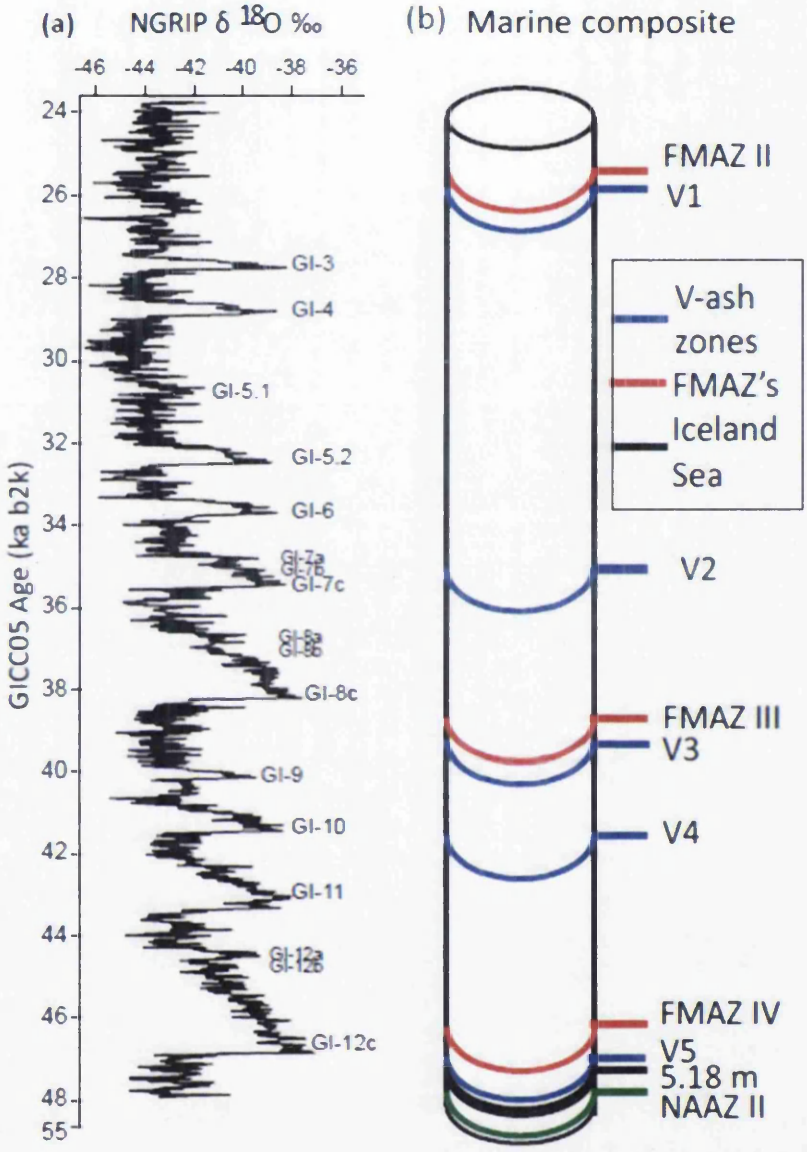

Figure 2.5 North Atlantic marine tephrochronological framework aligned to (a) NGRIP for schematic purposes to illustrate stratigraphic position. (b) Marine tephra occurrences are shown schematically based upon their relative stratigraphic position (Lackschewitz and Wallrabe-Adams, 1997; Voelker et al., 2000; Rasmussen et al., 2003; Wastegård et al., 2006).

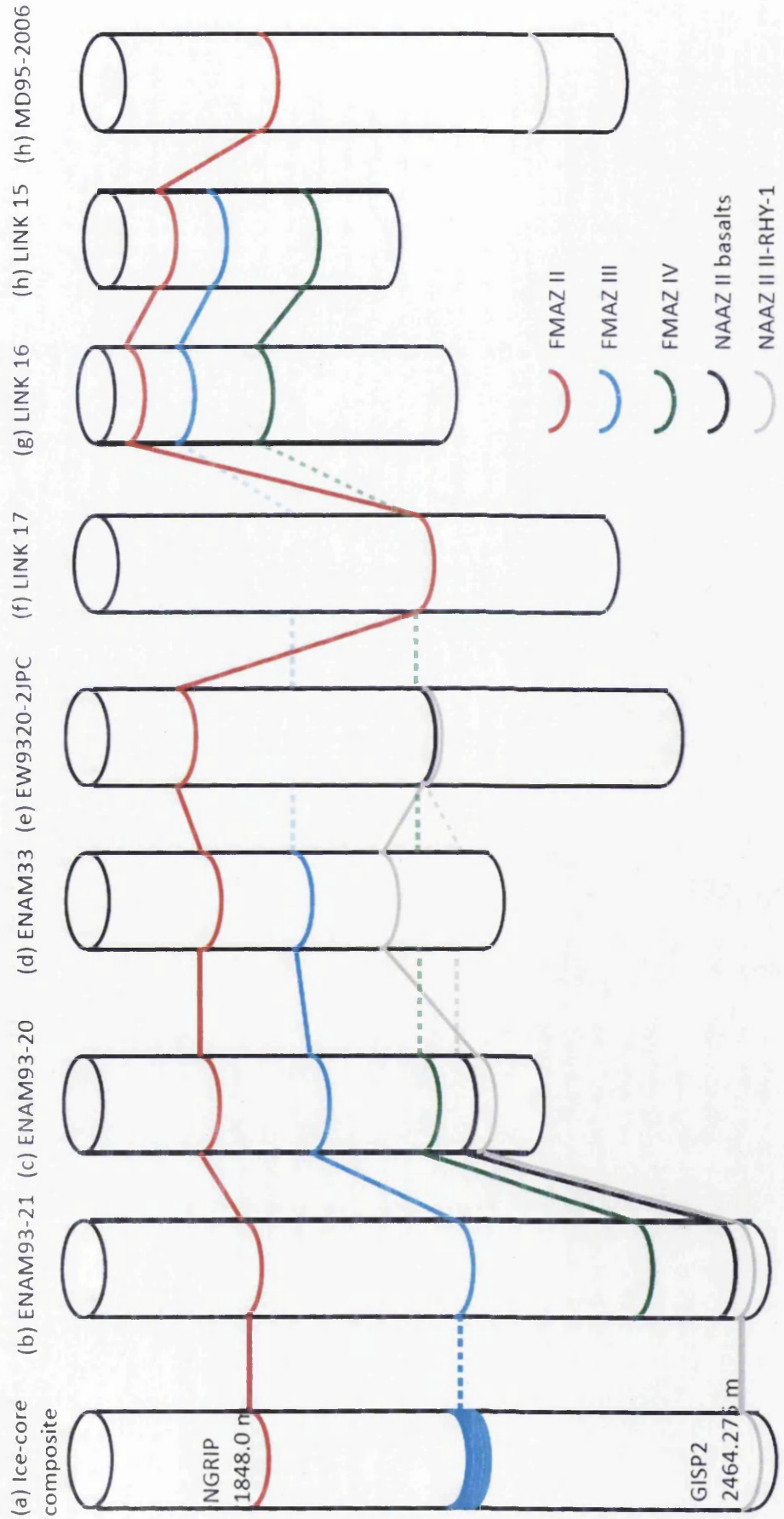

Figure 2.6 North Atlantic tephrostratigraphic framework and potential ice-marine correlations. (a) Tephra deposits found within the Greenland ice-cores are correlated to geochemically equivalent horizons present within North Atlantic marine cores. (b-h) Stratigraphic position of tephra deposits within cores found in the Faroes region (Rasmussen et al., 2003; Wastegård et al., 2006; Wastegård and Rasmussen, 2014) and Barra Fan (Austin et al., 2012).

The study of high-resolution marine sequences has revealed a temporal separation between the II-RHY-1 and other basaltic components, which may have been deposited ca. 2000 years later (Wastegård et al., 2006) (Fig 2.6). Both basaltic and rhyolitic components have been found at the same stratigraphical depth in EW-3JPC2, which may be a reflection of low sedimentation rate or secondary re-working. The potential separation between components highlights that caution should be given to tie-lines defined by correlations with the NAAZ II and, at present, the II-RHY-1 component offers the most significant value for tephra correlations (Austin and Abbott, 2010).

2.5.1.2 VZ Ash Zones (V1-V5)

A suite of five ash zones (V1, V2, V3, V4, V5) have been detected by Lackschewitz and Wallrabe-Adams (1997) in five individual marine cores in the Reykjanes Ridge (Fig 2.8). Glass-shards are basaltic in composition and sourced from Icelandic volcanism (Fig 2.9). Relative ages of the ash layers were determined through their position in the chronostratigraphical framework derived from the $\delta^{18}O$ record, orbital tuning and radiocarbon dates. Downcore ash records reveal characteristic variations that can be correlated between records, although it is not possible to correlate single ash peaks. Ash layers have been divided into several geochemically similar groups based upon time-equivalent intervals with similar peaks (Lackschewitz and Wallrabe-Adams, 1997) (Fig 2.8). The ash zones are documented within the following time intervals; V5 (52,500-46,200 yr B.P), V4 (45,500-41,000 yr B.P), V3 (41,000-36,500 yr B.P), V2 (36,500-29,800 yr B.P), V1 (28,400-20,000 yr B.P).

An additional distinct peak, Vx, has been discovered within the V1 ash zone solely in SO82-5 (Fig 2.8). The V1-V5 ash zones exhibit a wide geochemical range within each deposit and display an affinity to a variety of Icelandic source volcanoes (Fig 2.9). The Vx peak exhibits a homogeneous geochemistry and displays strong affinity to the Hekla system. The V1-V4 deposits correlate with high amounts of IRD (Fig 2.8) and in conjunction with geochemical heterogeneity (Fig 2.9) imply the ash zones were deposited via iceberg rafting and likely to contain an amalgamation of individual eruptions.

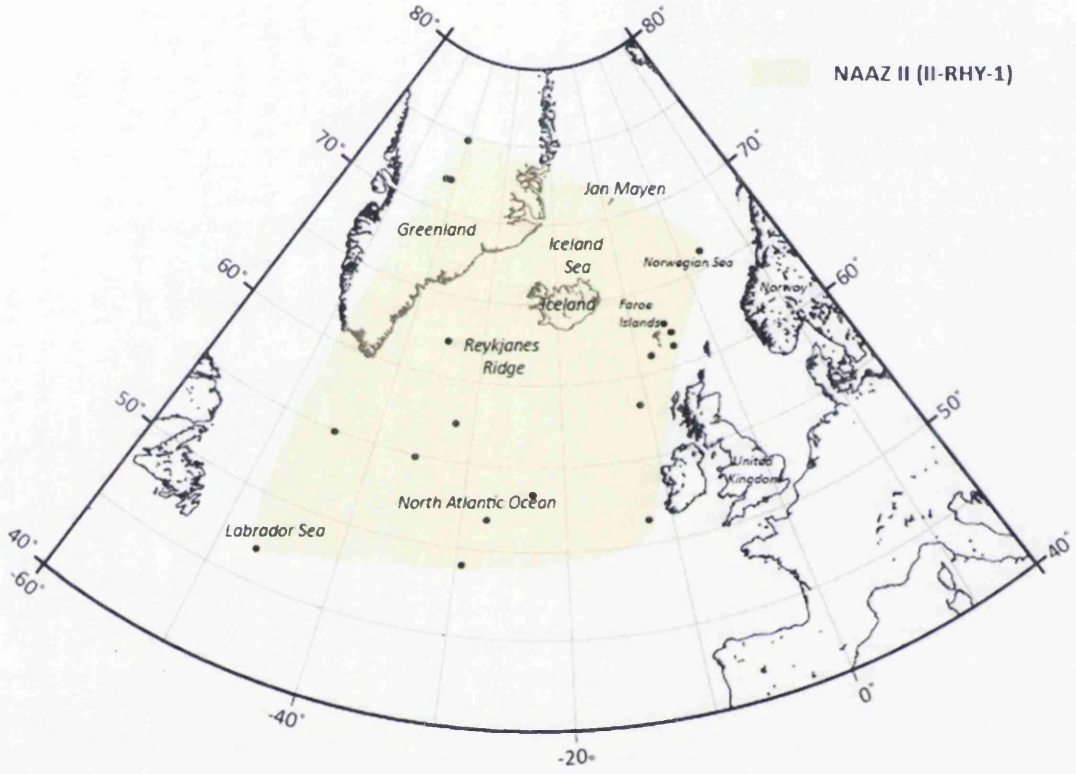

Figure 2.7 Distribution of the NAAZ II (II-RHY-1) within the North Atlantic (Ruddiman and Glover 1972; Kvamme et al., 1989; Gronvöld et al., 1995; Lackschewitz and Wallrabe-Adams, 1997; Zielinski et al., 1996; Haflidason et al., 2000; Austin et al., 2004; Wastegård et al., 2006; Brendren et al., 2011).

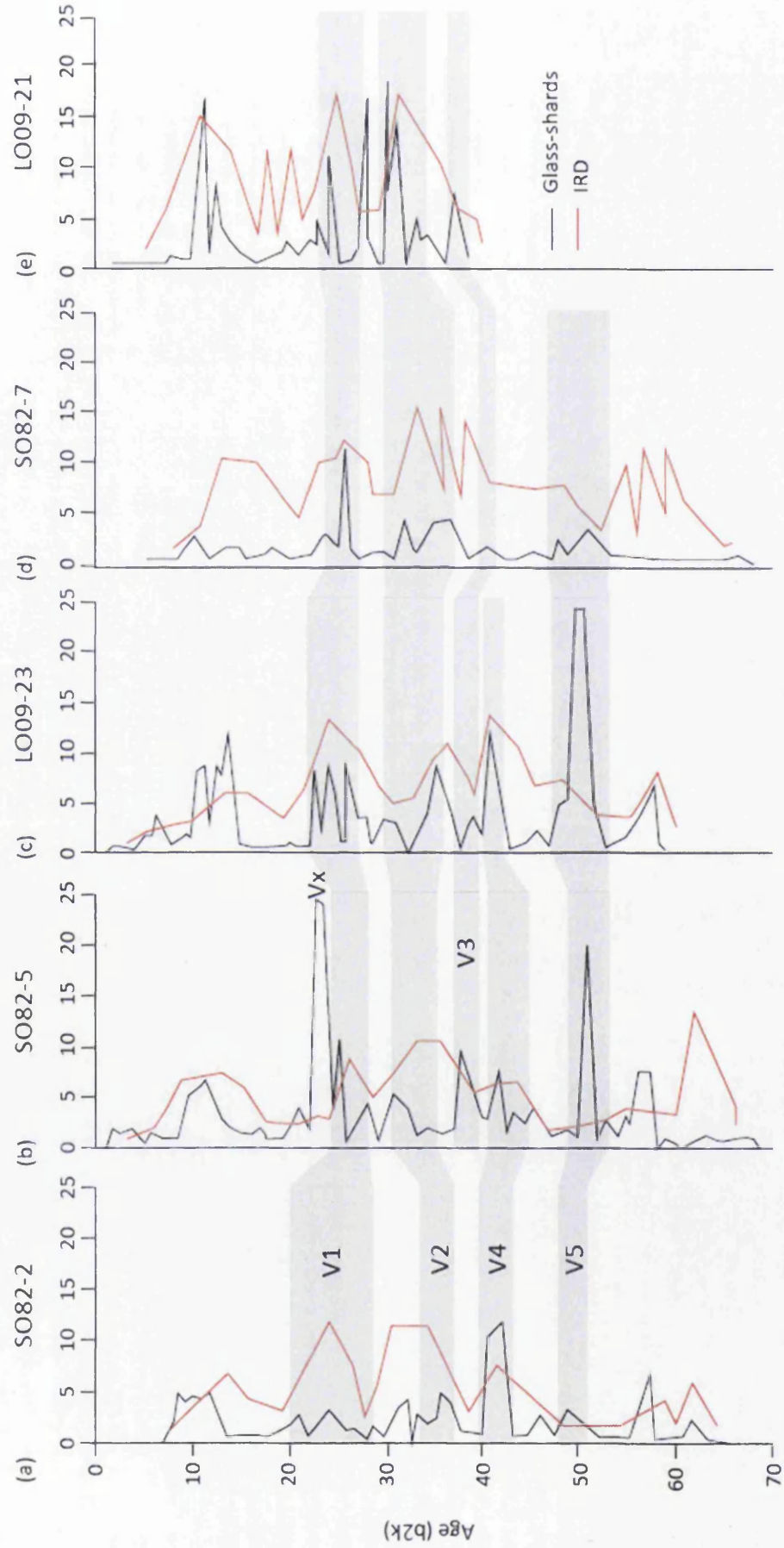

Figure 2.8 Amount of glass shards and IRD (given as % of 125-500 µm fraction) of analysed cores from the Reykjanes Ridge after Lackschewitz and Wallrabe-Adams (1997). The positions of the V1-V5 ash zones are based upon time-equivalent intervals with similar ash and geochemical peaks. Accumulation rates of IRD are also presented alongside glass-shard counts (g/cm^2*10^3).

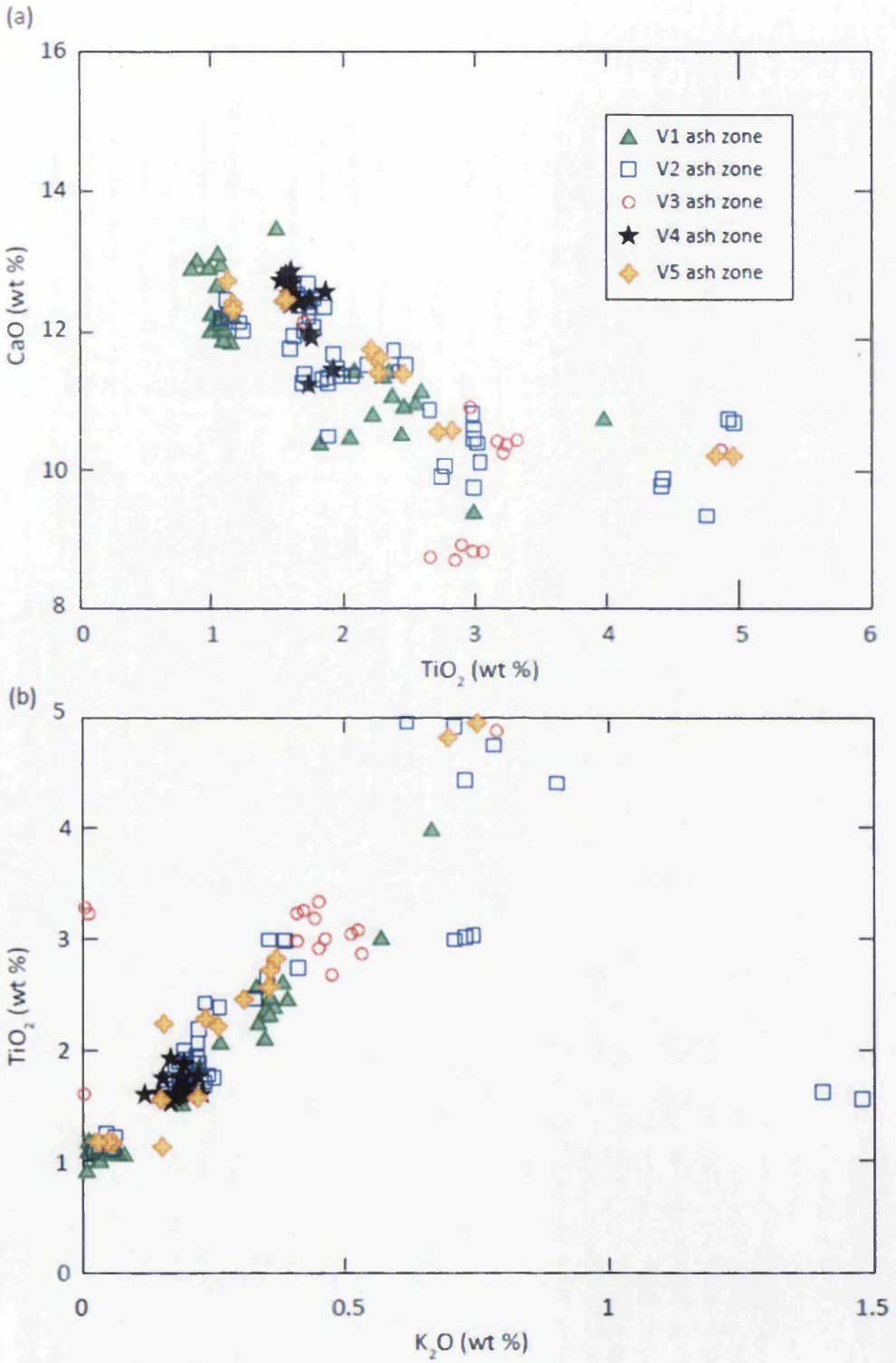

Figure 2.9 Major oxides (wt%) of the V1-V5 ash zones derived from four marine cores on the Reykjanes Ridge (Lackschewitz and Wallrabe-Adams, 1997). All data have been normalised to 100% total oxide concentrations.

As such, their use as isochronous markers may be limited. However, V5 and Vx have no corresponding IRD signal and suggest they were either deposited from a primary process or local sediment gravity flows (Fig 2.8). These two deposits have the potential to act as isochronous tie-lines between the Reykjanes Ridge and other North Atlantic records.

2.5.1.3 Faroe Marine Ash Zones II, III and IV

Investigations in the Faroes region during the past decade have identified three new MIS 3 tephra deposits; FMAZ II, III and IV (Rasmussen et al., 2003; Wastegård et al., 2006, Wastegård and Rasmussen, 2014). The FMAZs exhibit a basaltic composition and vary in geochemical homogeneity, stratigraphic position and dispersion within sequences (Fig 2.5). Each horizon exhibits similar geochemical compositions to the V ash zones described on the Reykjanes Ridge and these will be explored within chapter 4 to establish potential correlations between records (Fig 2.10).

2.5.1.4 FMAZ II

FMAZ II was first discovered in marine cores near the Faroe Islands as a black visible horizon that varies from 2-10 cm in thickness and was thought to have been deposited by primary airfall (Rasmussen et al., 2003). The tephra occurs in DO-3 in all analysed cores, shortly after the warmest peak of the interstadial according to magnetic susceptibility measurements (Rasmussen et al., 2003). The deposit has been dated to 22,900-23,300 ^{14}C years, derived from numerous Faroese cores. The geochemistry is similar in all cores and displays affinity to the Hekla/Vatnafjöll volcanic system (Wastegård et al., 2006) (Fig 2.10a). A record of the FMAZ II has additionally been discovered in the coarse-size fraction within a core from the Barra Fan (Austin et al., 2012) and the Labrador Sea (Wastegård et al., 2006). This highlights a wide distribution in the North Atlantic, likely to have been aided by ice-rafting to more distal locations (Fig 2.11). A secondary geochemical population, FMAZ II-2, has been discovered solely in ENAM33 (Fig 2.10a).

2.5.1.5 FMAZ III

FMAZ III was originally described in the Faroes region as the '33 ka tephra', where it forms a visible scattered tephra zone spanning the transition into the peak warmth of DO-8, identified in the ratio between benthic foraminifera abundances (Rasmussen et al., 2003) (Fig 2.11). In ENAM93-21, the deposit forms a dispersed zone spread over 40 cm, with a division of fresh basaltic particles in the lower 25 cm and higher abundances of weathered, larger particles in the upper 15 cm, considered to be ice-rafted (Rasmussen et al., 2003). Assigning an isochron position has been hampered by the highly dispersed nature of the ash zone. The majority of shards within the deposit exhibit an affinity to the Grímsvötn system but differ in homogeneity between cores, which was initially suggested to equate to tephra sourced from different stages of a single eruption (Wastegård et al., 2006) (Fig 2.10b). A sub-ordinate population, FMAZ III-2, was derived from ENAM93-21 and exhibits a different source origin, highlighting the variation in geochemical compositions with the deposit (Fig 2.10b).

Recent ice-core investigations have detected a suite of eruptions with similar geochemistry to shards derived from the FMAZ III in the marine environment (see section 2.5.3.3). As a consequence, Bourne et al. (2013) suggest that the FMAZ III most likely represents a complex ash zone in the marine environment made up of material from several closely timed eruptions (Fig 2.10c). This has major implications for establishing tephra correlations during this period and a re-evaluation of the deposit is required to assess whether individual, stratigraphically equivalent horizons seen in the ice can be resolved in the marine realm.

2.5.1.6 FMAZ IV

The FMAZ IV is a recent discovery and appears as a thick black horizon in a number of marine cores in the Faroe Shetland Channel (Wastegård and Rasmussen, 2014) (Fig 2.10d, 2.11). The deposit exhibits an affinity to the Grímsvötn system and is thought to have been deposited during DO-12 and dates to ca. 47,000 years BP according to age model estimates (Wastegård and Rasmussen, 2014).

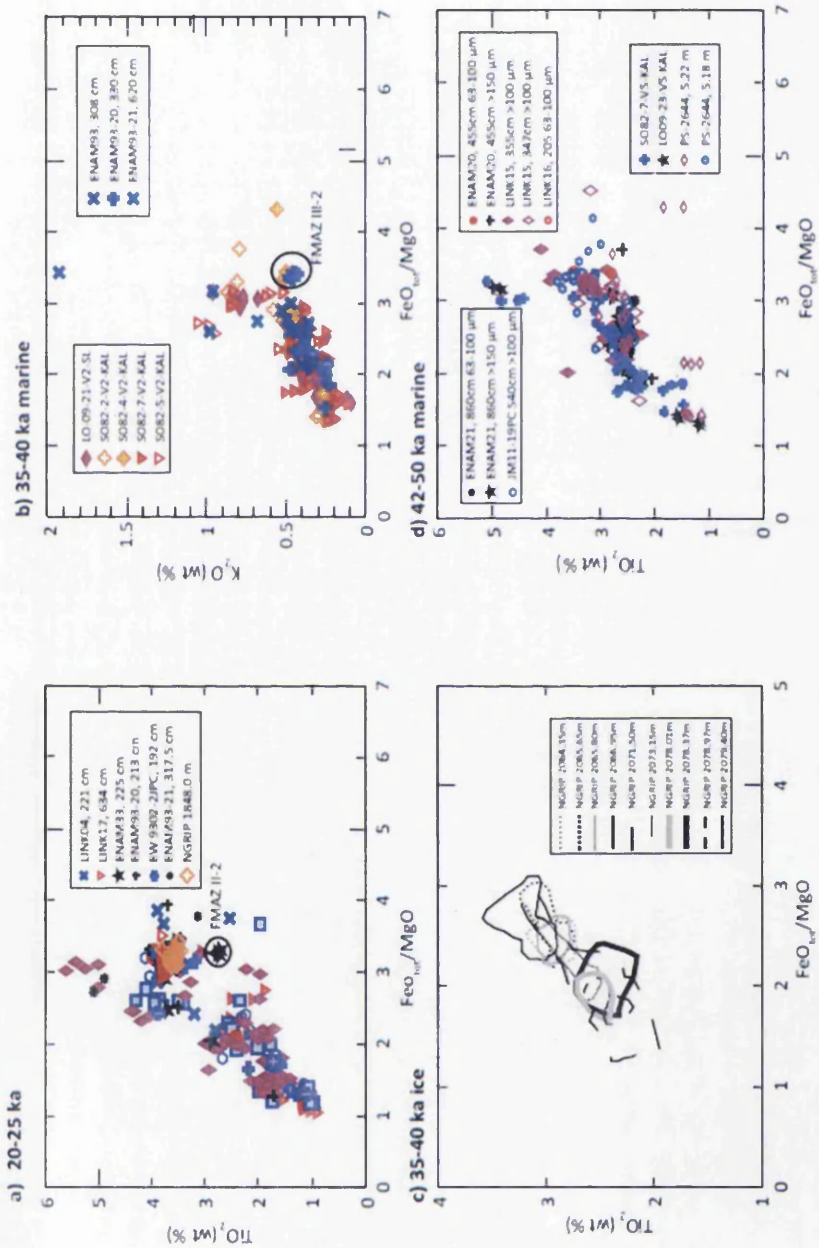

Figure 2.10 Major oxide results (wt%) for glass shards from a variety of marine and ice-core data-sets. (a) Geochemical results for reported FMAZ II deposits in the Faroes region, Labrador Sea (Wastegård et al., 2006) and NGRIP (Davies et al., 2008) and the V1 deposit from the Reykjanes Ridge (Lackschewitz and Wallrabe Adams, 1997). (b) FMAZ III derived from cores in the Faroes region (Wastegård et al., 2006) and the V2 ash zone from the Reykjanes Ridge (Lackschewitz and Wallrabe-Adams, 1997). (c) Geochemical compositional envelopes for cryptotephra deposits identified in NGRIP between 38-40 ka (Bourne et al., 2013). (d) FMAZ IV derived from Faroese cores (Wastegård and Rasmussen, 2014), the V5 ash zone (Lackschewitz and Wallrabe-Adams, 1997) and tephras from the Icelandic deep-sea core PS-2644 (Voelker and Haflidason, 2015).

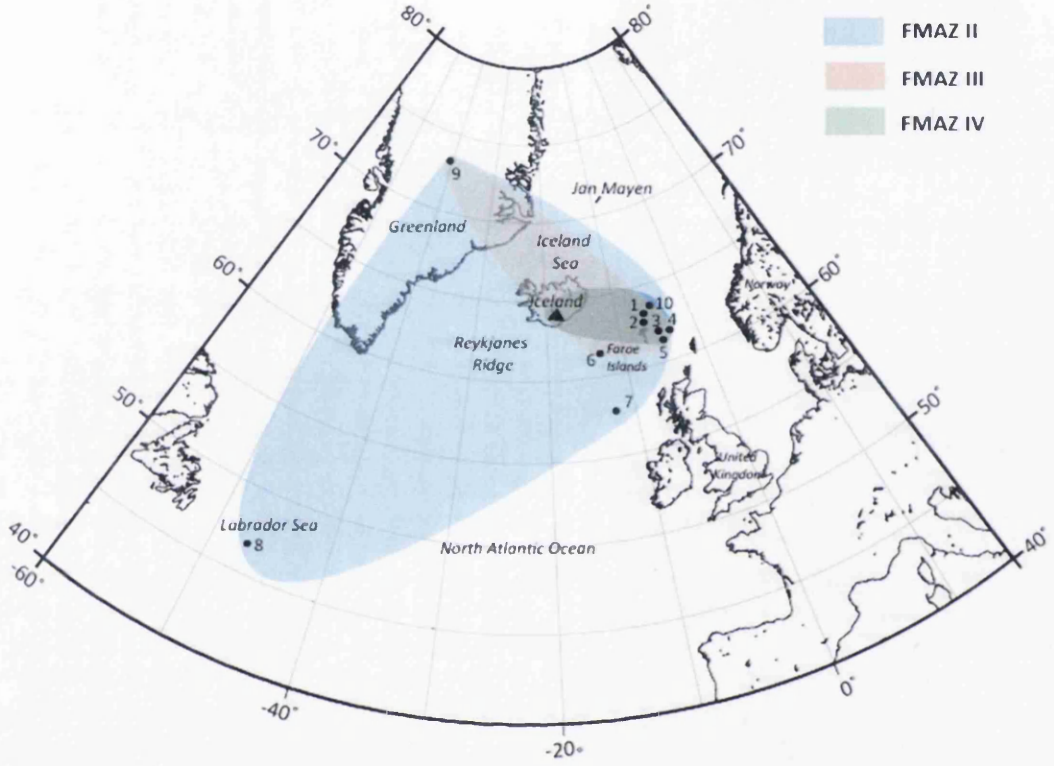

Figure 2.11 Distribution of the FMAZ II, III and IV within the North Atlantic. 1: ENAM93-21 (Rasmussen et al., 2003). 2: ENAM93-20 (Rasmussen et al., 2003). 3: LINK 16 (Wastegård et al., 2006). 4: LINK 17 (Wastegård et al., 2006). 5: LINK 15 (Wastegård et al., 2006). 6: ENAM33 (Rasmussen et al., 2003). 7: MD95-2006 (Austin et al., 2012). 8: EW 9302-2JPC (Wastegård et al., 2006). 9: NGRIP (Davies et al., 2008, 2010). 10: JM11-19PC (Wastegård and Rasmussen, 2014).

The deposit exhibits a similar geochemical composition to the V5 ash zone and a basaltic layer presented in Voelker et al. (2000) (see section 2.5.1.7), both of which fall within a similar stratigraphic position (Fig 2.10d).

2.5.1.7 Icelandic sea tephras (PS2644)

A deep-sea core sequence, retrieved from the northwestern margin of Iceland has revealed fifty-one tephra deposits of varying composition, homogeneity and source location (Voelker and Haflidason, 2015). The majority of these results have recently been published and as a result are not utilised within the thesis. However, two basaltic deposits, 5.18 m and 5.22 m, in the lower part of MIS 3 have been previously reported in Voelker et al. (2000) and have been used for comparisons where applicable (Fig 2.10d). Correlations between planktonic $\delta^{18}O$ and IRD records of sediment core PS2644 and the $\delta^{18}O$ record of GISP2 suggest deposition occurred after the onset of H5 in DO-12 (Fig 2.12). Both deposits are heterogeneous and display affinity to a variety of eruptive centres (Fig 2.10d). However, a large basaltic component with a Grímsvötn affinity is reported in 5.18 m and is used for a number of geochemical comparisons (Fig 2.10d).

Voelker and Haflidason (2015) suggest many of the deposits within the record may represent useful chronostratigraphic markers. However, the sequence is characterised by numerous indistinct peaks, a predominance of geochemical heterogeneity and a relatively high IRD signal throughout (Fig 2.12). These are characteristic secondary depositional signals that suggest ash is likely to have been derived from ice-rafting, gravity flows and subsequent re-working, which greatly affects the integrity of the tephra deposits. Careful stratigraphic and geochemical scrutinisation should be exercised when utilising data reported in Voelker and Haflidason (2015) to prevent erroneous synchronisation.

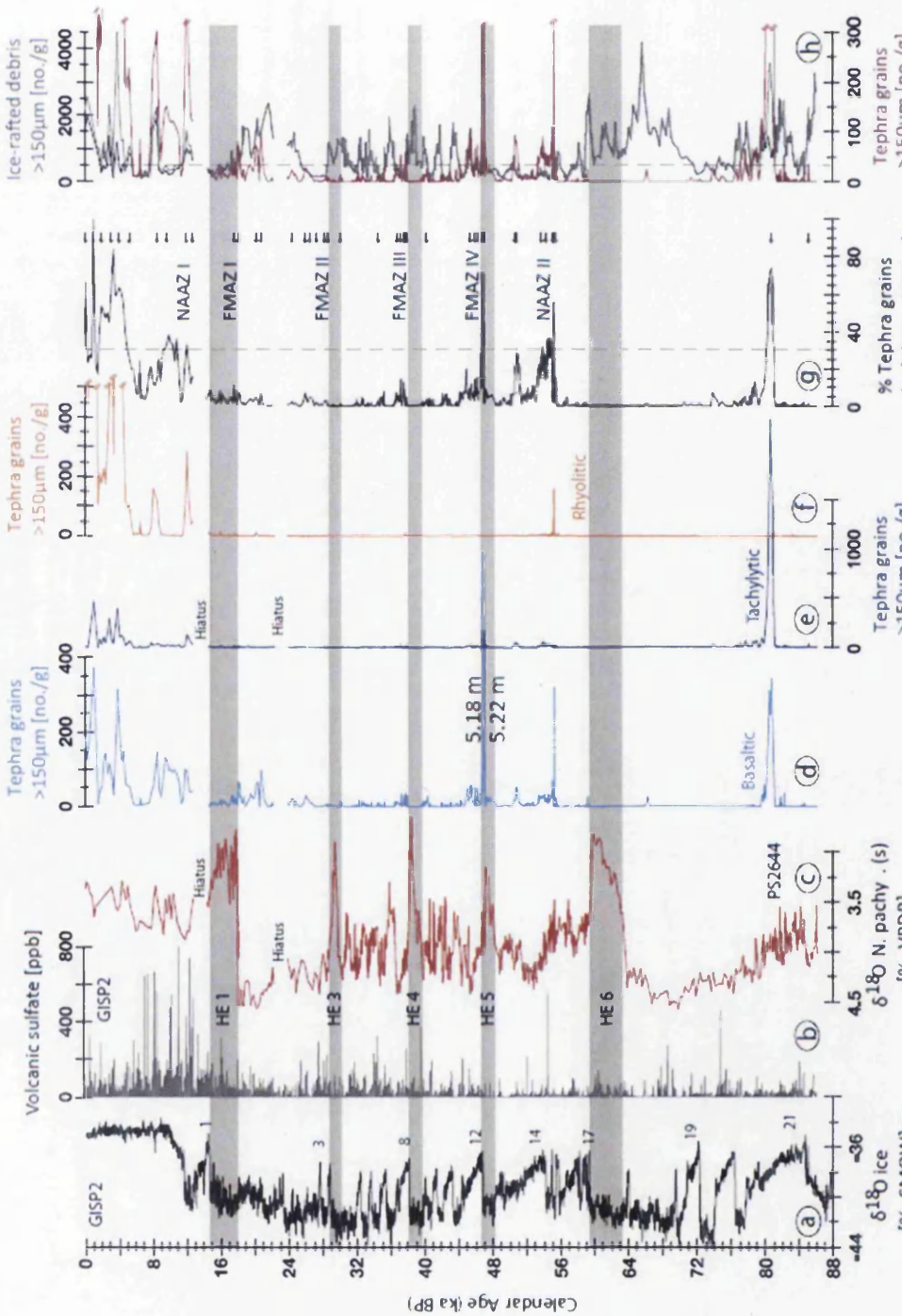

Figure 2.12 Tephra abundances for the PS2644 sequence in comparison to GISP2, volcanic sulphate records and planktonic foraminifera derived from Voelker and Haflidason (2015). The grey levels indicate layers that were sampled for geochemical analysis by Voelker and Haflidason (2015). Positions of the 5.18 m and 5.22 m tephras referred to in the framework have been highlighted. Positions of the FMAZ's have also been indicated.

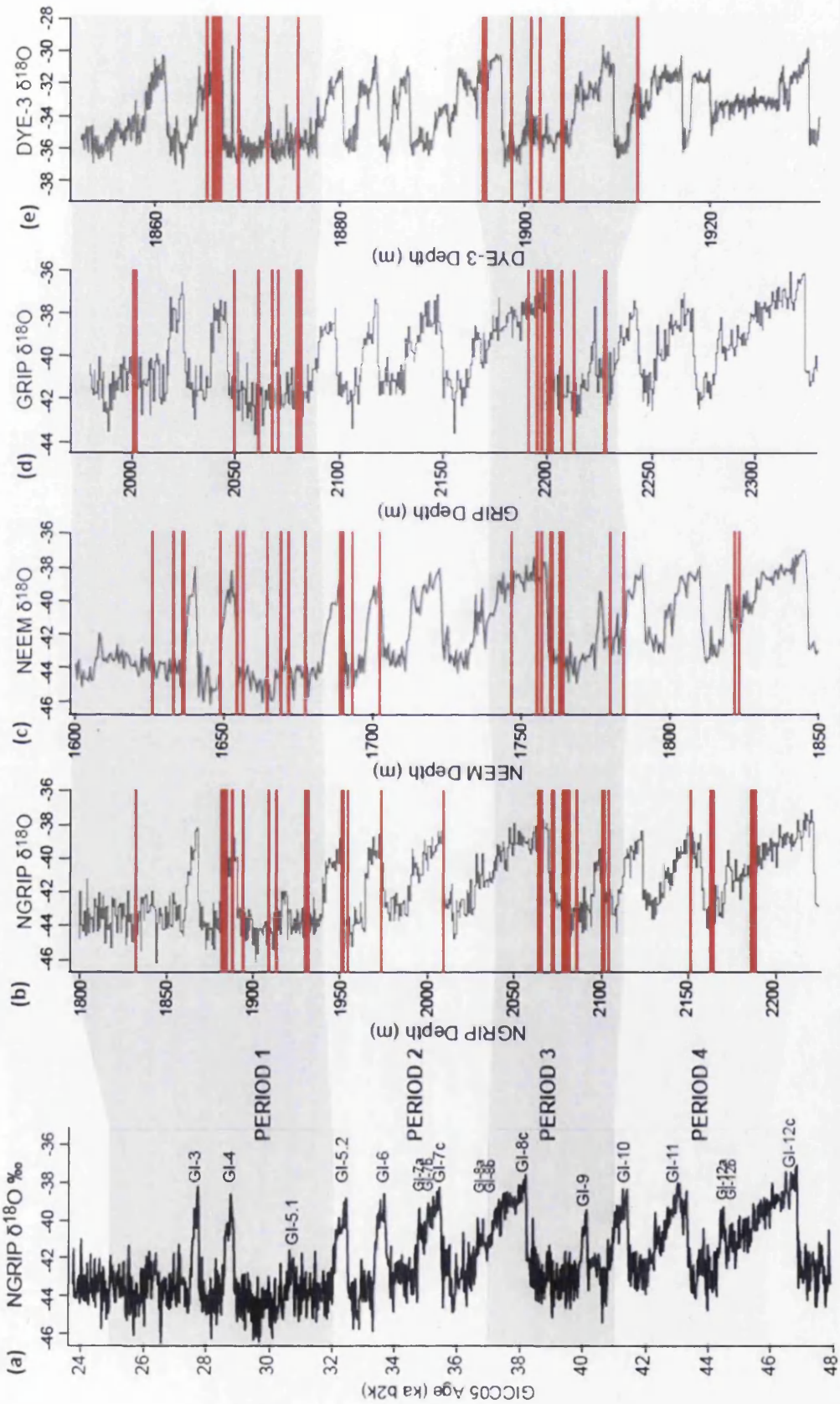

Figure 2.13 North Atlantic ice-core tephrostratigraphic framework. (a-e) Stratigraphic position of tephra horizons identified within four different Greenland ice-cores, adapted from Bourne et al. (2015). Each deposit is represented by a red line and plotted against the oxygen isotope stratigraphy. The NGRIP GICC05 timescale is also shown.

2.5.2 Greenland ice-core framework

Early ice-core tephra studies focused upon the presence of easily identifiable visible layers in the Greenland ice-cores, such as the NAAZ II in GISP2 and GRIP (Grönvold et al., 1995; Zielinski et al., 1996). More recent investigations have identified cryptotephras present within the records, using peaks in acidity and sulphate records to target sampling windows for identifying tephra deposits (Mortensen et al., 2005; Davies et al., 2010; Abbott et al., 2012; Abbott and Davies 2012; Coulter et al., 2012). In some instances, glass shards were detected in the ice without an associated acidity peak (Davies et al., 2010). Consequently, Bourne et al. (2013, 2015) have conducted a systematic search to reduce the over reliance on chemical indicators in order to augment a comprehensive framework of volcanic events preserved within the Greenland records.

Continuous sampling has recently been undertaken on four Greenland ice-cores (NGRIP, GRIP, NEEM and DYE-3) between 25-45 ka and ninety-nine newly identified horizons were assigned an age based upon the GICC05 timescale (Bourne et al., 2015) (Fig 2.13). The majority of shards were <50 μm and recent advancements in EPMA detection limits permitted robust major-element geochemical characterisation (Hayward, 2012) of deposits present within the ice. Major element signatures indicate ninety-three horizons exhibit a basaltic composition and display an affinity to Grímsvötn, Katla and Kverkfjöll systems, demonstrating the dominance of Icelandic basaltic volcanism. The frequency of eruptions and predominance of individual eruption centres varies throughout the record (Fig 2.13). A number of these deposits could be traced between ice-cores and have subsequently acted as reference horizons to facilitate the transfer of the GICC05 timescale to the NEEM and GRIP ice-cores (Rasmussen et al., 2013; Seierstad et al., 2014). This work greatly enhances the construction of a volcanic event stratigraphy for the last glacial period and widens the use of potential tephra horizons suitable for the synchronisation of the ice-cores to other disparate palaeoarchives. Nineteen tephra deposits within this framework constrain rapid climate events of interest and may hold significant value if they can be detected in

the marine realm. Three horizons have been traced between ice and marine archives and allow insight into climatic phasing relationships (Fig 2.6). Section 2.5.3 assesses the robustness of these correlations and their potential for assessing leads and lags.

2.5.3 Current ice-marine correlations

2.5.3.1 GISP2 2464.275 m, GRIP 2430.95 m (NAAZ II)

The discovery of a visible tephra within GISP2 at 2464.275 m and GRIP 2430.95 m with a rhyolitic geochemical composition, corresponds to an age estimate of 53,310 ± 2660 b2k (Grönvold et al., 1995; Bender et al., 1994). The deposit exhibits a similar geochemical composition to the II-RHY-1 component of the NAAZ II identified in the marine environment (Fig 2.5). The rapid cooling event seen in GISP2 oxygen isotopes is matched by a rapid rise in the relative abundance of N. *pachyderma* (sinistral) in the MD95-2006 marine core, indicating a fall in summer sea surface temperatures > 8°C (Austin et al., 2004). This has been used to suggest the cooling transition at the end of GI-15 was synchronous between the atmosphere and oceans, demonstrating the successful synchronisation of these deposits (Austin et al., 2004; Brendryen et al., 2011).

2.5.3.2 NGRIP 1848.0 m (FMAZ II)

NGRIP 1848.0 m was identified between 1848.0-1848.1 m and exhibits a basaltic geochemical composition with an affinity to the Hekla/Vatnafjöll system (Davies et al, 2008). The horizon exhibits an exceptionally similar geochemistry to the FMAZ II identified from numerous Faroese cores and is dated to 26,740 ± 390 b2k using the GICC05 timescale (Fig 2.13) (Davies et al., 2008). According to the NGRIP stratigraphic position, the tephra falls within a cold period ca. 1000 years after the onset of GI-3, which is consistent with its position in the marine cores. This suggests a close coupling of the atmospheric and oceanic systems during this time (Davies et al., 2008). The stratigraphic position of the tephra, deposited during a prolonged

period, precludes an assessment of rapid climate transitions but demonstrates the potential for synchronising between the ice and oceans.

2.5.3.3 NGRIP 2066.95 m (FMAZ III)

Previous work on the GI-8 interval in the ice-cores identified a single tholeiitic basalt horizon, NGRIP 2066.95 m (38,122 ± 723 b2k) and Davies et al. (2010) proposed a correlation to the FMAZ III identified in the marine environment based upon the broad overlap of geochemistries. Alongside the NAAZ II and the FMAZ II, the FMAZ III was thought to represent one of the few tie-points between the ice-cores and North Atlantic marine records (Abbott and Davies, 2012) (Fig 2.13). The stratigraphic position in the ice-cores suggests that deposition occurred ca. 100 years after the onset of GI-8 warming and was suggested to represent a key tephra for establishing phase relationships in the climate system (Davies et al., 2010; Davies et al., 2012). Given the dispersed nature of the ash in the marine environment, establishing a secure isochronous position was a key objective to permit successful synchronisation and transfer of the climatic signal. This initially formed the overarching aims of this thesis, but was subsequently modified following the identification of fourteen new tephra deposits in NGRIP spanning GI-8-GI-9 (~38,000-40,500 b2k) (Bourne et al., 2013) (Fig 2.10c, Fig 2.13).

With two exceptions, the suite of tephra horizons identified by Bourne et al. (2013) exhibit a tholeiitic basaltic composition that could be discriminated by subtle differences in TiO_2. Each individual horizon fell within the broad compositional range of the FMAZ III defined by Wastegård et al. (2006) and suggest this deposit is far more complex and challenging than previously envisaged. As such, the FMAZ III could no longer be correlated to NGRIP 2066.95 m defined by Davies et al. (2010) and could not be utilised as a secure marine-ice tie-point. Bourne et al. (2013) recommends it may be fruitful to conduct investigations in high sedimentation cores outside of the Faroes region to increase the likelihood of detecting one or two components, rather than the full suite of eruptions documented in the Greenland ice-cores. This prompted the search for individual components in high sedimentation areas such as MD04-2829CQ and MD99-2281. In order to optimise their use as potential isochrons, a detailed high-resolution cryptotephra investigation is necessary

to fully categorise the geochemical and taphonomic variability of the FMAZ III in the marine environment. Given the stratigraphic value of the FMAZ III to resolve phasing relationships in the climate system, these recommendations form the central aims of the thesis. Although the work of Bourne et al. (2013) shed new light on the complexity of the FMAZ III, the overall goals of achieving synchronisation remained unaffected.

2.5.4 Complications of the current framework

As demonstrated by the recent discovery of fourteen horizons straddling GI-8-GI-9, the occurrence of compositionally similar tephras within a short time interval presents a number of challenges (Bourne et al., 2013). Despite their useful stratigraphic position, their potential value to link different records rests on their distinct geochemical composition relative to others close in age (Bourne et al., 2015). Major element geochemistry may not be sufficient for establishing secure correlations between tephra deposits in these instances. Trace element analysis may be necessary to facilitate geochemical discrimination (Davies, 2015). Trace elements show greater variability than major elements because they are more strongly affected by internal magmatic processes such as crystallisation and assimilation (Pearce et al., 2010). This study additionally aims to test correlations using trace element characterisation, where necessary, to permit robust comparisons.

The current North Atlantic framework relies on the completeness of the Greenland ice-core records to document a volcanic event stratigraphy from the last glacial period. However, this is unlikely given the complexity of eruption plume dynamics and favoured wind dispersal patterns south of Iceland (Larsen et al., 1981). Consequently, horizons may be present in marine cores that cannot be correlated to the ice because of the absence of an equivalent horizon. However, the extensive framework of ice-core horizons (Fig 2.13) provides ample opportunity for detecting geochemically similar deposits in the marine environment and this study aims to build upon the existing marine framework (Fig 2.4,2.5). This will permit the integration of records and insightful comparisons of the climatic and environmental records that they constrain (Davies et al., 2014).

2.6 Conclusions

- D-O events are a common feature of the last glacial period, expressed as rapid climate fluctuations in a variety of proxy sequences. However, dating uncertainties and issues associated with tuning have plagued the integration of records, precluding an assessment of leads and lags in the climate system

- Ice cores (recording atmospheric changes) and marine cores (recording oceanic changes) can be synchronised through the use of independent marker horizons to provide an insight into climatic phasing relationships. This forms the TRACE synchronisation goals and is a central theme of the thesis.

- The adoption of cryptotephrochronology has greatly increased the area over which deposits can be traced. Advancement in geochemical fingerprinting techniques has increased the ability to characterise small shards and the robustness of tephra correlations.

- Taphonomic issues in the marine environment have provided a variety of challenges to robustly assess the integrity of tephra deposits. The use of diagnostic indicators is necessary to unravel depositional processes and successfully integrate primary isochrons into a marine tephrochronological framework.

- Ten tephra horizons forming the current marine tephrochronological framework exhibit a range of geochemical and depositional characteristics. Further analysis is necessary to assess the integrity of the deposits, potential correlations between existing horizons and their value as isochronous markers.

- The marine environment offers untapped potential to increase the number of available tephra isochrons that can be built into the existing framework. This can then be used to trace coeval deposits in the ice-core framework and facilitate synchronisation.

Chapter 3 Methodology

3.1 Introduction

In order to develop the MIS 2 and MIS 3 tephrochronological framework for the North Atlantic region, samples were taken from four individual marine sequences retrieved from the North Atlantic and Norwegian Sea. Extraction techniques were employed to detect tephra deposits within these sequences. Each tephra deposit was geochemically characterised and assessed for their depositional integrity. The following sections provide information on; a) the marine cores sampled; b) tephra extraction methods; c) major and trace element analysis; d) statistical treatment of data-set; e) techniques used to assess depositional integrity; f) construction of thin-sections for micromorphological analysis and; g) instrumental μCT parameters used to reconstruct 3D structures of tephra deposits.

3.2 North Atlantic marine cores

Four marine cores from the North Atlantic, recovered previously from numerous cruise expeditions, were sampled through collaboration with various European institutions (see table 3.1). The coring sites are located on a NE-SW transect across the eastern Atlantic and Norwegian Sea (Fig 3.1). The ideal criteria for core selection are as follows:

1. Cores should have been retrieved from high sedimentation areas;
2. Sites should contain a well-resolved and high-resolution D-O signal between approximately 16-55 ka;
3. D-O proxy reconstructions should be supported by an independent chronology;

4. Sites should be located away from the main IRD belt to minimise tephra sourced from ice-rafting;
5. Sufficient core material should be available to enable continuous U-channel sampling.

Unfortunately, not all of the above criteria could be met for each site. For example, the availability of MD04-2829CQ material was insufficient for U-channel sampling so individual 1 g samples were obtained instead. An abundance of material was available from JM11-19PC and this was used for additional thin-section and μCT experimentation (see sections 3.9, 3.10). A limited sampling window was targeted from MD99-2281 to trace a specific composite of tephra deposits within DO-8 in a region of exceptionally high-sedimentation (see table 3.1).

Table 3.1 Core details for each marine sequence. MD04-2829CQ was sampled at the School of Earth and Ocean Sciences, Cardiff University. JM11-19PC was sampled at the Centre for Arctic Gas Hydrate, Environment and Climate, University of Tromsø. MD99-2281 was sampled at EPOC, University of Bordeaux. MD95-2010 was sampled at the Department of Earth Science, University of Bergen. Age ranges are based upon sampling intervals and equivalent ages derived from age models/tuning presented in Hall et al., (2011), Ezat et al. (2014), Zumaque et al., (2012), and Dokken and Jansen (1999) respectively.

Core name	Location	Co-ordinates	Water depth (m)	Depth interval analysed (cm)	Age range analysed (ka)
MD95-2010	Vøring Plateau	66°41'N, 4°34'E	1226	450-850	~23-41
JM11-19PC	North Faroe Slope	62°48.98''N 03°52.04' E	1179	190-628	~16-55
MD99-2281	Faroe Bank	60°21'N, 9°27'W	1197	1869-1900	~38-39
MD04-2829CQ	Rosemary Bank	58°56.93'N, 9°34.30'W	1743	300-1007	~18-41

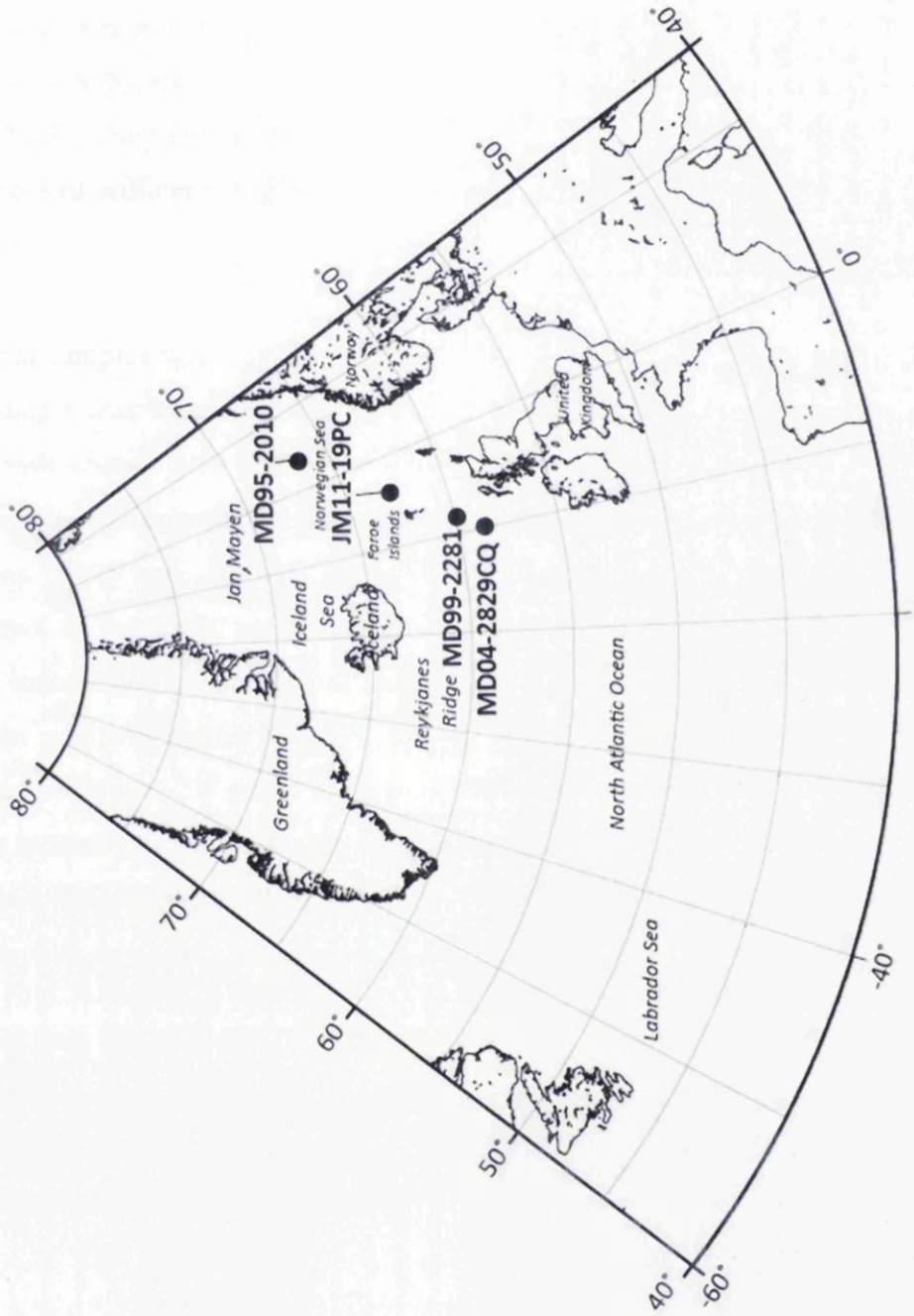

Figure 3.1 Location map including the network of cores on which the thesis has focused

3.3 Tephra extraction of marine sediments

The tephra extraction method employed was based on a modified procedure outlined in Turney (1998), Blockley et al. (2005) and adapted for marine sediments by Abbott et al. (2011). The method involves a stepped flotation protocol that isolates material from the host sediment at different stages within the procedure (Fig 3.2) (Blockley et al., 2005).

Sediment samples were freeze dried and 0.5 g of dry weight (gdw) sediment from each sample was weighed for tephra analysis. The sediment was then immersed in dilute hydrochloric acid (HCl) (10%) overnight to remove carbonate material. Each sample was subsequently wet-sieved through meshes into three separate grain-size fractions (>125 μm, 80-125 μm and 25-80 μm). Density separation was then performed on the 25-80 μm grain-size using the heavy liquid sodium polytungstate (SPT), separating the sample into three separate density fractions. The first float at 2.3 g/cm^3 removes lighter material, mostly the biogenic component such as diatoms. The second float at 2.5 g/cm^3 isolates rhyolitic tephra shards from the host material as they typically exhibit a density between 2.3-2.5 g/cm^3. Basaltic material typically exhibits a density greater than 2.5 g/cm^3 and remains within the denser component together with any heavy minerogenic material.

Material from the >125 μm, 80-125 μm and 25-80 μm (2.3-2.5 g/cm^3) fractions were mounted in Canada Balsam on microscope slides for quantification of tephra content using optical microscopy (see section 3.6). Material with a density of >2.5 g/cm^3 was magnetically separated to further purify the basaltic material (see section 3.4).

3.4 Magnetic separation of shards

Basaltic tephra exhibits ferromagnetic properties, mainly due to the high Fe content and through the influence of paramagnetic elements such as Al, Mg and Na (Walden et al., 1999).

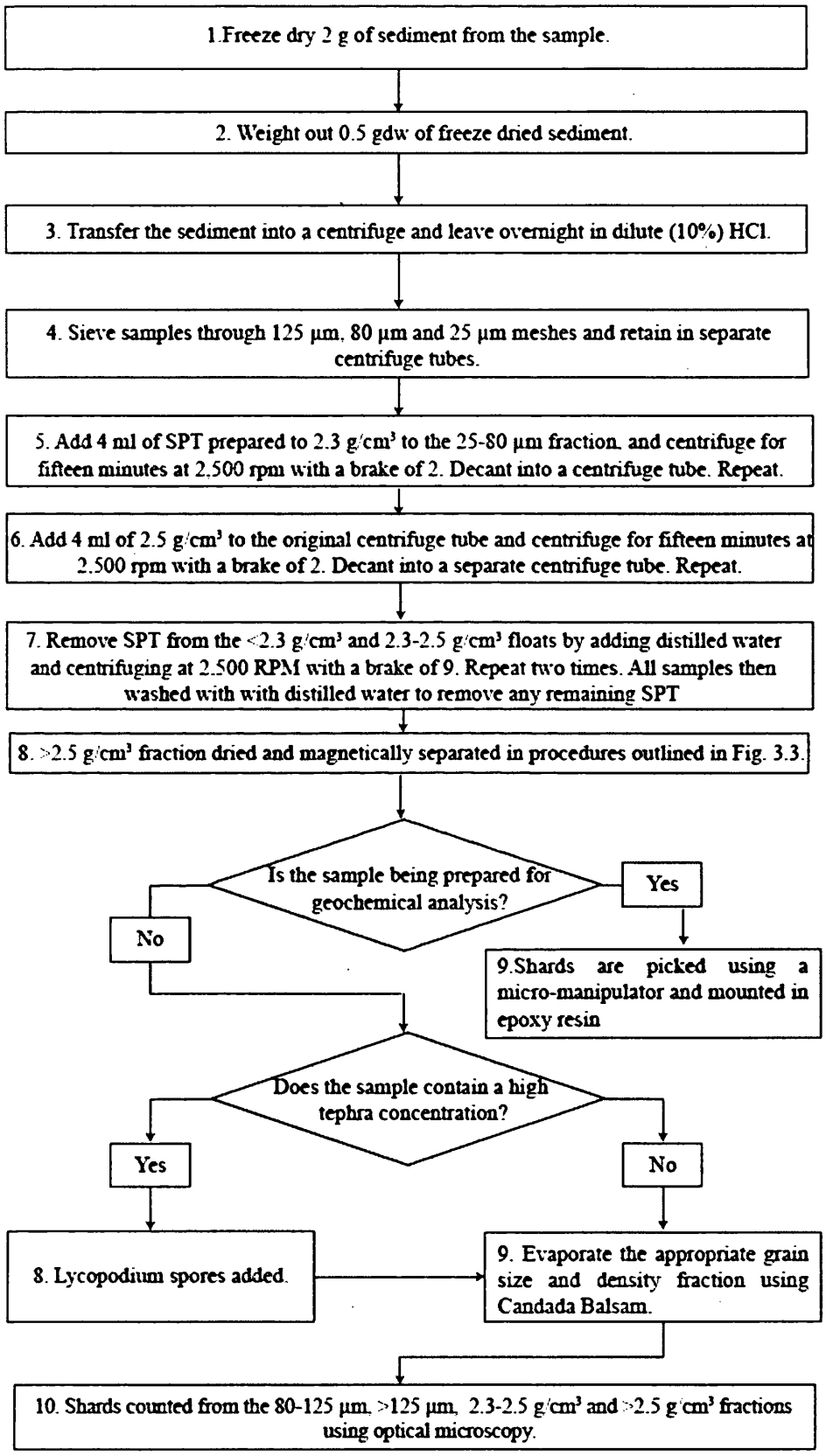

Figure 3.2 Summary of the stepped density flotation protocol modified from Turney (1998), Blockley et al. (2005) and Abbott et al. (2011).

This allows tephra shards to be separated from non-magnetic minerals, e.g. quartz, when a magnetic current is applied to the sample of interest (Froggatt and Gosson, 1982; Mackie et al., 2002). Previous experimentation has demonstrated enhanced efficiency of this technique by alteration of the magnetic field strength and the forward and sideway tilt of the apparatus (Froggatt and Gosson, 1982; Mackie et al., 2002).

With a Frantz IsoDynamic Magnetic Separator, a series of experiments were conducted to determine the optimal parameters to isolate basaltic material from marine sediments. Experimentation was conducted on one specific marine sample from a Faroe Islands core (LINK 16), which was known to contain basaltic tephra (Abbott et al., 2014). Ten sub-samples were extracted from this sample and the total tephra to minerogenic material ratio was counted (Table 3.2). Ratios have been used as it could not be assured that the total number of shards within each sub-sample was consistent and it was assumed that the ten sub-samples would exhibit the same ratio between tephra and mineral particles. Different parameters were used for each individual sub-sample i.e. the magnetic current, tilt and slope were altered and the ratio of basaltic shards to minerogenic particles was determined (Table 3.2). The non-magnetic fraction was mounted to quantify the percentage of tephra shards that may have failed to be separated. The percentage of tephra in both fractions was then quantified. The parameters that delivered the most effective recovery of tephra were identified as a current of 0.85 nA, tilt of -15° and a slope of 22.5°. A stepped protocol for this process has been developed and is presented in Figure 3.3. These parameters were then employed throughout the study to purify any basaltic shards present within marine sequences and improve efficiency during shard counting.

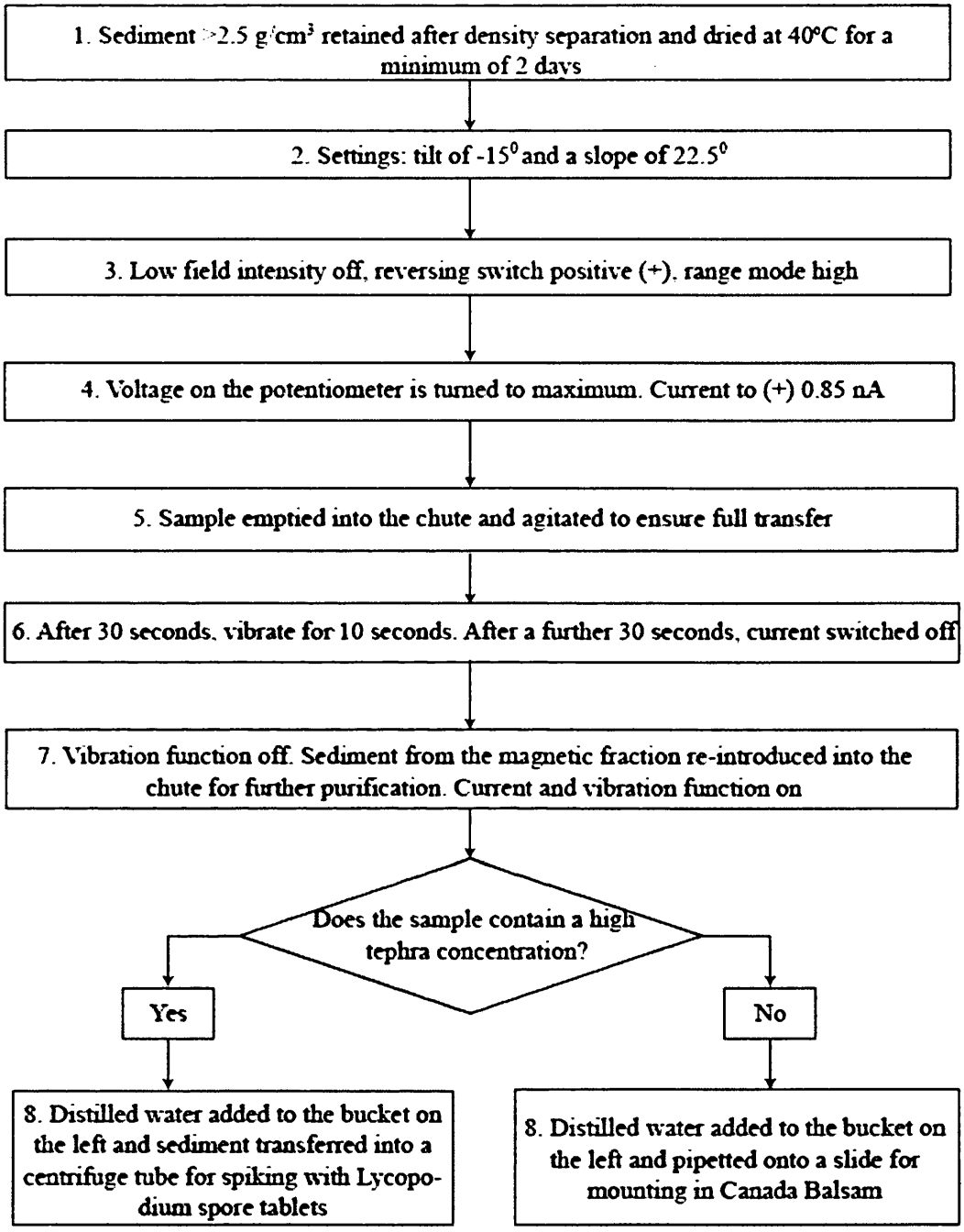

Figure 3.3 Summary of the protocol for the magnetic separation of basaltic shards from mineral-rich sediments using a Franz IsoDynamic Magnetic Separator.

Table 3.2 Magnetic separator parameters used for detecting the most effective recovery of tephra shards. The control sample (CTRL) was not magnetically separated and was counted to obtain the known ratio of tephra to minerogenic particles. Total percentages of tephra in relation to the total number of mineral grains are presented from the magnetically separated fraction and non-magnetic fractions. Code LA8 delivered the most effective recovery of basaltic tephra shards.

Code	Tilt (°)	Current (nA)	Slope (°)	Repeat	Tephra/mineral ratio magnetic fraction (%)	Tephra/mineral ratio in non-magnetic fraction (%)
CTRL					12.0/88.0	
LA1	-10	0.5	15	0	14.0/86.0	5.0/95.0
LA2	-15	0.55	15	1	6.0/94.0	4.2/95.8
LA3	-20	0.6	15	2	10.4/89.6	5.6/94.4
LA4	-15	0.65	15	1	10.0/90.0	1.8/98.2
LA5	-15	0.75	20	2	12.4/87.6	0.2/99.8
LA6	-15	0.85	25	2	19.4/80.6	0.4/99.6
LA7	-15	0.85	10	2	23.4/76.6	0.4/99.6
LA8	**-15**	**0.85**	**22.5**	**2**	**23.6/76.4**	**0.2/99.8**
LA9	-18	0.85	20	2	10.2/89.8	0.6/99.4

3.5 Lycopodium spiking of samples

A palynological quantification technique, previously applied to the study of tephra by Gehrels et al. (2006) and Bourne (2012) was employed in samples where there were exceptionally high numbers of basaltic glass shards present in the >2.5 g/cm^3 fraction (>1,000 per 0.5 gdw). In this technique, a known number of spores are added to the sample and the ratio between those grains and the tephra shards is determined to allow the number of tephra shards to be quantified. This technique was applied to samples from marine core JM11-19PC.

A Lycopodium spore tablet was added to the magnetically separated residue and dissolved in 5 ml of distilled water in a centrifuge tube. These samples were placed in a water bath at 50°C for two hours to ensure complete dissolution of the tablet. A dilute (10%) solution of HCl (2 ml) was then added to remove any remaining sodium bicarbonate. The spiked sample was then washed three times with distilled water by centrifugation and finally 5 ml of distilled water was added to the centrifuge tube. The solution was shaken vigorously to mix the sample and eight drops of the mixture were pipetted onto a microscope slide and mounted in Canada Balsam. This amount was deemed to be the optimal volume to cover the slide beneath the cover slip, similar to the 500 µl recommended by Gehrels et al. (2006). Glass shards were counted alongside Lycopodium spores in each sample across three vertical transects per slide. The concentration of tephra shards, C, was calculated using Eq.3.1.

Eq. 3.1: $$C = l \times \left(\frac{a}{bd}\right)$$

Where a) is the glass shard count, b) is the Lycopodium spore count, d) is the sample dry weight, l) is the number of Lycopodium spores in each tablet (n=20,848 from the sample batch used within the investigation) according to the manufacturer estimate determined using an electronic particle counter. This methodology was adapted for high-resolution sampling intervals, where three tablets (i.e. 62,544 spores) were added to the magnetically separated residue due to the exceptionally high tephra concentrations.

3.6 Tephra identification using optical microscopy

Glass shard concentrations within marine sediments were quantified using a high-powered light microscope. Morphological and optical properties are used for identifying tephra glass shards. Glass particles exhibit a range of characteristic morphologies i.e. blocky, platy and cuspate features. Glass fragments may also contain open vesicle networks (Heiken and Wohletz, 1985). Typically, silicic glass shards are colourless and exhibit a range of platy and cuspate morphologies.

The main optical difference between tephra and minerals is that most minerals show interference colours under cross-polarised light. Rapid cooling of magma during the formation of glass causes tephra particles to exhibit a non-crystalline structure (isotropic) as opposed to minerals which exhibit a crystalline structure (anisotropic) (Enache and Cummings, 2006). Examination of isotropic glass shards with cross-polarised light does not affect the vibration plane of light coming from the lower polariser and the upper polariser will absorb the light. This causes the tephra to extinguish and appear dark in the microscopic field. In contrast, anisotropic minerals rotate the plane of polarization, scattering the light, and show birefringence colours.

The Becke line method is an additional optical property for distinguishing tephra particles. The Becke line is a rim of light that appears inside or outside of the grain boundary, depending on the contrast in refractive indices between the particle and the mounting medium. If the distance between the sample and the objective is increased, the Becke line moves into the material with the higher index of refraction (Enache and Cumming, 2006). Rhyolitic glass exhibits a refractive index of 1.5, lower than that of the mounting medium Canada Balsam (1.55). Thus, the Becke line will move outwards from rhyolitic shards, which contrasts to inward movement of many minerals which have a refractive index >1.55. Basaltic material exhibits a refractive index >1.55 and therefore the Becke line will move into the shard when the stage is defocused. This is the same as many minerals, but the morphological and colour characteristics of basaltic shards are more distinctive (Enache and Cummings, 2006).

3.7 Geochemical analysis

3.7.1 Preparation of slides for geochemical analysis

Samples selected for geochemical analysis were re-prepared using the density and magnetic separation procedures outlined previously. Samples containing tephra were pipetted in water into a slide-well and individually picked using a micro-manipulator with a ~80 μm diameter. Shards were then transferred onto a frosted slide and secured using epoxy resin. To prepare shards for geochemical analysis, polished sections through the glass shards are necessary. This removes post-depositional surface alteration and hydration, which could induce absorption and reduce the amount of x-rays reaching the spectrometers (Hunt and Hill, 1993).

Samples were ground down using silicon carbide paper and polished using nine, six and one μm diamond suspension to expose polished glass shard surfaces with a mirror finish. The slides were then immersed in petroleum spirit and placed in an ultra-sonic bath for five minutes. This removed any diamond suspension that may have adhered to the surface. A carbon coat was added to the surface of the slide to prevent charging during EPMA analysis. Colloidal graphite paint was applied on the surface to the edge of the slide to ensure an electrical earthed contact was obtained via the sample holder (Hunt and Hill, 1993).

3.7.2 EPMA analysis

Oxide concentrations of ten major and minor elements were analysed using wavelength dispersive (WDS) EPMA at the Tephrochronological Analytical Unit at the University of Edinburgh, using a Cameca SX100 electron micro-probe equipped with five vertical WD spectrometers. The geochemical composition is determined as the X-ray energy generated is individual to each element and the intensity proportional to the concentration of the element present (Hunt and Hill, 1993).

The operating conditions have been modified from Hayward (2012) and two different EPMA operating setups were used. For the first setup, three sets of column

conditions were employed and a 3 μm beam diameter was used throughout the analyses of deposits with small shard diameters. Analysis using narrow beams requires extremely low beam currents, which are normally associated with energy dispersive analysis, to prevent sodium loss (Hayward, 2012). As such, NaO_2 and Al_2O_3 were determined using an accelerating voltage of 15 kV and a beam current of 0.5 nA. The exceptionally low beam current of 0.5 nA was used in this setup following initial calibration to prevent sodium loss (Hayward, pers comm). Secondly, MgO, K_2O, CaO, FeO and SiO_2 were determined using an accelerating voltage of 15 kV and a beam current of 2 nA. Thirdly, P_2O_5, TiO_2 and MnO were determined using accelerating voltage of 15 kV and a beam current of 60 nA. Counting times were 20 s at the peak position and 10 s for background for all elements except MnO (60 and 60 s).

For the second EPMA setup two column conditions were used. Na_2O, MgO, Al_2O_3, SiO_2, K_2O, CaO, and FeO were determined using an accelerating voltage of 15 kV and a beam current of 2 nA and P_2O_5, TiO_2, and MnO were determined using an accelerating voltage of 15 kV and a beam current of 60 nA. A 5 μm beam diameter was used on coarser grained shards analysed within the thesis. Counting times were 20 s at the peak position and 10 s for background for all elements except TiO_2 (30 and 15 s), MnO (50 and 40 s) and FeO (40 and 20 s).

Pure metals, simple silicate minerals and synthetic oxides, including andradite were used for calibration, and the secondary standards Lipari and BCR2g were analysed regularly to monitor elemental drift and to assess the accuracy of the shard analyses (see appendix). These were recorded for both analytical set ups. Both analytical set-ups produced similar secondary standard analyses, which permitted robust comparisons between samples run using either column condition. The co-ordinates for each shard were carefully recorded and reference crosses were etched into the resin and offset from the shards. This allowed the same shards to be re-located for LA-ICP-MS analysis.

3.7.3 LA-ICP-MS analysis

Trace-element characterisation of individual shards from one marine and one ice-core horizon were obtained using an LA-ICP-MS system at the Institute of Geography and Earth Sciences, Aberystwyth University during two analytical periods in one day. The system couples a Coherent GeoLas 193nm Excimer laser with a Thermo Finnigan Element 2 high-resolution sector field mass spectrometer (Pearce et al., 2011). Due to the small grain sizes of the ice-core horizon, a laser with a beam diameter of 10 μm and a fluence of 10 J/cm^2 was pulsed at 5 Hz with a flash duration of ~10 ns. The marine horizon contained considerably larger material but a 10 μm laser beam diameter was used consistently for all analyses to limit any differential impact of fractionation effects. As a correlation between the marine and ice-horizons was being tested, the samples were analysed 'side-by-side' over the course of a day to limit any potential influence of instrumental differences over longer time periods (Pearce et al., 2014). An internal standard (^{29}Si) previously analysed for each shard during EPMA analysis was utilised and NIST 612 silicate glass was used as the calibration standard.

The background level of elements within the system were determined by the systematic acquisition of measurements between individual grain analyses when no sample was being ablated i.e. a gas blank, and removed when calculating concentrations. Trace element concentrations were then calculated using methods outlined in Pearce et al. (2007). A correction factor was applied to remove bias in analyses caused by fractional affects (Pearce et al., 2011). Analyses of the secondary standard BCR2g were monitored at the end of the analyses.

3.7.4 Data normalisation and statistical treatment

Glass shards preserved in the marine realm are susceptible to variable levels of post-depositional hydration (Wallrabe-Adams and Lackschewitz, 2003; Abbott et al., 2011). As such, the results of the EPMA analysis were normalised to 100% total oxide values (i.e. an anhydrous basis) to remove any variability that may be apparent when comparing data-sets from different depositional environments that have not experienced comparable levels of post-depositional hydration (Abbott et al., 2011;

Pearce et al., 2014). All analyses with total oxide values <93% were rejected as these may represent inaccurate EPMA analyses that may not be attributable to hydration.

For correlation of geochemical data with published tephra horizons, all data were normalised for comparison purposes. Graphical comparisons were made using biplots and similarity coefficients (SC) to calculate the similarity between data-sets of major elements (Borchardt et al., 1972). SC are calculated using Eq. 3.2:

Eq.3.2: $$d_{(1.2)} = \frac{\sum_{k=1}^{n} R_k}{n}$$

Where $d_{(1,2)}=d(_{2,1})$ is the similarity coefficient for the comparison between samples one and two, k is the element number, n is the number of elements, $R_k = X_{k1}/X_{k2}$ if $X_{k2} \geq X_{k1}$ or X_{k2}/X_{k1} if $X_{k1}>X_{k2}$, X_{k1} is the concentration of element k in sample 1 and X_{k2} is the concentration of element k in sample 2 (Borchardt et al., 1972). SCs are obtained using mean values for elements which have all been normalised. Only oxides with concentrations >1.0 wt% have been used for comparisons.

SCs are expressed between 0.6 and 1 and values closer to 1 indicate greater similarity between the data-sets. Numerical values in excess of 0.95 suggest a possible tephra match (Begét et al., 1992). However, further inspection of the data sets presented within the study suggests this may not always be the case i.e. closely spaced eruptions with similar geochemistry. Where comparisons have been made within the thesis, only those with values with SC >0.95 have been expressed. Values between 0.90-0.94 are thought to indicate tephras that originate from the same volcanic source. Values below 0.9 are indicative of unrelated tephras.

3.8 Assessing depositional integrity

In addition to assessing shard concentrations and geochemical fingerprinting, an examination of taphonomic processes in cryptotephra investigations is crucial. This can be achieved by analysing numerous diagnostic indicators. Specifically, high-resolution shard concentrations are employed to create a shard distribution profile,

which can assist in the likely stratigraphical placement of the isochron i.e. peak shard occurrence. The relative concentrations of specific grain-size diameters (25-80 μm, 80-125 μm, >150 μm) that form the concentration profiles can then be used to assess the likelihood of primary and secondary depositional processes. The position of the isochron determined using shard concentration profiles is then extracted for geochemistry.

Geochemical homogeneity can be used to test whether shards are sourced from a single eruption, or from multiple eruptions, which would typically exhibit a heterogeneous distribution. The position of the isochron can then be compared to IRD flux at the corresponding depth interval to assess the likely contribution from iceberg rafting. Analysis of; a) shard concentration profiles; b) grain-size; c) geochemical homogeneity and; d) IRD co-variance, are routinely employed throughout this investigation.

3.9 Sedimentology: preparation of thin-sections

Undisturbed sediment samples from marine core JM11-19PC were extracted in U-channels (20 x 20 x 200 mm) spanning the onset of tephra deposition and the decline in tephra shard deposition associated with the FMAZ II, III and IV (Fig 3.4) (see chapters 4 and 7). The following procedure was conducted alongside Dr Adrian Palmer at the Department of Geography, Royal Holloway using methods adapted from Palmer et al. (2008).

Initial drying of the samples was conducted to aid polymerization during impregnation. The acetone replacement method was employed to limit cracking of silty-clay rich sediment during drying (Meer and Menzies, 2011). The sediment was immersed in acetone and replaced every seven days for six weeks. After complete drying of the sample, resin was mixed with 3 ml of MEKP-LA3 (catalyst) and poured onto the sample. The samples were then placed into a vacuum chamber and the pressure was incrementally increased for seven hours to ensure the resin was gradually drawn into all of the pore spaces. This process does not cause any disruption to the fabric of the sample. The samples were then left to harden for a

further six weeks and heated at 65°C for fifteen hours to ensure complete curing of the sample.

Following curing, the sample was split in half using a Buehler Delta Chopcutter. In order to attach the sample to a glass-slide with a perfect bond, it was necessary to create a flat, polished surface. 75, 40, and 20 μm diamond fixed abrasive wheels were used in this part of the process to flatten the block then 14 μm silicon carbide papers to polish it. This was achieved using a Buehler Metaserv grinder polisher at 250 revolutions per minute. The sample could then be attached to a glass-slide using Epothin Resin and Hardener and placed under a spring-loaded jig for twenty hours.

Once the block had been successfully bonded to the glass slide, a section suitable for hand-polishing was created using a CS-10 Cut-off Saw and the Jones Shipman Surface Grinder. The saw is used to trim the block from the slide leaving 1 mm of excess sample on the slide. The Jones and Shipman exhibits precision controls which allows the sample to be ground down to ~60 μm thickness. Hand polishing of the section was achieved using diamond polish on the grinder polisher and subsequently ground down to a 25-35 μm thickness. Cover slipping of the thin-section was then conducted using resin to bond the slip to the slide. Excess resin was etched away from the slide and cleaned for microscopic analysis. Micromorphological and microstratigraphical analysis were performed using a standard petrographic microscope with a rotating stage with magnification in the 2-40 x range.

3.10 Using μCT to visualize tephra deposits in three-dimensions

3.10.1 μCT instrumentation

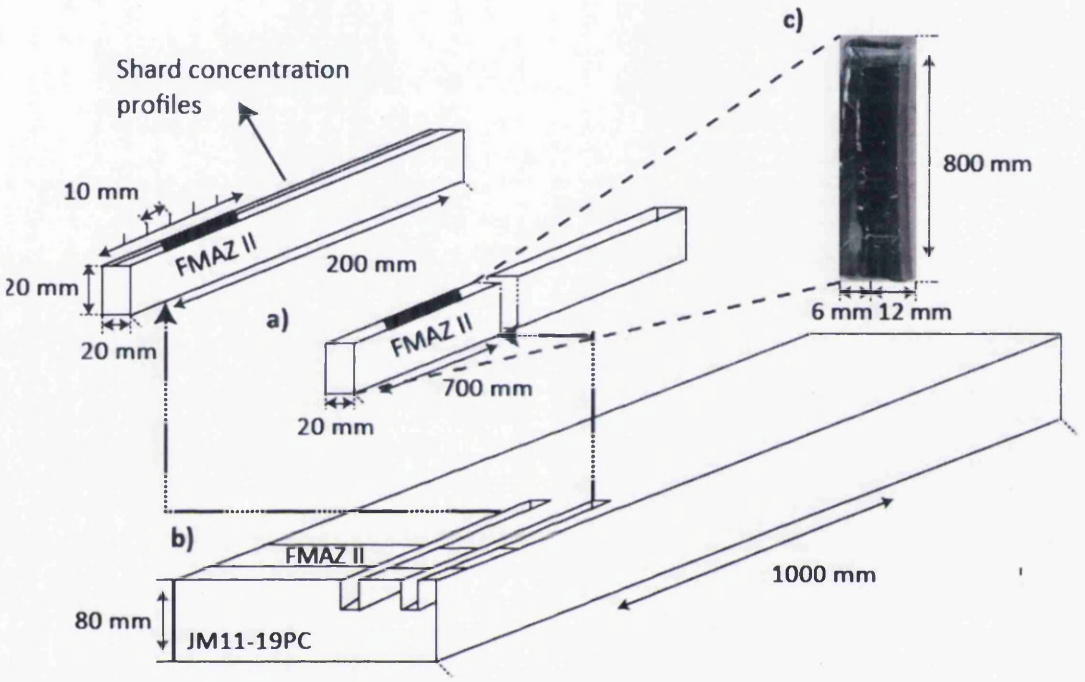

Figure 3.4 Schematic summary of the U-channel sampling from marine core JM11-19PC. Two U-channels, with the dimensions 20 mm x 20 mm x 200 mm extracted parallel to each other for a) generating shard concentration counts and b) thin-section and tomographic analysis. c) Resin impregnated block.

In order to utilise X-ray microtomography for 3D visualization of tephra deposits, it was first necessary to constrain the greyscale contrasts (amount of X-rays scattered or absorbed by the sample) between tephra and non-tephra grains. For this purpose an artificial specimen was created in a ~20 mm length of plastic drinking straw of ~5 mm internal diameter. A ~2 mm thick layer of pure basaltic tephra (>2.5 g/cm^3) was added between two layers of freeze-dried, marine sediment known to be devoid of tephra and composed of a mixture of heavy and light mineral grains (Fig 3.5b).

The straws were analysed using a Nikon XT H 225 microfocus X-ray tomography system, with a 1.3 Megapixel Varian PaxScan 2520 amorphous silicon flat panel digital X-ray imager, in reflection mode with a tungsten target. Dr Mark Coleman (College of Engineering, Swansea University) helped to derive the optimal operating conditions for investigating tephra. X-ray tube voltages between 50-100 kV were trialed as these are similar to those derived by Ketcham and Carlson (2001) to distinguish between quartz and orthoclase. These minerals exhibit a small density contrast (2.65 g/cm^3 vs 2.59 g/cm^3) of a similar magnitude to the density contrast expected between tephra and marine sediment. Low voltages are favoured as photoelectric absorption is the dominant attenuation mechanism at energies <100 kV. The practical importance of this phenomenon is that photoelectric absorption is proportional to Z^{4-5} of the attenuating material, and as a result, low energy X-rays are more sensitive to differences in composition than higher energy ones (Ketcham and Carlson, 2001). Scans revealing the most effective contrast were performed using a 50 kV X-ray tube voltage, a current of 550 μA, with an exposure of 1000 ms, averaging four images per rotation step of 0.119°, resulting in 3016 images per scan and a voxel (3D pixel) size of 4.7 μm. The tomograms were reconstructed from 2D projections using a Nikon cone-beam reconstruction algorithm and proprietary software. The commercial software VGStudio Max 2.1.5 and free software Drishti were used to view the reconstructed data, 2D greyscale slices and rendered 3D volumes.

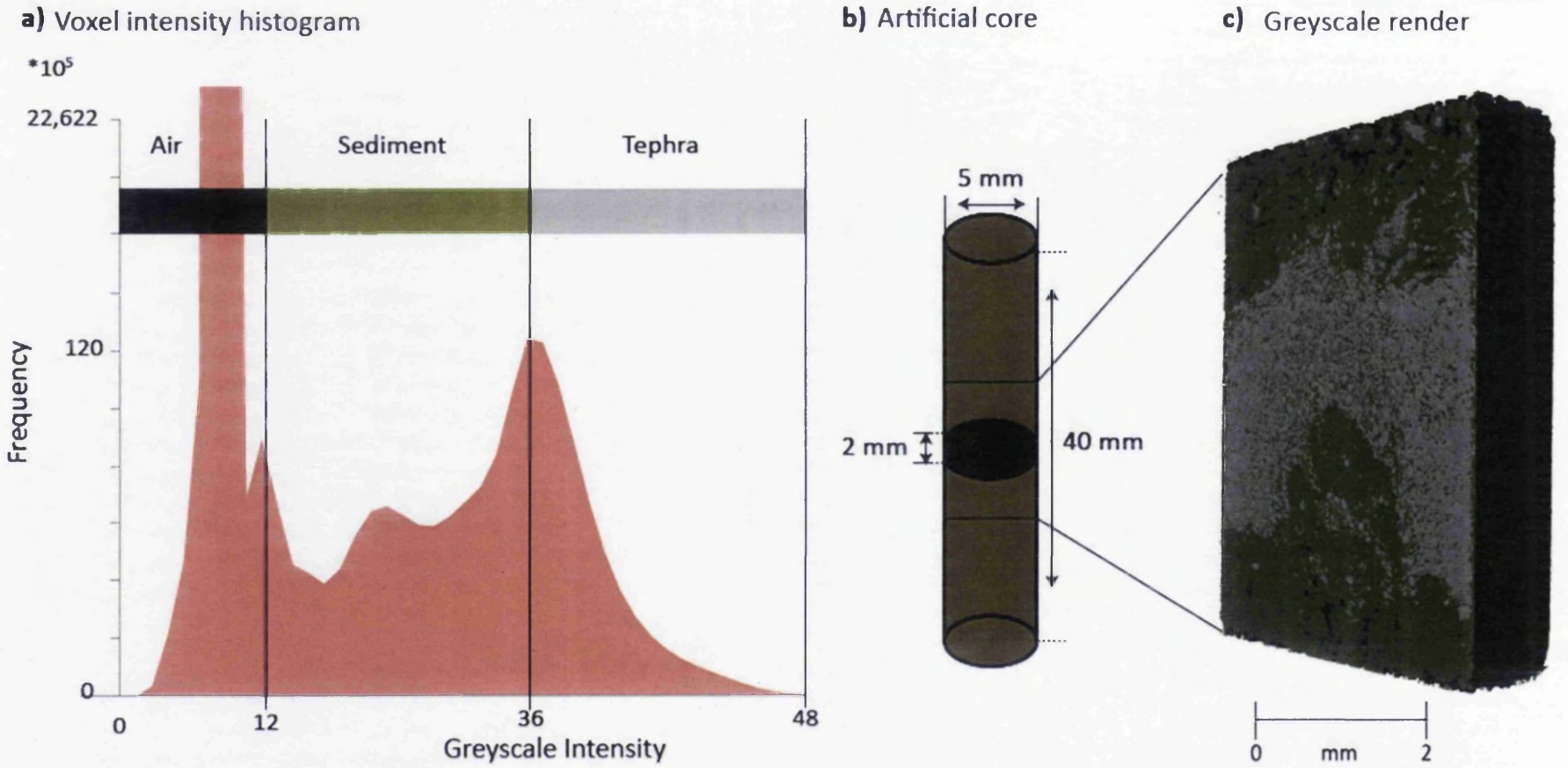

Figure 3.5 Example of the μCT procedure used to identify tephra in a straw and resin impregnated blocks. a) Voxel-intensity histogram. The vertical lines denote the thresholds defined by the histogram to isolate air, sediment and tephra. b) Schematic representation of the artificially created straw. c) 3D render of the straw. Grey = tephra; Green = sediment.

3.10.2 Delineating tephra using voxel-intensity histograms

From the μCT analysis of the straw, a histogram of voxel (3D pixel) intensities is produced. This plots the frequency or number of occurrences of voxels of a particular intensity, which is related to density, within the overall scan. The peaks allow us to qualitatively segment the image into different phases by placing thresholds between peaks, which correspond to air, sediment and tephra (Gonzalez and Woods, 2008) (Fig 3.5a). In order to identify the threshold that differentiates between the tephra and sediment phases, the threshold value is moved until the tomographic render resembles the expected visual structure of the artificial straw i.e. a lateral tephra horizon surrounded by sediment devoid of tephra (Fig 3.5b.c).

Despite the similarity in density of tephra and sediment, a distinct tephra deposit was successfully revealed when the threshold is placed at a greyscale intensity of 36 (Fig 3.5a,c). The basaltic tephra in Figure 3.5a has a higher absorption coefficient and/or contains a higher-Z composition than the surrounding sediment dominated by quartz. However, one limitation in defining instrument parameters is the overlap between the sediment and tephra phase distributions which reflect a common problem with qualitative intensity-based segmentation (see Landis and Keane, 2010). In Figure 3.5a, an overlap of greyscale intensities is apparent between high-density sediment and lower-density tephra. Segmentation at the peak of the tephra distribution (Fig 3.5a) excludes some lower-density tephra (occurring between 20-36 greyscale intensity) and therefore represents a minimum estimate of the total abundance of tephra present.

The drinking straw experiments show that tephra layers preserved within marine sediment can be successfully imaged using suitable experimental μCT parameters. Defining thresholds, however, is a qualitative procedure and scan specific. As a result, absolute thresholds that will distinguish between tephra and sediment in a range of different depositional contexts and scans cannot be defined.

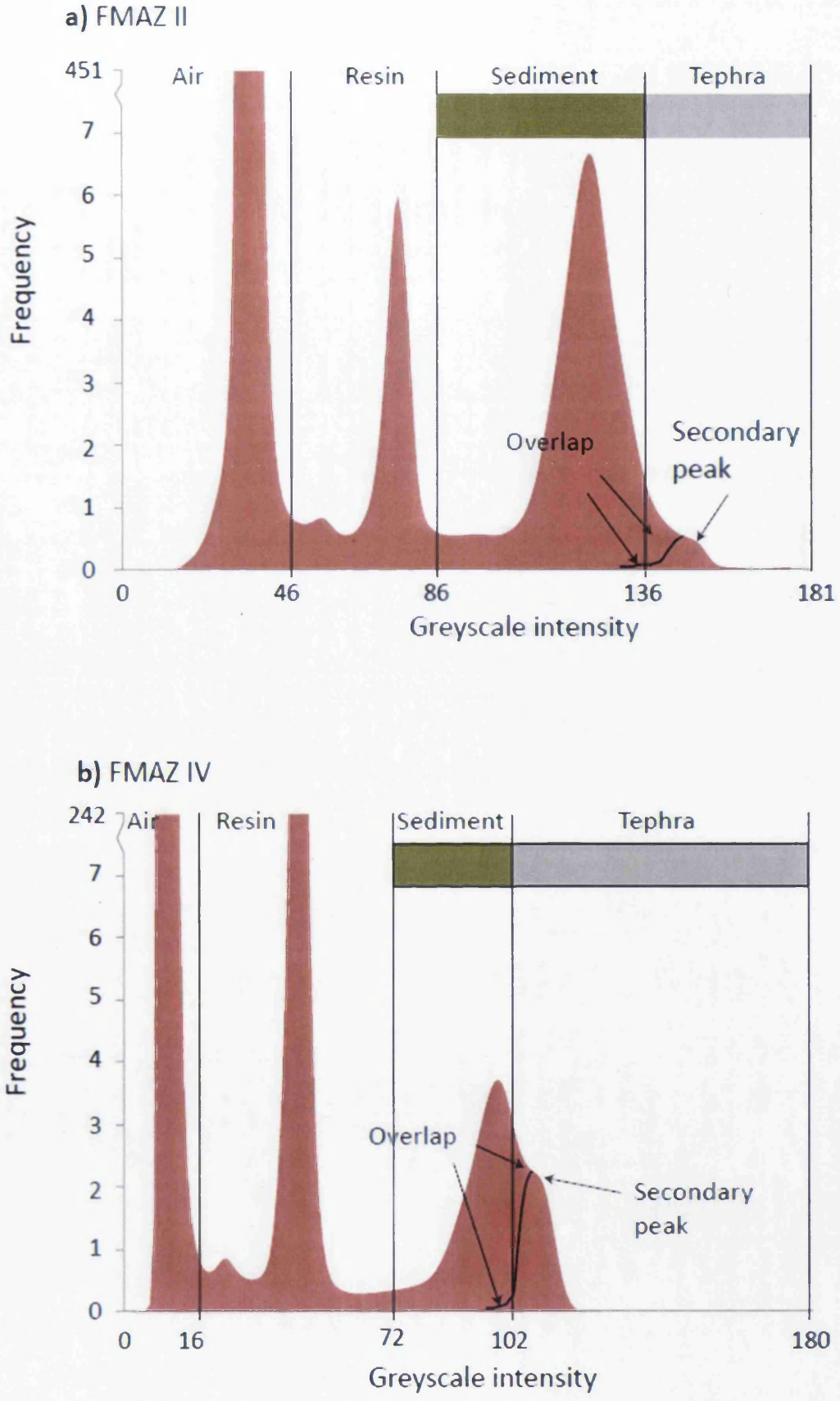

Figure 3.6 Voxel-intensity histograms generated by the tomographic analysis of the FMAZ II and IV resin-blocks respectively. Vertical lines denote the thresholds defined by the histogram to isolate air, resin, sediment and tephra.

The approach presented here provides optimal instrument parameters but requires the validation and placement of thresholds with known areas of tephra. μCT scans of tephra deposits presented in the study were performed using the resin-impregnated blocks created during thin-section preparation (Fig 3.4). Thresholding was performed in conjunction with visual tephra comparisons between the thin-section and corresponding tomographic render (see section 3.10.3).

3.10.3 Validating μCT grey-scale thresholds using thin-sections

The intensity-based segmentation procedure, outlined in section 3.9.2, was applied to the voxel intensity histograms generated for the FMAZ II and IV deposits preserved within resin-impregnated blocks. Thin-sections of these deposits were used to define the threshold values (Fig 3.6). In comparison to the artificially-created specimen, the intensity peaks for these cores are less pronounced and a distinct shoulder is observed at the falling limb of the sediment peak (Fig 3.6). The higher greyscale intensity values that form this shoulder are thought to represent secondary peaks that equate to areas of concentrated tephra particles that are of a higher density relative to the surrounding sedimentary matrix (Fig 3.6). This is confirmed by comparing the greyscale 2D μCT slice from the surface of the resin-impregnated block with the previously acquired 2D thin-section image from the same surface (Fig 3.7, 3.8).

A striking similarity is revealed between the μCT-derived tephra distribution, and the darker areas of concentrated tephra shards seen in thin section (Fig 3.7a,b). For example, the greatest concentration of tephra, shown in grey, occurs at the sub-horizontal, sharp contact at 304-304.5 cm depth in the FMAZ II (Fig 3.7ci,di). A 2.5× magnification of this structure from the thin-section confirms the presence of structureless, abundant, well-sorted tephra shards (Fig 3.7di). In addition, below the main shard concentration peak, irregularly aligned packages of concentrated tephra shards, surrounded by a coarse-silt matrix, correspond with μCT-derived tephra-rich areas (Fig 3.7cii,ciii).

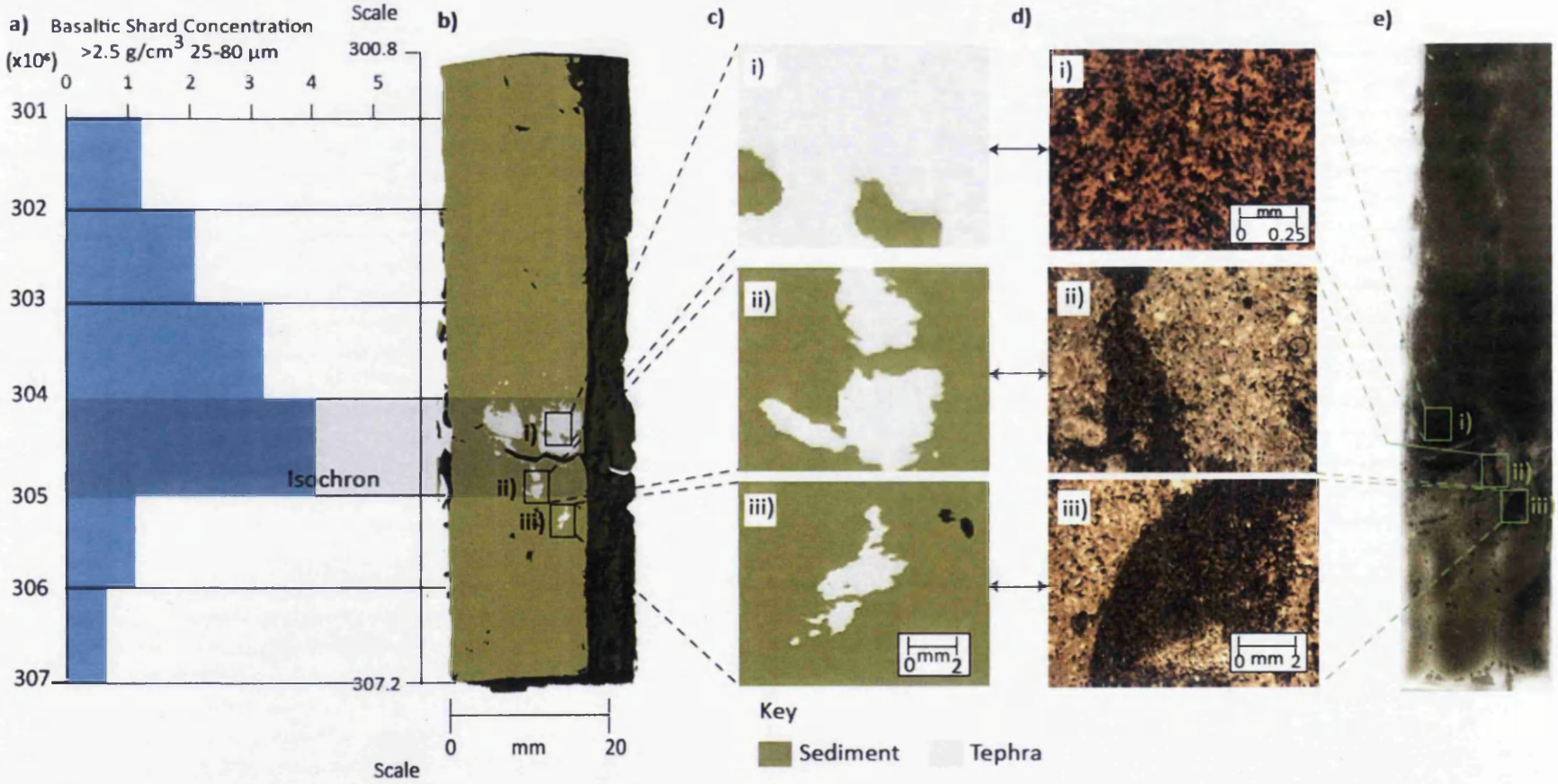

Figure 3.7 Composite thin-section and µCT greyscale summary of the FMAZ II used to validate thresholds defined in Fig 3.6. (a) Shard concentration profile (25-80 cm). (b) Greyscale 2D reconstruction from the surface of the resin block. (c) Indicative greyscale features presented in 4x magnification aligned to (d) corresponding microfacies features derived from thin-section analysis. (e) Thin-section scan. c)+d) i. Predominantly grey and structureless, aligned to massive, well-sorted abundant tephra shards. ii. Typical of the second unit, composed of multiple packages of grey (tephra) in a matrix of green (sediment), aligned to a vertically orientated tephra lens, composed of abundant well-sorted tephra shards within a coarse-silt matrix. iii. Package of vertically orientated grey within a matrix of green aligned to a vertically orientated package of tephra, ~4.2 mm in height, composed of well-sorted tephra shards within a coarse-silt host matrix.

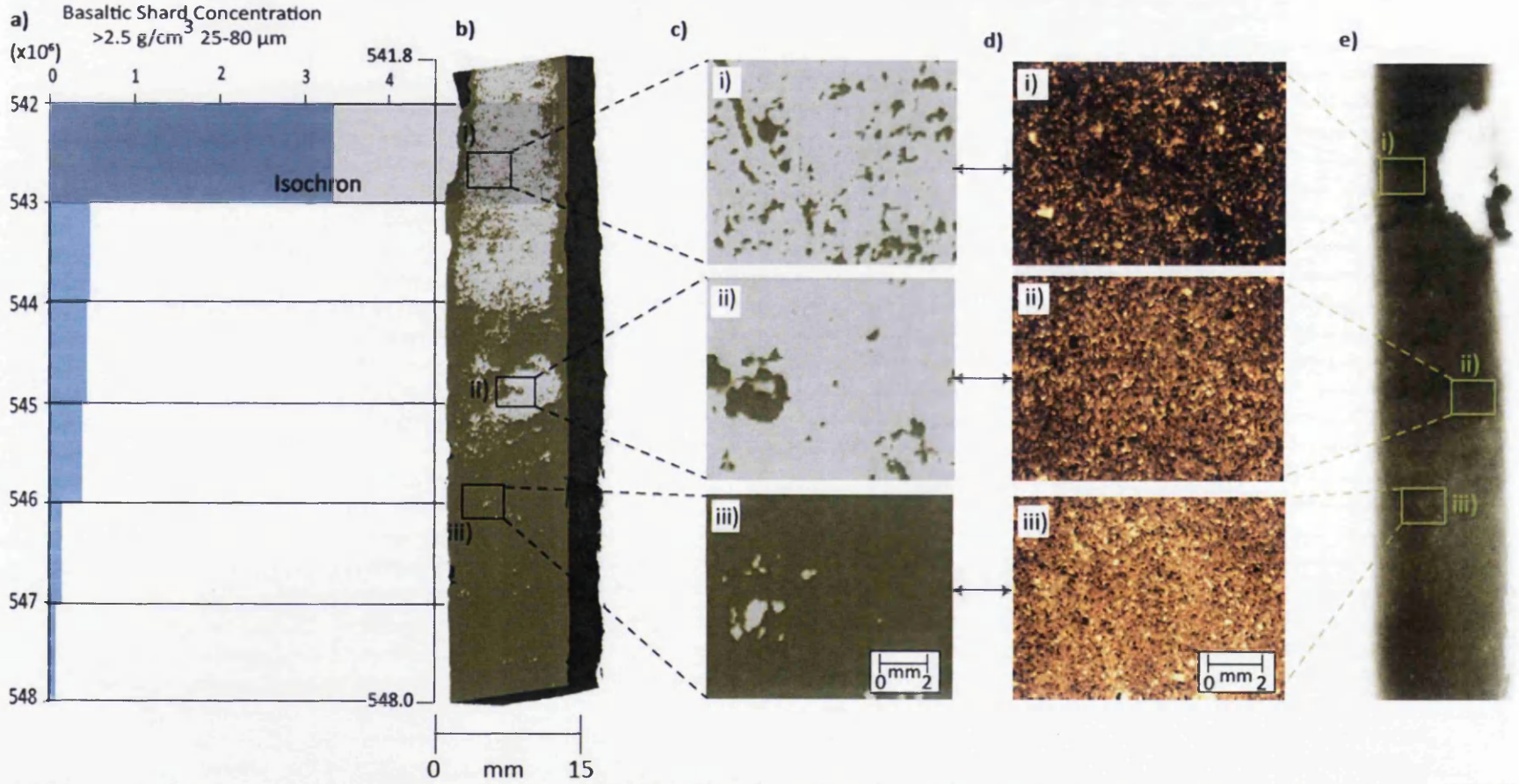

Figure 3.8 Composite thin-section and µCT greyscale summary of the FMAZ II used to validate thresholds defined in Fig 3.6. (a) Shard concentration profile (25-80 cm). (b) Greyscale 2D reconstruction from the surface of the resin block. (c) Indicative greyscale features presented in 4x magnification aligned to (d) corresponding microfacies features derived from thin-section analysis. (e) Thin-section scan. c)+d) i. Predominantly grey with occasional packages of green dispersed randomly throughout, aligned to massive, moderately sorted, abundant tephra shards. ii. Predominantly grey with a large green circular package, aligned to moderately-sorted coarse-silts with glass-shards distributed randomly throughout. iii. Occasional packages of grey distributed randomly within a green matrix, aligned to moderately-sorted coarse-silts, with occasional glass shards in low concentrations.

It is worth noting that the shape of the tephra lobes below the isochron exhibit a slightly different geometry to those observed in thin section and this may be because the thin section was cut from a slightly different angle and plane. This may also be due to the nature of the segmentation process which may not completely separate tephra in lower concentrations from the host marine sediments. For FMAZ IV, however, the lowest concentration of tephra is represented by sporadic grey packages within a green-shaded matrix in the 2D μCT render (Fig 3.8cii). A 4x magnification of this feature from thin-section confirms the presence of a coarse-silt matrix with occasional well-sorted tephra shards.

The excellent agreement between the features observed in the thin-sections and the 2D μCT-derived reconstructions support the threshold definition and intensity-based segmentation procedures. In these examples, it is demonstrated that concentrated tephra areas are represented by a secondary peak/shoulder with higher greyscale intensity values (Fig 3.6). The prominence of this shoulder/secondary peak relative to the sediment phase is shown to vary between deposits due to contrasting tephra/sediment concentrations and mineral compositions (Fig 3.6). Nonetheless, the visual confirmation approach indicates that the voxel intensity diagrams are appropriate for delimiting tephra and sediment and allow a three-dimensional reconstruction of the tephra deposits. Three-dimensional structures observed in these two samples are discussed in Chapter 7.

Chapter 4 Tephrochronology of North Atlantic marine core JM11-19PC between ~16-55 ka

4.1 Introduction

The aim of this chapter is to produce a tephrostratigraphy record for North Atlantic marine core JM11-19PC spanning MIS 2 and 3 (~16-55 ka BP). The core site is susceptible to the deposition of exceptionally high tephra concentrations including three visible macrotephra horizons (FMAZ II, III, IV), previously identified by Ezat et al. (2014). Tephra shard concentration profiles, grain-size characteristics, degree of geochemical homogeneity and shard co-variance with IRD are investigated. These features allow a thorough assessment of primary ash-fall preservation and help to unravel the depositional mechanisms operating in the ocean environment. Major element results from three separate grain-size fractions are used to capture the full compositional range of the FMAZ deposits and help to improve their stratigraphical placement. Cryptotephra deposits are investigated to provide a full tephrostratigraphical record for this core. The geochemical compositions of all identified tephras are compared to previously published marine and ice-core tephra deposits.

4.2 JM11-19PC: core location, oceanographic setting and proxy record

The JM11-19PC core was retrieved by the R-V *Jan Mayen* in May 2011 from 1179 m water depth on the central North Faroe Slope in the Southeastern Norwegian Sea

(62°48'98'' N 03°52'04'' E) (Fig 4.1). The core is ~11 m long and penetrates into MIS 6 sediments at the base. Two depth intervals spanning MIS 2 and part of MIS 3 are investigated: 183-553 cm and 600-635 cm. Whole core magnetic susceptibility was measured on-board using a Geotek MSCL core loop sensor following procedures outlined in Rasmussen et al. (1996). Eleven radiocarbon dates have been measured on monospecific planktonic foraminifera (calibrated using INTCAL Marine 13) to provide a chronological framework for this record (Ezat et al., 2014; Reimer et al., 2014) (Fig 4.2). Proxy investigations include high-resolution foraminifera Mg/Ca analyses to reconstruct bottom water circulation during D-O events (Ezat et al., 2014).

As the JM11-19PC record is a recently acquired sequence, no IRD counts currently exist. Instead, the IRD record for neighbouring core, ENAM 93-21 is employed (Fig 4.1, 4.3). The FMAZ II and III deposits, along with peaks and troughs in the magnetic susceptibility records, are used to establish correlation points between JM11-19PC and ENAM93-21.

The core consists predominantly of coarse silty-clays that vary in colour (Fig 4.4). The darker layers have been interpreted to correlate with interstadial events, and lighter with stadial events (Ezat et al., 2014). The FMAZ II can be seen as a distinct 2 cm thick black macrotephra at ~303 cm on an XRF scan (Fig 4.4). The FMAZ III is not a visible horizon and is present at ~430 cm according to analysis conducted by Ezat et al. (2014). However, the shard concentration profile for this deposit is diffuse and use of this deposit as a marine-ice tie point may be erroneous in this instance (Bourne et al., 2013). The FMAZ IV is a thick black macrotephra present between ~543-545 cm. Tephra is also present between 543 cm and 500 cm appearing as black smears (Fig 4.4). The FMAZs, NAAZ II and the additional fourteen AMS dates have been used by Ezat et al. (2014) to construct an age model for the record (Fig 4.2) and linear interpolation between anchor points provides a sedimentation rate (Ezat et al., 2014) (Fig 4.4). This work builds upon previous low-resolution tephra investigations conducted by Ezat et al. (2014) and additionally explores the presence of cryptotephra within the fine grained fraction. This will permit an assessment of depositional processes and re-evaluate the position of the tephra isochron based upon the new data set.

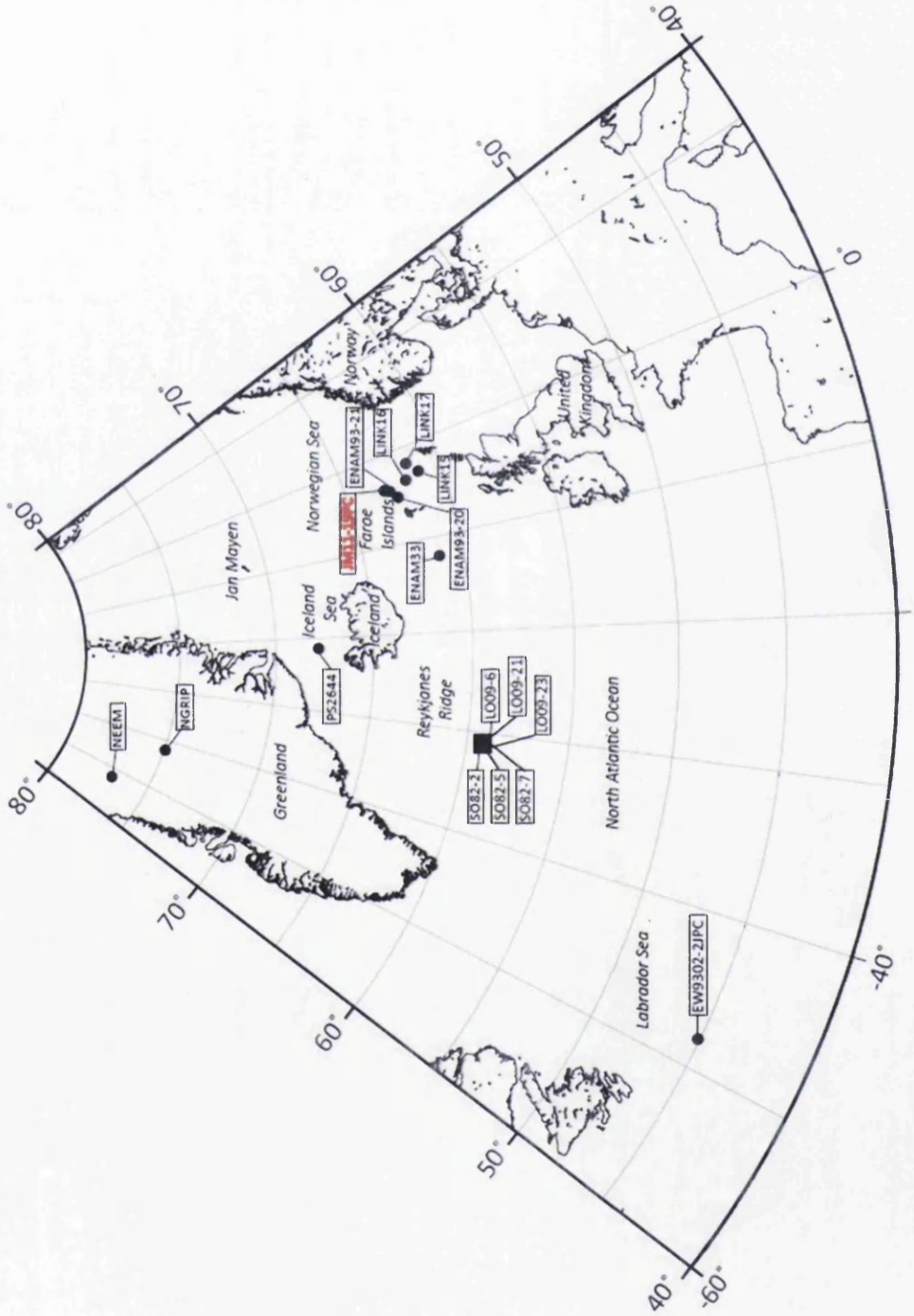

Figure 4.1 Location of the core JM11-19PC. The location of other North Atlantic marine and Greenland ice-cores mentioned in the chapter are also shown.

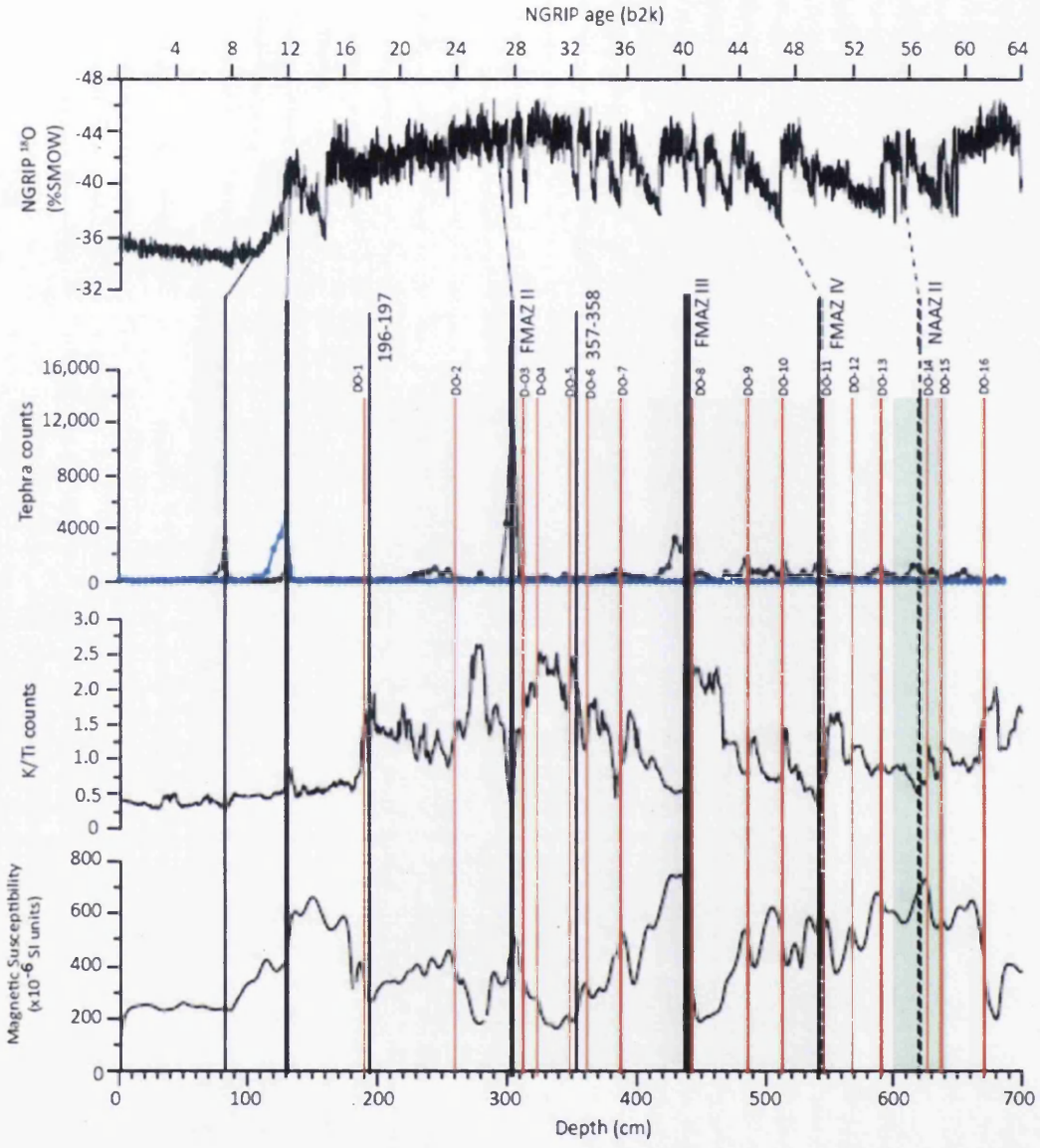

Figure 4.2 Magnetic susceptibility and XRF-K/Ti ratios for core JM11-19PC from Ezat et al. (2014). Black lines marks the depths of the tephra horizons identified in this study and Ezat et al. (2014). Red lines denote the start of the interstadials. The grey area denotes the core sequence analysed contiguously in this investigation. The green area indicates the low resolution investigation to trace the NAAZ II.

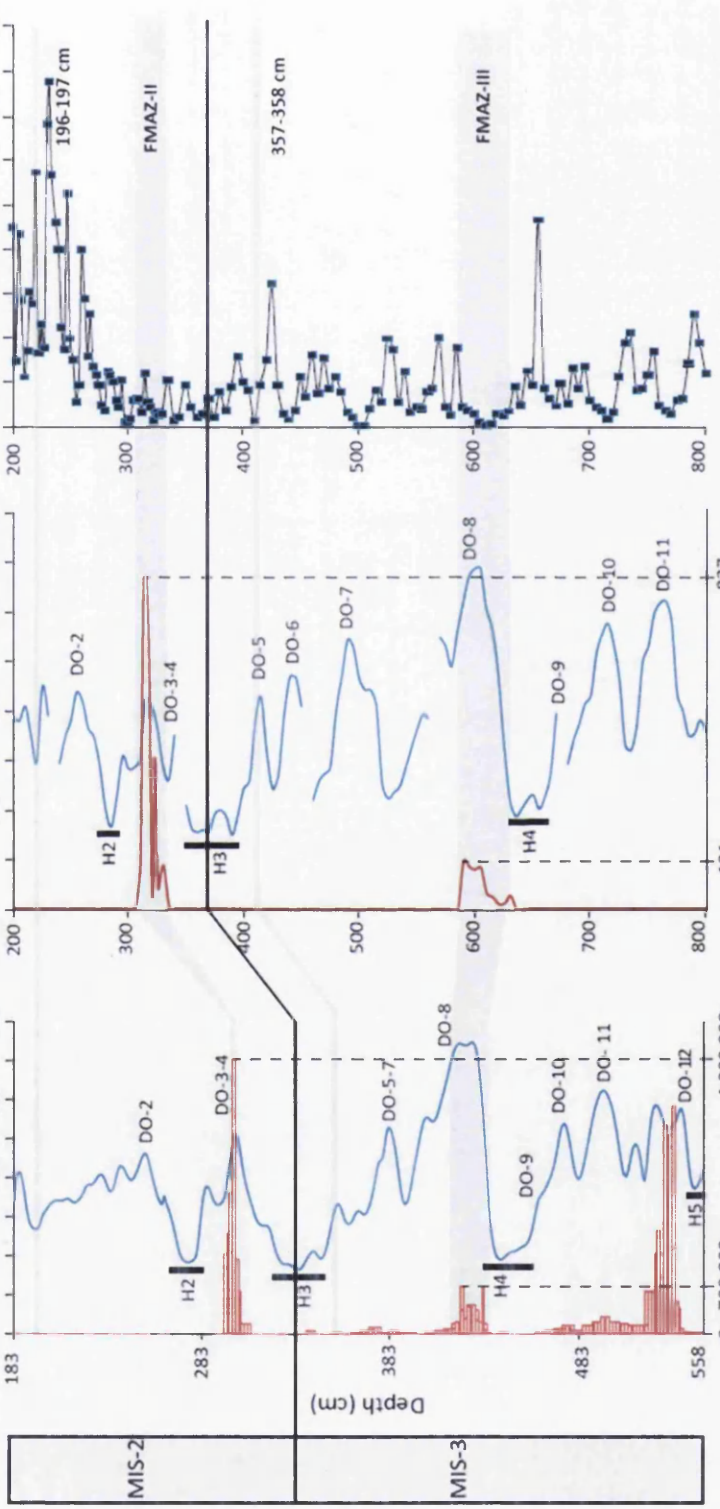

Figure 4.3 Magnetic susceptibility, tephra stratigraphy and IRD record for marine core ENAM93-21. a) Magnetic susceptibility for JM11-19PC with corresponding tephra counts within this study with a density > 2.5 g/cm^3 within the 25-80 µm fraction b) Magnetic susceptibility for ENAM93-21 with corresponding tephra counts from the >150 µm fraction (Rasmussen et al., 2003). c) Number of ice-rafted grains >500 µm per gdw (IRD) in ENAM93-21 (Rasmussen et al., 1996). The grey bars represent correlation between records based upon the position of the FMAZ II and FMAZ III horizons in both sequences. H = Heinrich event approximate positions. DO = Dansgaard-Oeschger event following the recommendations in Rasmussen et al. (2014).

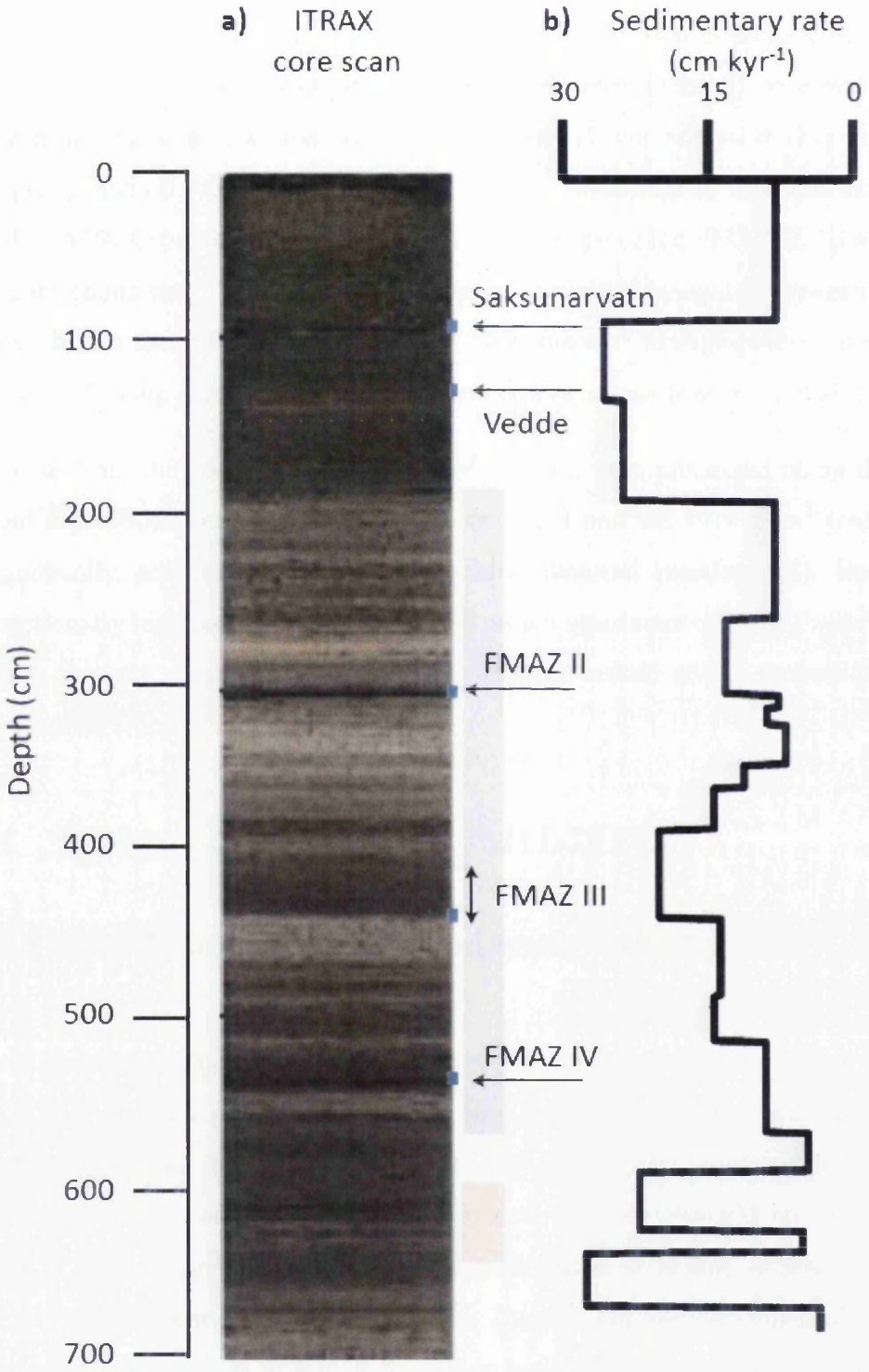

Figure 4.4 (a) High resolution core image obtained by ITRAX core-scanner of the upper 7 m of JM11-19PC (Ezat et al., 2014). Arrows represent positions of FMAZ horizons based upon Ezat et al. (2014) and refined based upon analysis presented in this study. Sedimentation rate based upon the tuned age model of Ezat et al. (2014). The grey bar denotes the section of the core analysed contiguously in high resolution. The red bar denotes the core section analysed in low-resolution to trace the NAAZ II.

4.3 Sampling strategy

The tephra content of the record between 183 and 553 cm was initially investigated at low-resolution (5 cm contiguous samples) and then intervals of elevated shard concentrations were analysed at high-resolution (1 cm samples) (Fig 4.5). This sampling interval was chosen to overlap similar stratigraphic intervals covered in MD04-2829CQ (see chapter 5) and to ensure coverage of the FMAZ II, III and IV. 5 cm contiguous samples (25-80 μm fraction only) were investigated between 600-635 cm to locate the position of NAAZ II. This specific stratigraphical interval was chosen following previously obtained coarse tephra counts from Ezat et al. (2014).

Material from the 25-80 μm fraction in all samples was processed using the heavy liquid separation procedure outlined in section 3.3 and the >2.5 g/cm^3 fraction was magnetically separated to purify the basaltic material (section 3.4). Due to the exceptionally high tephra content (>10,000 brown shards per 0.5 gdw) within the 25-80 μm fraction, samples within this fraction were spiked with Lycopodium spores (see section 3.5).

4.4 Tephra horizons within JM11-19PC

4.4.1 Shard concentrations and tephra stratigraphy

Shard concentrations from different densities and size fractions are shown in Figure 4.5. Four distinct peaks in the 25-80 μm fraction have been identified at low resolution, relative to background values, with the highest concentration of brown shards (~3 million shards per 0.5 gdw) present between 298-303 cm. Specifically, peaks in brown shard concentration were identified at ~304 cm, ~424-443 cm, ~545 cm and 618-623 cm (Fig 4.5) (Table 4.1). The 304 cm and 545 cm peaks span the stratigraphical positions of the visible tephra beds (Fig 4.4) and the 424-443 cm and 618-623 cm peaks overlap with tephra-rich horizons identified by Ezat et al (2014). Elevated shard concentrations in the coarser 80-125 μm and >125 μm fractions also coincide with these peaks. As the concentrations bracketing the three uppermost peaks were relatively high, tephra concentrations were determined at high-resolution

up to ~10 cm above and below each peak to fully capture the fluctuations in shard concentrations (Fig 4.5).

The fourth peak at ~618-623 cm has not been quantified in high resolution. Concentrations of colourless and brown shards were exceptionally high between 618-623 cm and it was considered a sufficient chronological fix-point for this record (Rasmussen, pers comm). Within the 2.3-2.5 g/cm^3 fraction, a background of ~500 colourless shards occurs throughout the core, with three distinct peaks identified between 193-198 cm, 353-358 cm and 618-623 cm (Fig 4.5e). High-resolution samples were investigated ~5 cm above and below the two uppermost peaks to constrain the stratigraphical position of these deposits. High resolution shard counts reveal peaks at 196-197 cm and 357-358 cm (Table 4.1).

4.4.2 JM11-19PC 196-197 cm

4.4.2.1 Shard descriptions and concentration

A peak of 20,000 colourless shards (per 0.5 gdw) at 196-197 cm marks the first major influx of tephra particles and is overlain by a gradational upward tail (Fig 4.5). The shards exhibit a variety of cuspate morphologies and are highly vesicular in appearance. The deposit falls within interstadial DO-2 according to low magnetic susceptibility values and rapidly decreasing K/Ti counts (Fig 4.2). An age of 15,663 ± 190 ka b2k is derived from radiocarbon dating at a depth of 195 cm, which falls 1 cm above the peak in shard concentration (Fig 4.2) (Ezat at el., 2014). Comparison with nearby core ENAM93-21 suggests a strong coeval IRD signal during the period of deposition and is likely to be an ice-rafted deposit (Rasmussen et al., 2003) (Fig 4.3).

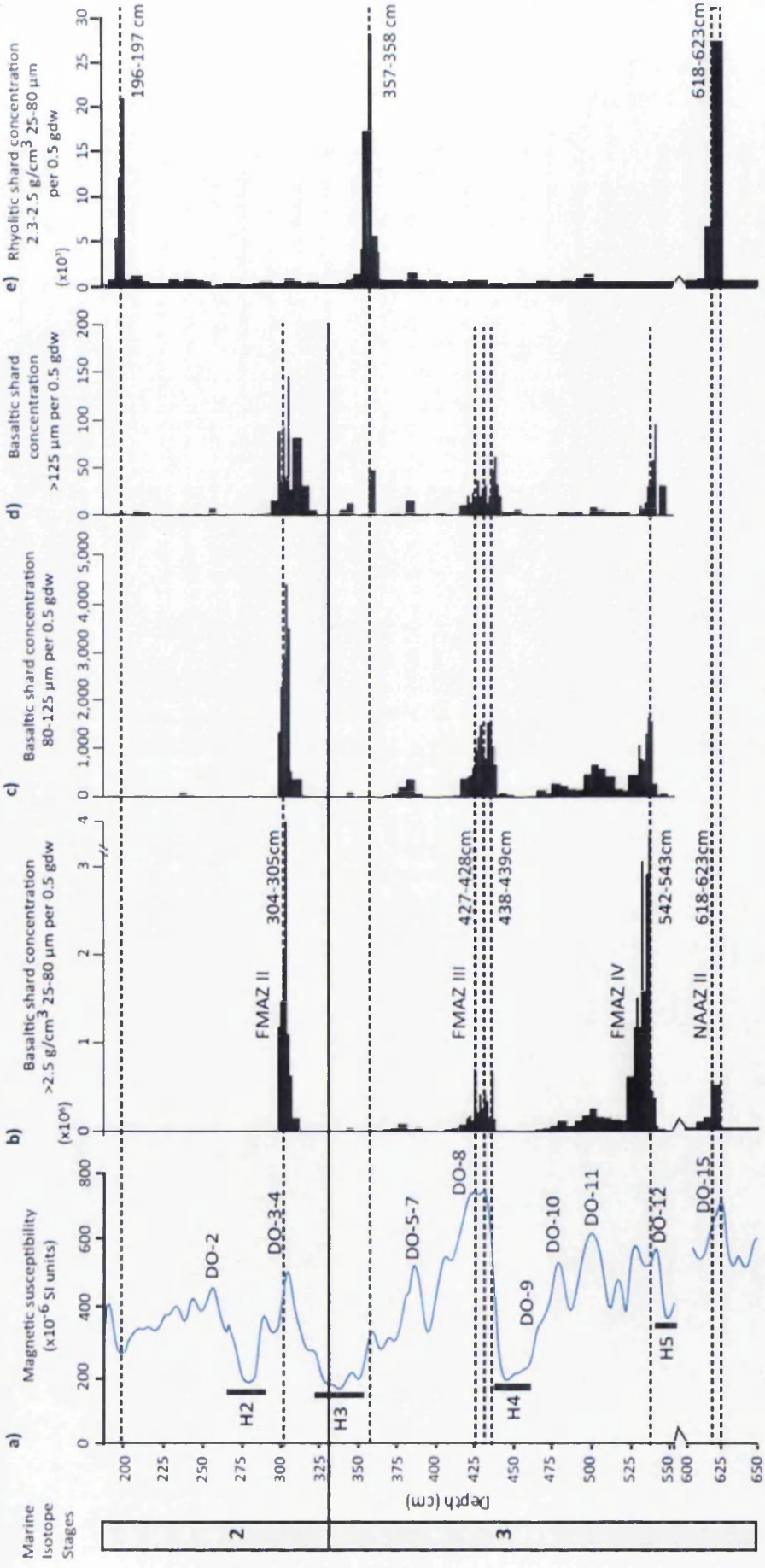

Figure 4.5 High and low resolution tephra stratigraphy for MIS 2 and late MIS 3 section from the JM11-19PC core. a) Magnetic susceptibility b) Number of basaltic shards with a density > 2.5 g/cm^3 within the 25-80 µm fraction. c) Number of basaltic shards within the 80-125 µm fraction. d) Number of basaltic shards within the >125 µm fraction. Grey dotted lines denote samples for which glass shards were extracted for geochemical analysis. H = Heinrich event approximate positions based on Ezat et al. (2014). DO = Dansgaard-Oeschger event and the number denotes the associated Greenland Interstadial event following the recommendations of Rasmussen et al. (2014). gdw = grams dry weight sediment.

Table 4.1 Summary of basaltic and rhyolitic tephra deposits found within JM11-19PC. Age estimates and climatic stratigraphy are derived from radiocarbon measurements (Ezat et al., 2014), magnetic susceptibility and correlations to tephras with established age estimates. Interpretations are based upon evidence presented in the chapter.

Tephra Layer (cm)	Shards per 0.5 gdw	Climatic event	Age estimate (ka)	Geoche-mistry	Composition	Volcanic Source	IRD signal	Signal	Depositional process	Potential isochron?
196-197	21,000	DO-2	~15.7	RHY	Heterogeneous	Unknown	Yes	Secondary	Ice-berg rafting	No
304-305	$4*10^6$	DO-3	~27.7	TB	Homogeneous	Kverkfjöll	No	Primary	Airfall	Yes
357-358	28,000	DO-5	~31.1	RHY	Homogenous	Katla	No	Primary	Airfall	Yes
423-443	750,000	DO-8	~38.5	TB	Heterogeneous	Grímsvötn	No	Secondary	Airfall/ bottom current	No
542-543	$3*10^6$	DO-12	~48	TB	Homogeneous	Grímsvötn	No	Primary	Airfall/Bottom currents	Yes
618-623	750,000	DO-15	~55	TB/ RHY	Homogeneous	Grímsvötn Tindfjallajökull	No	Primary	Airfall	Yes

4.4.2.2 Geochemistry and source identification

Twenty-five single shards were analysed by EPMA and reveal a heterogeneous rhyolitic composition (Fig 4.6). The variability of major oxides is most apparent within SiO_2 concentrations that vary between 71.4-77.8 wt% and K_2O concentrations of 3.1-5.4 wt%. Despite the observed heterogeneity, twelve shards form a moderately homogeneous cluster (population one). Distinctive geochemical characteristics of this population include FeO concentrations of ~1.05-1.87 wt%, TiO_2 concentrations of ~0.12-0.16 wt% and K_2O concentrations of ~3.81-4.31 wt% (Table 4.2). This population overlaps slightly with the Tindfjallajökull source envelope on FeO vs CaO and SiO_2 vs K_2O biplots (Fig 4.7b,d) but this overlap is not observed on other geochemical biplots. Shards from this population appear unrelated to any source on FeO vs Al_2O_3 biplots (Fig 4.7). Six shards exhibit K_2O concentrations >5 wt% and form the second population (Fig 4.6). The only reported proximally derived material that exhibit geochemistries with similarly high K_2O content originate from the Snæfellsjökull system in western Iceland, but only two data analyses exist for this volcanic center (Jónasson et al., 2007). However, the second population in 196-197 cm does not correspond with other major oxides and this prevents a source from being assigned. The scattered geochemical composition suggests this deposit is the product of numerous different eruptions from a variety of volcanic centers (Fig 4.7).

4.4.2.3 Wider correlations and depositional processes

Population one from 196-197 cm shows some affinity to glass shard analyses derived from the Borrobol and other compositionally similar tephras e.g. Penifiler, KOL GS-2 and Fosen tephra (Fig 4.8). The Borrobol tephra has been discovered in a number of Lateglacial sequences near the onset of GI-1 (Turney et al., 1997; Davies et al., 2004; Pyne O'Donnell et al., 2008).

Table 4.2 Mean and 1σ major element results of basaltic glass shards extracted from deposits found within JM11-19PC. Total oxide values are raw values prior to normalisation. All major elements are expressed as percentage weight. Total iron expressed as FeO. n = number of shards analysed.

Tephra Layer	Grain size (μm)	n	SiO_2	TiO_2	Al_2O3	FeO	MnO	MgO	CaO	Na_2O	K_2O	P_2O_5	Total
196-197 cm Population 1	25-80	12	76.45	0.15	12.77	1.44	0.04	0.08	0.85	4.31	3.98	0.01	94.82
			0.78	*0.01*	*0.59*	*0.24*	*0.01*	*0.03*	*0.09*	*0.42*	*0.27*	*0.01*	*1.04*
304-305 cm	25-80, 80-125, >125	85	49.82	3.70	12.93	15.34	0.24	4.80	9.08	3.09	0.57	0.42	97.61
			0.61	*0.06*	*0.41*	*0.46*	*0.01*	*0.21*	*0.23*	*0.25*	*0.05*	*0.04*	*1.22*
357-358 cm	25-80	28	71.48	0.38	13.73	3.53	0.11	0.28	1.46	5.28	3.70	0.05	96.85
			0.47	*0.04*	*0.41*	*0.24*	*0.02*	*0.04*	*0.09*	*0.24*	*0.11*	*0.01*	*1.62*
427-439 cm	25-80, 80-125, >125	156	49.81	2.94	13.20	14.07	0.23	5.83	10.38	2.85	0.43	0.26	98.42
			0.44	*0.31*	*0.47*	*0.93*	*0.02*	*0.59*	*0.65*	*0.22*	*0.07*	*0.04*	*1.09*
542-543 cm	25-80, 80-125, >125	71	50.32	2.59	13.27	14.15	0.23	5.75	10.26	2.80	0.39	0.23	98.03
			0.46	*0.10*	*0.24*	*0.53*	*0.01*	*0.30*	*0.36*	*0.19*	*0.04*	*0.02*	*0.95*
618-623 cm	25-80	29	50.46	2.61	13.11	13.63	0.23	5.94	10.58	2.78	0.40	0.27	98.14
			0.86	*0.01*	*0.62*	*0.31*	*0.01*	*0.03*	*0.09*	*0.24*	*0.18*	*0.01*	*0.79*
618-623 cm	25-80	9	75.64	0.17	11.60	2.58	0.07	0.01	0.57	5.07	4.38	0.00	96.04
			0.45	*0.00*	*0.48*	*0.20*	*0.00*	*0.01*	*0.05*	*0.20*	*0.09*	*0.00*	*1.30*

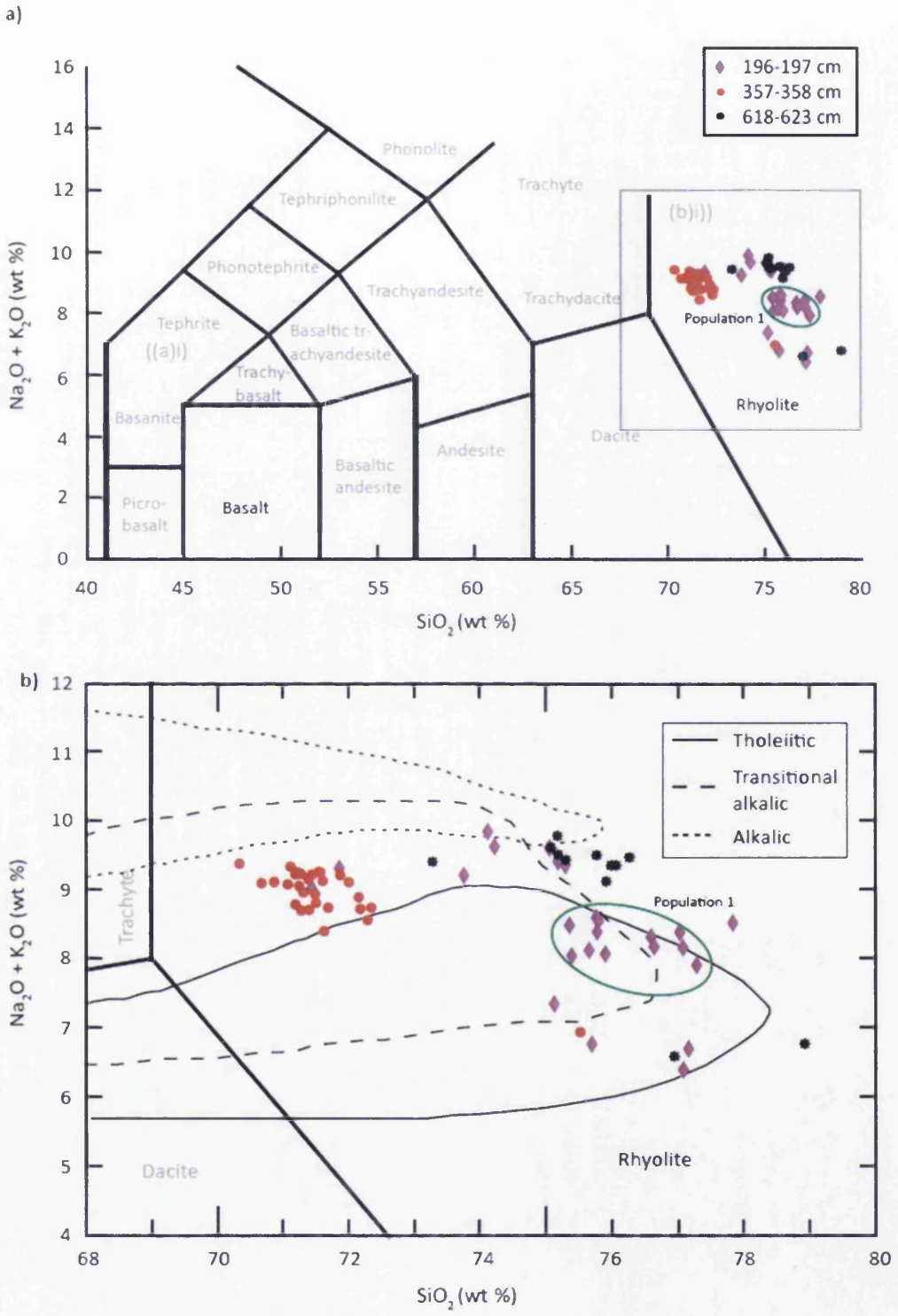

Figure 4.6 (a) Total alkalis vs silica plot for analyses from rhyolitic deposits found in JM11-19PC b) Inset of TAS plot focusing on the rhyolitic analyses. Chemical classification is defined by Le Maître et al. (1989). The compositional envelopes for the Icelandic rock suites are defined by Jakobsson et al. (2008). Population one of 196-197 cm has also been indicated.

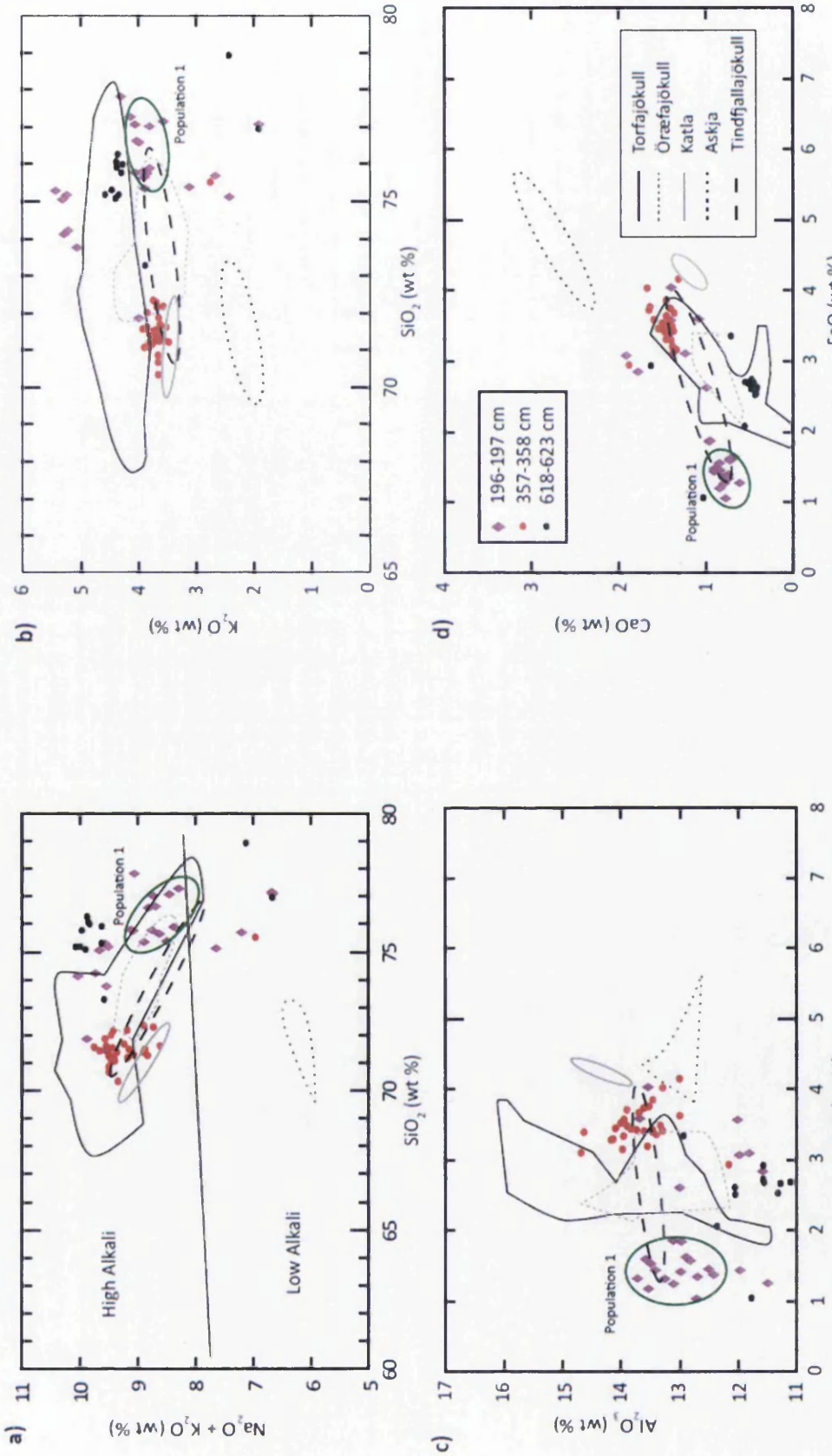

Figure 4.7 Glass shard analyses for three rhyolitic deposits found in JM11-19PC compared to geochemical envelopes for five different transitional alkali Icelandic source volcanoes based on individual whole rock analyses presented in Jónasson (2007). All data have been normalised to 100% total oxide concentration. The sub population in 196-197 has also been highlighted.

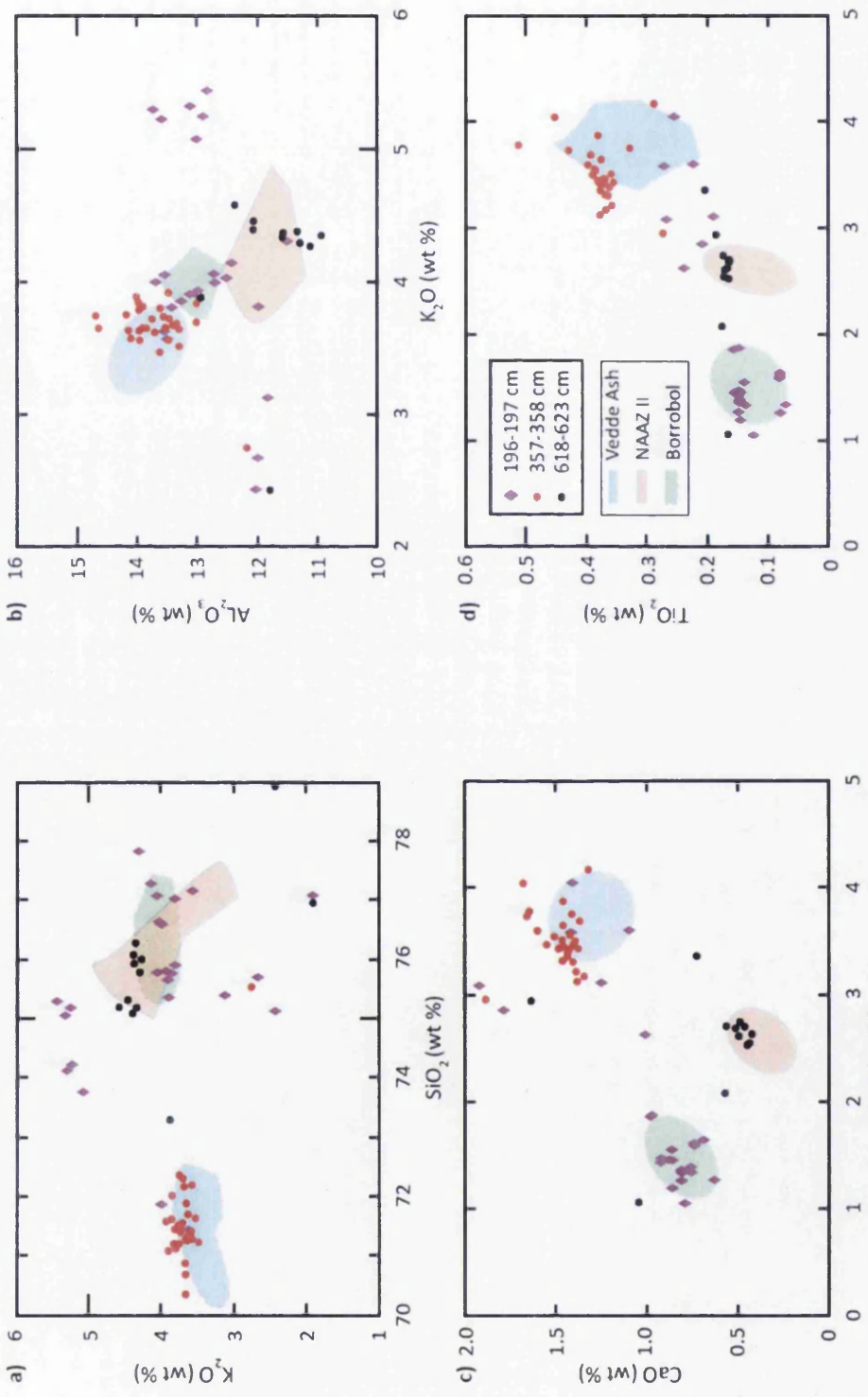

Figure 4.8 Major oxide results (wt %) for rhyolitic deposits found in JM11-19PC compared to tephras of similar geochemical composition. (a), (b), (c), (d) Major element oxides compared to geochemical compositional envelopes for the NAAZ II (Wastegård et al., 2006; Brendryen et al., 2011; Abbott, unpublished), Katla sourced rhyolites (Wastegård et al., 2002; Mortensen et al., 2005; Lane et al., 2012) and a combined Borrobol and Borrobol-like (Davies et al., 2003; Guðmundsdóttir et al., 2011; Matthews et al., 2011b; Cook, unpublished).

Similar material exhibiting Borrobol-like geochemical compositions have been found in different stratigraphic positions in Sweden (Davies et al., 2003), Scotland (Pyne O'Donnell et al., 2008; Matthews et al., 2011b) and the North Icelandic Shelf (Eiríksson et al., 2000; Guðmundsdóttir et al., 2011). Furthermore, new unpublished data suggests that tephras with compositions similar to the Borrobol in the ice are located in GI-1e and GS-2. Magnetic susceptibility and K/Ti ratio suggest 196-197 cm was deposited during interstadial conditions associated with DO-2 (Fig 4.2). Stratigraphically, the first population in JM11-19PC is likely to originate from the GS-2 occurrence of the Borrobol-like tephra found within the Greenland ice-cores.

Marine occurrences of Borrobol-like material have been discovered in MD99-2275 and MD99-2271 from the North Icelandic shelf, though these have been discovered above glacial sediments and in co-occurrence with a basaltic layer (Guðmundsdóttir et al., 2011), which is not a feature of JM11-19PC 196-197 cm. An additional Borrobol-like tephra has been detected in GS-2, derived from AMS ^{14}C dates and biostratigraphy, in cores HM107-04 and HM107-05 from North Icelandic marine sediments (Eiríksson et al., 2000). This deposit may be related to JM11-19PC 196-197 cm, but cannot be rigorously tested as not all geochemical data for this deposit has been reported.

The first population in 196-197 cm is compared to the GI-1e and GS-2 occurrences in the ice and other GS-2 marine deposits to assess any geochemical similarities between the deposits. Shards on the FeO vs TiO_2 biplot fall solely within the GI-1e occurrence of the Borrobol, but this is not reflected in other geochemical biplots (Fig 4.9c). Generally, glass shards from JM11-19PC are distributed equally across all three compositional envelopes, with varying degrees of overlap presented on different geochemical biplots. The strong geochemical heterogeneity exhibited by this horizon implies that the 196-197 cm deposit contains a secondary depositional signal (Fig 4.8). Strong covarying IRD influx suggests this horizon is likely to have been deposited from iceberg rafting which contains an amalgamation of numerous eruptions sourced from different volcanic centers. Consequently, this deposit cannot be utilised as an isochron for integration within the marine tephra framework.

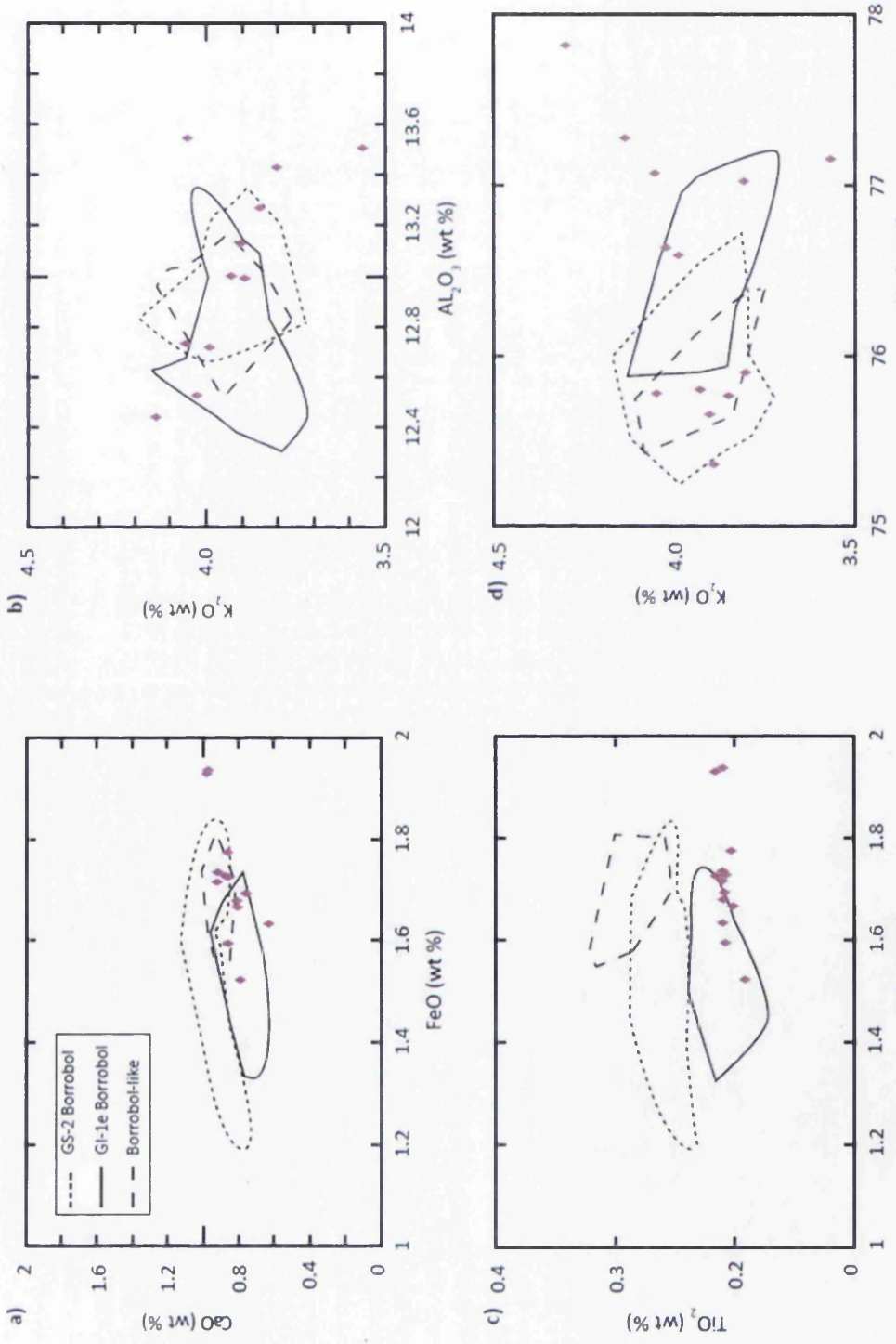

Figure 4.9 Major oxide results (wt %) for the first population in 196-197 cm compared to three geochemical composition envelopes of the GI-1e and GS-2 occurrences of the Borrobol tephra in GRIP, NGRIP and NEEM (Cook, unpublished) and Borrobol-like marine deposits (Eiríksson et al., 2000; Guðmundsdóttir et al., 2011).

4.4.3 JM11-19PC 304-305 cm

4.4.3.1 Shard descriptions and concentration

A visible black macrotephra forms a distinct 2 cm thick horizon between 303-305 cm depth and coincides with the highest shard concentration (>3 million shards in the 25-80 μm fraction and 147 in the >125 μm fraction between 304-305 cm) (Fig 4.4, 4.5). The sharp increase and decrease in the shard concentration profile over 6 cm suggests a pulse of tephra with limited post-depositional re-working. The shards are dark brown in colour and have a dense blocky morphology, with some showing a slightly vesicular appearance. An age of 27,709 ± 170 b2k is derived from radiocarbon dating at a depth of 305 cm which falls within the visible macrotephra bed (Fig 4.4) (Ezat at el., 2014).

4.4.3.2 Geochemistry and source identification

Eighty-nine single shards were analysed by EMPA, revealing a basaltic composition that spans the alkaline and tholeiitic rock series subdivision line defined on a TAS plot (Fig 4.10). In total, eighty-five shards form a tight homogeneous population, with only three clear outliers in the >125 μm fraction and one in the 25-80 μm fraction. Outliers have been omitted from further analyses. Distinctive geochemical characteristics include SiO_2 concentrations of ~47.7-51.0 wt%, TiO_2 concentrations of ~3.7 wt%, CaO concentrations of ~8.2-9.6 wt%, K_2O concentrations between ~0.4 and 0.8 wt% and FeO_{tot}/MgO ratios between ~2.8-3.7 (Table 4.2). These geochemical characteristics are more typical of a transitional alkali basaltic composition, suggesting a source from the Eastern or Southern Icelandic flank zones (Jakobsson, 1979). Comparisons with proximal Icelandic material demonstrate that the distinct geochemical population has a close overlap with material sourced from the Kverkfjöll system (Fig 4.11). This is in contrast to Wastegård et al. (2006) and Davies et al. (2008), who previously suggested a Hekla origin. However, there is a greater geochemical overlap with Kverkfjöll across all element biplots (Fig. 4.11)

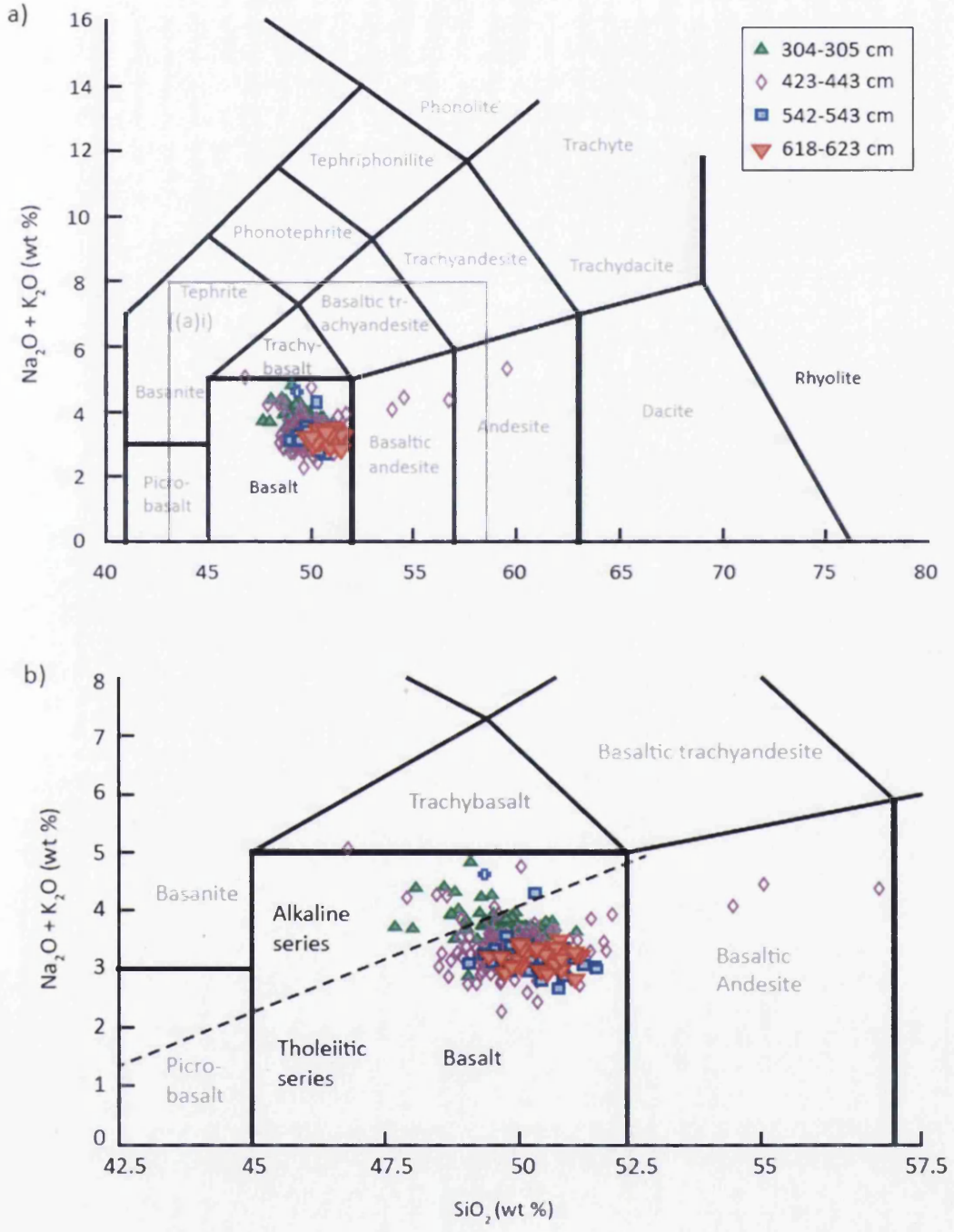

Figure 4.10 (a) Total alkalis vs silica plot for analyses from basaltic deposits found in JM11-19PC. (b) Inset of TAS plot focusing on the basaltic analyses. Chemical classification is defined by Le Maître et al. (1989). The dashed line represents the subdivision into alkaline and tholeiitic rock series defined by MacDonald and Katsura (1964).

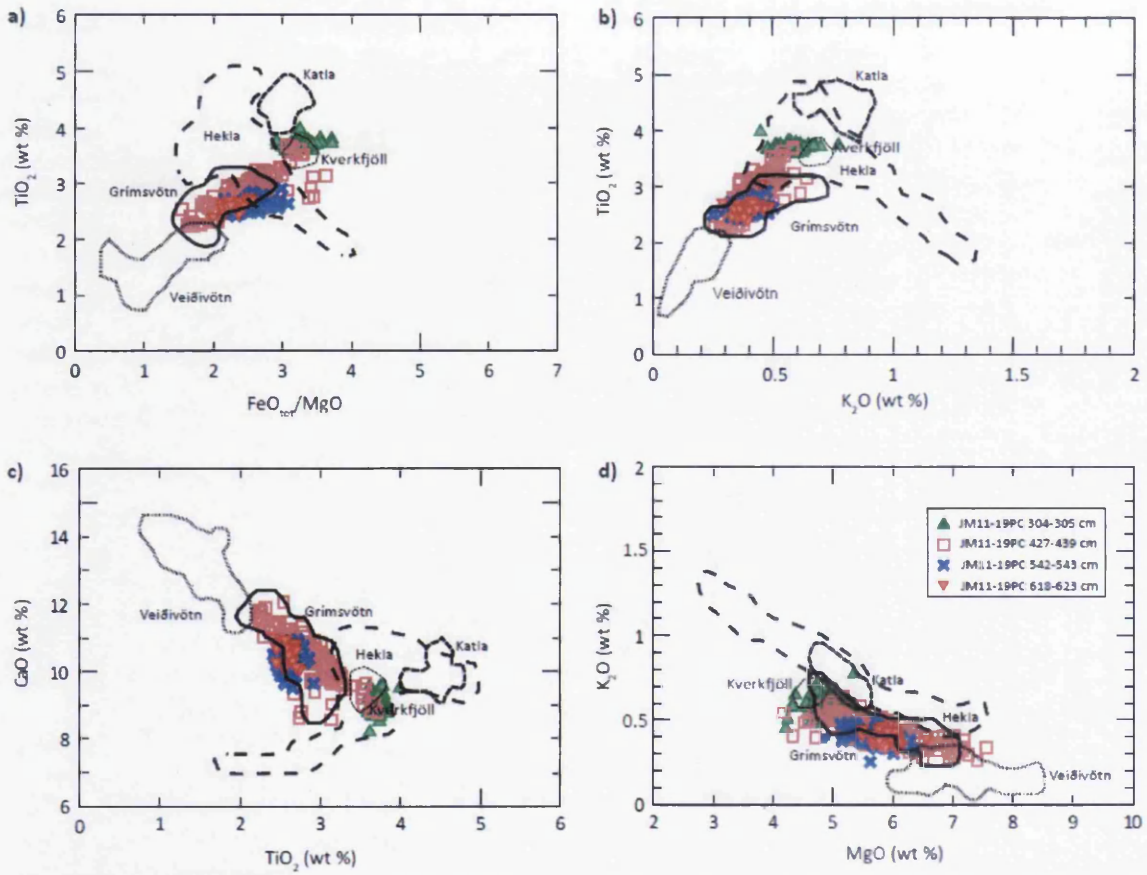

Figure 4.11 Glass shard analyses for the three FMAZs in JM11-19PC compared to geochemical envelopes for different source volcanoes based on individual whole rock analyses presented in Jakobsson (1979), Boygle (1994), Larsen et al. (2002), Óladóttir et al. (2008) and Jakobsson et al. (2008). Data have all been normalised to 100% total oxide concentration.

4.4.3.3 Wider correlations and depositional processes

Single glass shard analyses from JM11-19PC 304-305 cm show a strong affinity to the FMAZ II preserved in five other marine cores from the Faroes region and the NGRIP ice-core with an average similarity coefficient of 0.988 (Rasmussen et al., 2003; Wastegård et al., 2006; Davies et al., 2008) (Fig 4.12). JM11-19PC and the NGRIP data-set exhibit a tighter geochemical population than observed for other North Atlantic marine cores (Fig 4.12). Glass shard analyses from other cores in the Faroes region reveal a wider scatter (Fig 4.12) which has been suggested to represent different phases of the same eruption. However, an eruption closely separated in time cannot be excluded (Wastegård et al., 2006). Alternatively, this scatter may result from the operation of bottom currents and the transportation of material from older eruptions to the site. No shards from JM11-19PC fall within the FMAZ II-2 sub-population originally identified by Wastegård et al. (2006) (Fig 4.12).

Glass shards analysed from JM11-19PC and LINK17 cores exhibit the tightest geochemical populations and plot consistently with the NGRIP 1848.0 m compositional envelope (Fig 4.12). This suggests deposition was likely controlled by one dominant primary process in the Faroes region and several lines of evidence suggest this tephra was deposited isochronously. Firstly, the relative concentration of coarse-grained shards (>125 μm) is low in this deposit and the dominant grain size i.e. 25-80 μm is typical for primary airfall or sea-ice rafted deposits at this core site (Fig 4.5). Secondly, the absence of a strong coeval IRD signal suggests that iceberg rafting was not responsible for deposition (Fig 4.3). This horizon represents a well-resolved primary deposit that can be used as an isochron in high precision correlation studies.

The geochemical population of JM11-19PC 304-305 cm displays some affinities to the V1 ash zone deposited in marine cores on the Reykjanes Ridge (Lackschewitz and Wallrabe-Adams, 1997) (Fig 4.13). According to the magnetic susceptibility record for JM11-19PC the V1 ash zones fall in a similar stratigraphic position to the 304-305 cm horizon (see section 2.5.1.2).

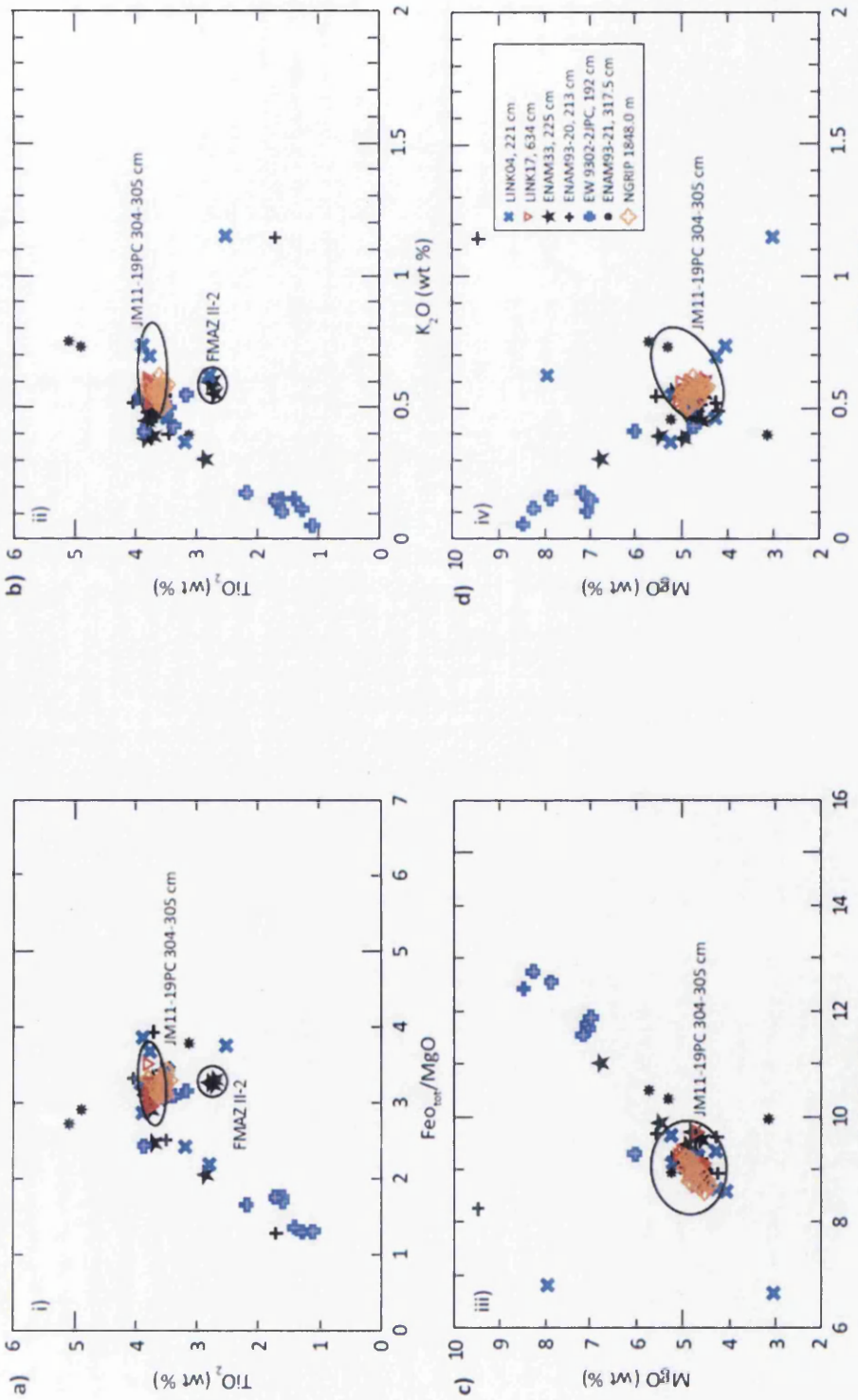

Figure 4.12 Major oxide results (wt%) for glass shards from the FMAZ II deposit. (a-d) The JM11-19PC 304-305 cm compositional envelope is derived from shard analyses obtained from all grain size fractions investigated in this study. An envelope rather than individual data points are shown for clarity. Geochemical results for other reported FMAZ II deposits in the Faroes region and Labrador Sea (Wastegård et al., 2006) and NGRIP are shown (Davies et al., 2008). The FMAZ II-2 compositional envelope is defined by Wastegård et al. (2006).

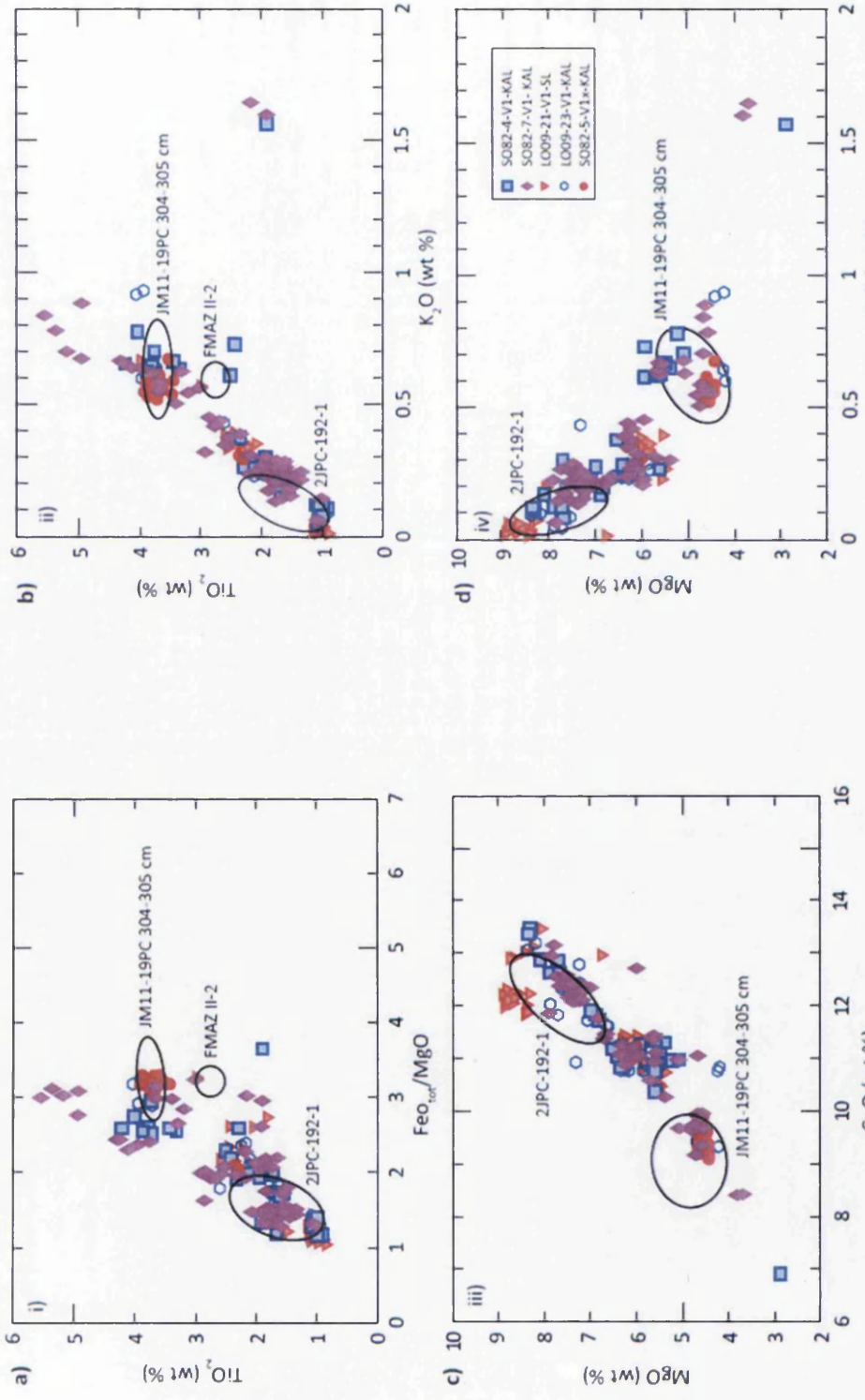

Figure 4.13 Major oxide results (wt%) for glass shards from the FMAZ II deposit. (a-d) Geochemical envelopes for the 2JPC-192-1 (a geochemical population present in EW9302-2JPC) and JM11-19PC 304-305 cm deposits compared to V1 and Vx glass shard analyses derived from five marine cores on the Reykjanes Ridge (Lackschewitz and Wallrabe-Adams, 1997). Data have all been normalised to 100% total oxides concentrations.

However, the V1 deposit is heterogeneous (Fig 4.13) and co-varies with high IRD - a diagnostic feature of iceberg-rafted deposits. A notable sub-peak, SO82-5-V1x-KAL, contains a homogeneous population with no coeval IRD signal and exhibits a high similarity coefficient value of 0.972 with JM11-19PC 304-305 cm (Fig 4.13).

4.4.4 JM11-19PC 357-358 cm

4.4.4.1 Shard description and concentrations

This deposit forms a distinct 1 cm horizon between 357-358 cm (~28,000 colourless shards per 0.5 gdw) and represents the peak in shard concentration (Fig 4.5). The sharp increase and gradational upward tail in shard concentration suggests a pulse of tephra with moderate depositional re-working. The relatively high tephra concentrations ~3 cm below the peak may be indicative of increased levels of bioturbation. Shards in this horizon are highly vesicular and exhibit a cuspate morphology. A radiocarbon-derived age of 31,103 ± 180 b2k is from 350 cm and provides a lower age boundary for this horizon (Ezat et al., 2014). Magnetic susceptibility measurements indicate the deposit occurs before the onset of H3 during DO-5 (Fig 4.2).

4.4.4.2 Geochemistry and source identification

Twenty-nine single shards have been geochemically analysed and reveal a homogenous rhyolitic composition with all shards plotting within the field for the transitional rock suite on the TAS plot (Fig. 4.6b). One clear outlier with a SiO_2 concentration of >75% has been omitted from further analysis. Distinctive characteristics of the main population are SiO_2 concentrations of ~70.52-72.63 wt%, FeO_{tot} concentrations of ~13.00-14.68 wt%, CaO concentrations of ~1.32-1.68 wt%, TiO_2 concentrations of ~0.29-0.51 wt% and K_2O concentrations of 3.48-4.02 wt% (Table 4.2). It is difficult to determine the likely source of this tephra with no apparent and consistent relationship with the main transitional alkali sources (Fig

4.7). However, comparisons with other distal tephra deposits suggest an affinity to the Katla system (see below).

Geochemical datasets are compared from distal tephra occurrences from widespread Lateglacial eruptions to assist in source assignation. Comparisons are confined to Lateglacial tephras, despite a significant difference in age and stratigraphy, as these represent the most rigorous geochemical analyses of Katla rhyolites. Several Katla sourced eruptions i.e. Vedde, AF555, and Suduroy tephras were compiled to create a Katla compositional envelope (Wastegård et al., 2002; Matthews et al., 2011b; Lane et al., 2012) (Fig 4.8). A similarity coefficient of 0.951 indicates a common source between JM11-19PC 357-358 cm and Katla rhyolitic glass shards. This is illustrated on a number of geochemical biplots, where the population of shards frequently plots within the Katla composition envelope (Fig 4.8). However, Figure 4.7 shows no source similarity with Katla. This may be attributed to the limited number of proximal analyses used to create the geochemical envelope in Figure 4.7 in comparison to a large data-set of distal tephra occurrences in Figure 4.8.

4.4.4.3 Wider correlations and depositional processes

Only two horizons of rhyolitic composition have been reported in the ice-core framework for 25-45 ka and these display an affinity to material sourced from Hekla (Bourne et al., 2015). Significantly different geochemical compositions i.e. CaO values >4 wt% and K_2O concentrations <3 % highlight that no shards from the 357-358 cm deposition show affinity to these horizons. Compositional comparisons suggest that this horizon represents a previously undetected Katla-sourced eruption. The geochemical homogeneity and dominance of fine-grained shards (25-80 μm) strongly implies primary deposition. Iceberg rafting is unlikely to have assisted in tephra delivery as there is no coeval IRD signal derived from nearby Faroes core ENAM93-21 (Fig 4.3). A distinct feature of this deposit is an upward and downward tail on the shard concentration profile (Fig 4.5). This may be evidence of bioturbation and mixing, with the peak equating to the correct stratigraphical placement of the isochron. The evidence presented suggests the horizon has been deposited isochronously, likely via primary airfall. Although no ice-core correlative

currently exists for this horizon, it may be possible to utilise this horizon as an isochron if it can be traced in other marine records (Table 4.1).

4.4.5 JM11-19PC 424-443 cm

4.4.5.1 Shard descriptions and concentration

This deposit straddles the warming transition of DO-8 (Fig 4.5). The deposit forms a complex and diffuse zone of tephra that exhibits two indistinct concentration peaks in the 25-80 μm fraction. Peaks in the fine-grained fraction are not mirrored in the coarser-grained fractions, which contain multiple peaks across 13 cm and there is no correspondence between the peaks in the different grain sizes (Fig 4.5). Total shard concentrations are lower than the other FMAZ deposits with ~700,000 shards in the fine fraction and sixty-two in the >125 μm fraction. Shards exhibit a variety of different colouration within this deposit that range from a dark yellow to brown and are predominantly vesicular.

Glass shards from each of the peaks at 438-439 cm and 427-428 cm in all grain-size fractions and the mid-point at 434 cm (25-80 μm fraction only) were extracted and prepared for geochemical analysis. In total, 170 single-glass shards were analysed for geochemistry. A correlation of the JM11-19PC tephra record with that of neighbouring core ENAM93-21 suggests that no coeval IRD signal is associated with this deposit (Fig 4.3). A radiocarbon age of 37,410 ± 890 b2k is derived from a depth of 430 cm, which falls within the stratigraphic interval of this ash zone (Ezat at al. (2014) (Fig 4.2, 4.4).

4.4.5.2 Geochemistry and source identification

Major element analyses from 170 individual shards are classified as basaltic and three are classified as andesitic (Fig 4.10). In total, 156 shards form a relatively heterogeneous population and seventeen outlier shards appear unrelated to the main population and cannot be regarded as additional sub-populations (Fig 4.14).

Geochemical characteristics of this deposit include SiO_2 contents of ~48.5-51.1 wt%, K_2O concentrations of ~0.4 wt%, TiO_2 concentrations of ~2.3-3.7 wt%, CaO concentrations of ~8.8-12.1 wt% and MgO concentrations between ~4.7 and 7.6 wt% (Table 4.2). These characteristics are typical of a tholeiitic basalt, with the TiO_2 and K_2O concentrations implying a Grímsvötn origin (Jakobsson, 1979) (Fig. 4.11). Although a volcanic source can be determined for the material in this deposit, glass shards from each individual depth occupy the full range of Grímsvötn-sourced material. Moreover, biplots of TiO_2 vs CaO and FeO_{tot}/MgO vs TiO_2 highlight the heterogeneity and wide range for these oxides (Fig 4.11a,b). Six shards fall within the FMAZ III-2 envelope, previously defined by Wastegård et al. (2006), though it is not believed that this sub-population is significant enough to represent an additional population related to the FMAZ III (Fig 4.14)

Eleven outlier shards display a wide range of geochemistries and fall outside both populations on a number of elemental oxides (Fig 4.10a,b). Three shards exhibit notably higher TiO_2 concentrations (>4 wt%) and are typically associated with Katla sourced basalts (Jakobsson, 1979). It is particularly interesting to note that three shards exhibit an andesitic composition with high SiO_2 concentrations (>56 wt%). Material of these compositions have been identified in distal peat deposits in the Faroe Islands. These display a close affinity to the Hekla system and are typically compositionally more evolved (Wastegård et al., 2008).

4.4.5.3 Wider correlations and depositional processes

Glass-shard analyses from the main geochemical population show strong similarities with the FMAZ III deposits from three other marine cores in the Faroes region (Rasmussen et al., 2003; Wastegård et al., 2006) (Fig 4.14c,d). The geochemical composition of these previously published deposits exhibit a similar wide-ranging spread to the JM11-19PC 427-439 cm deposit. This can be clearly observed on TiO_2 vs CaO and FeO_{tot}/MgO vs K_2O biplots (Fig 4.14c,d).

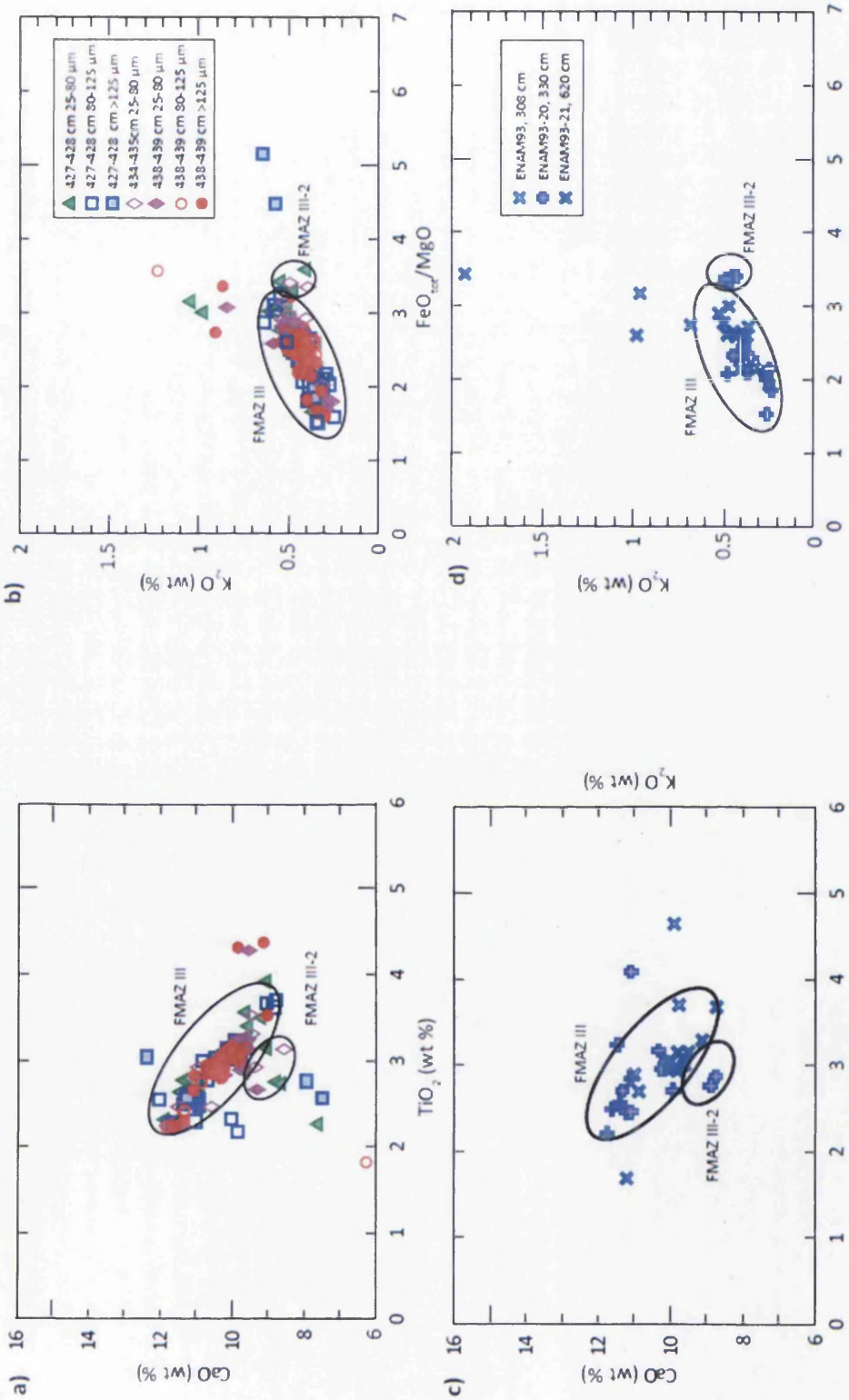

Figure 4.14 Major oxide results (wt%) for the FMAZ III deposit identified in JM11-19PC. (a), (b) The FMAZ III compositional envelope is derived from the main geochemical population from 427-439 cm and the FMAZ III-2 is a sub-population defined by Wastegård et al. (2006). (c), (d) 427-439 cm FMAZ III and FMAZ III-2 envelopes compared to glass shards from three marine cores in the Faroes region (Wastegård et al., 2006).

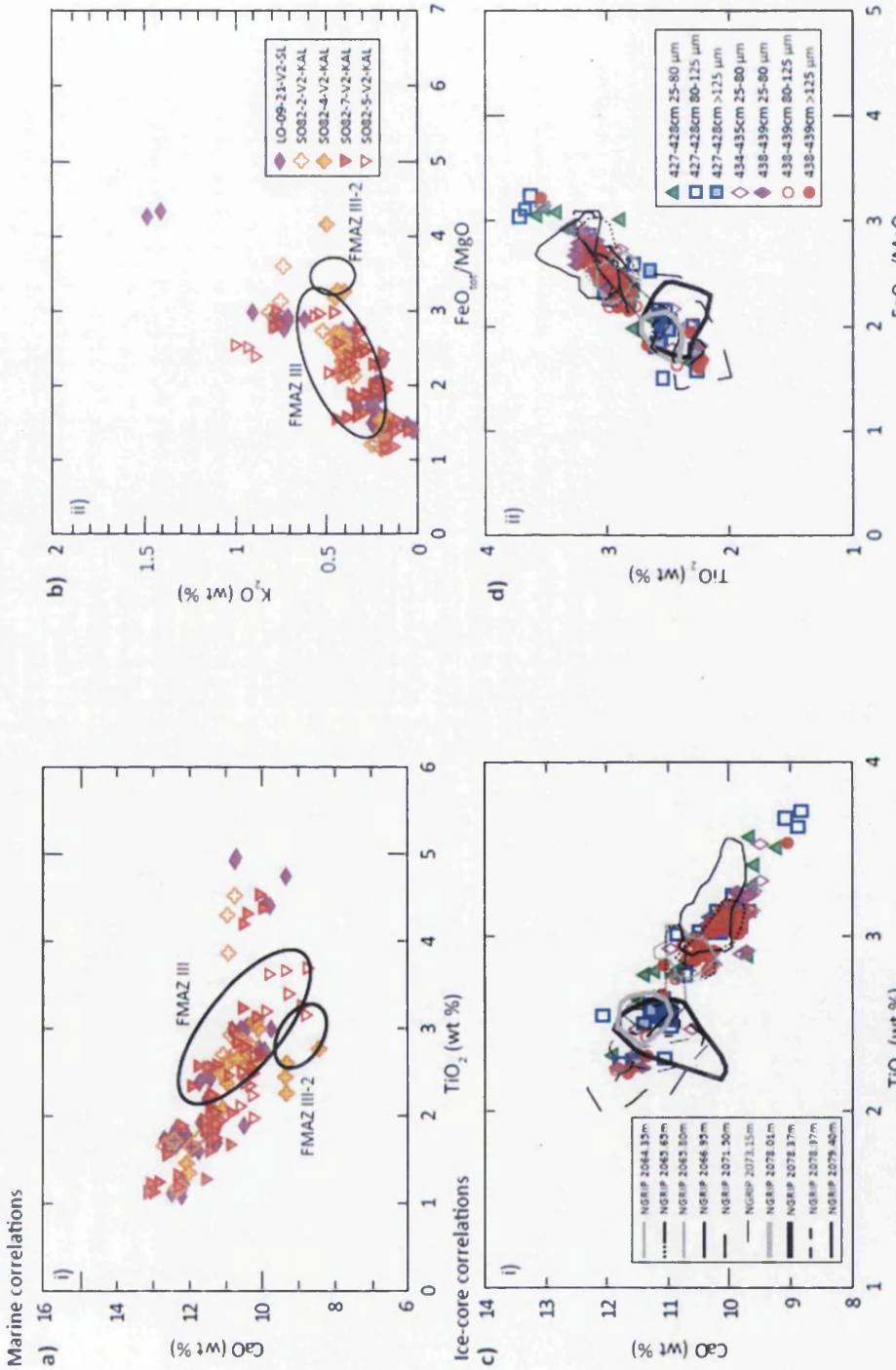

Figure 4.15 Major oxide results (wt%) for the FMAZ III deposit identified in JM11-19PC. (a), (b) JM11-19PC FMAZ III and FMAZ III-2 compositional envelopes compared to the V2 ash zone identified in four marine cores in the Reykjanes Ridge (Lackschewitz and Wallrabe-Adams,1997). (c), (d) Glass shard analyses from JM1-19PC 427-439 cm compared to geochemical compositional envelopes for cryptotephra deposits identified in NGRIP between 38,048 ± 721 b2k and 38,826 ± 740 b2k (Bourne et al., 2013). The data have all been normalised to 100% total oxide concentration.

Figure 4.15c,d highlights how the wide geochemical range of the FMAZ III deposit in JM11-19PC straddles the compositional fields for ten of the cryptotephra deposits identified in NGRIP during this time period (38,048 ± 731 b2k and 38,826 ± 740 b2k) and across DO-8 (Bourne et al., 2013). Due to the heterogeneity of the glass shard populations from the individual depth intervals between 427 and 439 cm, they cannot be exclusively correlated to a single-ice core horizon.

Wastegård et al. (2006) proposed that a correlation may exist between the V2 ash zone and the FMAZ III. The V2 ash zone has been dated to 36.5-29.8 ^{14}C ka BP in five cores on the Reykjanes Ridge (Lackschewitz and Wallrabe-Adams, 1997). The V2 ash zone exhibits a heterogeneous geochemical signature and coincides with a high input of IRD sourced from active erosion on the Icelandic ice sheet. A number of shards fall within the JM11-19PC 427-439 cm compositional envelope (Fig 4.15a,b), although the wider geochemical spread across all elemental oxides prevents a correlation between the two deposits.

The diffuse nature of the FMAZ III deposit, which contains multiple peaks in shard concentration, combined with geochemical heterogeneity suggests either the operation of iceberg rafting and/or post-depositional processes (Table 4.1). Iceberg rafting is unlikely due to the absence of a coeval IRD signal (Fig 4.3) and the low proportion of coarse-grained shards (>125 μm) (Fig 4.2). The evidence suggests that primary airfall or sea-ice rafting is the dominant transport process, but implies that another process may have operated to modify this depositional signal. The geochemical similarities between this deposit and ten separate volcanic events identified in NGRIP over this time period (Bourne et al., 2013) suggest that the FMAZ III is an amalgamation of glass shards sourced from several closely timed Grímsvötn eruptions. The sediment accumulation rate in the marine environment (20 cm/kyr^{-1}) (Ezat et al., 2014) is most likely too low to preserve each deposit as a discrete entity. It is postulated that bottom currents and bioturbation further contributed to form the amalgamation of this tephra deposit, following deposition via primary airfall. This deposit demonstrates that the integrity of the isochron, despite being a product of primary airfall, is compromised by the frequency of eruptions and low core-resolution. The FMAZ III forms a diachronous surface; whilst the deposit may be useful for broad marine correlations, its use as a high-precision isochronous tie-point is limited.

4.4.6 JM11-19PC 542-543 cm

4.4.6.1 Shard description and concentrations

A visible thick black macrotephra (6 cm) was deposited during the early stages of DO-12 and after H5, according to high magnetic susceptibility values (Fig 4.4, 4.5). A sharp lower boundary and rapid increase in shard concentration is evident at 542-543 cm (Fig 4.5). In the 25-80 μm fraction, a peak shard concentration of ~2.9 million shards per 0.5 gdw is observed. It is suggested that this peak equates to the correct stratigraphic placement of the isochron. The initial major influx in the 80-125 μm fraction is 1 cm below this peak. The slight depth offset could be due to different settling velocities through the ocean, or the greater movement of heavier material through soft sediment (Enache and Cumming, 2006). Shards at 542-543 cm are yellowish-brown in colour, have a vesicular appearance and display a variety of platy morphologies. The shard concentration profile forms a similar upward tail to the 298-303 cm deposit, although the decline in concentration is more gradual in this horizon, forming a tailed, gradational distribution that spans a ~40 cm interval. This can be seen visibly in the core (Fig 4.4) and is reflected in the relatively high fine-grained shard concentrations of >1 million per 0.5 gdw throughout the 10 cm high-resolution sampling interval (Fig 4.5). A radiocarbon age of 48,162 ± 1890 b2k is derived from 555 cm, providing an upper age boundary for this deposit (Ezat et al., 2014) (Fig 4.2) (Table 4.1).

4.4.6.2 Geochemistry and source identification

Seventy-four single shards were analysed by EPMA revealing a homogeneous basaltic composition. Three outliers are observed, with one in the 25-80 μm fraction and two in the 80-125 μm fraction. Geochemical characteristics of the main population are SiO_2 concentrations of ~49.0-51.4 wt%, K_2O concentrations of ~0.4 wt% and TiO_2 and MgO concentrations of ~2.6 wt% and ~5.8 wt% respectively (Table 4.2). These geochemistries are characteristic of the tholeiitic rock suite, and the latter two oxides suggest a strong affinity to the Grímsvötn system (Jakobsson et al., 2008) (Fig 4.11).

4.4.6.3 Wider correlations and depositional processes

Tephra deposits of tholeiitic basaltic composition dominate the marine and ice-core records between 41,000 and 46,000 b2k, whilst Katla sourced basalts have additionally been detected in marine sequences (Bourne et al., 2015, Wastegård and Rasmussen, 2014). A comparison with tephra deposits from four other marine cores in the Faroes region suggests a strong statistical similarity (SC= 0.982) with the recently discovered FMAZ IV tephra (Wastegård and Rasmussen, 2014). This can be clearly observed on FeO_{tot}/MgO vs TiO_2 and CaO vs MgO biplots (Fig 4.16a,d). JM11-19PC exhibits a tighter distribution of geochemistries in comparison to other cores analysed in the Faroes region, and only glass shards isolated in LINK 15 have a sub-population with a Katla affinity, according to high TiO_2 values >4 wt% (Wastegård and Rasmussen, 2014). No Grímsvötn sourced shards appear in the Greenland ice-core framework within this stratigraphic period (Bourne et al., 2015).

Wastegård and Rasmussen (2014) suggest that a potential correlation exists between the FMAZ IV and the V5 ash zone found in two cores on the Reykjanes Ridge, with an age estimate of 46.2-52.5 ^{14}C ka BP (Lackschweitz and Wallrabe-Adams, 1997). This estimate falls within the radiocarbon age constraint derived from 555 cm in JM11-19PC (Fig 4.2) (Ezat et al., 2014). The V5 ash zone has no coeval IRD signal, but exhibits a heterogeneous geochemical distribution (Lackschewitz and Wallrabe-Adams, 1997). One of the populations from the V5 ash zone in core SO82-7-KAL shows affinity to a number of shards which fall within the JM11-19PC 542-543 cm compositional envelope (Fig. 4.17). A statistical similarity coefficient of 0.951 suggests a correlation may exist between the two deposits, although the absence of shard concentration profiles and heterogeneity prevents a full correlation as the stratigraphic position of the Reykjanes Ridge record is uncertain.

A number of basaltic horizons deposited during MIS 3 have been reported in core PS2644 in the Iceland Sea, NW of Iceland (Voelker et al., 2000) (see section 2.5.1.7). Two horizons lie in a similar stratigraphic position to JM11-19PC 542-543 cm, based upon the planktonic foraminfera $\delta^{18}O$ record (Voelker et al., 2000; Wastegård and Rasmussen, 2014).

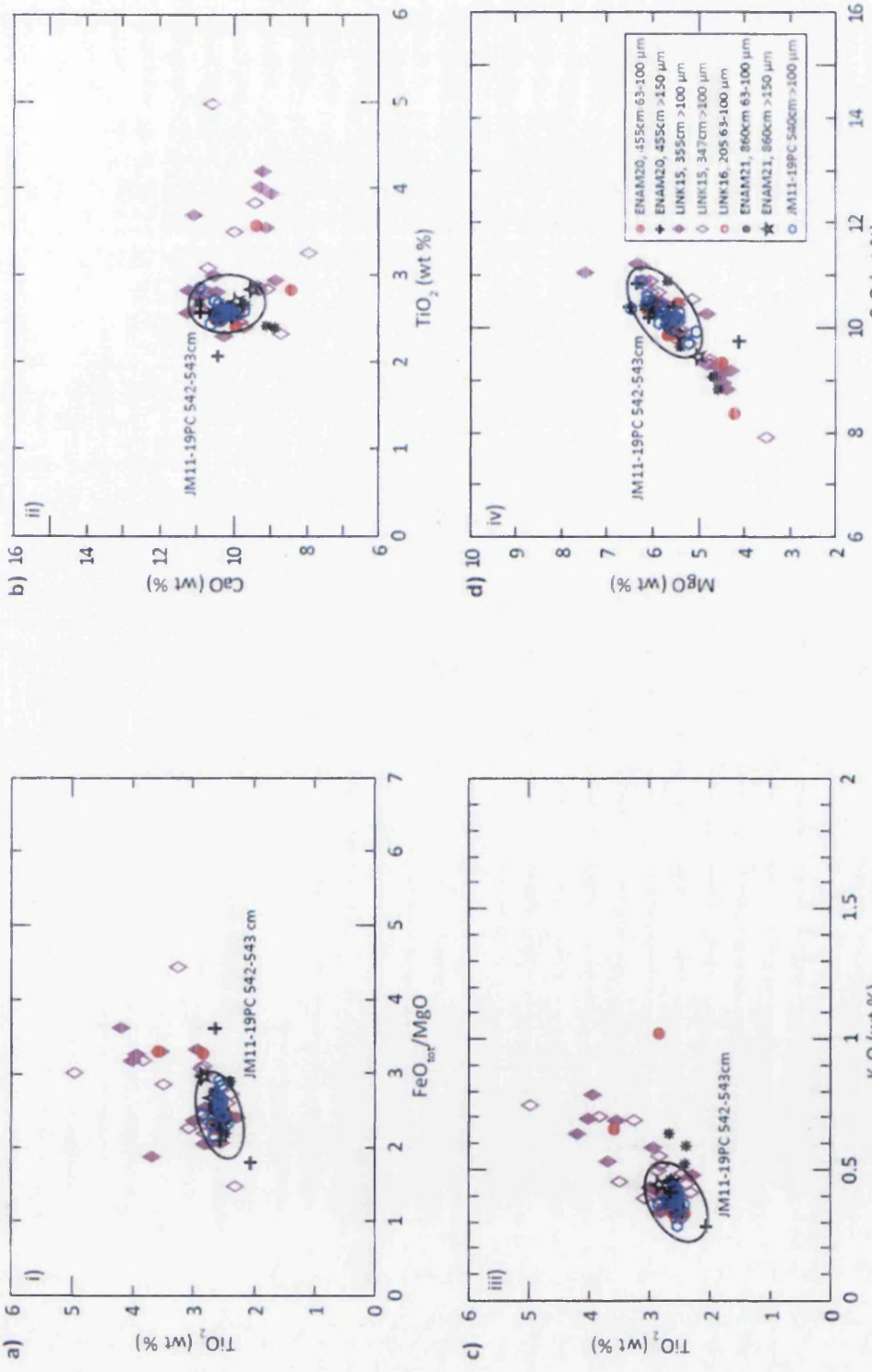

Figure 4.16 Major oxide results (wt%) for the FMAZ IV deposit identified in JM11-19PC. (a-d) 542-543 cm compositional envelope derived from glass shard analyses from all grain-size fractions. The envelope is compared to tephra deposits from four other marine cores from the Faroes region and additional JM11-19PC glass shard analyses reported by Wastegard and Rasmussen (2014). Data have all been normalised to 100% total oxide concentrations.

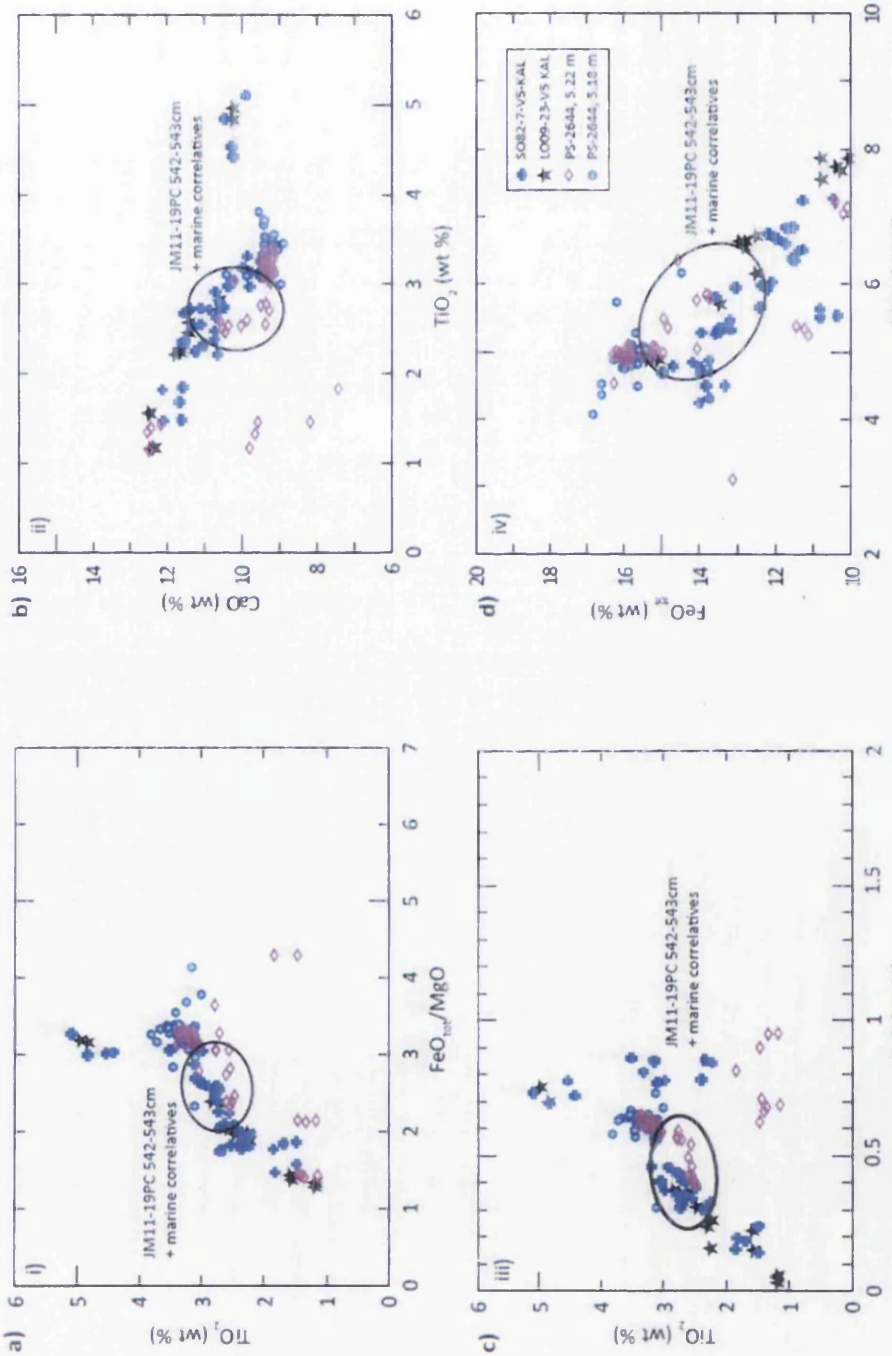

Figure 4.17 Major oxide results (wt%) for the FMAZ IV deposit identified in JM11-19PC. (a-d) 542-543 cm compositional envelope derived from glass shard analyses from all grain-size fractions. The envelope is plotted alongside glass shard analyses from the V5 ash zone compiled from two marine cores of the Reykjanes Ridge (Lackschewitz and Wallrabe-Adams, 1997) and two horizons derived from one marine core in the Iceland Sea (Voelker et al., 2000). Data have all been normalised to 100% total oxide concentration.

The horizon at 5.18 m within PS-2644 has a relatively homogeneous population but exhibits higher TiO_2, FeO and K_2O concentrations than JM11-19PC 542-543 cm. The horizon at 5.22 m is heterogeneous with multiple geochemical populations, although some shards display an affinity to the JM11-19PC 542-543 cm compositional envelope (Fig 4.17). The heterogeneity of this deposit makes it difficult to provide a correlative link between the Faroes region and the Iceland Sea.

The geochemical homogeneity of the FMAZ IV deposit in JM11-19PC and other cores in the Faroes region strongly implies primary deposition. Several lines of evidence suggest that this tephra was deposited isochronously, most likely via primary airfall. Firstly, the concentration of coarse-grained shards (>80 μm) is low and the dominant grain size (<80 μm) is typical for atmospherically derived deposits. Secondly, geochemical similarities between this deposit and the V5 ash zone in core SO82-5, which exhibits no coeval IRD signal, suggests iceberg rafting was not responsible for its deposition. In addition, a distinct feature of this deposit is an upward tail on the shard concentration profile (Fig 4.5). This evidence may suggest high rates of bioturbation and upward mixing (e.g. Jumars and Wheatcroft, 1989; Abbott et al., 2013; Todd et al., 2014) or re-working by stronger bottom currents during interstadial conditions following primary deposition onto the sea-floor (Fronval et al., 1998). It is also possible that the distinct upward tail may be a reflection of several closely timed eruptions, though this cannot be presently resolved in the absence of a direct ice-core correlative.

The presence of glass shards of Katla composition in the nearby LINK 15 sequence implies that the processes controlling deposition at this particular site may have been different to those operating at other core locations. This may be a reflection of different bottom current transport pathways. The absence of an ice-core correlative to the FMAZ IV may additionally be a consequence of differing atmospheric dispersal pathways conducive to deposition south of Iceland.

4.4.7 JM11-19PC 618-623 cm

4.4.7.1 Shard description and concentrations

This deposit forms a zone of high tephra concentration spanning ~10 cm. Both brown and colourless shards are identified and deposited during DO-15 as indicated by high magnetic susceptibility values and decreasing K/Ti ratios (Fig 4.2, 4.5) (Table 4.1). A very sharp rise in brown shards is evident in the fine-grained fraction, increasing from 10,000 shards in 623-628 cm to ~450,000 shards per 0.5 gdw between 618-623 cm (Fig 4.5). The stratigraphical interval between 618-623 cm represents the peak and first major influx in tephra concentration. Concentrations are relatively high in the adjacent sampling interval between 613-618 cm (~50,000 shards per 0.5 gdw) and may reflect the continued input of tephra or post-depositional re-working. Shards in the >2.5 g/cm^3 fraction at 618-623 cm are yellow in colour, exhibit a range of platy morphologies and some are vesicular in appearance.

Colourless shard concentrations increase from ~500 shards to ~29,000 shards between 623-628 and 618-623 cm (~29,000 shards per 0.5 gdw). Similarly to the >2.5 g/cm^3 fraction, this interval represents the peak and first major influx in tephra shards. Concentrations are relatively high in the sample above the peak (~7,000 shards per 0.5 gdw). Shards exhibit a platy and cuspate morphology and few are vesicular in appearance.

4.4.7.2 Geochemistry and source identification

EPMA analysis of thirty-three single shards in the >2.5 g/cm^3 fraction are classified as basaltic (Fig 4.10), with three clear outliers that have significant geochemical differences. Geochemical characteristics of the main population include SiO_2 concentrations of ~49.4-51.1 wt%, K_2O concentrations of ~0.32-0.48 wt%, TiO_2 concentrations of ~2.40-2.75 wt% and MgO concentrations of ~5.50-6.58 wt % (Table 4.2). These geochemistries are characteristic of the tholeiitic rock suite and suggest a strong affinity to the Grímsvötn system (Jakobsson et al., 2008) (Fig 4.11).

Twelve single-shard analyses from the 2.3-2.5 g/cm^3 fraction in this deposit are classified as rhyolitic and nine shards form a homogeneous population (Fig 4.8). Distinctive geochemical characteristics of the main population are SiO_2 concentrations of ~75.08-76.27 wt%, CaO concentrations of ~0.42-0.57 wt%, TiO_2

concentrations of ~0.16-0.18 wt%, FeO_{tot} concentrations of 2.08-2.74 wt% and K_2O concentrations of ~4.27-4.58 wt% (Fig 4.8a,b) (Table 4.2). Two outliers with K_2O concentrations <2 wt% were detected.

4.4.7.3 Wider correlations and depositional processes

A comparison of basaltic deposits from four other marine cores in the Faroes region, Labrador Sea and Reykjanes Ridge suggest a strong similarity between the II-THOL-2 component of the NAAZ II complex and the basaltic shard population at 618-623 cm (Fig 4.18) (Lackschewitz and Wallrabe-Adams, 1997; Rasmussen et al., 2003; Wastegård et al., 2006). The rhyolitic population of this deposit exhibits a strong similarity with the II-RHY-1 component of the NAAZ II derived from a variety of pan-Atlantic records (Wastegård et al., 2006; Brendryen et al., 2011; Abbott, unpublished) (Fig 4.8, 4.18). However, unlike other cores found in the Faroes region and Reykjanes Ridge, no glass shards exhibit any affinity to the other basaltic NAAZ II components (II-THOL-1/II-TAB-1) (Fig 4.18).

North Atlantic cores ENAM93-21, ENAM93-20 and SO82-5 contain an initial mixed layer consisting of the II-RHY-1 and II-TAB-1 components, followed by an upper basaltic component consisting entirely of the II-THOL-2 population (Haflidason et al., 2000; Wastegård et al., 2006). JM11-19PC, however, is dominated entirely by the co-occurrence of the II-RHY-1 and II-THOL-2 components, with no stratigraphic separation identified with the low resolution counts. This is similar to core EW9302-2JPC in the Labrador Sea that contains an amalgamation of both II-RHY-1 and II-THOL-1 components at the same stratigraphic interval (Wastegård et al., 2006).

The co-occurrence of two eruptive phases has been interpreted to represent either a low temporal resolution or an ice-rafting event that supplied a mixture of components (Austin et al., 2004; Wastegård et al., 2006). As JM11-19PC exhibits a similar sedimentation rate to that of the surrounding Faroese cores, it is unlikely that the co-occurrence of both components is related to low temporal resolution in this instance.

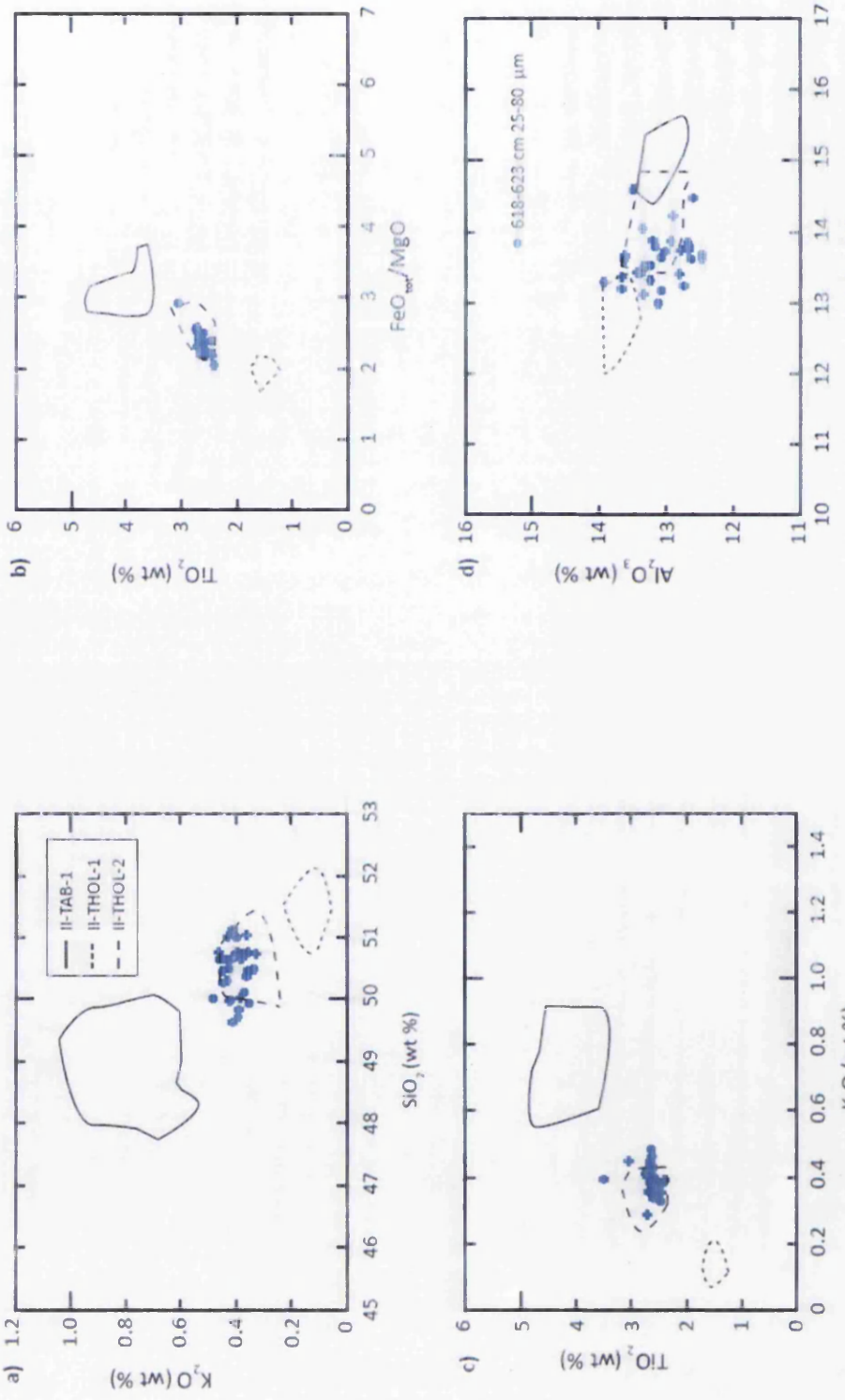

Figure 4.18 Major oxide results (wt%) for the basaltic component of 618-623 cm found in JM11-19PC compared to geochemically similar tephras. (a), (b), (c), (d) Major elemental oxides compared to geochemical compositional envelopes for basaltic components of the NAAZ II from marine cores ENAM 93-20, MD95-2009, ENAM 93-21 and EW9302-2JPC (Wastegård et al., 2006).

High-resolution counts are needed to test this suggestion and identify if a separation may exist within the 5 cm interval.

The strong geochemical homogeneity exhibited by 618-623 cm deposit and the dominance of fine-grained shards strongly implies primary deposition (Table 4.1). However, the co-occurrence of the rhyolitic component in JM11-19PC suggests that the eruptions were either contemporaneous or the operation of secondary depositional mechanisms. In the absence of detailed IRD data for all cores, it is difficult to fully disentangle the depositional history of the NAAZ II deposit in JM11-19PC. Nonetheless, the rapid input of this deposit provides an independent chronological anchor for the record.

4.5 Developing a tephrostratigraphy for JM11-19PC

4.5.1 Assessing depositional controls and isochronous integrity

The assessment of down-core shard concentration profiles allied to rigorous geochemical characterisation from three separate grain sizes provides important evidence for determining the mode of tephra delivery to the sea-bed (Table 4.1). Six discrete deposits exhibit a distinctive shard concentration profile that indicates a variety of depositional controls operating throughout the core sequence. Tephras at 196-197 cm, 357-358 cm, FMAZ II (304-305 cm) and NAAZ II (618-623 cm) in JM11-19PC exhibit a typical profile for a tephra largely unaffected by post-depositional modification (Table 4.1). The geochemical homogeneity and dominance of fine grained shards in the FMAZ II and 357-358 cm horizons indicates primary deposition and adds confidence that these deposits represent well-resolved isochronous horizons. However, the geochemical heterogeneity and a coeval IRD signal for the deposit at 196-197 cm probably indicates the operation of secondary processes such as ice-rafting. This compromises the integrity of the tephra deposit and reinforces the importance of employing a range of indicators to fully decouple the operation of primary and secondary depositional mechanisms.

The FMAZ IV (542-543 cm) in JM11-19PC forms a thick deposit with a significant upward tail on the shard concentration profile, consistent with observations from other Faroese cores (Wastegård and Rasmussen, 2014). The deposit exhibits a homogeneous geochemical composition and a predominance of fine-grained shards, which are diagnostic features of primary deposition (Table 4.1). The upward tail is suggested to be products of post-depositional reworking by ocean bottom currents. Bottom current activity is likely to be stronger during interstadial periods and the ability to remobilise previously deposited material is higher. An understanding of ocean currents and the climatic regime associated with tephra deposition can provide a further insight into the operation of modification mechanisms and assist in the placement of the isochron.

The FMAZ III deposit in JM11-19C exhibits a significantly different shard concentration profile with numerous peaks spread diffusely over 20 cm. The deposit exhibits a wide compositional envelope, has no coeval IRD peak and is dominated by the presence of fine-grained deposits, suggesting primary deposition. However, the diffuse distribution and correlation to all ten separate volcanic events recorded in the ice-cores suggests that the frequency of eruptions during this time period has compromised the integrity of this deposit (Table 4.1). We refer to this deposit as an ash zone and suggest that this term be used solely descriptively to depict the dispersion of tephra through a core, without any preconceived notions of geochemical characteristics and depositional processes. If individual components can be identified within the ash zone using diagnostic techniques outlined above, then the deposit could reveal discrete isochrons. Implicit in this definition is that the FMAZ II and FMAZ IV are ash zones that form well-defined isochronous horizons.

4.6 Conclusions

The principal findings of this chapter are:

- Four basaltic horizons have been identified in JM11-19PC. Major element characterisations of each horizon demonstrate various degrees of geochemical homogeneity and exhibit an affinity to the FMAZ II, III, IV and II-THOL-2 component of the NAAZ II.
- Depositional processes have varied temporally through the sequence and contain both primary and secondary signatures.
- Correlation to existing ice and marine archives indicate that the FMAZ II and FMAZ IV are well-resolved primary deposits that can be used as isochrons. Key primary features of these two horizons are well-defined shard concentration peaks, homogeneous geochemical signatures, a high percentage of fine-grained shards and the absence of a coeval IRD signal.
- The FMAZ III is a diffuse and heterogeneous deposit. The integrity has been compromised by the frequency of eruptions during the period of deposition. The deposit represents a stratigraphic marker for DO-8 and may potentially be utilised for low resolution marine-marine correlations.
- The II-THOL-2 component of the NAAZ II in JM11-19PC exhibits key primary features. However, the co-occurrence of the rhyolitic II-RHY-1 component at the same stratigraphic interval makes it difficult to fully unravel the depositional history of this deposit.
- Two additional rhyolitic cryptotephra horizons have been identified in JM11-19PC. The deposit at 196-197 cm exhibits a heterogeneous geochemical signature, with some affinity to Borrobol-like tephra deposited during GS-2 and

demonstrates key secondary depositional characteristics. The 357-358 cm horizon exhibits an affinity to Katla and is likely to represent a previously undetected eruption. This deposit has the potential to act as a high-precision isochronous marker horizon.

Chapter 5 Tephrochronology of North Atlantic marine core MD04-2829CQ between 18-41 ka b2k

5.1 Introduction

The aim of this chapter is to produce a MIS 2 and 3 tephrostratigraphical record for North Atlantic marine core MD04-2829CQ. This core has a high sedimentation rate and exhibits a continuous high resolution D-O signal between 18-41 ka b2k as reconstructed from a variety of proxy data (Hall et al., 2011). Such a high-resolution record presents an ideal opportunity for tracing tephras preserved within the Greenland ice-cores (Bourne et al., 2015), facilitating synchronisation between the marine and cryospheric depositional realms. Detailed geochemical and stratigraphic descriptions are provided for three cryptotephra deposits from four volcanic events identified in this sequence. Major and trace element compositions are employed to suggest a possible volcanic source and test potential correlations with previously published marine and ice-core tephra deposits. Shard concentration profiles are derived for each horizon and the corresponding proxy signal are assessed to explore the depositional history of the tephra deposits. This permits an assessment of the stratigraphic integrity of each isochron which helps in building a full tephrostratigraphical record for this sequence.

5.2 Core location, oceanographic setting and proxy record

Marine core MD04-2829CQ (58°56.93'N, 9°34.30'W) was retrieved at 1743 m water depth on a contourite drift located southeast of the Rosemary Bank in the northern

Rockall Trough (RT) (Fig 5.1) during the *R/V Marion Dufresne* cruise MD141 (Hall et al., 2011). The core was pinpointed for rigorous stratigraphic investigation to reconstruct the variability of the British-Irish Ice Sheet (BIIS) and ocean current migrations during the last glacial period. The core location is sensitive to hydrographic conditions and is located just inside the boundary of the present-day Sub-Arctic Front (SAF) (Dickson et al., 1988) (Fig 5.1). Deep water circulation in the northern Rockall trough is controlled by Norwegian Sea Deep Water (NSDW) overflowing the Wyville-Thomson Ridge from across the Faroe-Shetland Channel and then west to the Faroe Bank, where the core is situated (Knutz et al., 2001; Hall et al., 2011).

The core is ~10 m long and extends back to ~41 ka b2k, but only the depth interval ~3-10 m, covering 18-41 ka, has been analysed in this investigation. A chronostratigraphic framework has been derived for the core from twenty-four AMS ^{14}C dates. The resulting age model has been extended and fine tuned by tuning the relative abundance of *N. pachyderma* sin. to the GISP2 ice-core $\delta^{18}O$ record. The age model has been independently constrained by the identification of the Laschamp excursion in the magnetic record (~41 ka b2k) (Hall et al., 2011). There is a clear D-O signal recorded in the abundance of *N. pachyderma* sin. (2 cm resolution) (Hall et al., 2011) (Fig 5.2).

5.3 Sampling strategy

Tephra concentrations were initially inspected within 6 cm contiguous samples between 300-1007 cm depth. Intervals with elevated shard counts relative to background levels were subsequently analysed at a 1 cm resolution (see section 5.3.1). In addition, replicate samples between 800-830 cm, 850-880 cm and 920-950 cm, taken from different lateral positions in the sequence, were re-investigated at 1 cm resolution. Shard concentrations were exceptionally low and replicate counts provide a check on the lateral variability of the cryptotephra deposits. Material from the 25-80 μm fraction was processed using the heavy liquid separation procedure outlined in section 3.3 and the >2.5 g/cm^3 fraction was magnetically separated to purify the basaltic material (section 3.4).

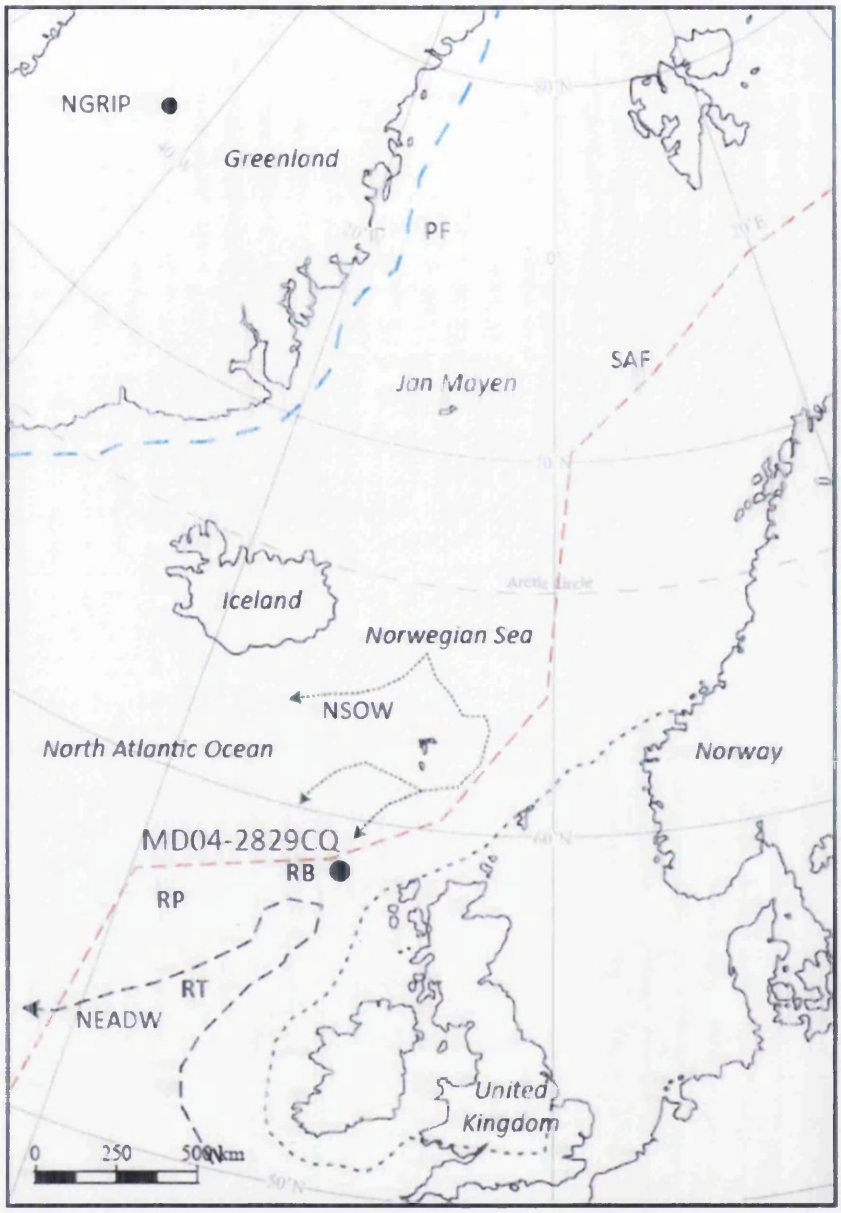

Figure 5.1 Location map of marine core MD04-2829CQ with the approximate pathways of present day deep water masses (Hall et al., 2011), major hydrographic fronts (Dickson et al., 1988; Zumaque et al., 2012) and maximum extents of the northeastern European and Faroe Islands ice-sheet during the LGM (Hall et al., 2011). RB = Rosemary Bank. RT = Rockall Trough. RP = Rockall Plateau.

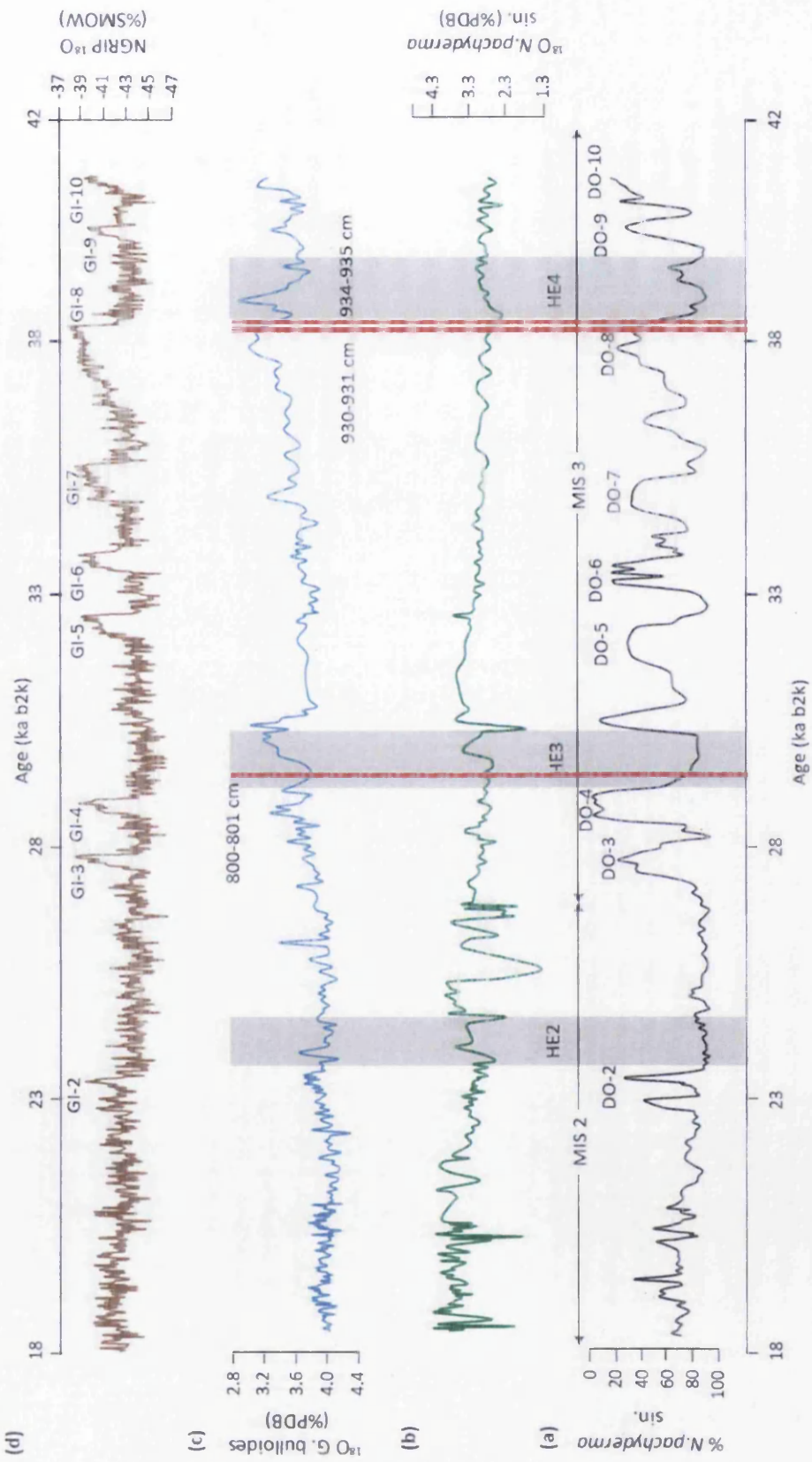

Figure 5.2 Proxy data derived from MD04-2829CQ (Hall et al., 2011). (a) % *N.pachyderma* sin. (b) *N.pachyderma* sin. ^{18}O record (c) G. bulloides ^{18}O record (d) The NGRIP ^{18}O record is also included for reference and modified from the GISP2 record presented in Hall et al. (2011). Grey vertical bars represent Heinrich events. The approximate positions of basaltic tephra horizons identified in the high resolution counts have been included in red, based upon the Hall et al. (2011) age model.

116

5.3.1 Shard concentrations and tephrastratigraphy

Low-resolution shard concentrations from all density and size fractions are shown in Figure 5.3. Areas with increased levels of shards relative to background values were sampled at a high resolution, indicated by the grey intervals on Figure 5.3. Three distinct peaks are observed in the low-resolution >2.5 g/cm^3 (25-80 μm) fractions with the highest concentration of brown shards (seventy-five per 0.5 gdw) found between 798-804 cm. A small corresponding peak is observed between 798-804 cm in the >125 μm size fraction. The remaining peaks in the >2.5 g/cm^3 fraction occur at 492-498 cm and 894-900 cm, but there are no corresponding peaks in the coarser-grained fractions for these horizons. High-resolution counts were occasionally extended by up to 2 cm beyond the 6 cm low-resolution windows to aid the refinement of the stratigraphic position of shard concentration peaks. High-resolution samples from 492-498 cm and 894-900 cm did not contain any tephra particles following repeat analyses and have been omitted from further investigation. Successful high resolution investigations revealed the presence of cryptotephra deposits at 800-801 cm, 930-931 cm and 934-935 cm and these will be discussed within the following sections (Table 5.1). The majority of brown shards in the 930-931 cm and 934-935 cm horizons were detected solely in high-resolution within the 2.3-2.5 g/cm^3 fraction. These depths were sampled because they contained elevated colourless shards (see below) and no brown shards were detected in low resolution.

Within the 2.3-2.5 g/cm^3 fraction, exceptionally low concentrations of colourless shards (approximately four shards per 0.5 gdw) occur throughout with no distinct peaks observed. Elevated levels of colourless shards (ten shards per 0.5 gdw) were found between ~930-950 cm. Two sets of replicate high-resolution 1 cm samples were obtained from two different lateral positions spanning this depth interval. High-resolution investigations were conducted on samples between 800-830 cm, 850-880 cm and 920-950 cm to assess the stratigraphy and geochemical composition of the background of colourless shards.

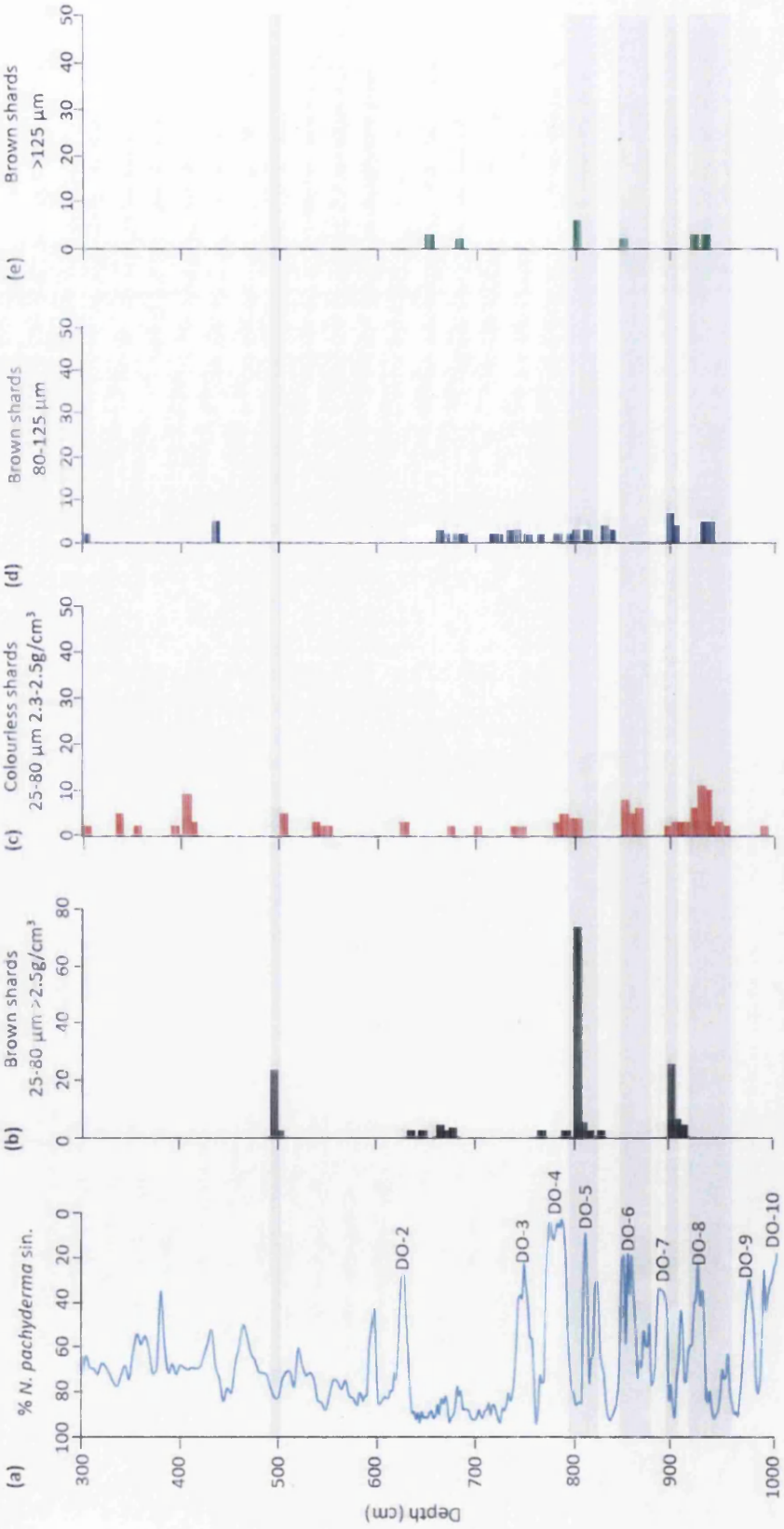

Figure 5.3 Low resolution (6 cm) tephra stratigraphy for MD04-2829CQ. (a) % *N. pachyderma* sin. (Hall et al., 2011). (b) Number of brown shards with a density >2.5 g/cm^3 within the 25-80µm fraction. (c) Number of colourless shards with a density 2.3-2.5 g/cm^3 within the 25-80µm fraction. (d), (e) Number of brown and colourless shards with the 80-125µm and >125µm fractions respectively. The grey bars denote areas re-sampled for high resolution.

Table 5.1 Summary of basaltic and rhyolitic tephra deposits found within MD04-2829CQ. Age estimates have been derived from the Hall et al. (2011) age-depth model. Interpretations are based upon analysis presented throughout the chapter.

Cryptotephra Layer (cm)	Shards per 0.5 gdw (25-80 µm)	Climatic event	Age estimate (ka b2k)	Geochemistry	Volcanic Source	Input signal	Depositional process	Potential isochron?	Lateral continuity
800-801	187	DO-5	~30	TB	Grímsvötn/ Kverkfjöll	Primary	Airfall	Yes	Yes
810-811	15	DO-5	~29	RHY	Katla/ Tindfjallajökull	Secondary	Bottom currents	No	No
930-931	36	DO-8	~38	TB	Grímsvötn	Primary	Airfall/ bottom current	Yes	No
934-935	36	DO-8	~38.3	TB	Grímsvötn	Primary	Airfall	Yes	No
934-935	51	DO-8	~38.3	RHY	Katla/ Tindfjallajökull	Secondary	Bottom currents	No	No

5.4 Basaltic cryptotephra horizons within MD04-2829CQ

5.4.1 MD04-2829CQ 800-801 cm

5.4.1.1 Shard descriptions and concentrations

The highest shard concentrations (187 shards per 0.5 gdw in the 25-80 μm fraction and 121 shards in the >80 μm fraction) were identified within the 800-801 cm deposit (Fig 5.4) (Table 5.1). Elevated shard concentrations are confined to a 1 cm interval, suggesting rapid input of tephra with limited post-depositional re-working (Fig 5.4). There is no indication of a gradational increase or decrease in tephra concentration bracketing this horizon. The shards have a dark brown colour, exhibit a dense blocky morphology and are highly vesicular in appearance. The horizon falls within Heinrich 3 (29-31 ka b2k) as indicated by high IRD concentrations and low % *N. pachyderma* sin. (Hall et al., 2011) (Fig 5.2). The age model provided by Hall et al. (2011) suggests this horizon was deposited at ~30 ka b2k.

5.4.1.2 Geochemistry and source identification

EPMA analyses from thirty-six individual shards confirm the basaltic (tholeiitic series) composition of this deposit (Fig 5.5). Overall, the deposit exhibits a bimodal composition with two homogenous populations and no significant outliers are observed. The bimodality is best expressed in the CaO and TiO_2 concentrations (Fig 5.6). Eighteen shards from the 25-80 μm fraction form the first population and no shards from the >80 μm fraction contribute to this population. Distinctive geochemical characteristics include K_2O concentrations between ~0.19-0.26 wt%, average TiO_2 concentrations of ~2.52 wt% and CaO and MgO concentrations of ~10.37 wt% and ~5.83 wt% respectively (Table 5.2).

Table 5.2 Mean and 1σ major element results of basaltic glass shards extracted from deposits found within MD04-2829CQ. Total oxide values are raw values prior to normalisation. All major elements are expressed as percentage weight. Total iron expressed as FeO. n = number of shards analysed.

Tephra layer	Composition	Source	Grain size (μm)	N	SiO_2	TiO_2	Al_2O_3	FeO	MnO	MgO	CaO	Na_2O	K_2O	P_2O_5	Total
800-801 cm pop 1	Basaltic	Grímsvötn	25-80, >80	18	50.39	2.52	13.40	13.81	0.22	5.83	10.37	2.82	0.40	0.23	98.00
					0.76	0.08	0.39	0.84	0.01	0.55	0.69	0.16	0.06	0.02	0.95
800-801 cm pop 2	Basaltic	Kverkfjöll	25-80, >80	18	50.33	3.43	13.01	15.01	0.24	4.71	9.21	3.10	0.59	0.38	97.76
					0.47	0.09	0.49	0.42	0.01	0.17	0.26	0.13	0.03	0.02	1.06
930-931 cm	Basaltic	Grímsvötn	25-80, >80	31	50.00	2.61	13.55	13.43	0.22	6.09	10.57	2.88	0.40	0.27	98.17
					0.43	0.18	0.56	0.75	0.01	0.48	0.42	0.25	0.05	0.03	1.04
934-935 cm	Basaltic	Grímsvötn	25-80	39	50.72	2.27	14.47	11.93	0.20	7.38	12.02	2.71	0.31	0.21	97.84
					0.83	0.06	0.53	0.42	0.01	0.22	0.25	0.20	0.02	0.01	1.07

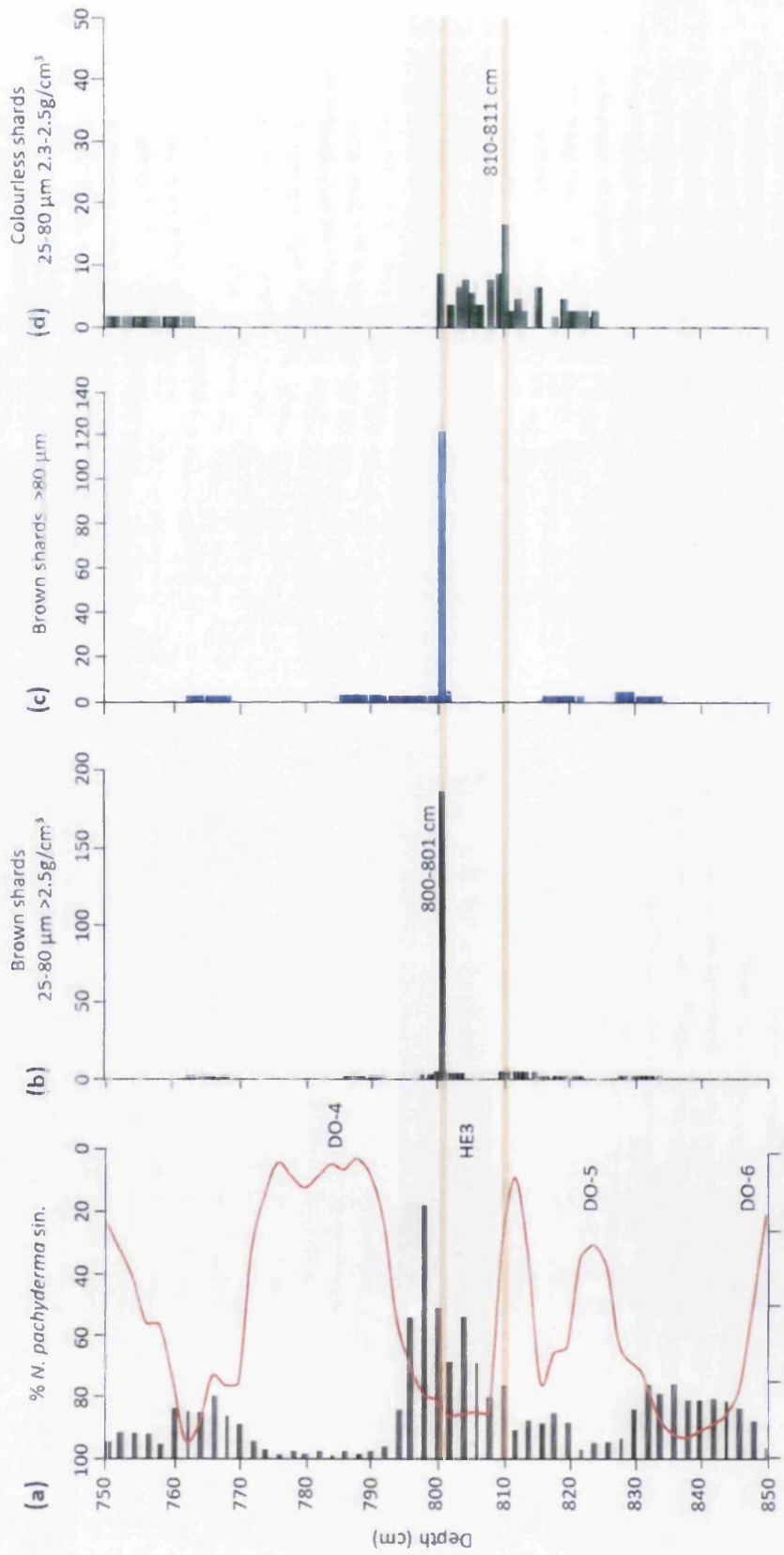

Figure 5.4 Low and high resolution (1 cm) tephra stratigraphy between 750-850 cm in MD04-2829CQ. (a) % *N. pachyderma* sin. and total IRD grains (Hall et al., 2011). (b), (c) Number of brown shards identified within the 25-80 µm and >80 µm fractions respectively. (d) Number of colourless shards within the 2.3-2.5 g/cm^3 density fraction. The orange lines denote the peak in glass shard concentrations at 800-801 cm and 810-811 cm and represent depths taken for geochemical analysis. Grey bar denotes approximate position of Heinrich 3.

The latter two oxide values are characteristic of the tholeiitic rock suite and suggest a strong affinity to the Grímsvötn system in the Eastern Volcanic Zone of Iceland (Jakobsson et al., 2008). This can be clearly observed on and CaO vs TiO_2 geochemical biplots (Fig 5.6).

Population two is defined by eighteen shards (six shards from the 25-80 μm fraction and twelve shards from the >80 μm fraction). All coarse grained shards analysed from 800-801 cm fall within this population. Distinctive characteristics include average K_2O concentrations of ~0.59 wt%, TiO_2 concentrations of ~3.43 wt% and CaO and MgO concentrations of ~9.21 wt% and ~5.16 wt% respectively (Table 5.2). The latter two oxide values are characteristic of the tholeiitic rock suite and plot largely within the Kverkfjöll volcanic system compositional envelope (Fig 5.6).

5.4.1.3 Wider correlations and depositional processes

Transitional alkali and tholeiitic basaltic tephras dominate the Greenland ice-core record between 25-32 ka b2k (Bourne et al., 2015). The interval brackets the approximate age of this horizon according to radiocarbon measurements and the age-depth model derived by Hall et al. (2011). Stratigraphically, the 800-801 cm horizon falls during Heinrich 3 and precedes the warming associated with DO-4 (Fig 5.2). Ice-core tephra horizons found between GI-3 and GI-5 cluster within Katla and Kverkfjöll compositional envelopes (Bourne et al., 2015). A comparison with glass shard analyses from thirteen stratigraphically and geochemically similar cryptotephra horizons found within NGRIP, GRIP, NEEM and DYE-3 ice-cores highlights the geochemical range exhibited by Kverkfjöll deposits in this period (Fig 5.7). Despite similar compositions, small differences in TiO_2 concentrations are apparent and aid discrimination (Bourne et al., 2015). Population two of 800-801 cm shows affinities to ice-core horizons that exhibit mean TiO_2 values of > 3.2 wt% (Fig 5.7).

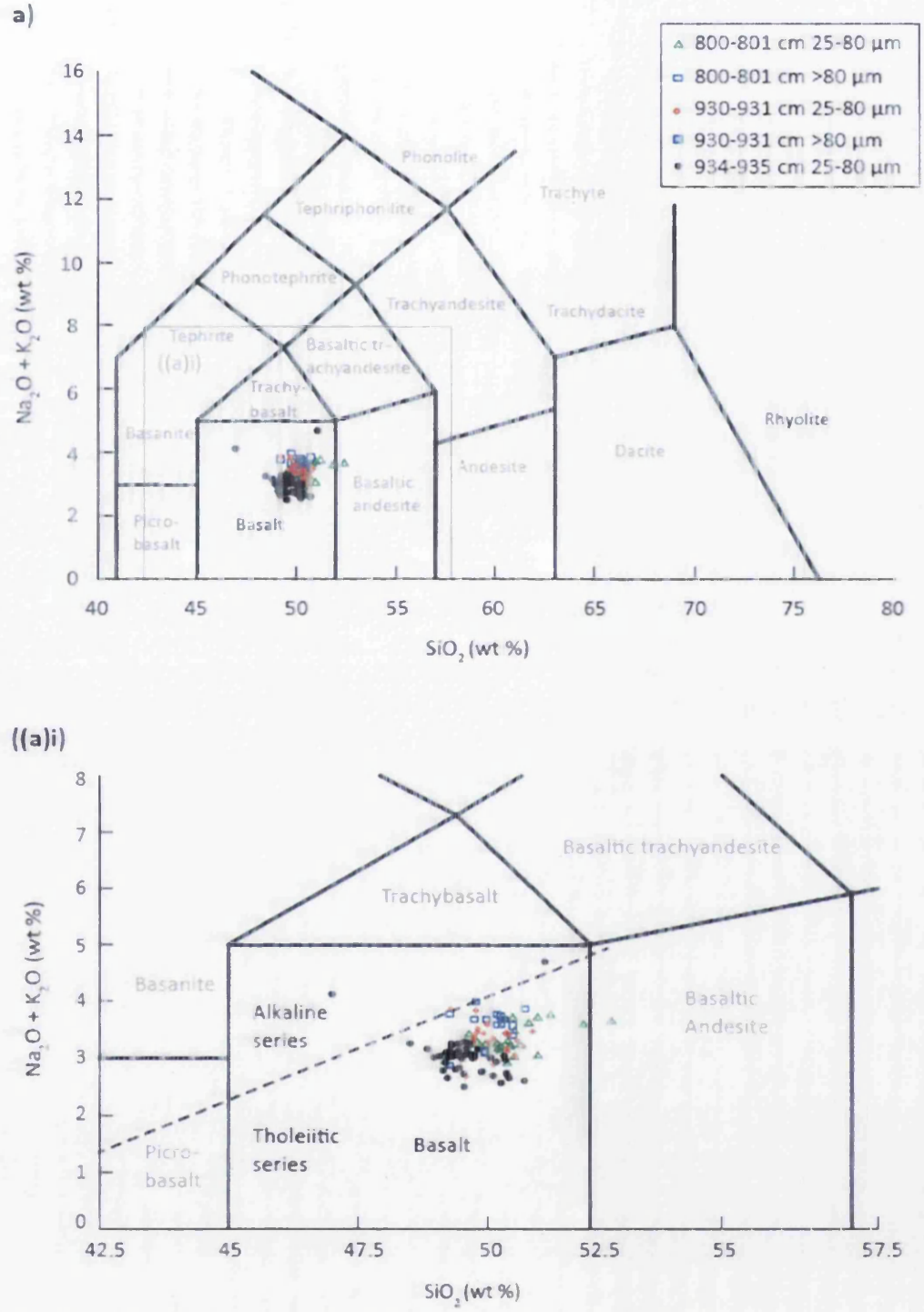

Figure 5.5 (a) Total alkalis vs silica plot for analyses from basaltic deposits found in MD04-2829CQ. (b) Inset of TAS plot focusing on the basaltic analyses. Chemical classification is defined by Le Maître et al. (1989). The dashed line represents the subdivision into alkaline and tholeiitic rock series defined by MacDonald and Katsura (1964).

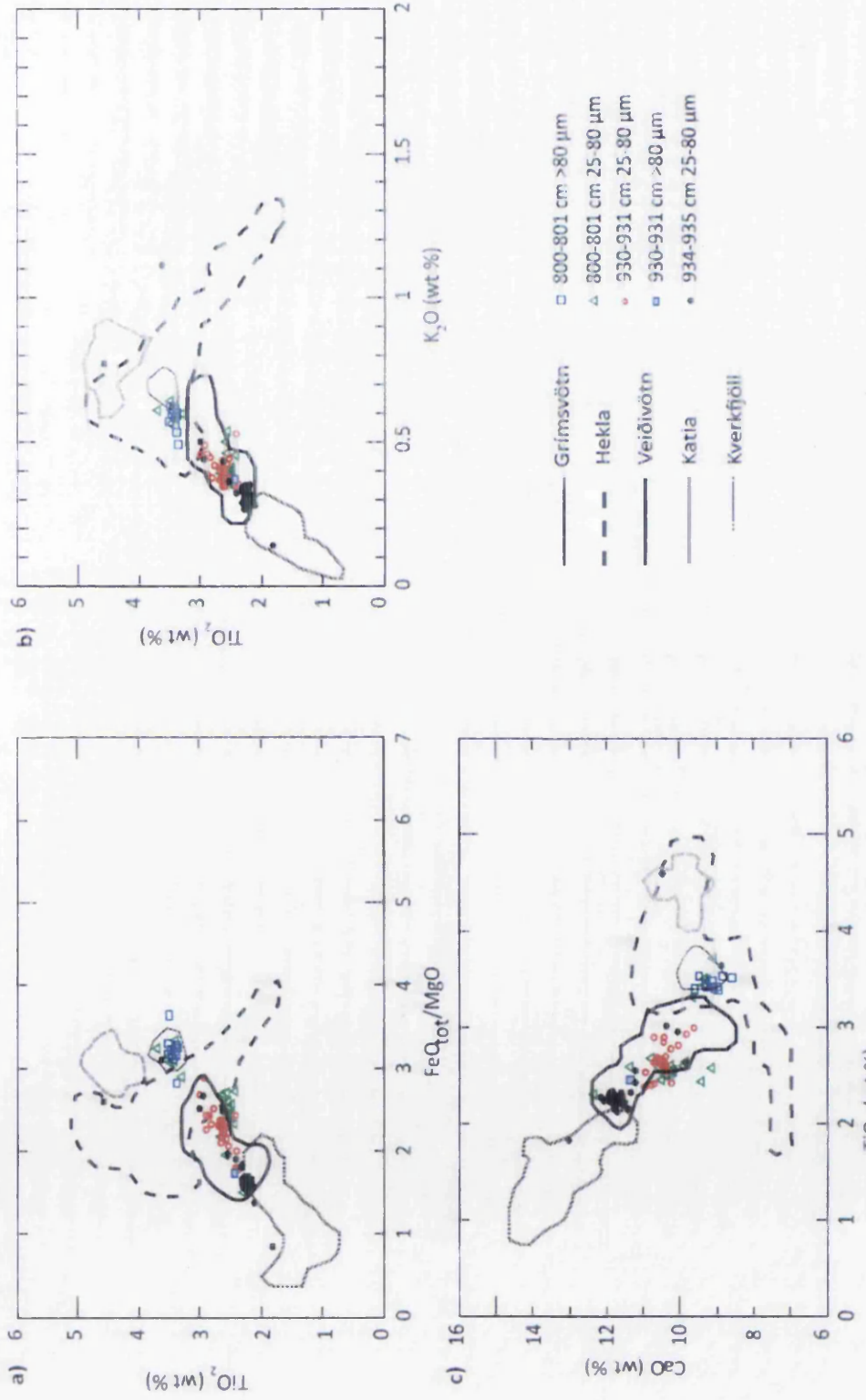

Figure 5.6 Glass shard analyses for three basaltic deposits found in MD04-2829CQ compared to geochemical envelopes for five different Icelandic source volcanoes based on individual whole rock analyses presented in Jakobsson (1979), Boygle (1994), Larsen et al. (2002), Óladóttir et al. (2008) and Jakobsson et al. (2008). All data have been normalised to 100% total oxides.

Several of these reveal a similarity coefficient value >0.97 (Table 5.3), though there is significant variability in some of the ice-core horizons in comparison to the relatively homogeneous 800-801 cm geochemical population (Fig 5.7). These have subsequently been excluded from further analysis. The strongest geochemical overlaps are observed between population two in 800-801 cm and NGRIP 1882.50 m, GRIP 2081.40 m and GRIP 2067.85 m (Fig 5.8). Due to the geochemical similarities between the ice-core deposits (Fig 5.8), it is not possible to assess the potential correlations without also considering their stratigraphic positions. The highest similarity coefficient of 0.991 exists between population two of 800-801 cm and NGRIP 1882.50 m (Table 5.3). However, this horizon falls stratigraphically on the cooling associated with GI-4 (28,594 ± 887 b2k), significantly after deposition of 800-801 cm which occurs during the peak stadial conditions associated with DO-5 (Fig 5.9). Unless there was significant downward migration of tephra shards through the marine sequence, it is unlikely that NGRIP 1882.50 m represents a correlative horizon.

In contrast, GRIP 2067.85 m and GRIP 2081.40 m are positioned in GI-5.1 and GS-5.2 respectively and fall in a relatively similar stratigraphic position to 800-801 cm (Fig 5.9). GRIP 2067.85 m probably represents the most stratigraphically-related deposit and may provide a direct ice-marine correlative (Fig 5.9). A tentative correlation to GRIP 2067.85 m can be suggested according to strong overlap with the TiO_2 vs MgO concentrations (Fig 5.8). Future trace-element analysis may help geochemically discriminate between these deposits and assist in providing a more secure correlation.

The first population in 800-801 cm exhibits a geochemical affinity to deposits sourced from Grímsvötn. However, no Grímsvötn-sourced horizons are present in the ice-core framework during the interval associated with deposition. It is interesting to note that ice-core horizons NGRIP 1931.60 m, GRIP 2064.35 m and DYE-3 1869.15 m, deposited between 25-32 ka b2k, exhibit outlying shards of Grímsvötn origin (Fig 5.7). Although the concentration of outlying shards is exceptionally small, this suggests that Grímsvötn may have been active during this period with only a few shards transported to Greenland.

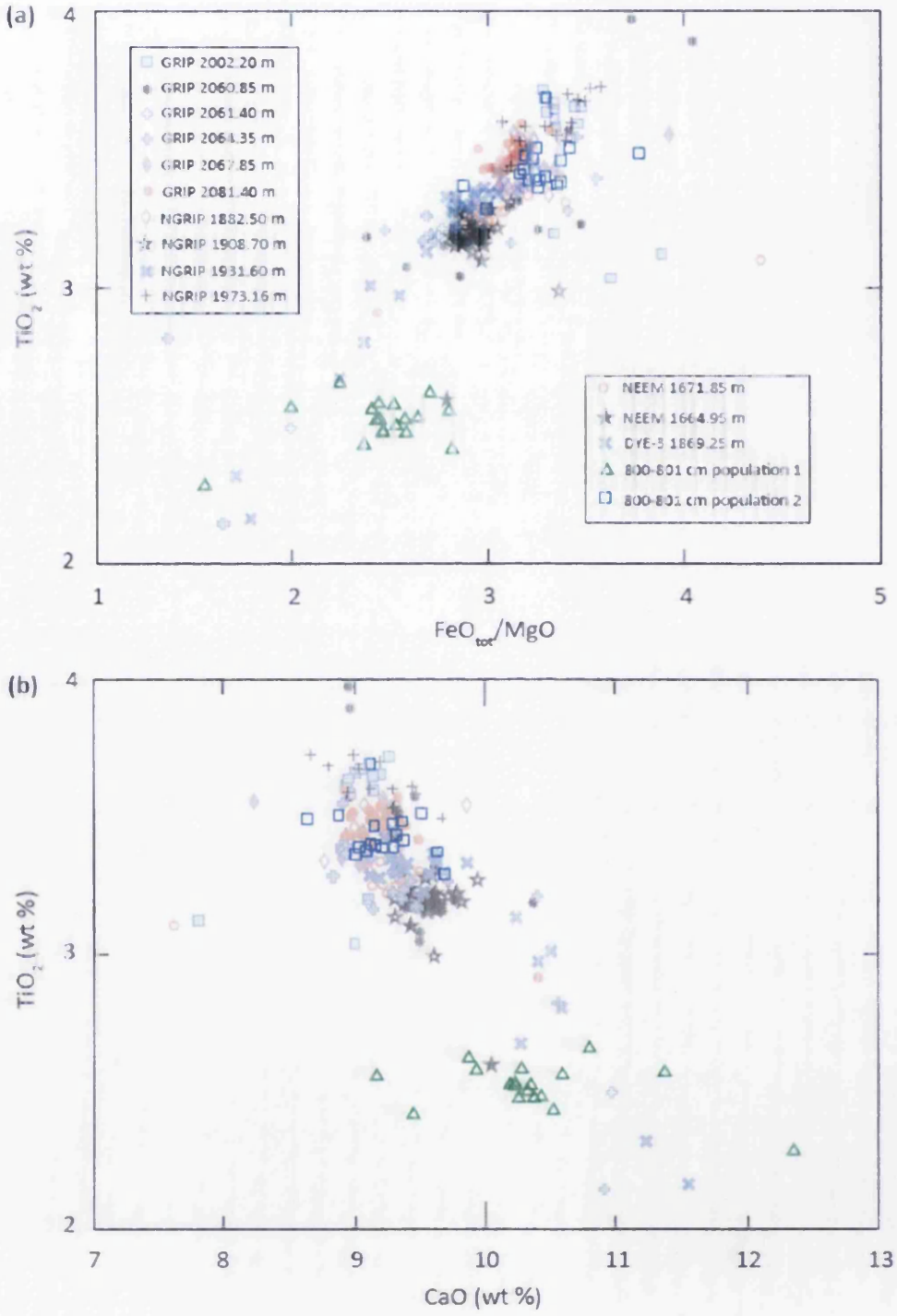

Figure 5.7 Major oxide results for the 800-801 cm deposit identified in MD04-2829CQ. (a), (b) Glass shard analyses compared to nine geochemical compositional envelopes for selected cryptotephra deposits identified in NGRIP, GRIP, NEEM and DYE-3 between 28,594 ± 885 b2k to 31,581 ± 1078 b2k (Bourne et al., 2015). All data have been normalised to 100% total oxide concentration.

Table 5.3 Similarity coefficients between the major element composition of the 800-801 cm second geochemical population and ice-core horizons from NGRIP, GRIP, NEEM and DYE-3 between (25-32 ka b2k) (Bourne et al., 2015).

Ice-core horizon	Age (b2k)	800-801 cm SC
GRIP 2002.20 m	26,544 ± 768	0.983
NGRIP 1882.50 m	28,594 ± 887	0.991
DYE 3 1869.15 m	29,400 ± 1000	0.933
GRIP 2060.85 m	30,066 ± 976	0.964
NGRIP 1908.70 m	30,082 ± 977	0.967
NEEM 1664.95 m	30,083 ± 977	0.953
GRIP 2064.35 m	30,353 ± 993	0.950
GRIP 2067.85 m	30,628 ± 1010	0.978
NEEM 1671.85 m	30,825 ± 1023	0.984
GRIP 2081.40 m	31,581 ± 1078	0.977
NGRIP 1973.16 m	33,686 ± 1207	0.975

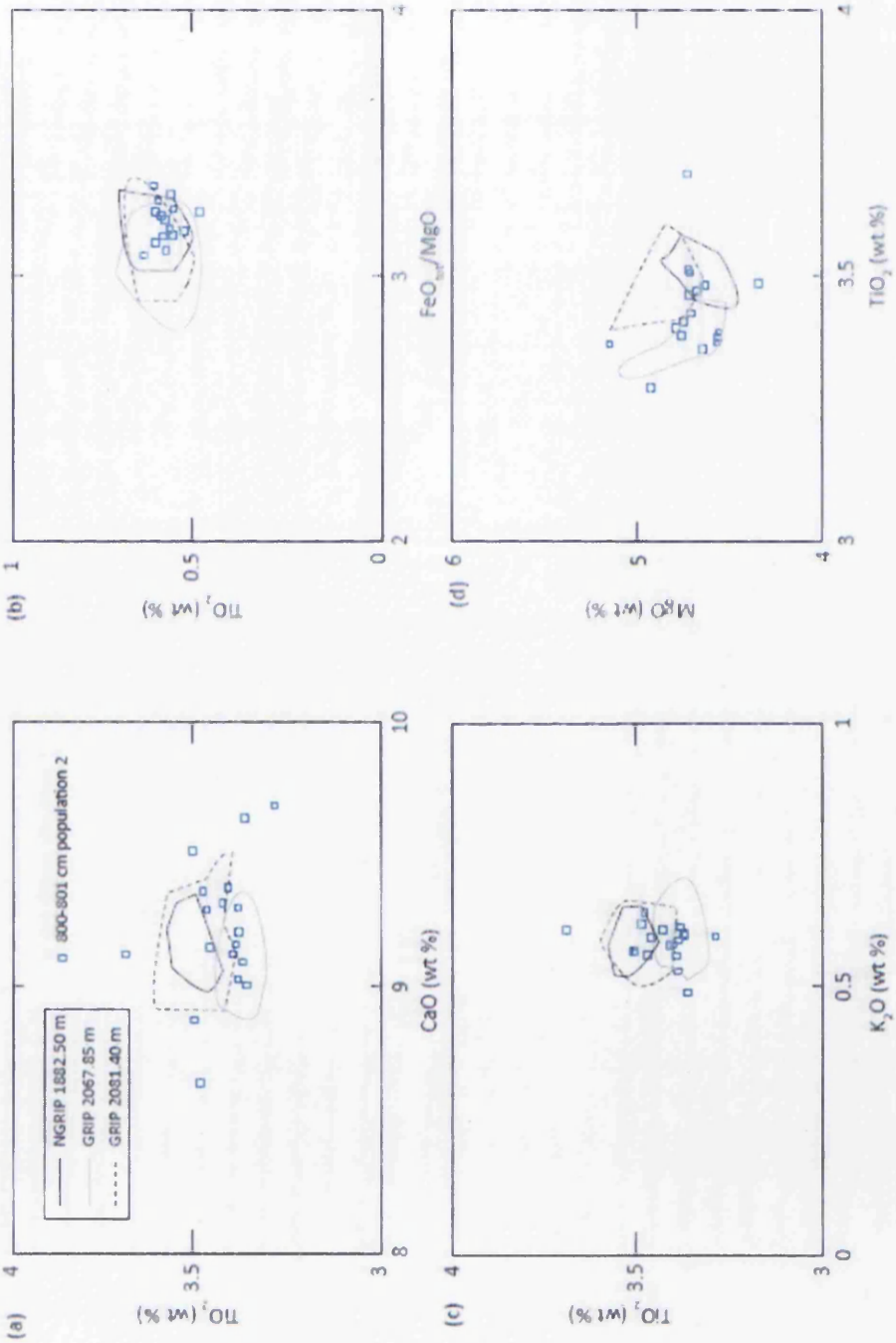

Figure 5.8 Major oxide results (wt %) for the second population in 800-801 cm identified in MD04-2829CQ. (a), (b), (c), (d) 800-801 cm population compared to glass shard analyses from three geochemically similar horizons identified in NGRIP and GRIP (Bourne et al., 2015). All data have been normalised to 100% total oxide concentration.

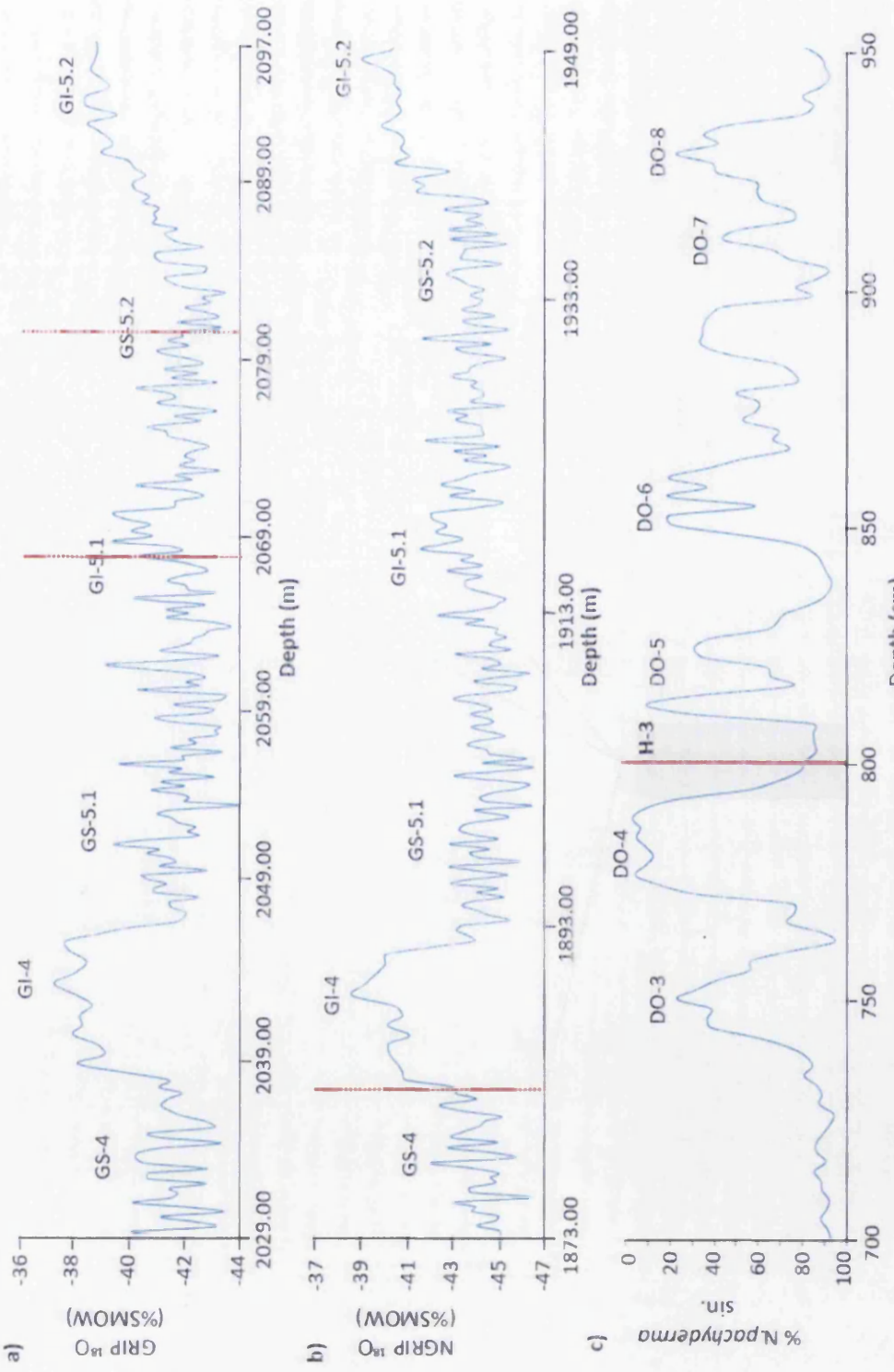

Figure 5.9 Stratigraphical comparison of tephra horizons NGRIP 1882.50 m, GRIP 2067.85 m and GRIP 2081.40 m with MD04-2829CQ 800-801 cm population two. a) GRIP ^{18}O record (GS-4 – GI 5.2). b) NGRIP ^{18}O record (GS-4 – GI 5.2). (c) MD04-2829CQ % *N.pachyderma* sin. (DO-3-DO-8) (Hall et al., 2011). Red lines denote tephra horizons and possible correlations. Grey bar denotes Heinrich 3.

However, this may also be a consequence of aeolian activity redistributing shards previously deposited on the ice-sheet surface. Nonetheless, this population may be sourced from a previously undiscovered Grímsvötn eruption.

A bimodal population in 800-801 cm may be the product of coeval eruptions or shards sourced from separate eruptions with a short temporal lag. 800-801 cm falls during a Heinrich event, as shown by low (21%) *N. pachyderma* sin. and high influx of IRD grains (Fig 5.4), suggesting high rates of ice-berg calving. This is demonstrated by the high concentration of coarse-grained tephra shards found within this horizon that range up to ~500 μm in diameter. Large grain sizes are greater than would be typically associated with primary atmospheric fallout and may represent transportation via iceberg rafting from proximal locations. This process can accumulate numerous eruptions onto the ice-sheet surface and delay deposition into the marine sequence by several millennia. However, typical diagnostic features of ice-rafted deposits include geochemical heterogeneity and a diffuse shard concentration profile, both of which are not features of 800-801 cm. It is suggested that the geochemical homogeneity and exceptional stratigraphical constrainment exhibited by this horizon are the product of primary airfall or sea-ice. The primary signal may overprint sediments that contain an additional ice-rafting signal. Large grain sizes within this horizon may be a consequence of sea-ice deposition, which does not affect the integrity of the deposit (Austin et al., 2004). Both populations may represent potentially useful isochronous horizons, providing a secure geochemical correlation can be established in future investigations (Table 5.1).

5.4.2 MD04-2829CQ 930-931 cm

5.4.2.1 Shard descriptions and concentrations

A distinct 1 cm peak of thirty-six brown shards per 0.5 gdw is observed in the 25-80 μm fraction between 930-931 cm (Fig 5.10) (Table 5.1). A sharp increase from zero shards

to thirty-six glass shards within 1 cm and a rapid cessation of input to zero shards at 929-930 cm suggests a pulse of tephra with limited depositional re-working. Only one shard was present in a replicate sample taken from a different lateral transect and no other shards were identified in surrounding samples (Fig 5.10c). This suggests that this tephra deposit may not be preserved as a continuous horizon and highlights the possible lateral variability of cryptotephra deposition (Table 5.1). The shards are light brown in colour and exhibit a platy morphology. The horizon falls within the peak warmth of DO-8 (~38.3 ka b2k), as indicated by the low abundance of *N. pachyderma* sin. (41%) (Hall et al., 2011) (Fig 5.2, 5.10).

5.4.2.2 Geochemistry and source identification

Major element results from thirty-one single shards reveal a basaltic tholeiitic composition (Fig 5.5). Overall, the deposit exhibits a reasonably homogeneous geochemical population. Twenty-nine shards from the 25-80 μm fraction and two from the >80 μm fraction form this population (Fig 5.11). Geochemical characteristics include SiO_2 concentrations of ~49.08-50.88 wt%, K_2O concentration of ~0.40 wt%, TiO_2 concentrations of ~2.23-2.98 wt%, CaO concentrations of ~9.63-11.67 wt% and MgO concentrations between ~5.22-7.32 wt% (Fig 5.10) (Table 5.2). These characteristics are typical of a tholeiitic basaltic composition, with the TiO_2 and K_2O concentrations typical of a Grímsvötn origin (Jakobsson, 1979) (Fig 5.6). Despite the relative homogeneity of the deposit, some elements exhibit a wide range of values i.e. K_2O (Fig 5.11a) and TiO_2 (Fig 5.11c). No significant outliers were detected in this deposit.

5.4.2.3 Wider correlations and depositional processes

Grímsvötn-sourced tephra deposits of tholeiitic basaltic composition dominate the marine and ice-core records between 37,200 – 41,200 b2k (Rasmussen et al., 2003; Wastegård et al., 2006; Bourne et al., 2015).

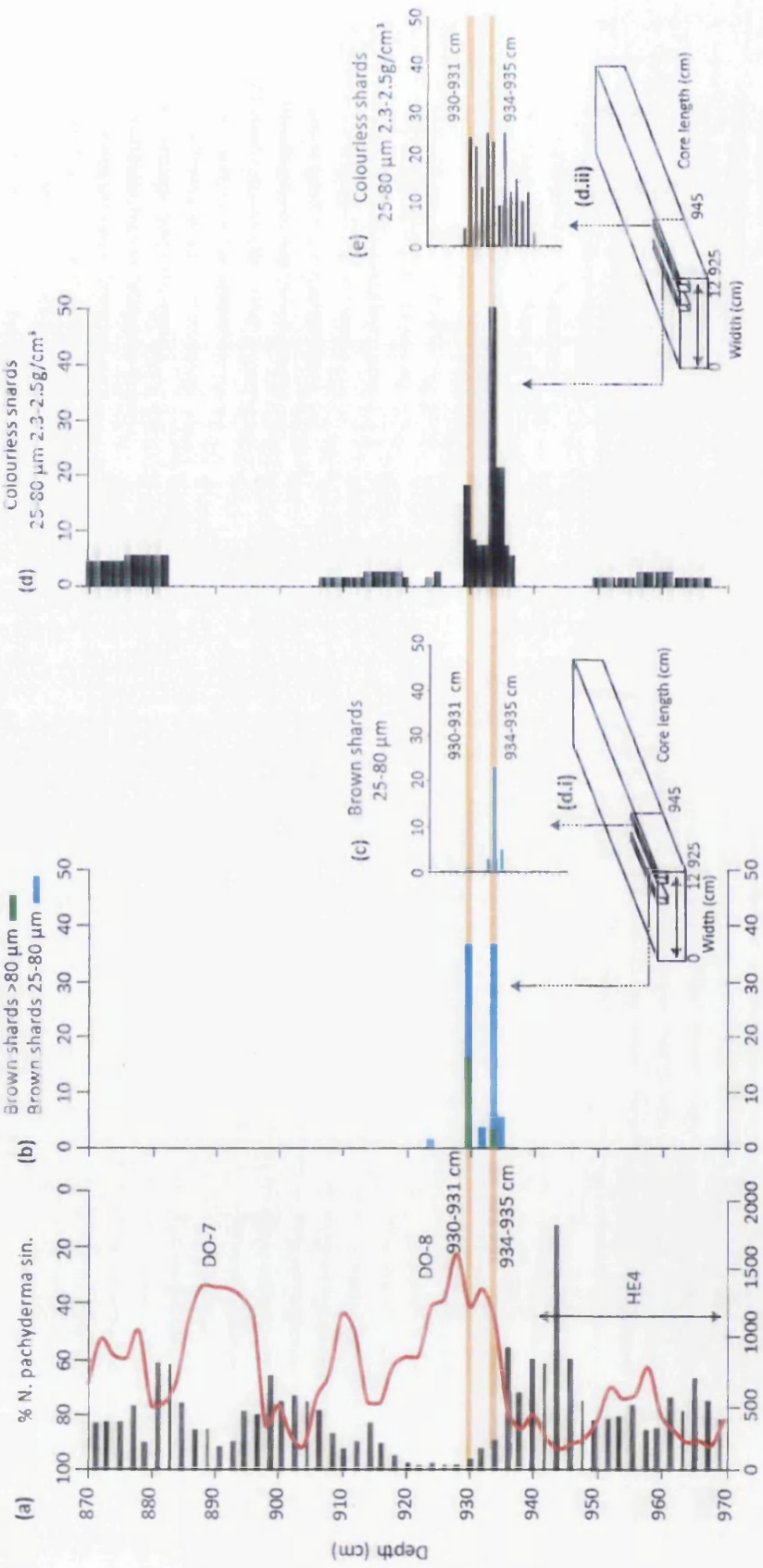

Figure 5.10 Low and high resolution (1 cm) tephra stratigraphy between 870-970 cm in MD04-2829CQ. (a) % *N. pachyderma* sin. and total IRD grains (Hall et al., 2011). (b) Number of brown shards identified within the 25-80 µm and >80 µm fractions at high resolution. (c) Replicate high resolution brown shard counts from a different lateral section of the core. (d(i), d(ii)) Positions of sample extraction for high resolution shard counts in the core. (d) Number of colourless shards within the 2.3-2.5 g/cm^3 density fraction. (e) Replicate high resolution colourless shard counts from a different lateral section of the core. The orange lines denote the peak in glass shard concentrations at 930-931 cm and 934-935 cm and represent depths taken for geochemical analysis.

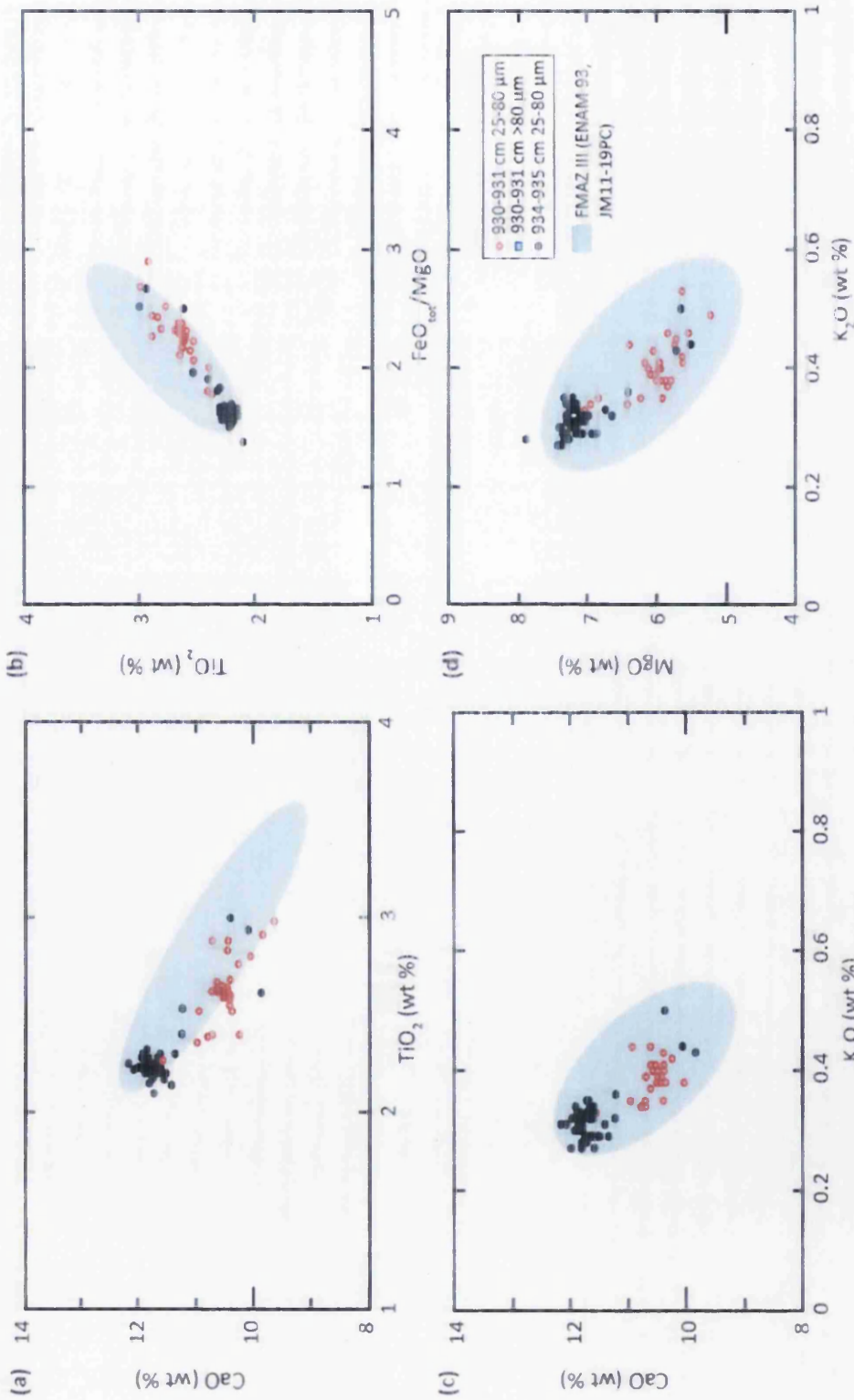

Figure 5.11 Major oxide results (wt %) for the 930-931 cm and 934-935 cm deposits identified in MD04-2829CQ. (a), (b), (c), (d) Major oxides compared to FMAZ III horizons from marine cores in the Faroes region (Wastegård et al., 2006; this study). All data have been normalised to 100% total oxide concentration.

Glass shard analyses from 930-931 cm plot within the broad FMAZ III compositional envelope derived from four other marine cores in the Faroes region (Rasmussen et al., 2003; Wastegård et al., 2006; this study) (Fig 5.11). 930-931 cm shows no consistent affinity to any of the fourteen volcanic events identified in NGRIP, GRIP and NEEM during this time period (Fig 5.12). This can be clearly observed on TiO_2 vs CaO and FeO/MgO vs TiO_2 geochemical biplots (Fig 5.12). This deposit may be sourced from a Grímsvötn eruption that is not preserved within the ice-core records.

The low concentration of coarse-grained brown shards (eighteen in the 80-125 μm fraction) and well-constrained nature of this deposit is typical of primary atmospheric fallout with minimal post-depositional modification. No diagnostic tailed shard distribution is present, indicating limited operation of bottom current re-working and/or bioturbation. However, this may be a consequence of low shard concentrations, which may not be of sufficient quantity to act as a tracer for bioturbative activity. The horizon occurs during DO-8 with no coeval IRD signal (Hall et al., 2011), suggesting iceberg calving is unlikely to have assisted in tephra delivery (Fig 5.10a). This horizon could potentially act as a high-precision isochronous marker, although no direct correlation can currently be established. The horizon falls within the broad FMAZ III marine compositional envelope derived from the Faroes region and may tentatively be useful for low resolution marine-marine correlations.

5.4.3 MD04-2829CQ 934-935 cm

5.4.3.1 Shard description and concentrations

This horizon forms a distinct 1 cm peak between 934-935 cm (thirty-six brown shards per 0.5 gdw in the 25-80 μm fraction and two shards in the >80 μm fraction) (Fig 5.10) (Table 5.2).

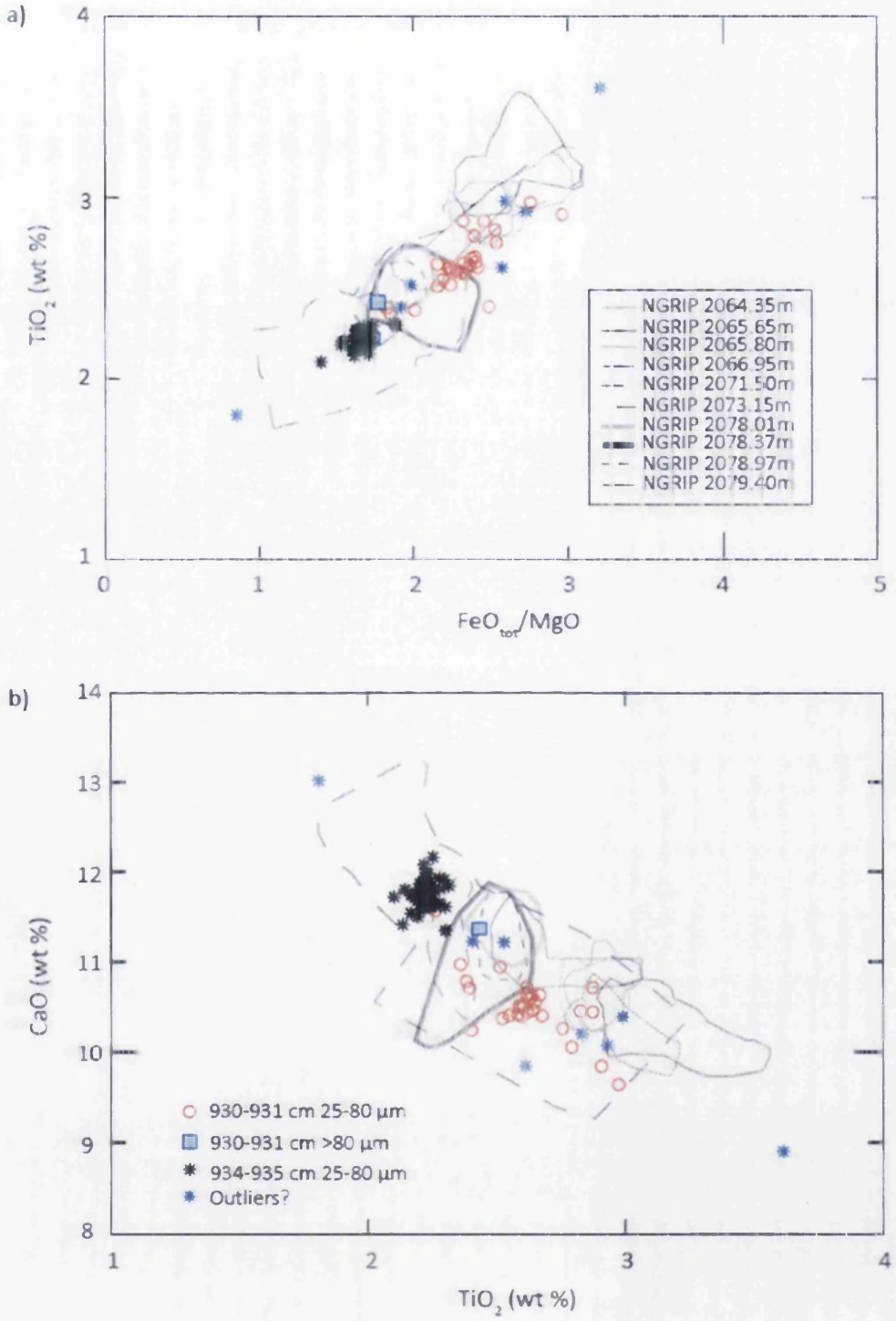

Figure 5.12 Major oxide results for the 930-931 cm and 934-935 cm deposits identified in MD04-2829CQ. (a) and (b) Glass shard analyses compared to geochemical compositional envelopes for cryptotephra deposits identified in NGRIP between 38,048 ± 721-38,826 ± 740 b2k (Bourne et al., 2013). All data have been normalised to 100% total oxide concentration.

A sharp increase from five to thirty-six shards between two contiguous 1 cm samples and a subsequent decline to five shards at 933-934 cm suggests a pulse of tephra with limited depositional re-working. Replicate samples taken from a different lateral position exhibit a concentration of twenty-three shards and highlight the lateral continuity of this horizon (Fig 5.10c) (Table 5.1). Shards are very light brown, exhibit a blocky morphology and display strong evidence of hydration. The majority of shards discovered in this horizon were detected in the 2.3-2.5 g/cm^3 fraction, possibly due to hydration processes altering the shard density. The horizon falls within the rapid warming limb of DO-8 as indicated by the decreasing abundance of *N. pachyderma* sin. (58 %) (Hall et al., 2011) (Fig 5.2, 5.10)

5.4.3.2 Geochemistry and source identification

Major element results from forty-nine single shards reveal a basaltic tholeiitic composition (Fig 5.5). The horizon exhibits a strongly homogeneous geochemical population. Ten outliers with notable differences in TiO_2, K_2O and Al_2O_3 concentrations were detected and subsequently removed from the data-set (these are highlighted in blue on ice-core comparison biplots) (Fig 5.12). Distinctive geochemical characteristics include SiO_2 concentrations of ~49.24-52.06 wt%, K_2O concentration of ~0.31 wt%, TiO_2 concentrations of ~2.13-2.39 wt%, CaO concentrations of ~11.48-12.64 wt% and MgO concentrations between ~6.96-8.00 wt% (Table 5.2). These characteristics are typical of a tholeiitic basalt composition, with the TiO_2 and K_2O concentrations implying an origin in the Grímsvötn system (Jakobsson, 1979) (Fig 5.6).

5.4.3.3 Wider correlations and depositional processes

Glass shard analyses from the 934-935 cm population fall within the compositional envelope of FMAZ III (Rasmussen et al., 2003; Wastegård et al., 2006; this study) (Fig 5.11). Specifically, it falls within the upper end of the FMAZ III composition on TiO_2 vs CaO biplots i.e. low TiO_2 values and high CaO concentrations. The deposit falls within

the lower end of the FMAZ III composition on TiO_2 vs FeO/MgO biplots and exhibits the lowest FeO/MgO concentrations within the FMAZ III envelope (Fig 5.11). The tight homogeneous population exhibited by 934-935 cm suggests that this horizon may be representative of a single eruption present within the FMAZ III complex.

A comparison of 934-935 cm with fourteen separate volcanic events identified in the Greenland ice-cores during this time period demonstrates that this falls tightly within the compositional envelopes of the correlated NGRIP 2071.50 m and NEEM 1759.65 m horizons (Fig 5.12, 5.13). These horizons exhibit the lowest TiO_2 and highest CaO values of all the ice-core horizons identified within this period and aid their discrimination from other Grímsvötn-sourced cryptotephra horizons. However, there is a relatively wide elemental spread in both ice-core correlative populations which may be the consequence of several factors. The geochemical variability may be indicative of several eruptive phases closely spaced in time and/or the product of aeolian re-working of previously deposited shards. The stronger homogeneity exhibited by main population in 934-935 cm in comparison to the stratigraphically equivalent ice-core horizons suggest that this deposit is likely to originate from a single phase of a Grímsvötn eruption.

The low concentration of >80 μm shards and predominance of shards in the 25-80 μm fraction are typically associated with deposits derived from primary atmospheric fallout. Absence of a diagnostic tailed shard distribution suggests post-depositional modification was minimal (Fig 5.10). The horizon was deposited on the warming limb of DO-8 with no coeval IRD influx (Fig 5.10a), which suggests iceberg calving is unlikely to have assisted in tephra delivery to the site. Strong geochemical homogeneity and similarity with NGRIP 2071.50 m and NEEM 1759.85 m horizons, as shown on biplots in Figures 5.12 and 5.13, suggest the 934-935 cm horizon is representative of a single primary input event.

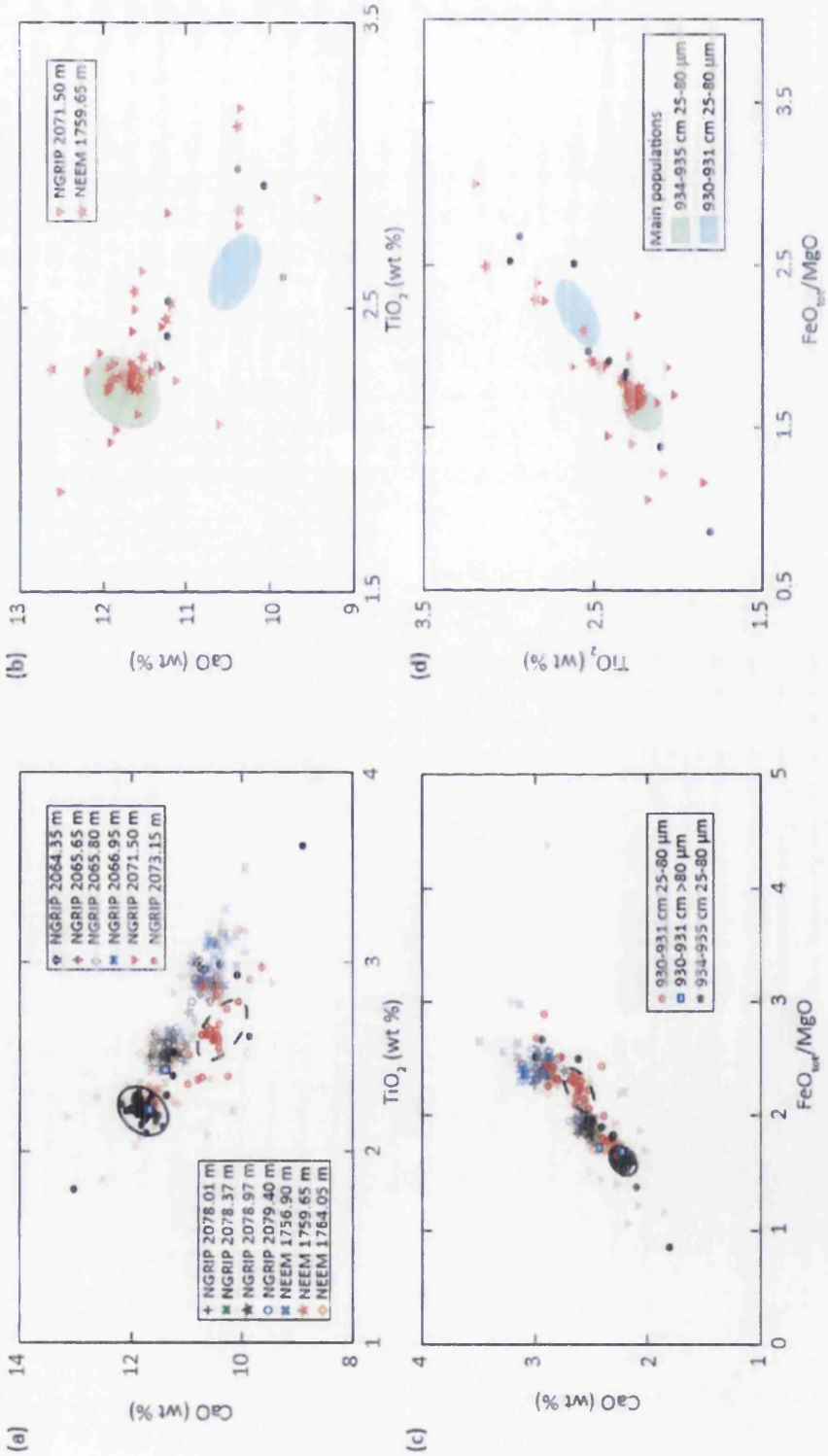

Figure 5.13 Major oxide results (wt%) for the 930-931 cm and 934-935 cm deposits identified in MD04-2829CQ. (a), (c) 930-931 cm and 934-935 cm major oxides compared to glass shard analyses from 13 geochemically similar horizons identified in NGRIP and NEEM (Bourne et al., 2015). (b), (d) 930-931 cm and 934-935 cm major oxides compared to the most geochemically similar horizons found in NGRIP and NEEM. The geochemical compositional envelopes are used to highlight the most abundant population of the 930-931 cm and 934-935 cm horizons. All data have been normalised to 100% total oxide concentration.

The perplexing absence of other horizons that constitute the FMAZ III may be a consequence of atmospheric dispersal pathways or variations in ocean gyres unfavourable to deposition at the site. Nonetheless, the stratigraphic integrity of this horizon has been demonstrated and major element correlations suggest the deposit may be utilised as a high-resolution isochronous marker between the ice and oceanic realms (Table 5.1). This correlation will be tested with trace element data (see section 5.4.4).

5.4.4 Trace element characterisation

5.4.4.1 Assessing comparability of marine and ice-core trace element data

Glass shards from 934-935 cm and NEEM 1759.85 m were analysed for their trace element composition to provide a secondary fingerprint and to test the proposed correlation between the horizons. A number of analyses were conducted in two analytical periods over the course of a single day; ice-core shards were analysed in both AM and PM sessions and marine shards were analysed in the PM session. As such, comparisons between data sessions are first employed to assess the reliability and comparability of the marine and ice-core data-sets.

Initially, shards from the same analytical period (PM) were compared. For a large number of elements, the ice-core data is generally lower in concentration than the marine data, as observed on Pr vs Ce and La vs Ce geochemical biplots (Fig 5.14a,b). When the AM ice-core data is included, there is greater overlap between the marine and ice-core shards, but the marine concentrations are generally higher than the ice-cores (Fig 5.14c,d). There are significant differences in concentrations of Ba, Rb and Nb exhibited by the AM and PM ice-core and marine data-sets (Fig 5.15). These differences are apparent in both the AM and PM datasets, which suggest that compositional differences are real and have not been affected by variability between different analytical periods.

5.4.5 Testing correlations using trace element data

The overall concentrations of REE's fall within the evolved classification of tholeiitic basalts presented in Óskarsson et al. (1982) (Fig 5.16a). The average REE profiles for the two basaltic horizons display a gentle gradient between La and Lu (Fig 5.16b). However, there are differences in the slopes of the deposits, most notably shown by differences in Ce, Tb and Lu concentrations. Both profiles fall within the Grímsvötn envelope constructed from trace-element end member characterisation by Óskarsson et al. (1982). Geochemical biplots were also constructed to test trace-element source assignation with Grimsvötn (Fig 5.16c,d). Generally, few shards plot within the Grímsvötn envelope, which may be due to the bulk analyses used to gain source characterisations, which may incorporate phenocrysts and lithic phases. Bulk analyses may also fail to detail the same heterogeneity of deposits that can be captured from single-shard analyses. In addition, small spot sizes may add variability due to analytical issues (Pearce et al., 2007). As such, Grímsvötn source envelopes provided by Meyer et al. (1985) may not offer sufficient diagnostic capabilities.

Geochemical biplots of Ba vs Rb and Ba vs Nb demonstrate significant compositional differences between MD04-2829CQ 934-935 cm and NEEM 1759.85 m, and no overlaps are observed between data points (Fig 5.15c,d). Barium concentrations are consistently <80 ppm in 934-935 cm and >80 ppm in NEEM 1759.85 m, with averages of 52.81 ppm and 115.95 ppm respectively (Fig 5.15c,d) (see appendix). Differences are additionally observed in niobium concentrations, with an average of 11.42 ppm in 934-935 cm and 6.61 ppm in NEEM 1759.85 m. Due to the incompatibility of barium, compositional differences cannot be attributed to differing levels of geochemical evolution or fractionation. This suggests the two samples are not genetically related and cannot be explained by shards originating from separate phases of an eruption.

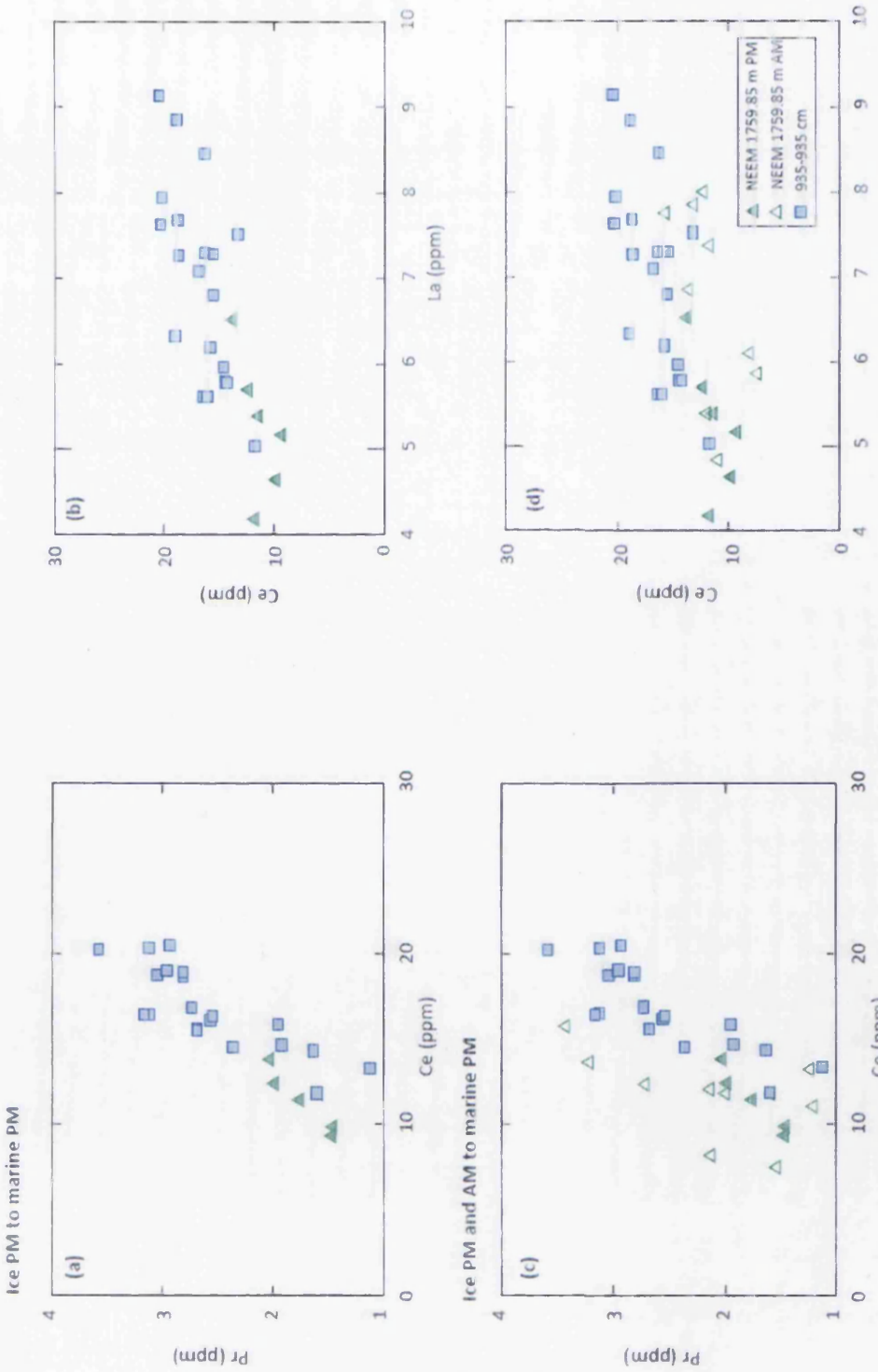

Figure 5.14 Trace element comparisons between the compositions of MD04-2829CQ 934-935 cm and NEEM 1759.85 m. (a), (b) Trace element comparisons between NEEM 1759.85 m analyses conducted in the PM session with 934-935 cm from the PM session. (c), (d), Trace element comparisons from NEEM 1759.85 m analyses conducted in the AM and PM session with 934-935 cm.

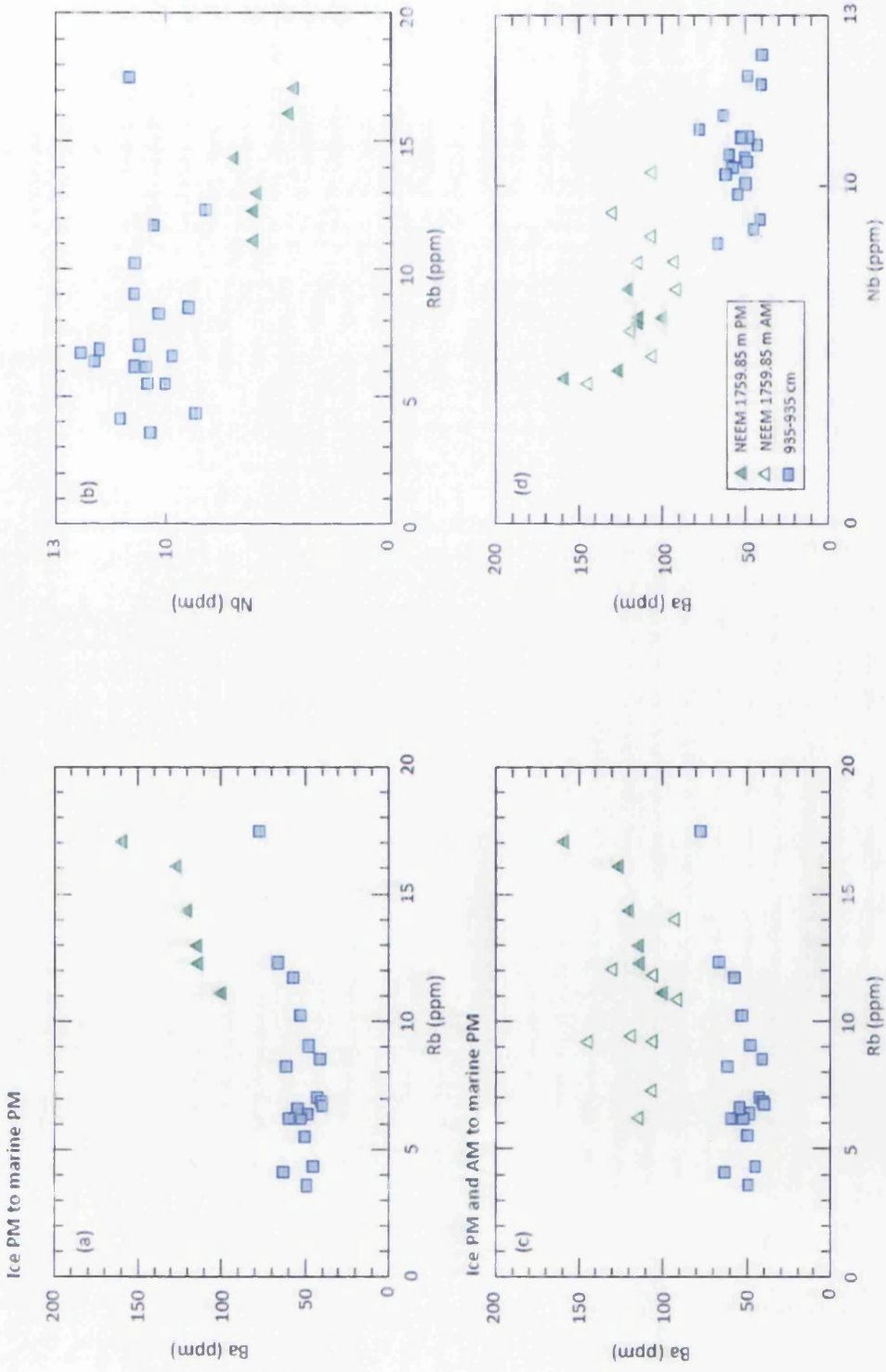

Figure 5.15 Trace element comparisons between the compositions of MD04-2829CQ 934-935 cm with NEEM 1759.85 m. (a), (b) Trace element comparisons from NEEM 1759.85 m analyses conducted in the PM session with 934-935 cm from the PM session. (c), (d). Trace element comparisons from NEEM 1759.85 m analyses conducted in the AM and PM session with 934-935 cm.

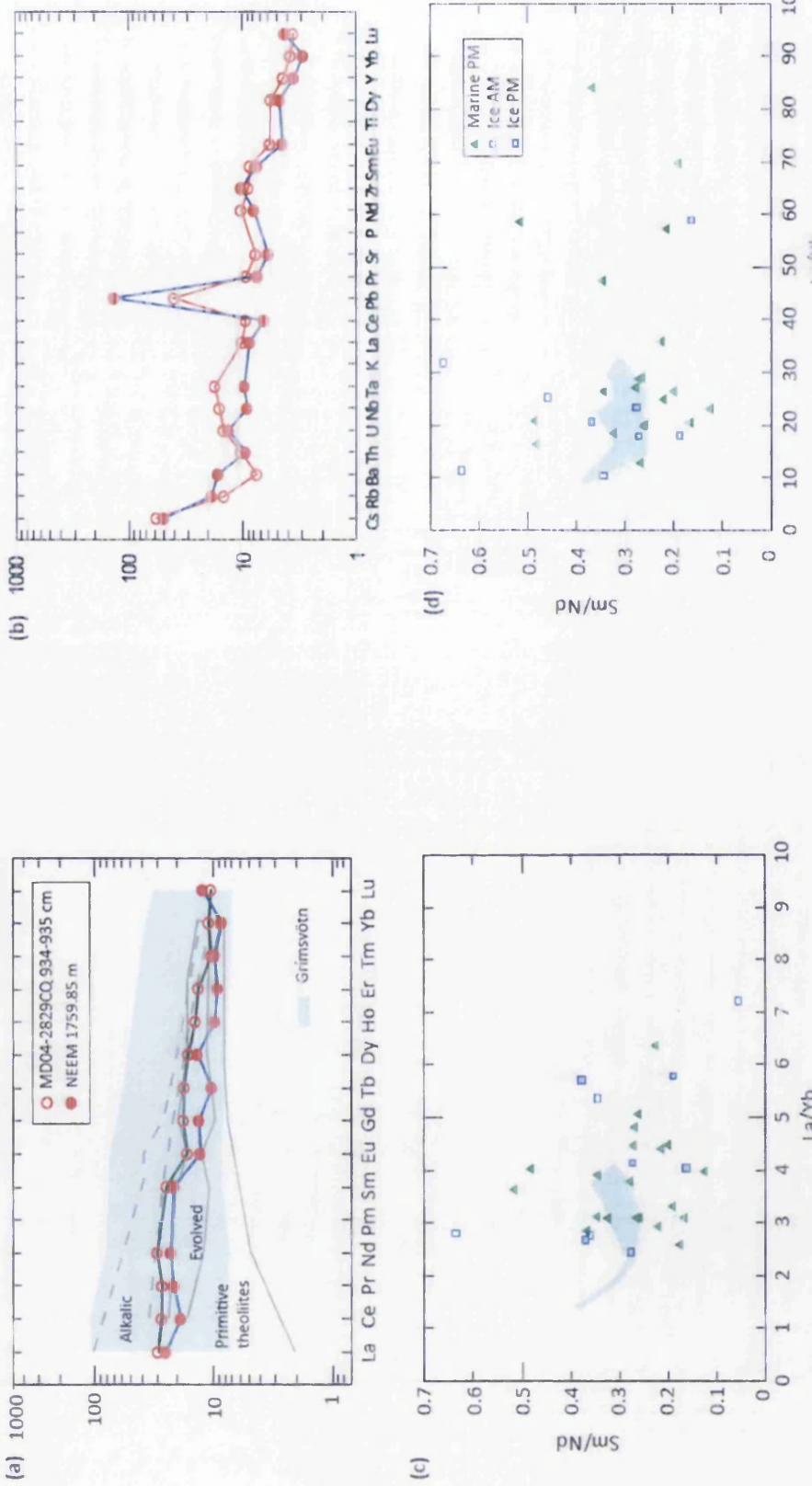

Figure 5.16 Trace element characterisations and source assignation of glass shards from NEEM 1759.85 m and MD04-2829CQ 934-935 cm. (a) Average chondrite-normalised REE profile for MD04-2829CQ 934-935 cm and NEEM 1759.85 m (AM and PM analytical sessions). Chondrite compositions from Sun and McDonough (1989). End member characterisations of Icelandic theoleiitic and alkaline basaltic material from Oskarsson et al. (1982). (b), (c), (d) Trace element ratio biplots. Source enveloped derived from Meyer et al. (1985).

Major element similarities indicate that the shards were derived from the same system, but differences in trace elements suggest they may have originated from separate magma chambers. This raises important questions regarding the frequency of Grímsvötn activity during DO-8 and suggests even though a large number have already been identified, more eruptions may have occurred throughout the last glacial period than are documented in the ice-cores. More work is necessary to capture the geochemical range of deposits preserved within the marine environment during DO-8 to fully assess the potential for ice-marine correlations (see section 6.7). The importance of employing trace-element analysis is highlighted in this instance to prevent erroneous correlations.

5.5 Rhyolitic horizons within MD04-2829CQ

5.5.1 MD04-2829CQ 810-811 cm

5.5.1.1 Shard descriptions and concentrations

A small indistinct peak between 810-811 cm contains a very low shard concentration (fifteen colourless shards per 0.5 gdw in the 25-80 μm fraction) (Fig 5.4) (Table 5.1). The sampling interval has an average background concentration of five shards per 0.5 gdw which fluctuates from a peak of fifteen to zero, which indicates frequent input of shards into the sequence (Fig 5.4). Shards exhibit a platy and fluted morphology with a varying concentration of vesicles. The horizon precedes Heinrich 3 (~31 ka b2k) as indicated by rapidly increasing % *N. pachyderma* sin. abundances (Hall et al., 2011) (Fig 5.2, 5.4).

5.5.1.2 Geochemistry and source identification

Eleven shards exhibit a rhyolitic composition with an affinity with the transitional alkali rock suite defined on the TAS plot (Jakobsson et al., 2008) (Fig 5.17). The deposit exhibits a distinct bimodal geochemical population (Fig 5.18).

Bimodality is most distinct within the FeO vs CaO geochemical biplot (Fig 5.18d) and no significant outliers from these populations were detected. The bimodality could imply each population has been sourced by a different volcanic system or one system with strong geochemical variability (Table 5.2).

Five glass shards form population one. Geochemical characteristics include SiO_2 concentrations of ~72.43 wt%, FeO concentrations of ~3.75 wt%, CaO concentrations of ~1.35 wt%, K_2O concentrations of ~3.67 wt% and TiO_2 concentrations of ~0.31 wt% (Table 5.4). Identifying a volcanic source for this horizon is confounded by a lack of data sources as only a few studies have reported geochemical charaterisations of proximal Icelandic silicic material (Larsen et al., 2001; Jónasson, 2007). This may not be sufficient to capture the full geochemical range exhibited by source volcanoes. A comparison of 810-811 cm with whole rock data from five transitional alkali volcanic systems is shown in Figure 5.18. The majority of population one fall within the Torfajökull compositional envelope on N_2O+K_2O vs SiO_2 biplots and some fall within the same envelope on FeO vs CaO biplots. However, shards additionally fall within the Katla and Tindfjallajökull envelopes on K_2O vs SiO_2 biplots and highlight that no consistent relationships can be identified (Fig 5.18).

Six shards form population two. Distinctive geochemical characteristics include SiO_2 concentrations of ~76.07 wt%, FeO concentrations of ~2.56 wt%, CaO concentrations of ~0.56 wt%, K_2O concentrations of ~4.19 wt% and TiO_2 concentrations of ~0.17 wt% (Table 5.4). On SiO_2 vs K_2O and FeO vs CaO biplots, there is an overlap within the Torfajökull compositional envelope but this is not consistent (Fig 5.18). Akin to the first population, there are no consistent relationships observed between geochemical biplots and a volcanic source cannot be ascribed.

Table 5.4 Mean and 1σ major element results of rhyolitic glass shards extracted from deposits found within MD04-2829CQ. Total oxides are raw values prior to normalisation. All major elements are expressed as percentage weight. Total iron expressed as FeO. n = number of shards analysed.

Tephra layer	Composition	Source	Grain size (μm)	n	SiO_2	TiO_2	Al_2O_3	FeO	MnO	MgO	CaO	Na_2O	K_2O	P_2O_5	Total
810-811 cm pop 1	Rhyolitic	Katla	25-80	5	72.43	0.31	12.72	3.75	0.15	0.23	1.35	5.36	3.67	0.04	97.14
					0.17	0.01	0.51	0.09	0.02	0.02	0.09	0.37	0.06	0.01	1.47
810-811 cm pop 2	Rhyolitic	Tindfjallajökull?	25-80	6	76.07	0.17	11.33	2.56	0.06	0.02	0.56	5.03	4.19	0.00	95.18
					0.36	0.02	0.59	0.40	0.01	0.07	0.32	0.36	0.25	0.01	0.87
934-935 cm pop 1	Rhyolitic	Tindfjallajökull?	25-80	5	75.31	0.17	11.95	2.58	0.07	0.01	0.43	5.19	4.28	0.00	95.28
					0.52	0.01	0.47	0.19	0.00	0.02	0.04	0.22	0.08	0.01	1.12
934-935 cm pop 2	Rhyolitic	Katla	25-80	11	71.48	0.33	13.15	3.98	0.15	0.19	1.45	5.49	3.73	0.04	97.42
					1.01	0.04	0.67	0.20	0.02	0.07	0.23	0.25	0.15	0.01	2.20

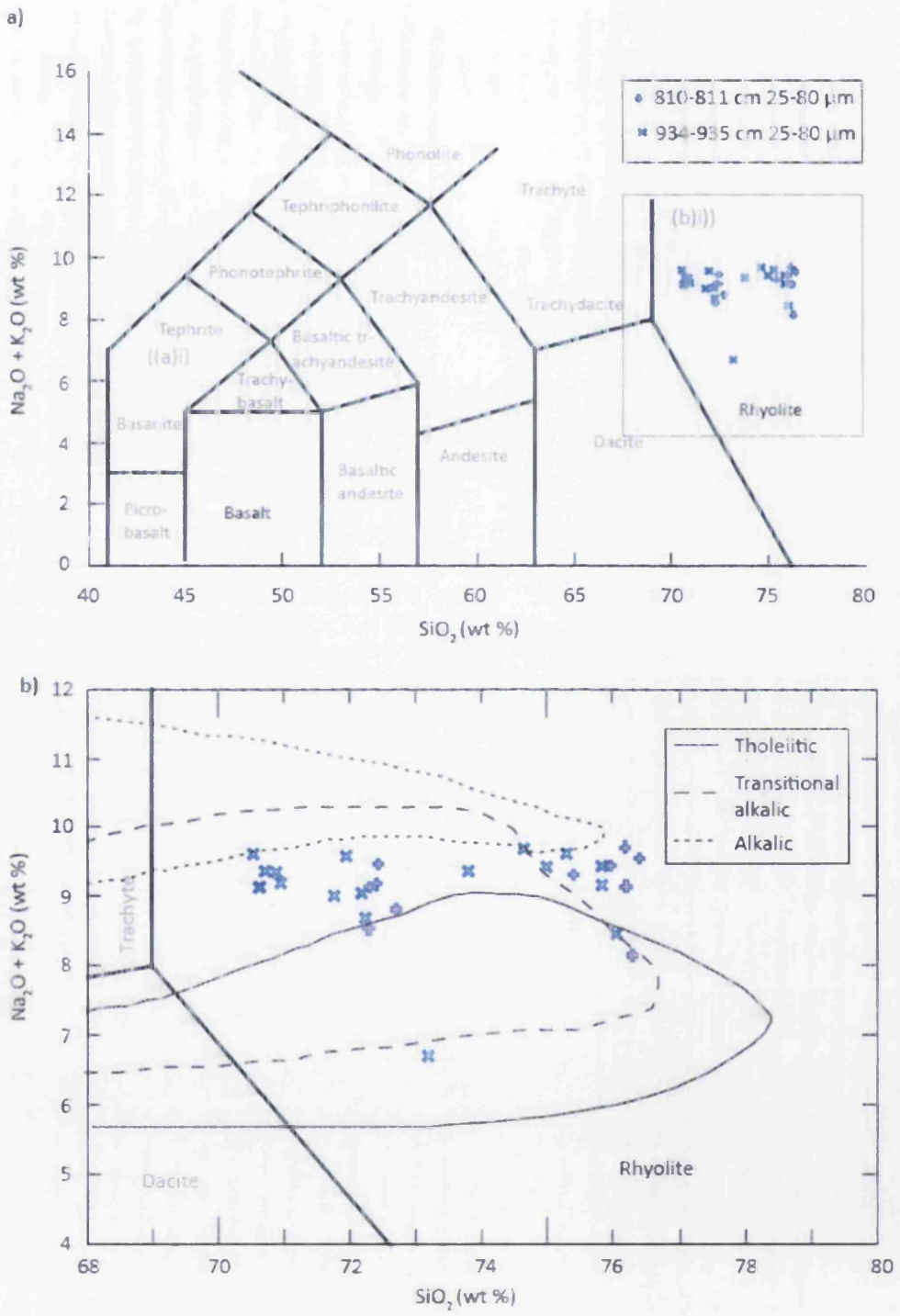

Figure 5.17 (a) Total alkalis vs silica plot for analyses from rhyolitic deposits found in MD04-2829CQ. (b) Inset of TAS plot focusing on the rhyolitic analyses. Chemical classification is defined by Le Maitre et al. (1989). The compositional envelopes for the Icelandic rock suites are defined by Jakobsson et al., (2008).

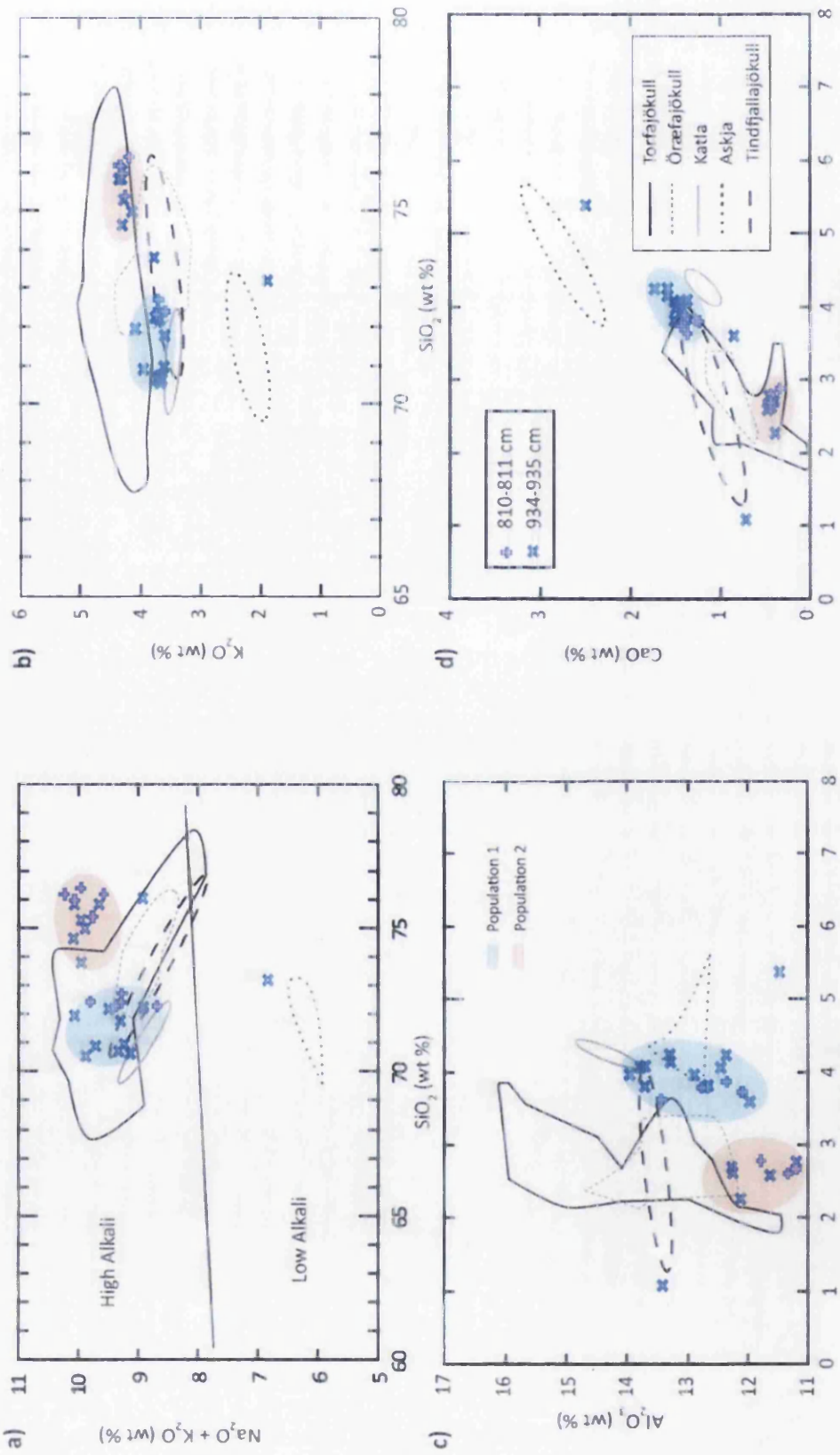

Figure 5.18 Glass shard analyses for three rhyolitic deposits found in MD04-2829 CQ compared to geochemical envelopes for five different transitional alkali Icelandic source volcanoes based on individual whole rock analyses presented in Jónasson (2007). All data have been normalised to 100% total oxide concentration.

5.5.1.3 Wider correlations and depositional processes

The constant low background of shards identified within the high-resolution shard concentration profile with peaks marginally above background levels suggest no isochron can be discerned. It is likely that shards have exhibited a long residency within the ocean environment and are subsequently derived from bottom current re-working. Comparisons made within this section focus on widespread and voluminous eruptions that have characterised Pleistocene marine records, even though these eruptions fall outside the appropriate stratigraphic interval.

Within the period of 25-32 ka b2k, only two deposits reported in the Greenland ice-core framework exhibit a rhyolitic/dacite composition and these display an affinity to products sourced from Hekla (Bourne et al., 2015). These ice-core deposits differ significantly from the 810-811 cm deposit on elements including SiO_2, CaO and TiO_2. The relative infrequency of rhyolitic deposits may be a reflection of changes in ash plume dispersion, or alternatively reflect limited silicic volcanic activity. The two rhyolitic populations present in 810-811 cm may represent two previously undiscovered silicic volcanic events or shards re-worked from previous eruptions that have a dispersal pathway towards this core site (Thornalley et al., 2011).

Although a source volcano for population one in 810-811 cm cannot be assigned using proximal volcanic data, some overlap with the Katla compositional envelope is demonstrated on SiO_2 vs K_2O biplots (Fig 5.18). Rhyolitic Katla sourced eruptions in early Holocene and Lateglacial marine deposits exhibit similar geochemical compositions to this population (Thornalley et al., 2011; Jennings et al., 2014). As the glass shards for these events were compositionally similar, this may indicate geochemical stability of the Katla magma system. Assuming continued magmatic stability, other known rhyolitic deposits from the Katla system i.e. Vedde Ash, AF5 and Suduroy tephras were compiled to create a geochemical composition envelope to check

for potential common sources with 810-811 cm (Fig 5.19) (Wastegård et al., 2002; Mortensen et al., 2005; Matthews et al., 2011b; Lane et al., 2012). A similarity coefficient of 0.976 indicates a strong common source similarity between population one in 810-811 cm and Katla sourced rhyolitic deposits. This is illustrated on a number of geochemical biplots where all shards from this population plot within the Katla compositional envelope on a number of element oxides (Fig 5.19). Single-shard analyses from distal occurrences of Katla shards are likely to capture the full compositional range of Katla products, as opposed to bulk data derived from proximal material. This may explain the differences in source assignation between Figure 5.17 and Figure 5.18.

A comparison of population two in 810-811 cm with the rhyolitic component of the NAAZ II complex (II-RHY-1) (see section 2.5.1.1) suggests a close geochemical similarity between these two deposits (Fig 5.19). Six shards from 810-811 cm plot consistently within the NAAZ II compositional envelope, derived from a number of pan-Atlantic marine cores (Fig 5.19) (Wastegård et al., 2006; Brendryen et al., 2011; Abbott, unpublished). Furthermore, characteristic bubble walled morphologies of the NAAZ II deposit are similar to those found in 810-811 cm. However, there is a significant temporal delay (~24 ka b2k) between the eruption and subsequent preservation at the core site (Fig 5.2). In the absence of covarying IRD influx at this depth, the delay is unlikely to be a feature of iceberg calving and is likely the consequence of substantial bottom current re-working.

The NAAZ II deposit is widely dispersed across the North Atlantic and often exhibits a thickness of ~20 cm with a distinctive upward tail (Austin et al., 2004; Wastegård et al., 2006). The exceptionally high input of rhyolitic shards into the marine system is likely to provide a source for ocean currents to constantly mobilise and redistribute glass shards across the ocean floor.

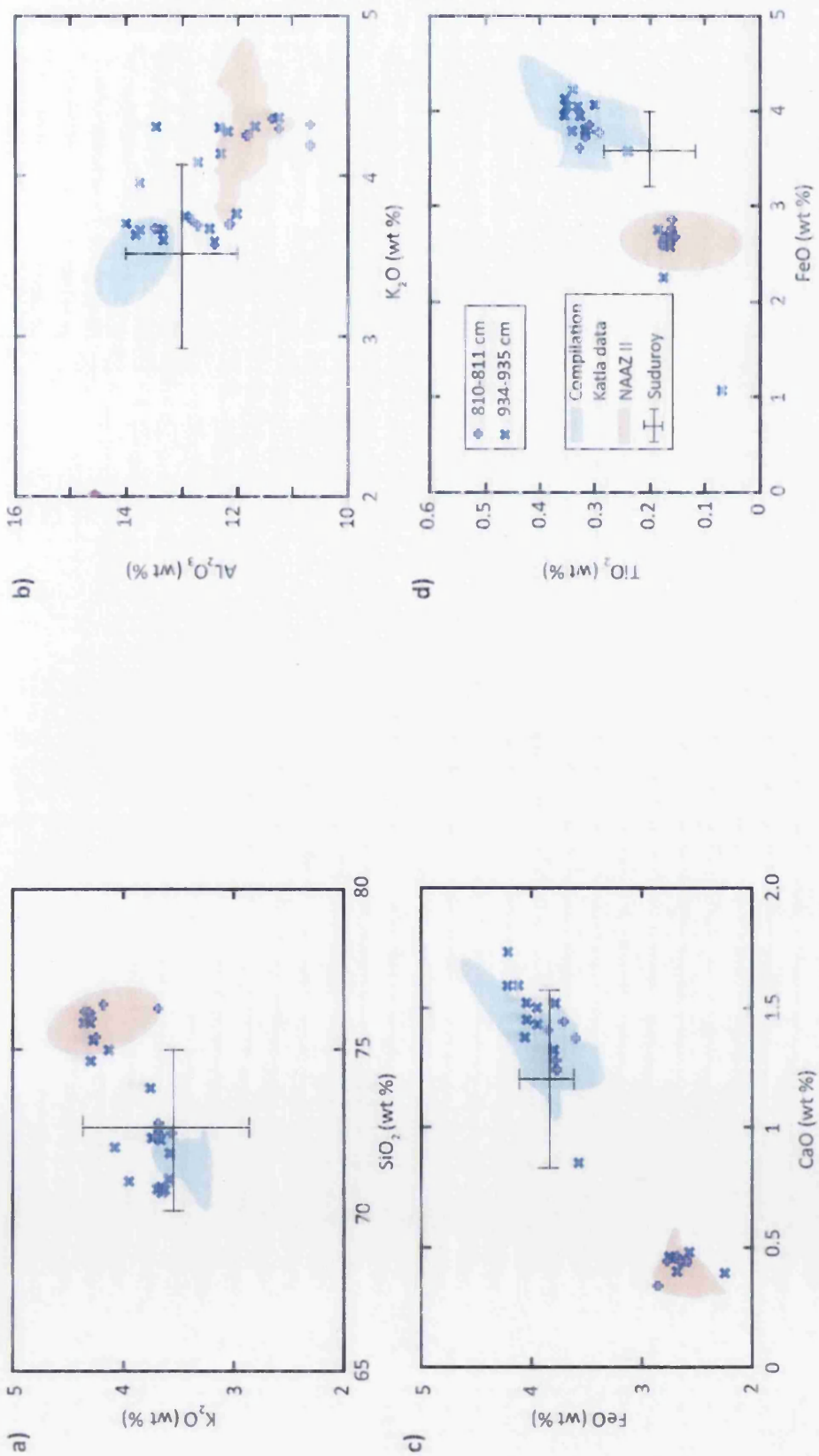

Figure 5.19 Major oxide results (wt%) for rhyolitic deposits found in MD04-2829CQ compared to geochemically similar tephras. (a), (b), (c), (d) Major elemental oxides compared to geochemical compositional envelopes for the NAAZ II (Wastegård et al., 2006, Brendryen et al., 2011, Abbott., unpublished), Vedde Ash, AF5 (Mortensen et al., 2005; Matthews et al., 2011b; Lane et al., 2012) and published data from the Suduroy (means and 2σ; Wastegård et al., 2002).

Furthermore, low geochemical totals for this population (~95.18 wt%) can be taken as an indicator of post-emplacement hydration and extended residence in the ocean environment (Jennings et al., 2014). The second population is likely to be composed of redistributed NAAZ II rhyolitic glass shards with a strong secondary transportation signal and cannot be considered isochronous.

5.5.2 MD04-2829CQ 934-935 cm

5.5.2.1 Shard descriptions and concentrations

This horizon forms a relatively distinct peak between 934-935 cm (fifty-one colourless shards 0.5 gdw in the 25-80 μm fraction) (Fig 5.10d) (Table 5.1). The 30 cm sampling interval encompassing the horizon has an average background concentration of nine shards per 0.5 gdw, fluctuating from a peak of fifty-one to zero. Replicate samples from a different lateral position between 929-942 cm do not exhibit a single distinct peak. This highlights the lateral variability of rhyolitic shards within the sequence. Shards exhibit a platy and fluted morphology with varying degrees of vesicularity and often occur attached to sedimentary and biological material retained during density floatation. The horizon falls on the warming limb of DO-8 and immediately precedes Heinrich 4 as indicated by rapidly decreasing % *N. pachyderma* sin. abundances (Fig 5.2, 5.10a) (Hall et al., 2011).

5.5.2.2 Geochemistry and source identification

EPMA results from eighteen individual shards reveal a rhyolitic composition with an affinity to the transitional alkali rock suite defined on the TAS plot (Jakobsson et al., 2008) (Fig 5.17). Overall, the deposit exhibits geochemical bimodality similar to 810-811 cm (Fig 5.18), which is most distinct within the FeO vs CaO geochemical biplot (Fig 5.18d). Two significant outliers were observed in this deposit which exhibit a notably low total alkali concentration of ~6.71 wt% in one shard, and one shard with a notably low FeO concentration of ~1.07 wt%.

Eleven shards form population one (Fig 5.18). Distinctive geochemical characteristics include SiO_2 concentrations of ~71.48 wt%, FeO concentrations of ~3.98 wt%, CaO concentrations of ~1.45 wt%, K_2O concentrations of ~3.73 wt% and TiO_2 concentrations of ~0.33 wt% (Table 5.4). There are no consistent relationships observed between this population and proximal Icelandic deposits and therefore a volcanic source cannot be ascribed (Fig 5.18).

Five glass shards form population two (Fig 5.18). Distinctive geochemical characteristics include SiO_2 concentrations of ~75.31 wt%, FeO concentrations of ~2.58 wt%, CaO concentrations of ~0.43 wt%, K_2O concentrations of ~4.28 wt% and TiO_2 concentrations of ~0.17 wt% (Table 5.4). Similarly to 810-811 cm, there are no consistent relationships observed between this population and proximal Icelandic deposits and this makes source assignation difficult (Fig 5.18).

5.5.2.3 Wider correlations and depositional processes

Population one overlaps with the first population in 810-811 cm with a similarity coefficient of 0.976 (Fig 5.19). It is likely this population also consists of a composite of Katla-sourced rhyolitic glass shards (Fig 5.19). The second population in 934-935 cm overlaps with the second population in 810-811 cm and exhibits a similarity coefficient of 0.984 (Fig 5.19). This geochemical population shares a common source to the NAAZ II (II-RHY-1) deposit, indicating a temporal delay of ~15 ka b2k between the eruption and subsequent emplacement. Similarly to 810-811 cm, there is no coincident peak in IRD concentration, suggesting the geochemical populations may be the result of a bottom current re-working and long residence time of some large-volume and widespread tephras.

The presence of a very similar geochemical bimodal composition to 810-811 cm indicates that the same secondary transport mechanisms have controlled deposition. The stratigraphic separation of 1.24 m between these deposits adds confidence to the notion that high silicic input into the marine system from the NAAZ II and Katla-sourced rhyolites have been redistributed by bottom currents.

5.6 Developing a tephrostratigraphy for MD04-2829CQ:

5.6.1 Assessing isochronous integrity: basaltic vs rhyolitic depositional controls

Analysis of three basaltic cryptotephra horizons in MD04-2829CQ reveals that each deposit occurs as a distinct 1 cm peak in shard concentration with sharp contacts to the underlying sediment, indicating rapid influx of basaltic glass shards. Absence of gradational upper boundaries following the peaks, coupled with the absence of a background brown shard signal indicates the occurrence of three distinct input events. Moderate homogeneity exhibited by 930-931 cm indicates primary airfall deposition and lateral discontinuity is a likely consequence of the patchy distribution and preservation of low shard concentrations. Strong geochemical homogeneity exhibited by 934-935 cm and the dominance of tephra shards in the 25-80 μm fraction strongly indicates primary deposition, demonstrating the isochronous integrity of this horizon. Despite only a 4 cm separation, both horizons exhibit significantly different geochemical compositions, which provides evidence that they are well constrained and derived from separate events.

A thorough systematic assessment of high-resolution shard concentration profiles derived from the 2.3-2.5 g/cm^3 fraction across several lateral transects, provides important information for assessing the stratigraphic integrity of rhyolitic deposits. Shard distributions are diffuse and suggest the operation of post-depositional re-working, resulting in a low shard background throughout the core. Variable concentrations between replicate samples taken from a different lateral position reflect the lateral discontinuity of these deposits. The 810-811 cm and 934-935 cm rhyolitic deposits exhibit similar bimodal geochemical populations. Both populations display strong affinities to NAAZ II (1I-RHY-1) and Katla rhyolities, which may indicate a significant temporal delay between the eruption and deposition. No rhyolitic deposits in this core can be considered to constitute peaks and represent a background signal of tephra with long residency times.

Contrasting diagnostic features of basaltic and rhyolitic deposits highlight the different mechanisms controlling cryptotephra deposition at this locality. The lower density and platy morphologies of rhyolitic shards may be more conducive to remobilisation than basaltic material and explain the continuous rhyolitic background signal. The 934-935 cm horizon exhibits a peak in basaltic shards and coincides with elevated levels of rhyolitic shards. This illustrates that different depositional processes have operated simultaneously i.e. primary airfall controlling basaltic deposition and bottom currents controlling rhyolitic deposition. As such, depositional mechanisms controlling the rhyolitic concentration profiles can be dissociated from the basaltic concentration profiles. This notion strengthens the interpretations of primary deposition for the basaltic deposits 800-801 cm, 930-931 cm and 934-935 cm and enhances the integrity of these horizons as isochronous markers.

5.7 Conclusions

- Three basaltic cryptotephra horizons have been identified in MD04-2829CQ. Major element characterisations of these horizons demonstrate a Kverkfjöll and Grímsvötn source for 800-801 cm and a Grímsvötn source for 930-931 cm and 934-935 cm.

- The 800-801 cm deposit exhibits a bimodal geochemical population that displays an affinity to Kverkfjöll and Grímsvötn. No potential Grímsvötn correlatives have been identified in the ice during this interval. The Kverkfjöll population exhibits a strong geochemical similarity with GRIP 2067.85 m and GRIP 2081.40 m. Despite coinciding with a strong IRD signal, the discrete nature of this horizon suggests the deposit was deposited isochronously. This may provide a useful isochron if trace element data can geochemically distinguish between the potential ice-core correlatives.

- The 930-931 cm horizon is considered a primary deposit. No direct ice-core correlative can be established, although this horizon may still be useful for low-resolution marine correlations to the FMAZ III complex.

- The 934-935 cm horizon is a primary deposit and exhibits strong geochemical homogeneity. This horizon represents a well-resolved isochronous marker and major element correlations with NGRIP 2071.50 m and NEEM 1759.85 suggest a marine-ice link can be established. However, trace element data indicates significant compositional differences between 934-935 cm and NEEM 1759.85 m, indicating the samples are not genetically related. As such, the 934-935 cm horizon cannot be correlated to the Greenland ice-cores.

- Investigation of the 2.3-2.5 g/cm^3 fraction reveals a continuous background of rhyolitic shards exhibiting the same bimodal geochemical populations. These share a common source with the NAAZ II (II-RHY-1) and a composite of Katla-sourced rhyolites. These shards have been vulnerable to intensive bottom current re-working; therefore no rhyolitic isochronous markers can be established in this core.

Chapter 6 The search for the FMAZ III in the NE Atlantic: tephrostratigraphical records from MD95-2010 and MD99-2281

6.1 Introduction

This chapter has two aims. Firstly, to present a tephrostratigraphical record for Norwegian Sea marine core MD95-2010 between 23-41 ka b2k and secondly, to explore the full geographical extent of the FMAZ III (or individual components of it) in the NE Atlantic. This will be achieved with a focus on MD95-2010 and a short sediment section from MD99-2281 (between 38-39 ka). MD95-2010 represents the most northerly investigated record and exhibits a well-resolved D-O signal, reconstructed from dinocyst and foraminifera assemblages (Dokken & Jansen, 1999; Eynaud et al., 2002). The site presents a potential opportunity to link ice-core and marine records to the Norwegian Sea and it is anticipated that the FMAZ III is preserved within the sampled sequence. The second investigated record, MD99-2281, exhibits an exceptionally high sedimentation rate and presents an opportunity to stratigraphically separate closely spaced eruptions preserved in both the ice-cores and marine core MD04-2829CQ, which are thought to form distinct components of the FMAZ III. As such, this core was specifically selected to trace individual components of the FMAZ III identified within MD04-2829CQ and sampling is limited to a high-resolution window between 38-39 ka.

6.2 5.2 MD95-2010: core location, oceanographic setting and proxy record

North Atlantic marine core MD95-2010 (66°41'N, 4°34'E) was retrieved from 1226 m water depth on the Vøring Plateau in the southern part of the Norwegian Sea during the IMAGES cruise MD 101 (Dokken & Jansen, 1999; Eynaud et al., 2002) (Fig 6.1). The core site is located on the main axis of the warm Norwegian Atlantic Current (NwAC) that transports Atlantic water masses northwards through the Nordic seas, as well as being close to the limit of the Fennoscandian ice-sheet (Mangerud et al., 1991).

The core is ~10.7 m long, covering MIS 2 and 3 and consists of dark grey silty clays alternating with greenish clays (Kissel et al., 1999). Twenty-eight AMS ^{14}C samples were measured and calibrated using the Bard (1998) 'glacial polynomial' (Dokken and Jansen, 1999). The resulting age model was constructed by directly correlating the positions of abrupt transitions recorded in magnetic susceptibility, $\delta^{18}O$ and IRD records to the GISP2 ice-core record, based on the assumption that these records represent stadial-interstadial variability (Dokken and Jansen, 1999). The NAAZ I and II have also been added to independently constrain the model (Kissel et al., 1999). High resolution dinocyst and foraminifera analysis (Fig 6.2) have been conducted by Eynaud et al. (2002), which shows good agreement with the $\delta^{18}O$ signal of the GISP 2 ice-core. However, between 30-48 ka, the correlation suggests a paradoxical response; when the Greenland $\delta^{18}O$ signal reflects warm conditions; the Norwegian Sea depicts cold SSTs with quasi-perennial sea-ice cover (Eynaud et al., 2002). This highlights the isolation of the Norwegian Sea and the potential to test oceanic responses in different regions of the North Atlantic, providing isochronous tephra horizons can be detected.

6.3 5.3.1 Sampling strategy: MD95-2010

The tephra content of the core sequence was investigated in a 4 m section between 450-850 cm (~23-41 ka b2k), bracketing the stratigraphic position and ages of tephra deposits found within MD04-2829CQ. The sampled section of the core is shown in Figure 6.2, plotted against magnetic susceptibility and dinocyst assemblages. Initially, the sequence was investigated at a 5 cm contiguous low-resolution.

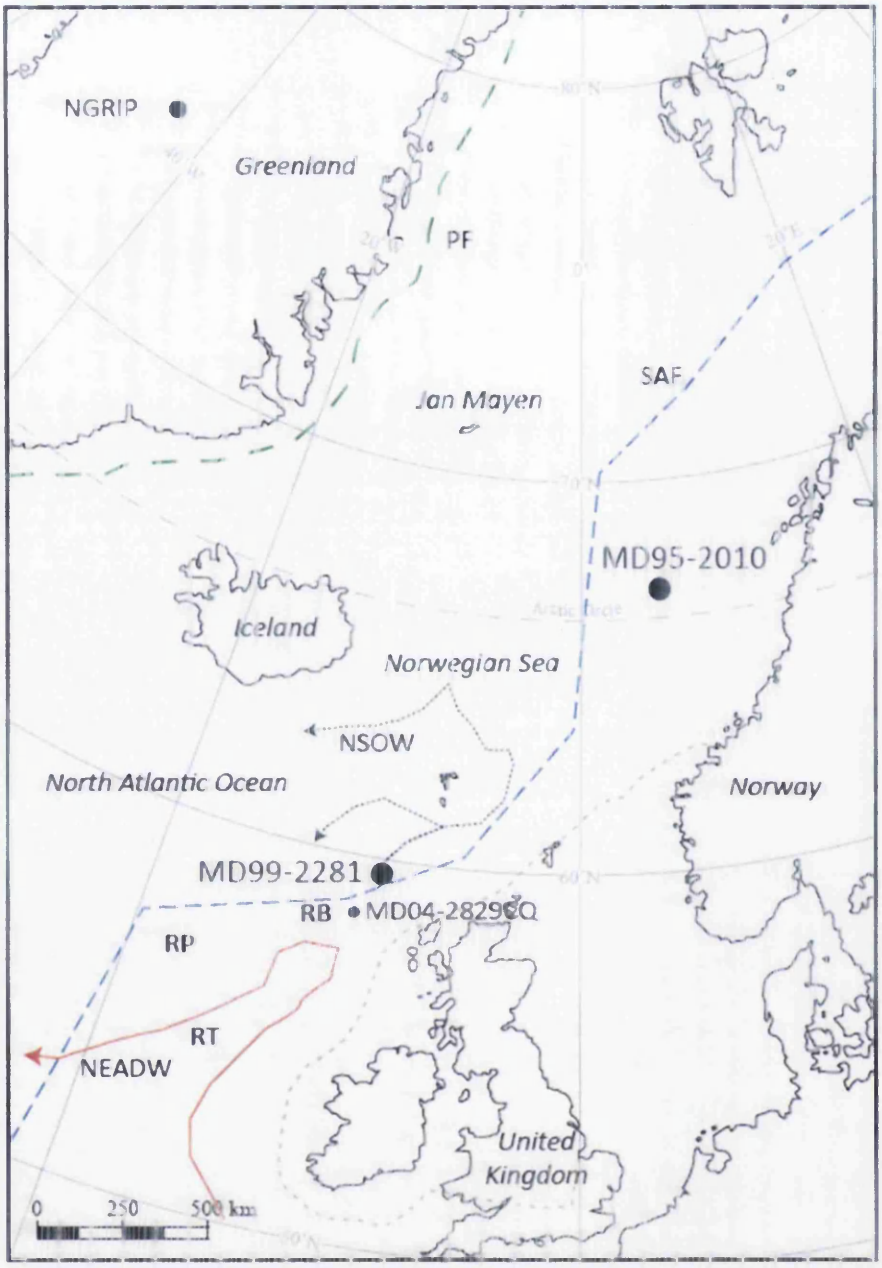

Figure 6.1 Location map of marine core MD95-2010 and MD99-2281 with the approximate pathways of present day deep water masses (Hall et al., 2011), major hydrographic fronts (Dickson et al., 1988; Zumaque et al., 2012) and maximum extents of the northeastern European ice-sheet during the LGM (Hall et al., 2011).

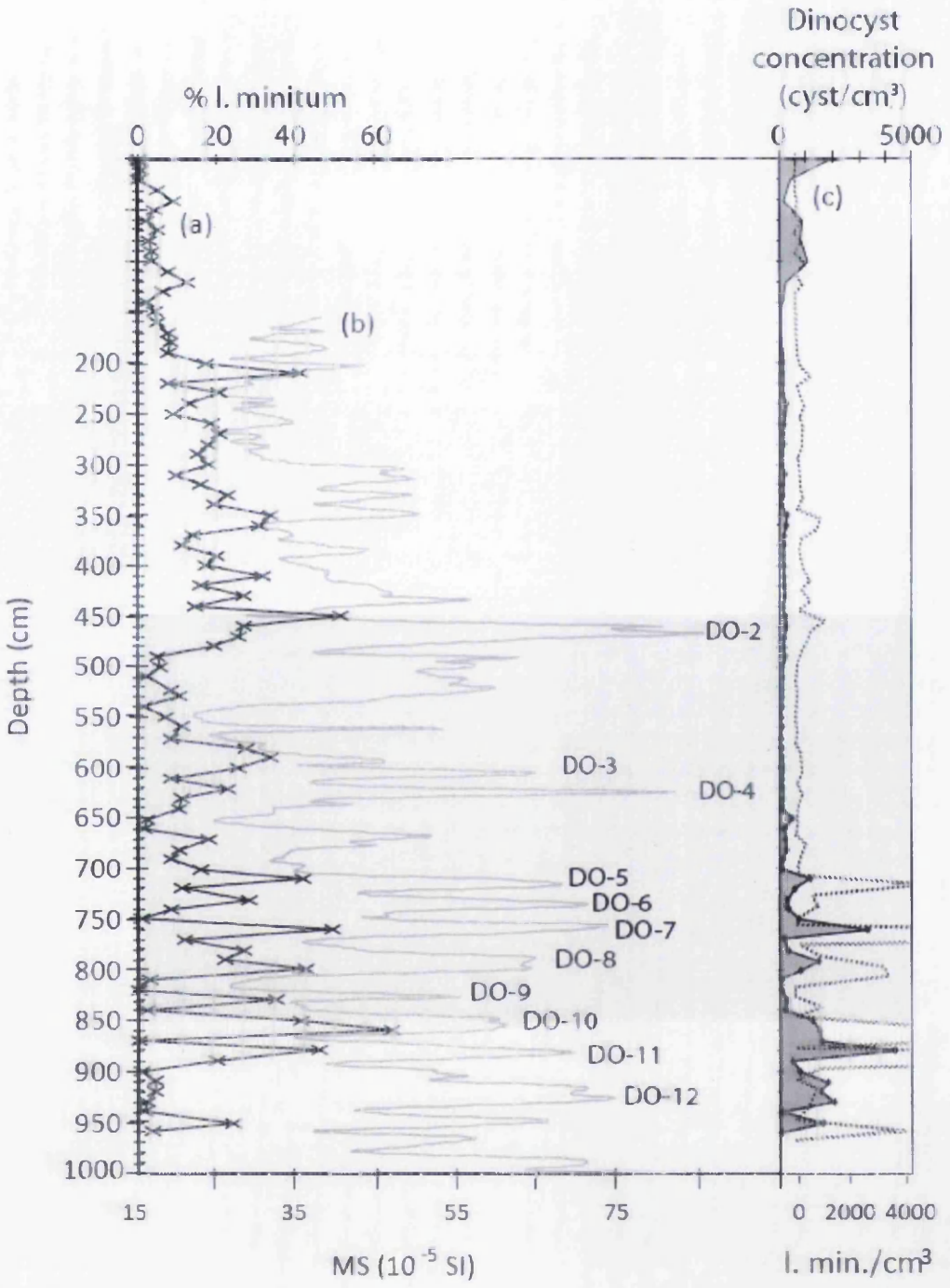

Figure 6.2 Variation of (a) l. minutum percentages with depth against (b) magnetic susceptibility and (c) total dinocyst concentrations after Eynaud et al. (2002). Concentrations of l. minutum are superimposed on the total dinocyst concentration graph. The grey highlighted area indicates the depths analysed for tephra concentration.

Two intervals with elevated shard counts were further analysed at a 1 cm high-resolution (Fig 6.3). Sediment from the 25-80 μm fraction was processed using the heavy liquid separation procedure outlined in section 3.3 and the >2.5 g/cm^3 fraction was magnetically separated to purify the basaltic material (see section 3.4).

6.4 Shard concentrations and tephrastratigraphy: MD95-2010

Low-resolution shard concentrations from different depths, densities and size fractions are shown in Figure 6.3 In total, 320 individual tephra slides, covering 4 m of core, were prepared and inspected for their tephra content. The predominant absence of tephra shards in all grain size and density fractions is notable in this record. An exceptionally low-level of brown shards was detected between 485-490 cm and 790-795 cm, consisting of two and four shards respectively in the 80-125 μm fraction (Fig 6.3b). As these were the only intervals containing shards, they were further investigated at 1 cm contiguous resolution between 483-493 cm and 788-797 cm. These intervals were selected to ensure full coverage of potential tephra deposits. Unfortunately, no shards were detected in high-resolution between 483-493 cm and have been omitted from further investigation. A low-level of shards (<15 per 0.5 gdw) were detected in high resolution between 787-797 cm in the >2.5 g/cm^3, 80-125 μm and >125 μm fractions. These samples were subsequently prepared for geochemical analysis. Within the 2.3-2.5 g/cm^3 fraction, there is a consistent background of ~1 shard per 0.5 gdw and no distinct peaks or sections of elevated colourless shard concentrations were detected across the whole studied interval (Fig 6.3f).

6.5 Cryptotephra deposits in MD95-2010: 788-798 cm

6.5.1 Shard concentration and descriptions

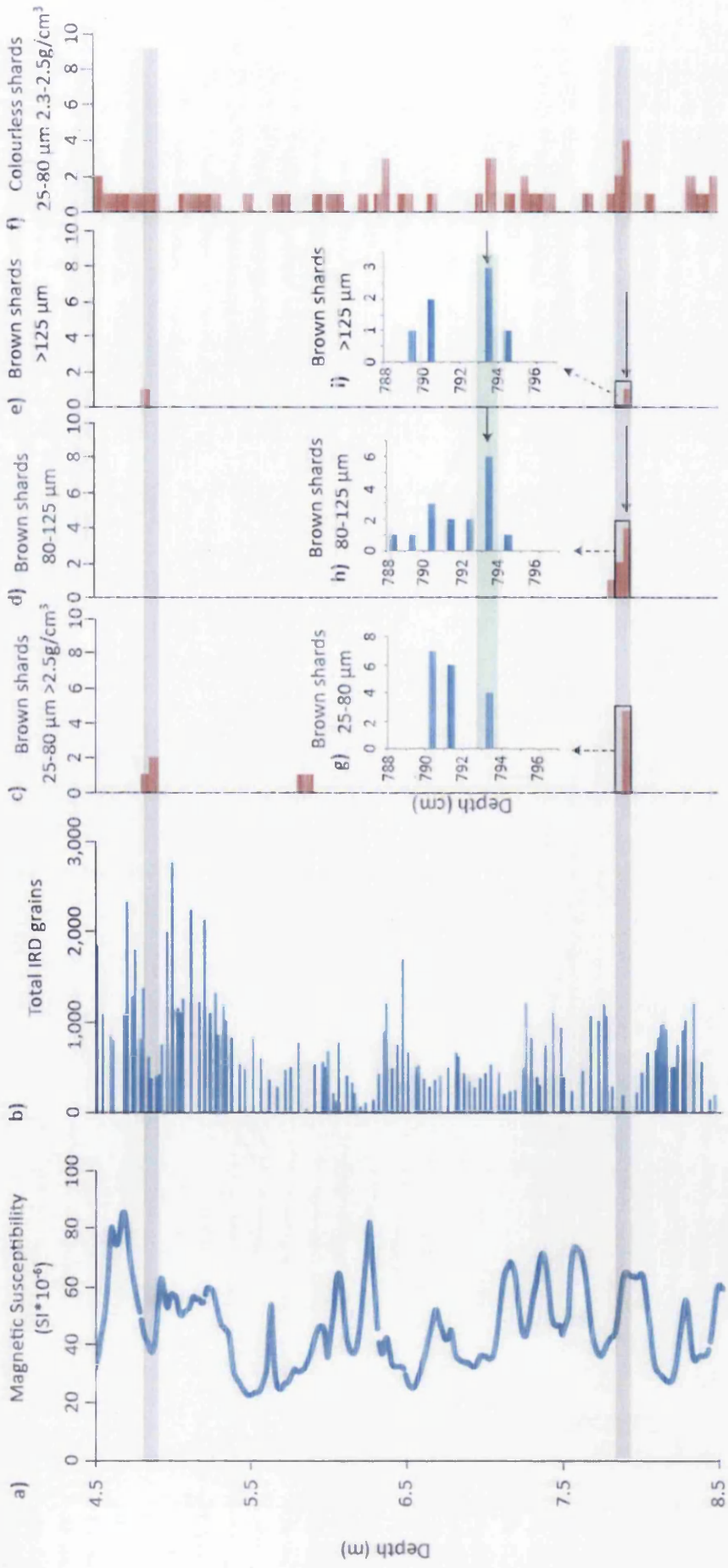

Figure 6.3 Low and high-resolution tephrostratigraphy for MD95-2010 between 450-850 cm. (a), (b) Magnetic susceptibility and IRD record derived by Dokken and Jansen (1999) (b), (c), (d), (e) Number of brown shards identified within the 25-80 µm, 80-125 µm and >125 µm fractions respectively. (d) Number of colourless shards within the 2.3-2.5 g/cm^3 density fraction. The grey line denotes the peaks in glass shard concentrations identified in low-resolution and the arrow represents the depth taken for geochemical analysis. (g),(h),(i) High-resolution brown shard counts between 788-797 cm.

This deposit forms a diffuse/patchy distribution between 788-797 cm. The concentration of shards is exceptionally low, with a peak of seven shards per 0.5 gdw in the 25-80 μm fraction between 790-791 cm (Fig 6.3c). A total of twelve tephra shards were detected in all grain sizes across this interval (Fig 6.3g,h,i). Six shards were identified between 793-794 cm in the 80-125 μm fraction and a total of fourteen tephra shards were detected across all grain sizes at this interval (Fig 6.3 g,h,i). This may represent the first input of tephra into the sequence and so shards from this depth were sampled for geochemical analysis. Shards exhibit a brown blocky morphology and show no signs of hydration. During preparation for geochemical analysis, shards were only detected in the 80-125 μm fraction and so only the coarse fraction has been geochemically characterised. This highlights the patchy distribution and lateral discontinuity of the tephra, which is more noticeable when dealing with shards in such low concentrations. As such, these shards cannot be considered of sufficient quantity to constitute an isochron.

The deposit straddles the peak warmth and falling limb of DO-8 according to the magnetic susceptibility record derived by Dokken and Jansen (1999) (Fig 6.3a). Total IRD concentrations are exceptionally low at this depth and suggest ice-rafting is unlikely to have assisted in deposition (Dokken and Jansen, 1999; Eynaud et al., 2002) (Fig 6.3b). The age of the 793-794 cm interval extracted for geochemical analysis equates to ~38.37 ka b2k according to the Dokken and Jansen (1999) age model. This interval falls within the later section of the FMAZ III and stratigraphically equivalent horizons present in the ice-core records.

6.5.2 Geochemistry and source identification

EPMA analyses from nine individual shards within the 80-125 μm fraction of 793-794 cm are classified as basaltic and fall within the tholeiitic series (Fig 6.4). Eight shards from the 80-125 μm fraction constitute a heterogeneous geochemical population. Geochemical characteristics of this deposit include SiO_2 concentrations of ~49.62-50.11 wt%, K_2O concentration of ~0.39 wt%, TiO_2 concentrations of ~2.36-3.04 wt%, CaO concentrations of ~10.37-11.52 wt% and MgO concentrations

between ~5.84-6.75 wt% (Table 6.1). The TiO_2 and K_2O concentrations imply an origin in the Grímsvötn system (Fig 6.5). One outlier shard with a TiO_2 contents of ~1.67 wt% and K_2O contents of ~0.23 wt% was also detected and excluded from further analysis.

6.5.3 Wider correlations and depositional processes

Glass shard analyses from 793-794 cm plot within the broad FMAZ III compositional envelope and potentially extend the known distribution of this ash zone to the Norwegian Seas (Wastegård et al., 2006) (Fig 6.6a,b). The V2 ash zone on the Reykjanes Ridge falls within a similar stratigraphic interval to the FMAZ III and has been compared to assess a potential correlation. Similarly to the FMAZ III in JM11-19PC, the shards share a common Grímsvötn component but the heterogeneity across all element oxides prevents a correlation from being established (Fig 6.6c,d). Figure 6.7 highlights how the wide geochemical range exhibited by 793-794 cm occupies a range of ice-core compositional envelopes deposited during this time-period. This suggests that the deposit in MD95-2010 is composed of a composite of shards sourced from a variety of closely spaced Grímsvötn eruptions.

MD95-2010 represents the most distal core to Iceland investigated within the thesis (~1300 km NE) and may explain the predominant absence of tephra. The only shards identified can be considered as a somewhat tenuous cryptotephra deposit with the majority of shards being >80 μm in size (Fig 6.3). Modeling studies have demonstrated ash clouds can transport cryptotephra particles <80 μm up to ~1000 km in 24 hours (Stevensson et al., 2015). This suggests that shards in the 25-80 μm should be the dominant grain-size component. In the absence of high IRD input during this interval (Fig 6.3b), the presence of coarse-grained shards may be a consequence of tephra delivery via sea-ice with a temporal lag (Austin et al., 2004).

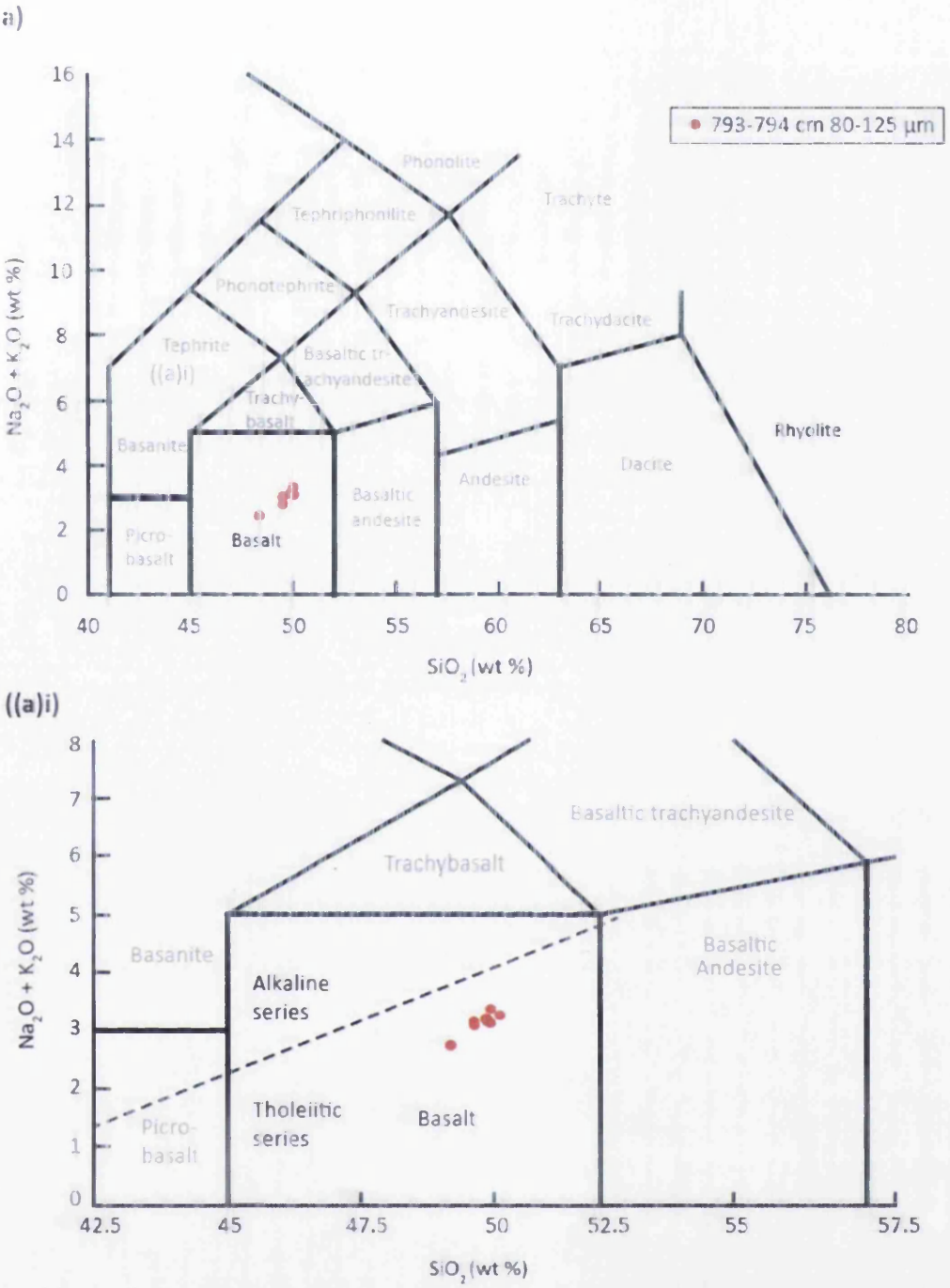

Figure 6.4 (a) Total alkalis vs silica plot for analyses from basaltic deposits found in MD95-2010. (b) Inset of TAS plot focusing on the basaltic analyses. Chemical classification is defined by Le Maître et al. (1989). The dashed line represents the subdivision into alkaline and tholeiitic rock series defined by MacDonald and Katsura (1964).

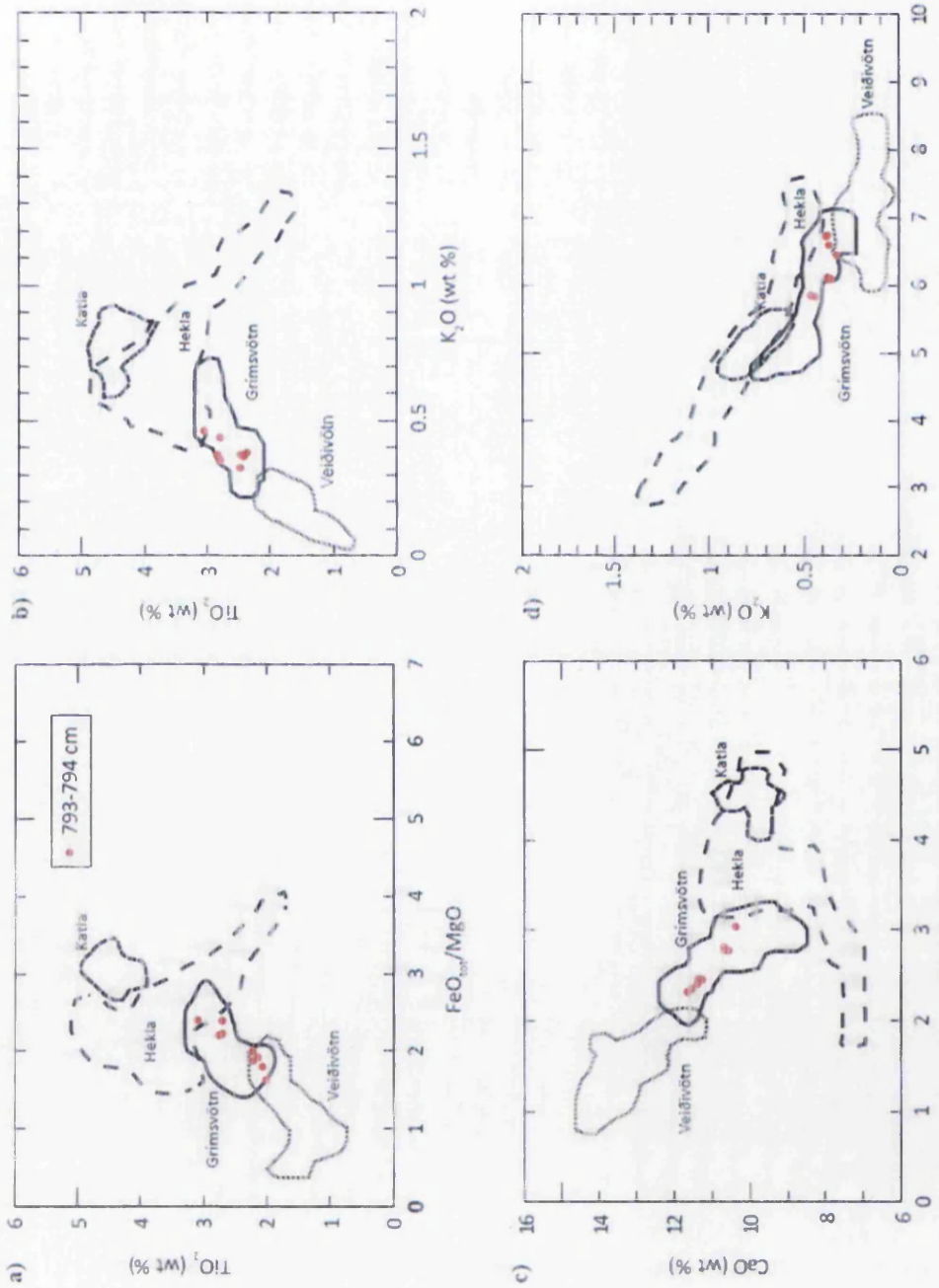

Figure 6.5 Glass shard analyses for MD95-2010 compared to geochemical envelopes for different source volcanoes based on individual whole rock analyses presented in Jakobsson (1979), Boygle (1994), Larsen et al. (2002), Oladóttir et al. (2008) and Jakobsson et al. (2008). Data have all been normalised to 100% total oxide concentrations.

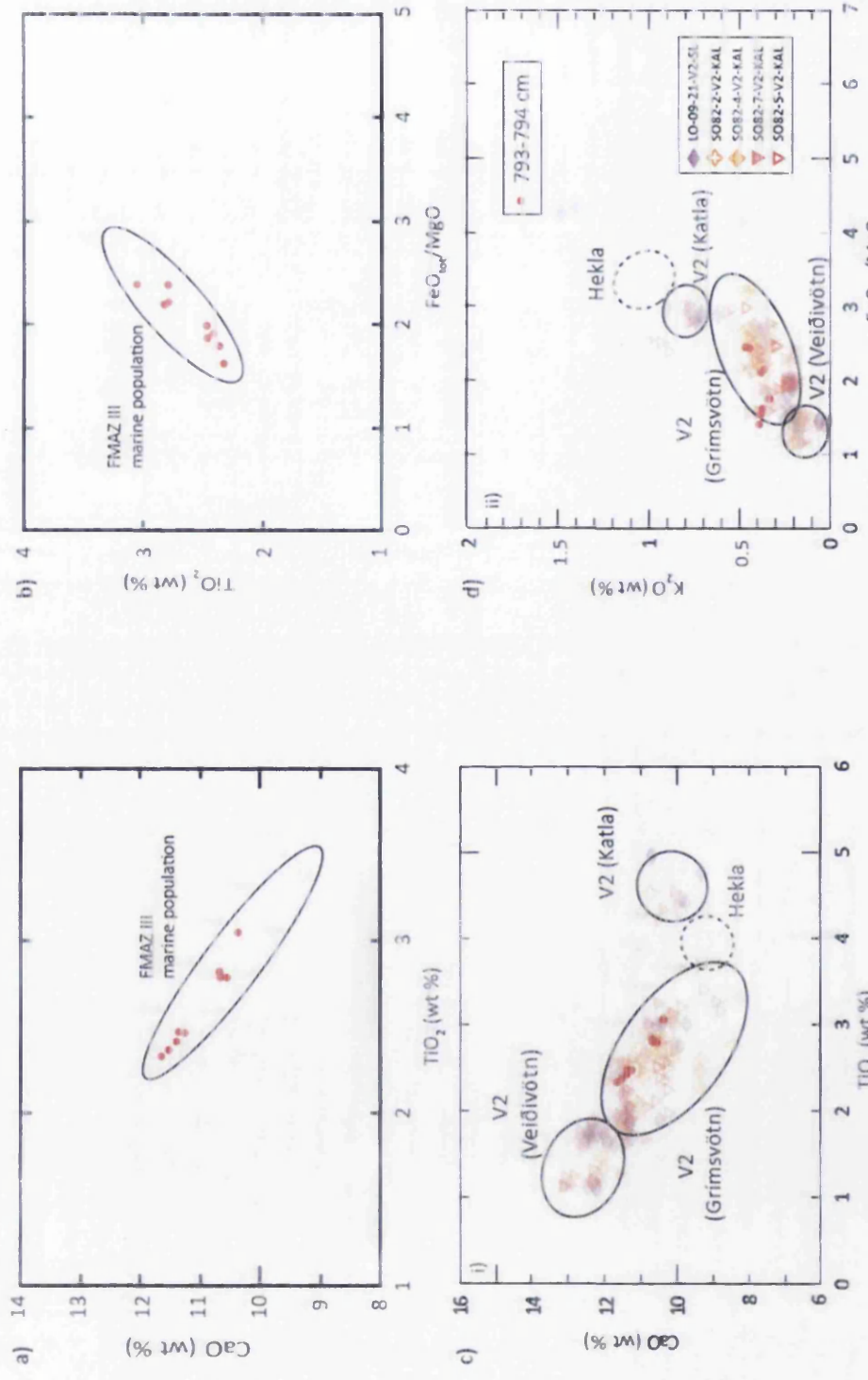

Figure 6.6 Major oxide results (wt %) for deposits identified in MD95-2010. (a), (b) Major oxides compared to FMAZ III deposits from marine cores in the Faroes region (Wastegård et al., 2006; this study). (c),(d) Major oxides compared to the V2 ash zone identified in four marine cores in the Reykjanes Ridge (Lackschewitz and Wallrabe-Adams, 1997). Three source envelopes encompassing the V2 data have been created for clarity. All data have been normalised to 100% total oxide concentration.

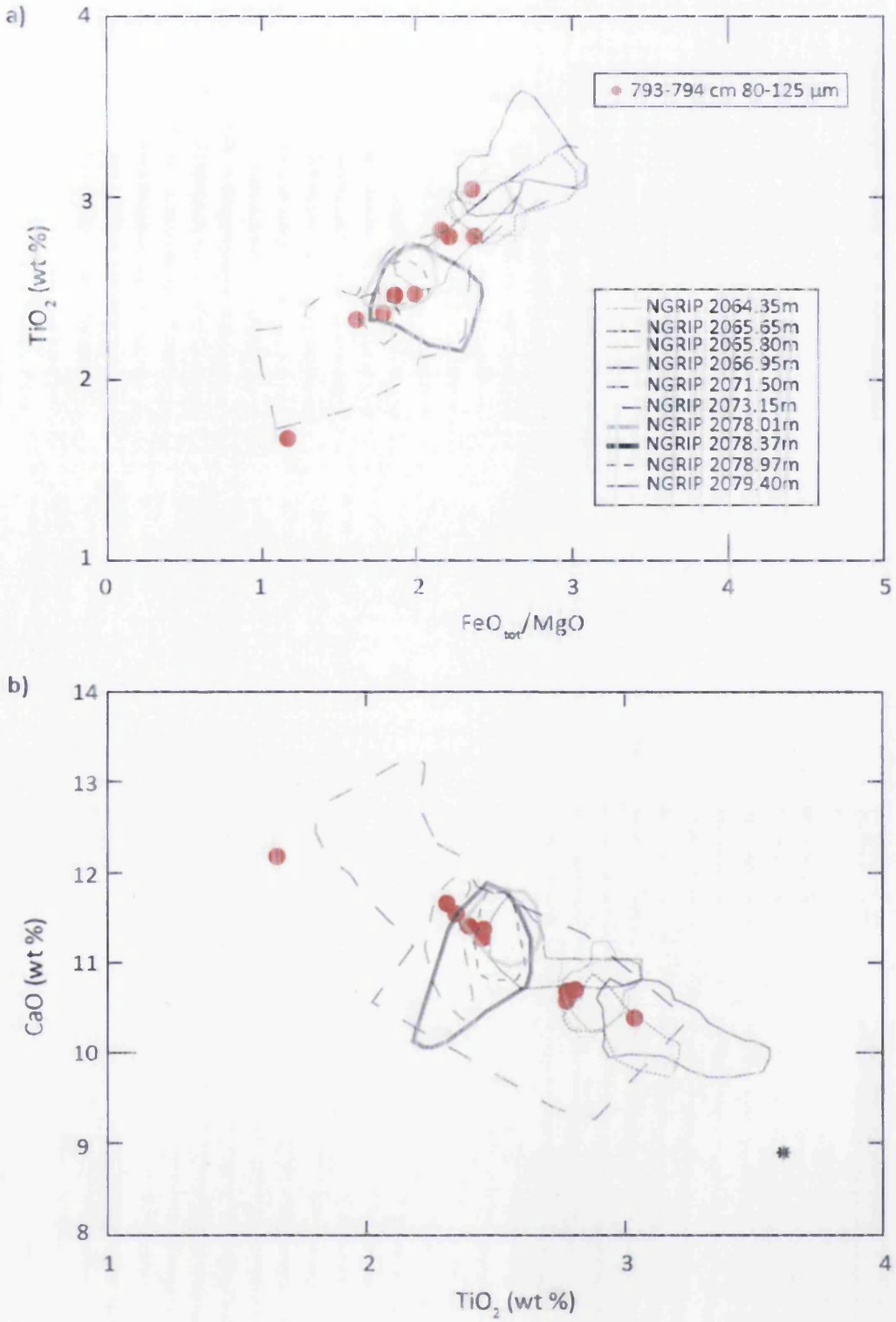

Figure 6.7 Major oxide results for each grain size from MD95-2010 between 793-794 cm. (a),(b) Glass shard analyses compared to geochemical compositional envelopes for cryptotephra deposits identified in NGRIP between 38,048 ± 721 b2k to 38,826 ± 740 b2k (Bourne et al., 2013). All data have been normalised to 100% total oxide concentration.

The presence of additional tephra shards in this deposit may be the consequence of bottom currents and/or additional influx from sea-ice.

Conversely, the persistence of sea-ice during MIS 3 (Eynaud et al., 2002) may have capped the site and prevented tephra from reaching the seabed. Although MD95-2010 is predominantly devoid of tephra, there may be tephra deposits present in other sections of the record, particularly during warmer interstadials and periods of reduced sea-ice cover. The exceptionally low concentrations and patchy distribution within 793-794 cm, in conjunction with geochemical heterogeneity suggests that the shards do not constitute a cryptotephra deposit that can act as an isochronous horizon. It is likely that several depositional mechanisms i.e. sea-ice and bottom currents brought isolated shards to the site, which may have been remobilised following deposition in other locations. Geochemical similarity and stratigraphical positioning within DO-8 suggests these shards are derived from the FMAZ III complex in the marine environment. As such, the shards may still tentatively be useful for low-resolution marine-marine correlations in DO-8, which permits a means to link other marine records to the Norwegian Sea.

6.6 Extending the search for the FMAZ III

Several cryptotephra deposits that are thought to form part of the FMAZ III complex have been identified between 38-39 ka b2k within MD95-2010, JM11-19PC and MD04-2829CQ. In JM11-19PC and MD95-2010, the FMAZ III deposit exhibits a heterogeneous geochemistry and contains a composite of numerous Grímsvötn derived eruptions spanning DO-8. This has affected their integrity and prevented precise correlations to the Greenland ice-cores. However, MD04-2829CQ contains homogeneous, stratigraphically constrained components of this ash zone and exhibits the potential to act as high-resolution isochronous markers (see section 5.6). In light of this information, MD99-2281 was selected to assess whether the tephras identified in MD04-2829CQ could be traced into this nearby core location. MD99-2281 exhibits an exceptionally high sedimentation rate (~1 cm/30 yrs), a well-resolved high-resolution D-O signal and the site is ideally situated ~150 km north of MD04-2829CQ (Zumaque et al., 2012). Given the frequency of eruptions during the

targeted interval, the high sedimentation rate should permit the stratigraphic separation of horizons constituting the FMAZ III complex. If the same isochronous horizons from MD04-2829CQ can be traced, this will allow a further assessment of their depositional integrity and corresponding proxy record. The following sections examine the targeted search for the FMAZ III in marine core MD99-2281.

6.7 MD99-2281; core location, oceanographic setting and proxy record

North Atlantic marine core MD99-2281 (60°21'N, 9°27'W) was retrieved at 1197 m water depth at the foot of the Faroe Bank located at the northern end of the Rockall Trough by the RV *Marion Dufresne* during the IMAGES V-MD99-114 cruise (Labeyrie et al., 1999) (Fig 6.1). The core is sensitive to hydrographic conditions and is presently located under the influence of the modified North Atlantic surface waters between the Arctic Front (AF) to the north and the sub-Arctic Front (SAF) to the south (Fig 6.1). The water mass distribution and deep circulation are primarily controlled by the bathymetric complexity of the Rockall Trough (Holliday et al., 2000). Similarly to MD04-2829CQ, previous palaeoceaongraphic investigations have demonstrated high sensitivity of the Faroe/Rockall area to millennial-scale climate variability and influence of the BIIS (Rasmussen et al, 1996; Eynaud et al., 2002; Hall et al., 2011).

The core sequence consists of 29 m of hemipelagic silty clays (Boulay, 2000) and spans MIS 2 and 3. The chronostratigraphic framework of the core has been derived from nine AMS ^{14}C dates measured on planktonic foraminifera from the top ~11 m. Four additional ^{14}C dates were obtained between ~12-19 m and calibrated using the 'glacial polynomial' after Bard (1998). The magnetic susceptibility record from MD99-2281 was then correlated to the GICC05 $\delta^{18}O$ record, an approach comparable to an event-based stratigraphy (Austin and Hibbert, 2012).

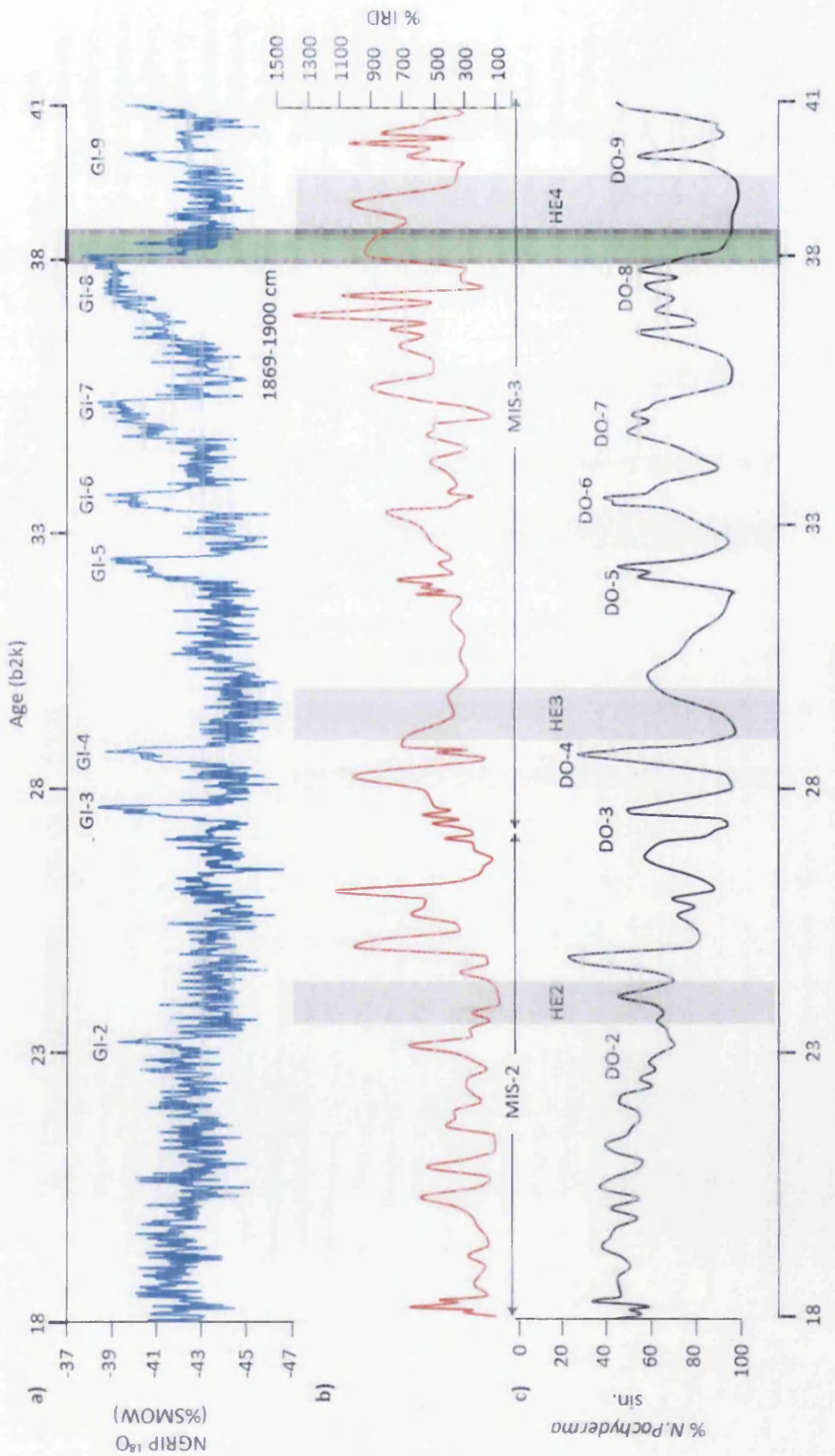

Figure 6.8 Targeted sampling interval for MD99-2281. (a) NGRIP ^{18}O record compared to the (b) MD99-2281 IRD record and (c) % *N.pachyderma* sin. in MD99-2281. Both proxies in MD99-2281 have been tuned to the Zumaque et al. (2012) age model. Lighter grey bars represent Greenland stadials. The green bar highlights the position of fourteen tephra horizons discovered by Bourne et al. (2015) during the time period 38-39 ka b2k. This represents the sampling interval to locate these tephras.

As a result, eighteen stratigraphic control points have been added to the AMS ^{14}C dates to create an age-depth model on the basis of linear interpolation between tie-points (Fig 6.8, 6.9). This has been independently constrained with the addition of the Laschamp excursion at ~41 ka b2k (Zumaque et al., 2012). Isotopic analysis of biogenic proxies, i.e. foraminfera and dioncyst assemblages at 10 cm contiguous intervals provide a high resolution reconstruction of coherent and sensitive oceanic response to MIS 3 climatic variability (Labeyrie et al., 2005; Zumaque et al., 2012) (Fig 6.8).

6.8 Sampling strategy: MD99-2281

In order to target depth intervals that are most likely to contain a range of FMAZ III deposits, an age-depth model and associated sedimentation rates were constructed after Zumaque et al. (2012) (Fig 6.9). Specifically, sediment between 1869-1900 cm equates to 38,079-38,843 b2k (Zumaque et al., 2012) and stratigraphically bracket deposits detected in MD04-2829CQ. These depths were analysed for their tephra concentration. The tephra content of this interval was sampled at a 1 cm contiguous high-resolution across three separate grain-sizes (25-80 μm, 80-125 μm, >125 μm). Material from the 25-80 μm fraction was processed using the heavy liquid separation procedure outlined in section 3.3 and the >2.5 g/cm^3 fraction was magnetically separated to purify the basaltic material (see section 3.4). Preliminary shard concentrations were quantified as containing <1000 shards and as such, spiking with Lycopodium spores was not deemed necessary.

6.8.1 Shard concentrations and tephrastratigraphy of MD99-2281

Shard concentrations from different depths, densities and size fractions are shown in Figure 6.10. Generally, there is a high concentration of brown and colourless shards within each grain-size fraction and they exhibit a complex diffuse distribution throughout the investigated section.

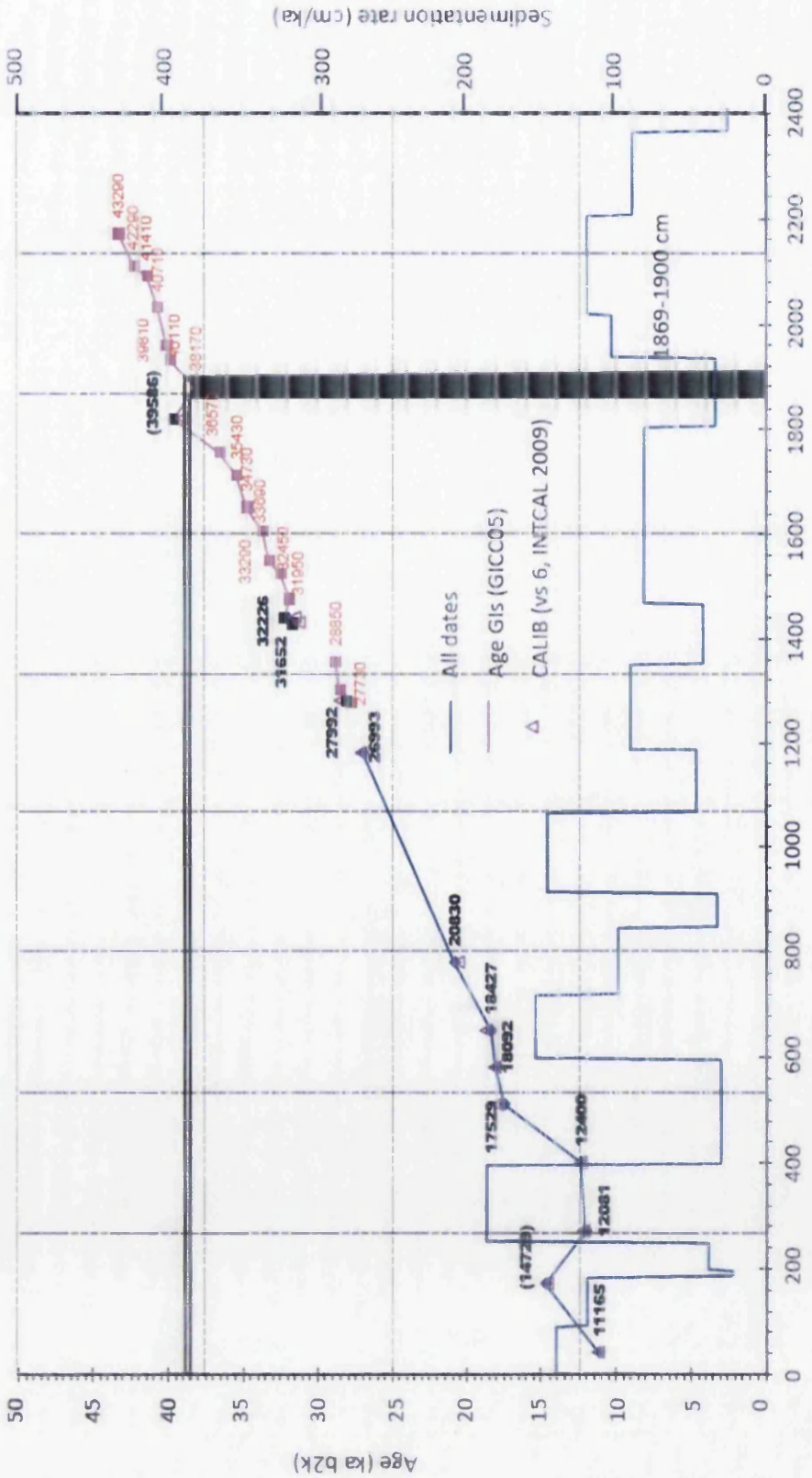

Figure 6.9 MD99-2281 age-depth model and sedimentation rate after Zumaque et al. (2012). Nine AMS ^{14}C dates have been derived for the top 11 m of the core. Eighteen additional stratigraphic tie-points are included. These are derived from linking magnetic concentration increases to the beginning of the GI warming and decrease to GS cooling. These have been correlated to chronostratigraphic ages from the GICC05 record. The age model has been constructed on the basis of linear interpolation between tie-points (Zumaque et al., 2012). The black column denotes the core depths which cover the period 38-39 ka b2k according to the age model.

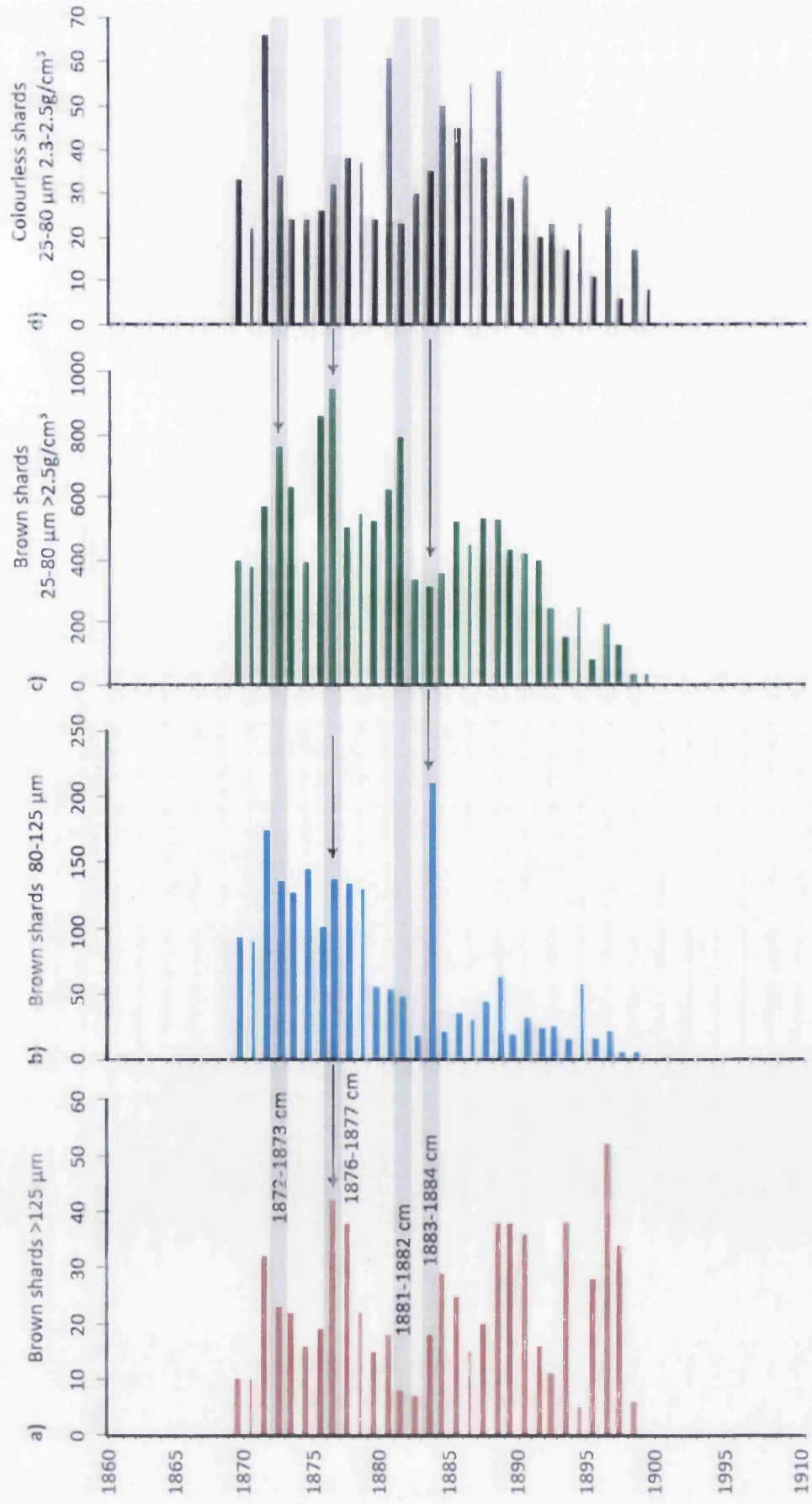

Figure 6.10 High resolution tephrostratigraphy for MD99-2281 between 1869-1900 cm. (a), (b), (c) Number of brown shards identified within the >125 µm, 80-125 µm and 25-80 µm fractions respectively. (d) Number of colourless shards within the 2.3-2.5 g/cm^3 density fraction. The grey lines denote the peaks in glass shard concentrations and the arrows represent depths taken for geochemical analysis.

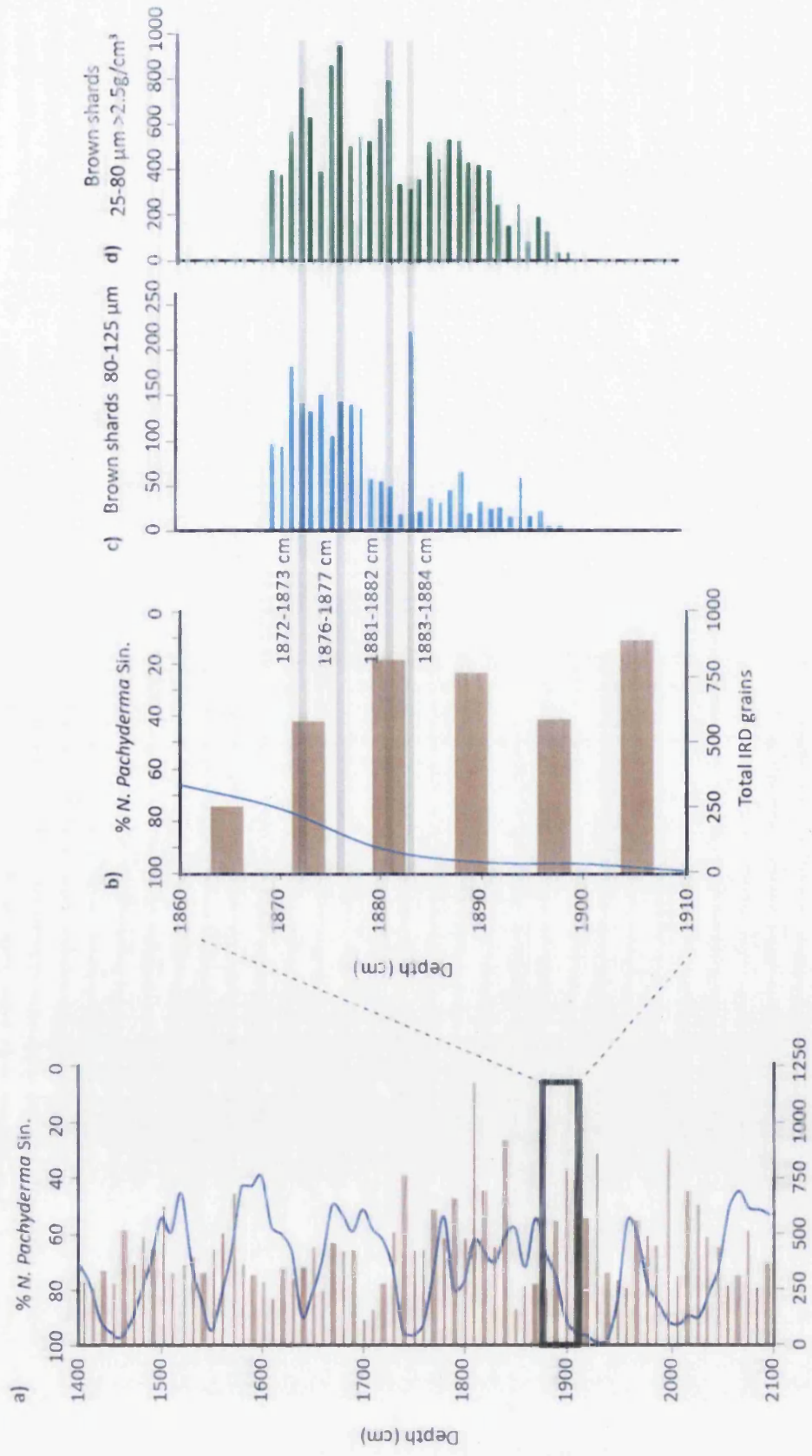

Figure 6.11 High resolution tephrostratigraphy for MD99-2281 between 1869-1900 cm. (a) % *N. pachyderma* sin. and IRD record from MD99-2281 between 1.4 - 2.1 m. (b) High resolution % *N. pachyderma* sin. and IRD record between 1.86 - 1.91 m. (c), (d) Number of brown shards identified within the 80-125 µm and 25-80 µm fractions respectively. The grey lines denote the peaks in glass shard concentrations and horizons geochemically analysed.

There are numerous indistinct peaks exhibited by each size fraction and these are not commonly mirrored by each equivalent grain-size. There are three main peaks in brown shard concentration in the 25-80 μm fraction (1872-1873 cm, 1876-1877 cm, 1881-1882 cm) but a high background of shards dilute the relative magnitude of the peaks (Fig 6.10c). Shards from each of the three main peaks were extracted for geochemical analysis and their stratigraphic position is illustrated on Figure 6.10. The most significant peak, relative to background concentrations, is exhibited in the 80-125 μm fraction at 1883-1884 cm, which has additionally been selected for geochemical analysis. Shards within each peak exhibit a light brown/yellowish colour and exhibit a strongly hydrated cuspate morphology

There is a similarly high background of colourless shards in the 2.3-2.5 g/cm^3 fraction. The highest concentration of colourless shards (sixty-five per 0.5 gdw) occurs at 1872-1873 cm. The addition of quantitative colourless shard counts highlights the consistent input of a range of cryptotephra shards throughout the investigated sequence. The deposit immediately proceeds the cooling of DO-9 and falls on the rising limb of DO-8 according to decreasing *N. Pachyderma* sin. percentages (Zumaque et al., 2012) (Fig 6.11). There is a moderate influx of IRD around the sampling interval, although the proxy resolution is lower than that of the tephra record (Fig 6.11).

6.9 Basaltic cryptotephra deposits within MD99-2281 1869-1890 cm

6.9.1 Geochemistry and source identification

6.9.1.1 1872-1873 cm

EPMA analyses of twenty-five shards within this horizon are classified as basaltic and twenty fall within the tholeiitic series on a TAS plot (Fig 6.12).

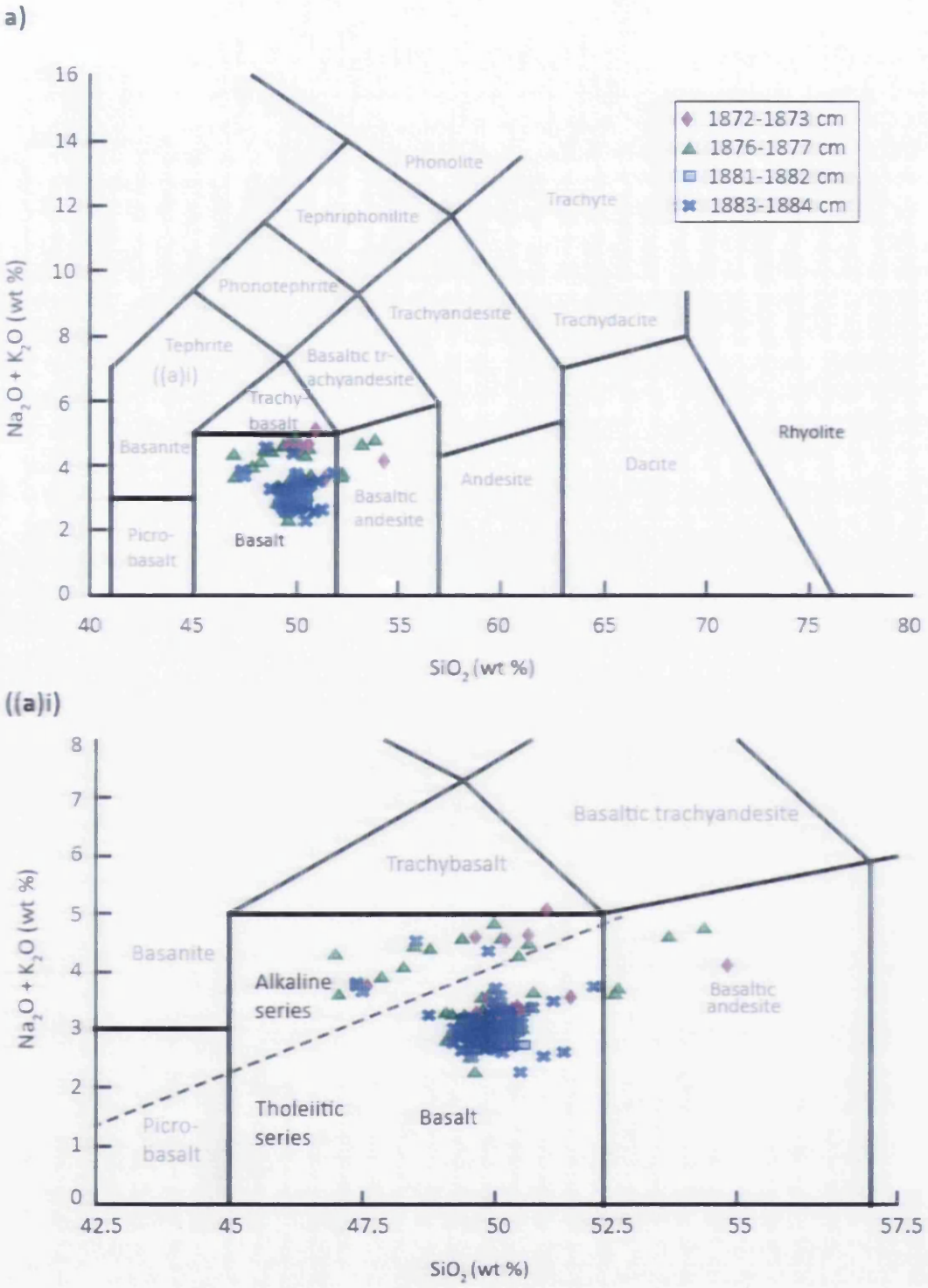

Figure 6.12 (a) Total alkalis vs silica plot for analyses from basaltic deposits found in MD99-2281. (b) Inset of TAS plot focusing on the basaltic analyses. Chemical classification is defined by Le Maître et al. (1989). The dashed line represents the subdivision into alkaline and tholeiitic rock series defined by MacDonald and Katsura (1964).

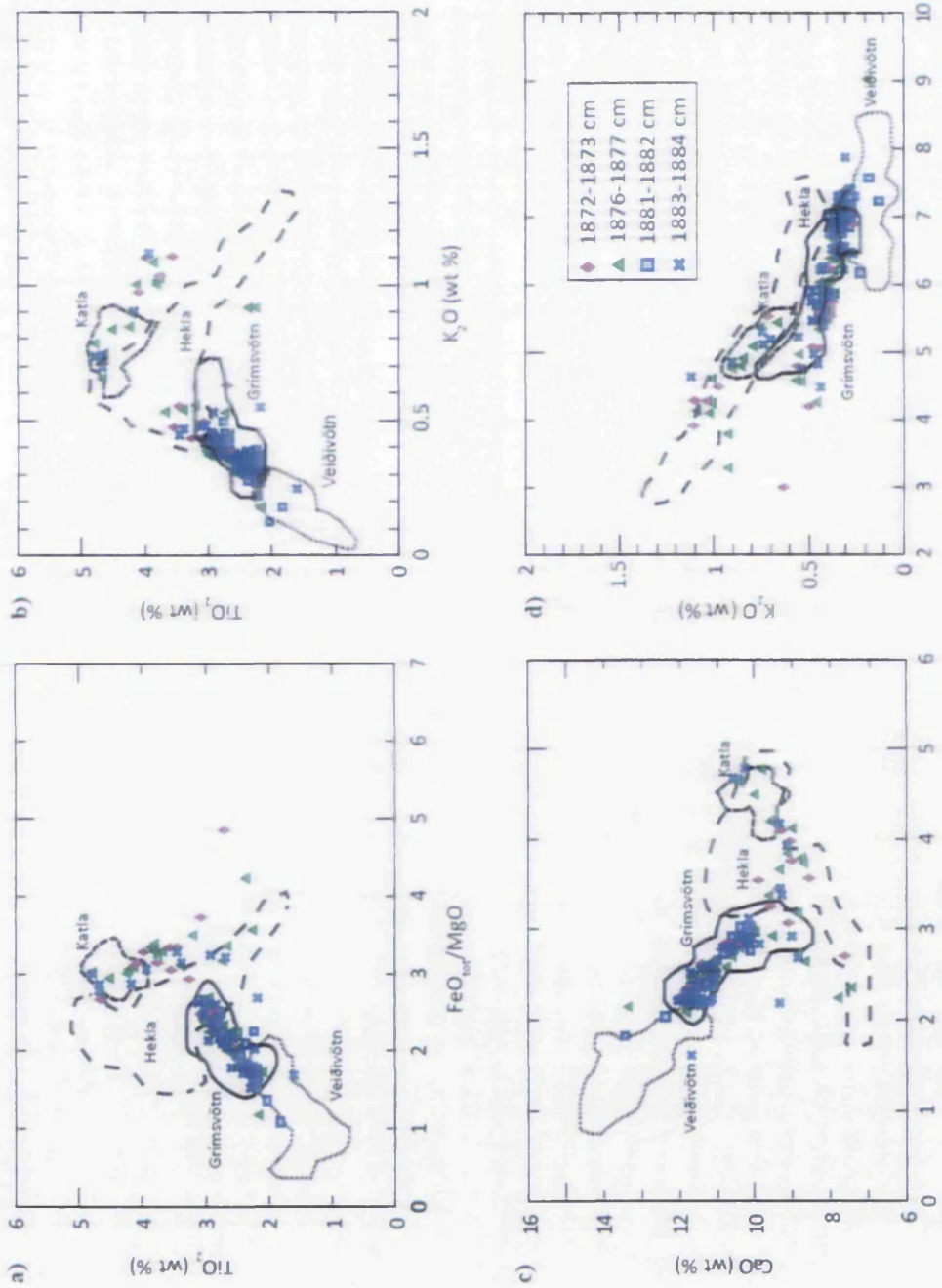

Figure 6.13 Glass shard analyses for MD99-2281 compared to geochemical envelopes for different source volcanoes based on individual whole rock analyses presented in Jakobsson (1979), Boygle (1994), Larsen et al. (2002), Óladóttir et al. (2008) and Jakobsson et al. (2008). Data have all been normalised to 100% total oxide concentrations.

The deposit exhibits a heterogeneous geochemical distribution. Five shards fall within the alkaline series of the TAS plot and highlight the heterogeneity of the deposit (Fig 6.12). Geochemical characteristics of the tholeiitic population include K_2O concentrations between ~0.26-0.63 wt%, TiO_2 concentrations between ~2.19-3.55 wt% and CaO and MgO concentrations of ~7.61-12.00 wt% and ~5.46 wt% respectively (Table 6.1). The latter two oxides suggest the tholeiitic basalts are sourced from the Grímsvötn system (Jakobbson et al., 2008) and this can be observed on a number of geochemical biplots (Fig 6.13). However, there is a significant range of data within this population. Four outliers exhibit TiO_2 concentrations >3.8 wt% and K_2O >0.7 wt%, indicating a potential affinity to the Hekla and Katla systems (Fig 6.13).

6.9.1.2 1876-1877 cm

EPMA analyses of fifty-six shards within this horizon are classified as basaltic and predominantly fall within the tholeiitic series on a TAS plot (Fig 6.12). The deposit exhibits a heterogeneous distribution. Forty-four shards fall within the tholeiitic series of the TAS plot and form the main population and twelve shards fall within the alkaline series (Fig 6.12). Geochemical characteristics of the tholeiitic population include K_2O concentrations between ~0.18-0.56 wt%. TiO_2 concentrations between ~2.09-3.38 wt% and CaO and MgO concentrations of ~8.63-13.34 wt% and ~6.35 wt% respectively (Table 6.1). CaO vs TiO_2 and K_2O vs TiO_2 biplots display a close affinity to the Grímsvötn system (Jakobsson et al., 2008) (Fig 6.13). Geochemical biplots highlight the heterogeneity and wide range of values for these oxides (Fig 6.13).

6.9.1.3 1881-1882 cm

EPMA analysis of twenty-five shards within this horizon are classified as basaltic and fall within the tholeiitic series on the TAS plot (Fig 6.12). The deposit exhibits a heterogeneous population. In contrast to 1872-1873 cm and 1876-1877 cm, no outlying shards sourced from other volcanic systems were detected in this deposit

(Fig 6.13). Geochemical characteristics include K_2O concentrations between ~0.16-0.32 wt%, TiO_2 concentrations between ~1.83-3.03 wt% and CaO and MgO concentrations of ~10.11-13.47 wt% and ~6.48 wt% respectively (Table 6.1). The latter two oxides suggest an affinity to the Grímsvötn system (Jakobsson et al., 2008) and this can be observed on numerous geochemical biplots (Fig 6.13).

6.9.1.4 1883-1884 cm

EPMA analyses of seventy shards within this horizon are classified as basaltic and sixty-five fall within the tholeiitic series on a TAS plot (Fig 6.12). A greater number of shards have been analysed for geochemistry as it appeared that during initial EPMA analysis, a distinctive geochemical composition may be present. However, it later became apparent that the deposit is heterogeneous. Sixty-five tholeiitic shards exhibit geochemical characteristics which include SiO_2 concentrations of ~48.71-51.81 wt%, TiO_2 concentrations of ~2.44 wt%, CaO concentrations of ~8.86-12.05 wt% and K_2O concentrations between ~0.25-0.55 wt% (Table 6.1). Despite the wide geochemical spread, these geochemical characteristics also share a common source similarity to Grímsvötn, as observed on a number of geochemical biplots (Fig 6.13). Five shards exhibit a TiO_2 concentration >4 wt% and are consistent with material sourced from Katla (Fig 6.13c,d).

6.9.2 Wider correlations and depositional processes

Glass shard analyses from tholeiitic shards in MD99-2281 indicate a Grímsvötn source and exhibit strong affinities to the FMAZ III deposit from other marine archives, as demonstrated on a range of geochemical biplots (Wastegård et al., 2006) (Fig 6.14a,b). The V2 ash zone on the Reykjanes Ridge falls within a similar stratigraphic interval to the FMAZ III and has been compared to assess a potential correlation (Fig 6.14c,d). The shards share a common Grímsvötn component but the heterogeneity across all element oxides prevents a correlation from being established.

Table 6.1 Mean and 1σ major element results of basaltic glass shards extracted from deposits found within MD99-2281 and MD95-2010. Total oxide values are raw values prior to normalisation. All major elements are expressed as percentage weight. Total iron expressed as FeO. n = number of shards analysed.

Tephra Layer	Composition	Source	Grain size (μm)	n	SiO_2	TiO_2	Al_2O3	FeO	MnO	MgO	CaO	Na_2O	K_2O	P_2O_5	Total
MD99-2281															
1872-1873 cm	Basaltic	Grímsvötn	25-80	20	50.30	2.80	13.35	13.62	0.22	5.69	10.52	2.79	0.41	0.30	98.88
					1.00	*0.37*	*0.59*	*1.17*	*0.03*	*0.96*	*1.05*	*0.23*	*0.09*	*0.10*	*0.79*
MD99-2281															
1876-1877 cm	Basaltic	Grímsvötn	25-80	44	49.89	2.57	13.78	12.91	0.22	6.35	10.99	2.66	0.37	0.25	98.78
					0.65	*0.33*	*0.54*	*1.19*	*0.02*	*0.88*	*0.97*	*0.23*	*0.07*	*0.06*	*0.55*
MD99-2281															
1881-1882 cm	Basaltic	Grímsvötn	25-80	20	49.95	2.46	13.91	12.53	0.21	6.48	11.26	2.62	0.35	0.23	98.95
					0.32	*0.34*	*0.58*	*1.36*	*0.02*	*0.65*	*0.79*	*0.14*	*0.09*	*0.05*	*0.53*
MD99-2281			25-80,												
1883-1884 cm	Basaltic	Grímsvötn	80-125	65	49.72	2.44	13.86	12.60	0.21	6.59	11.14	2.63	0.35	0.23	98.67
					0.51	*0.33*	*0.63*	*1.04*	*0.02*	*0.74*	*0.78*	*0.24*	*0.07*	*0.05*	*0.89*
MD95-2010															
793-794 cm	Basaltic	Grímsvötn	80-125	8	49.82	2.64	13.58	13.06	0.21	6.31	10.97	2.76	0.39	0.26	98.55
					0.20	*0.25*	*0.36*	*0.66*	*0.01*	*0.37*	*0.45*	*0.07*	*0.04*	*0.03*	*0.76*

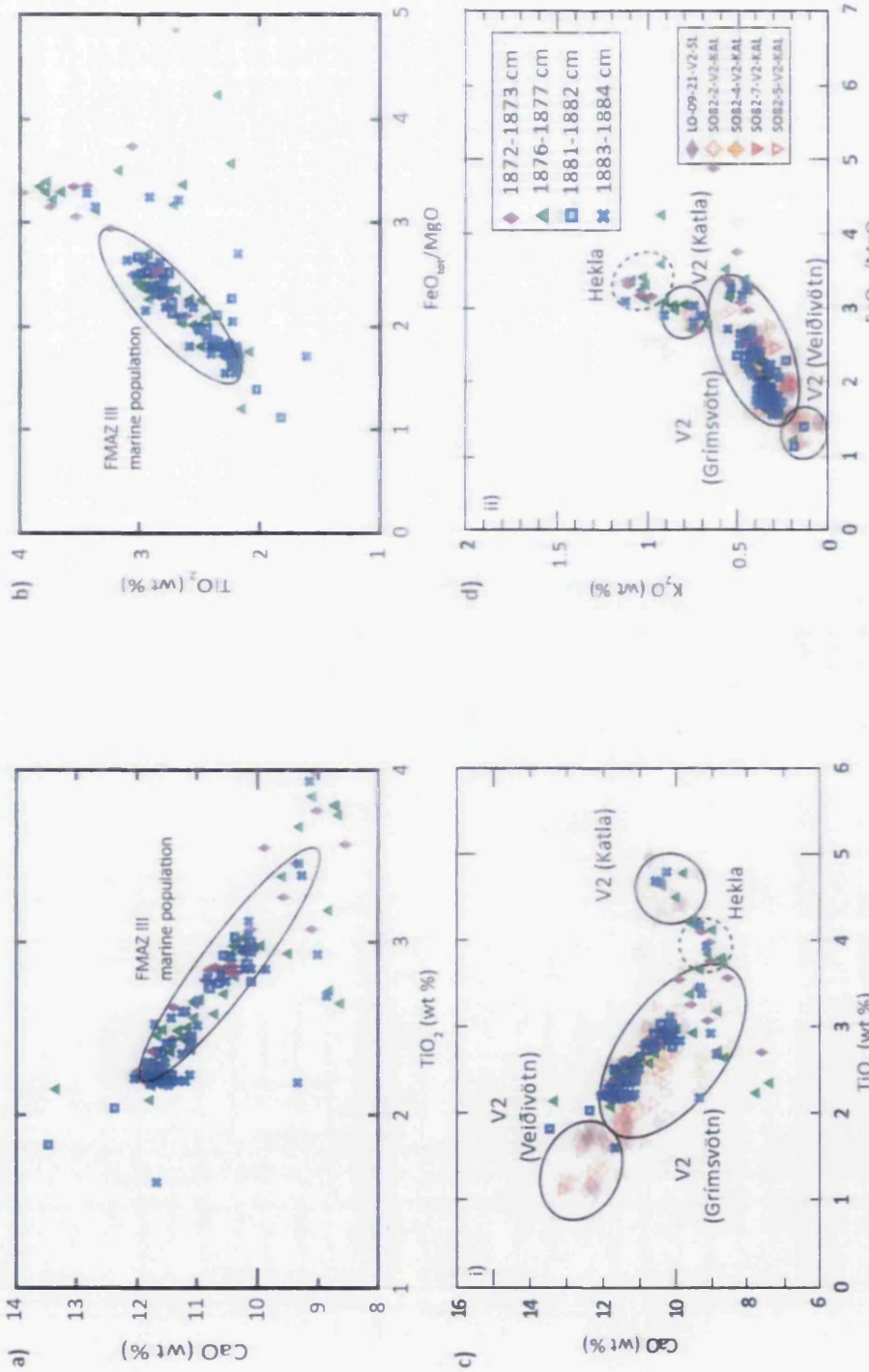

Figure 6.14 Major oxide results (wt%) for deposits identified in MD99-2281. (a), (b) Major oxides compared to FMAZ III deposits from marine cores in the Faroes region (Wastegård et al., 2006; this study). (c),(d) Major oxides compared to the V2 ash zone identified in four marine cores in the Reykjanes Ridge (Lackschewitz and Wallrabe-Adams, 1997). Three source envelopes encompassing the V2 data have been created for clarity. All data have been normalised to 100% total oxide concentration.

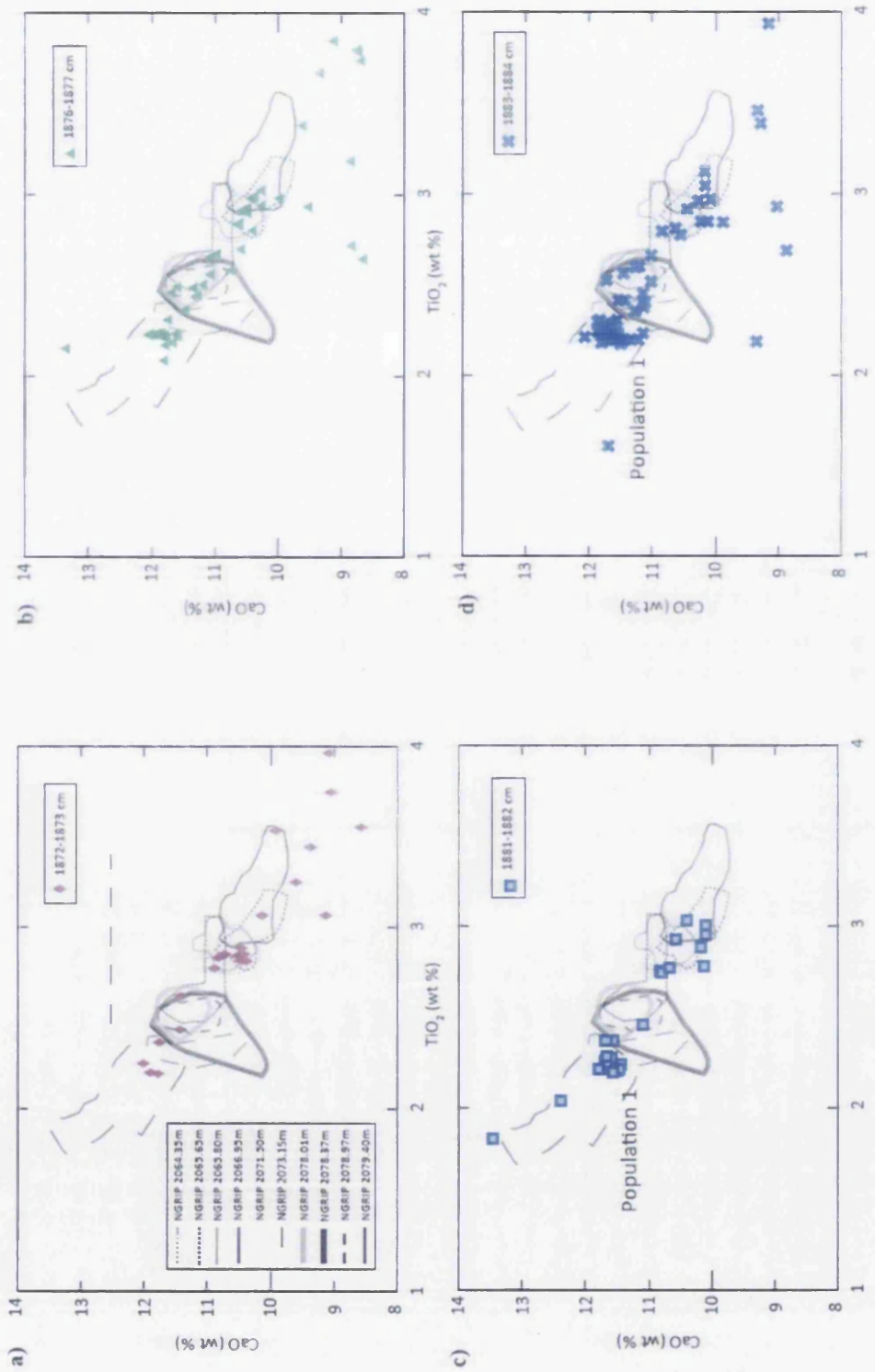

Figure 6.15 Major oxide results for each grain size from MD99-2281 between 1872-1884 cm. (a),(b),(c),(d) Glass shard analyses compared to geochemical compositional envelopes for cryptotephra deposits identified in NGRIP between 38,048 ± 721 b2k to 38,826 ± 740 b2k (Bourne et al., 2013). All data have been normalised to 100% total oxide concentration.

In order to test for potential correlations to stratigraphically equivalent horizons in the Greenland ice-cores, geochemical composition envelopes for each ice-core horizon were constructed and shards from individual depth intervals in MD99-2281 were plotted (Fig 6.15). Biplots of TiO_2 vs CaO were considered to provide the best way of geochemically discriminating between closely timed eruptions (Bourne et al., 2013). Generally, the wide geochemical distributions of shards in MD99-2281 straddle all of the ice-core envelopes (Fig 6.15). Shards that fall into individual compositional envelopes were counted to assess the relative proportion of individual NGRIP horizons that may contribute towards shards that occupy each depth interval in MD99-2281 (Fig 6.16). This method was employed to detect whether there were different inputs over various depths and to assess the potential contribution of stratigraphically equivalent NGRIP horizons with similar geochemical compositions. This may be useful for assessing whether shards from each depth interval were derived from the same volcanic event. This is a qualitative process and some shards fall into multiple compositional envelopes due to the overlapping geochemistry exhibited by some ice-core horizons. Similarity coefficients were not utilised in this instance due to the geochemical heterogeneity at each depth between 1869-1890 cm in MD99-2281. Similarity coefficients may polarise averages and prevent subtle geochemical differences exhibited by stratigraphically equivalent NGRIP horizons from being robustly compared.

Generally, the proportions of shards that exhibit similar geochemistries to stratigraphically equivalent NGRIP horizons are very similar across the four depth intervals (Fig 6.16). The majority of shards (~50%) exhibit a similar geochemistry to NGRIP 2071.50 m in 1881-1882 cm and 1883-1884 cm. There is an increase in the percentage of shards that exhibit a similar geochemistry to NGRIP 2064.35 m and NGRIP 2065.80 m at 1872-1873 cm and may reflect influx from different eruptions compared to lower depths. Generally, there is a similar input from multiple volcanic events with strong similarities to horizons in NGRIP within individual depth intervals. This suggests the frequency of eruptions has contributed to the high concentration of Grímsvötn sourced shards.

Figure 6.16 The relative abundances of shards in MD99-2281 that may be derived from Grímsvötn sourced horizons detected within NGRIP between 38,048 ± 721 b2k to 38,826 ± 740 b2k (Bourne et al., 2013). Uncorrelated refers to shards that do not fall within an ice-core compositional envelope and/or sourced from a different volcanic center. n is greater than the number of shards geochemically characterised as some shards fall into multiple geochemical fields.

This may have been perpetuated by elevated bottom-currents initiated during a period of bottom-water formation during DO-8 (Ezat et al., 2014). Co-variance with moderate IRD influx indicates that an ice-rafting component may have additionally contributed towards tephra delivery (Fig 6.11). Despite the high sedimentation rate, there is no clear stratigraphic separation of cryptotephra deposits observed in nearby core MD04-2829CQ. Furthermore, despite similar major element geochemistries, it is unclear whether the same suite of eruptions recorded in the FMAZ III in MD99-2281 are the same as those preserved in the Greenland ice-cores.

6.10 Conclusions

- An intensive tephrostratigraphic investigation of MD95-2010 proved unfruitful and is predominantly devoid of tephra. However, an area of isolated shards was detected between 787-797 cm. The geochemical heterogeneity and dominance of coarse-grained shards suggests secondary input. The stratigraphic position suggests that this tephra may be related to the FMAZ III but low concentrations raise important questions regarding the definition of cryptotephra deposits and isochrons.

- The presence of isolated shards that may be derived from the FMAZ III complex in MD95-2010 tentatively extends the known distribution of this ash zone in the North Atlantic to the Norwegian Seas. This may permit a means to link other marine records containing the FMAZ III complex and piece together oceanic changes that occur during DO-8 to other records in the North Atlantic.

- MD99-2281 exhibits a complex and diffuse shard concentration profile, characterised by elevated shard concentrations at different depth intervals. Each indistinct peak broadly corresponds with the FMAZ III geochemical compositional envelope derived from Faroese marine cores.

- The high sedimentation rate in MD99-2281 was unable to stratigraphically separate multiple closely spaced eruptions in DO-8, most likely due to the site proximity to ash dispersal pathways during a period of frequent Grímsvötn activity.

- Shards identified in this sequence show similarities to several ice-core horizons spanning DO-8 and suggest that each depth in MD99-2281 contains an amalgamation of shards sourced from several closely timed Grímsvötn eruptions. Despite exhibiting similar major element compositions, these may not be derived from the same eruptions preserved in the Greenland ice-cores. The presence of a moderate IRD signal in conjunction with a diffuse shard distribution indicates the operation of bottom currents and ice-rafting. This has compromised the integrity of the deposits and prevented the separation of distinct homogeneous horizons.

Chapter 7 Utilising sedimentology in marine tephrochronology

7.1 Introduction

The aim of this chapter is to examine the innovative application of thin-section and X-ray micro-tomography (μCT) techniques to visualise micro-sedimentological structures in 2D and 3D within marine tephra deposits. In chapter four, the taphonomic history and isochron position of the FMAZ II (304-305 cm) and FMAZ IV (542-543 cm) deposits in JM11-19PC have been assessed using conventional key diagnostic information such as shard distribution and size, geochemistry and IRD co-variance. Micro-sedimentological techniques are explored here to test the interpretations outlined in chapter four and assess their future contributions to marine tephrochronology. These FMAZs were selected as a suitable testbed for this work due to the excellent preservation of visible tephra horizons and availability of material in JM11-19PC. The aims of this chapter are: a) to use 2D thin-section analysis to explore micromorphological structures within the two FMAZs; b) to re-evaluate the taphonomic history of these tephra deposits using the visualisation of 3D structures and; c) to establish a protocol for applying 2D and 3D analytical methods to tephra deposits.

7.2 Sediment sampling

Two parallel U-channels with a 20 mm by 20 mm cross-sectional area were extracted from core-sections spanning both the FMAZ II (304-305 cm) and IV (542-543 cm) (Fig 3.6). Shard concentration profiles indicate that these U-channels span the onset of deposition, visible expression and overlying decline in tephra concentration of the two ash zones. Sediment samples from one U-channel were

used for quantifying the tephra content of the sequence (Fig 3.4a) and for extracting shards for geochemical analysis, as outlined in chapter three. Thin-sections were prepared from the second U-channel (Fig 3.4c) following procedures outlined in section 3.9. The resin-impregnated blocks produced for the thin-section work were then scanned using the μCT system and validation techniques outlined in section 3.10.

7.3 2D and 3D analysis of the FMAZ II

The following section utilises 2D and 3D sedimentological renders of the FMAZ II and IV to re-assess the mechanisms responsible for deposition and refine the position of the tephra isochron in light of this new evidence (Table 7.1, 7.2).

7.3.1 2D results

The FMAZ II deposit forms a thick 2 cm macro-tephra. This macro-sedimentology is presented in section 4.3.3. The deposit is characterised by two distinct units, based upon micro-sedimentological observations (Fig 7.1). The first occurs between 307 and 304.5 cm and consists of a poorly-sorted silty clay with occasional tephra shards (~55 μm in diameter), distributed within the matrix (Fig 7.1a). Occasional (~13 mm) lenses of well-sorted tephra grains up to ~200 μm in size are present in the top of this unit. Lenses are irregular, aligned horizontally and vertically within the host sediment (Fig 7.1b), and generally composed of sediment from unit two. The second unit identified between 304.5 cm and 298 cm is composed of well-sorted tephra dominated by shards of 25-80 μm (Fig 7.1d). Unit two has a sub-horizontal, sharp contact at 304-304.5 cm depth (Fig 7.1c). There is evidence of discrete lobate structures below this level in unit one; below the contact, material from unit two has penetrated into unit one. These features are explained as loading structures (see section 7.3.3.1). The tephra becomes less densely concentrated in the upper part of unit two and appears dispersed within a coarse-silty clay matrix (Fig 7.1d). No grading is observed within this tephra deposit and a similar shard size is apparent throughout this short core section.

Table 7.1 Summary of tephrostratigraphical analysis derived from the FMAZ II and IV using conventional techniques outlined in chapter four.

Tephra Layer	Shard profile	IRD signal?	Geochemistry	Depositional process	Modification Mechanism	Isochron position (cm)	Potential isochron?
FMAZ II	Peak with tails	No	Homogeneous	Primary airfall/ Sea-ice	Bottom currents	304-305	Yes
FMAZ IV	Peak with upward tail	No	Homogeneous	Primary airfall	Bottom currents	542-543	Yes

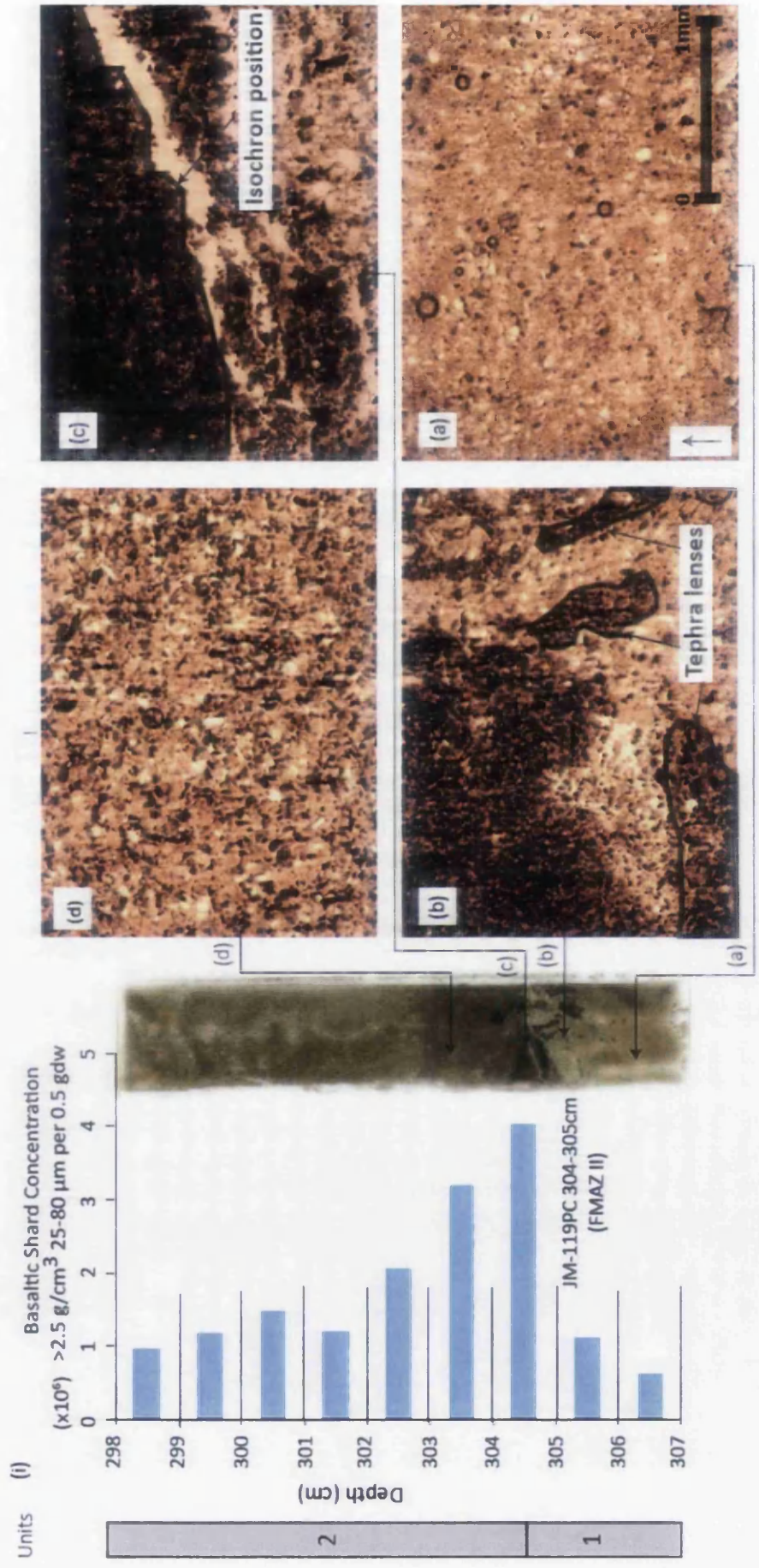

Figure 7.1 Thin-section micromorphology photomicrographs aligned to high-resolution shard concentration profiles (25-80 cm) for the FMAZ II. Units one and two are defined according to the micro-sedimentological features observed. (a) Unit one (307-304.5 cm) with a massive, relatively poorly-sorted matrix of silty clay. Light and dark brown glass shards are dispersed in low concentrations. (b) Irregular horizontally and vertically aligned lenses, composed of abundant well-sorted tephra shards. (c) Isochron position with a sharp contact of abundant well-sorted shards. (d) Unit two (304.5-298.0 cm); glass-shards are less densely concentrated in the upper part of this unit and more mixed within the host sediment.

7.3.2 3D results

The structure of this deposit is complex, with a number of additional features apparent between ~300.8-307.2 cm when viewed in 3D (Fig 7.2, 7.3). There are three distinct units that can be defined through their 3D sedimentological architecture, which includes an additional unit to those from the 2D reconstruction. The first occurs between ~304.5-307.2 cm and consists of numerous tubes of high tephra concentration that are orientated at different angles within the sediment. There is a large narrow ellipsoidal structure which is aligned vertically between ~304.9-306.5 cm, with a width of ~2 mm (Fig 7.2iv). In addition, a large tube is present that penetrates perpendicularly through the centre of this ellipsoid structure (Fig 7.2iii). The largest tube is approximately ~0.5 mm in width, ~20 mm long and has a noticeable curvature with a shift in orientation at ~304.9 cm.

The second unit occurs between ~304.0-304.5 cm and consists of a distinct blocky structure (Fig 7.2ii) representing a high concentration of tephra, with minor undulations at the base of this input. Despite the high concentration of tephra within this blocky structure, there are numerous sediment-filled burrows and voids penetrating throughout at numerous locations and angles with the best branched example having a sub-horizontal repose (Fig 7.3c). Thin veneers of sediment are also seen draping this blocky tephra structure (Fig 7.3b). These structures are observed by segmenting (threshold value defined in section 3.10) the tomographic data to digitally remove the tephra and visualise the sediment (Fig 7.3c).

The third unit occurs between ~300.8-304.0 cm and consists of a pyramidal-like structure between 303-304 cm comprised mainly of tephra shards. Shard distribution over 1 cm indicates a diffuse contact with the highest concentration of shards between 304.5-305.0 cm (Fig 7.2a).

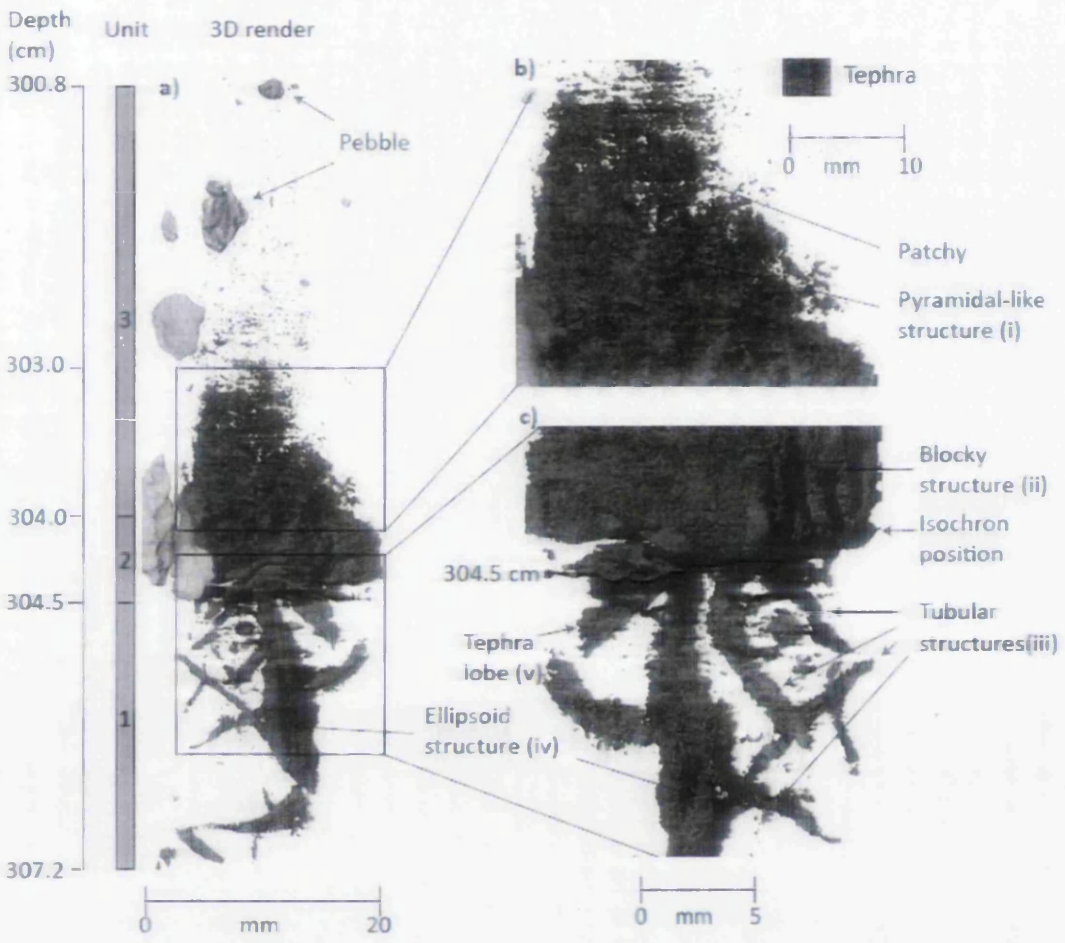

Figure 7.2 3D μCT render of the FMAZ II deposit. (a) Render of the whole resin block, displaying only the tephra phase. Structures have been magnified to highlight indicative sedimentological features in b) and c). The pebbles present in the render are artefacts of thin-section production.

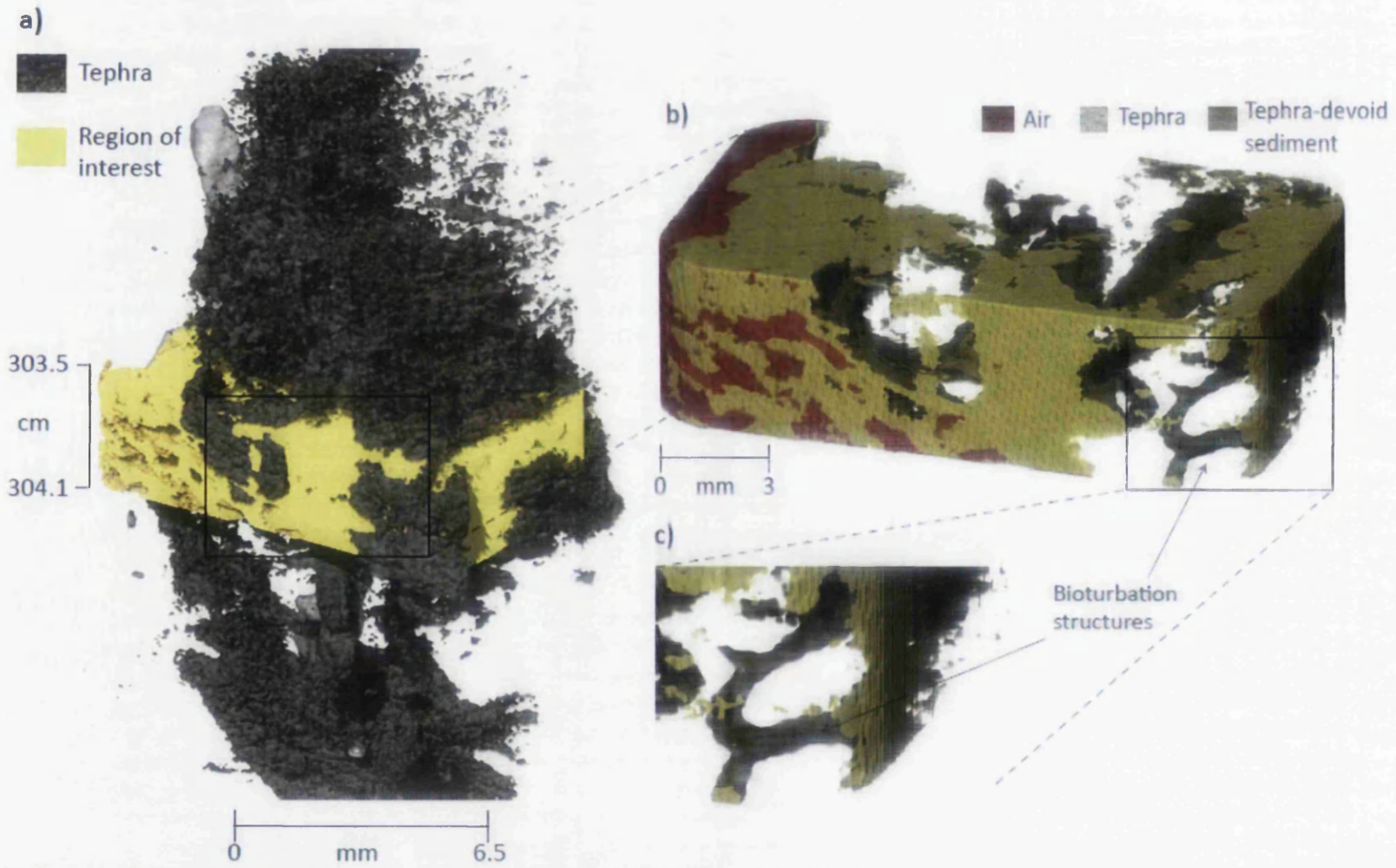

Figure 7.3 3D μCT render of the FMAZ II deposit. (a) Region of interest highlighted by the yellow box between 303-304.1 cm to show the presence of other intensity-phases i.e. sediment and air in this section. b) Region of interest showing sediment and air only. c) Magnification of b) to show bioturbation structures.

Tephra is more concentrated on one side of the scanned block, at a ~60° incline (Fig 7.2b). The concentration of tephra declines rapidly above 303 cm with a loss of any structure by ~303.2 cm (Fig 7.2a). The rest of this unit is characterised by sporadic and low concentration tephra packages.

7.3.3 Re-interpretation of depositional processes

7.3.3.1 Sedimentation rate

The presence of a geochemically homogeneous and fine-grained deposit has been previously interpreted to reflect primary airfall with bottom current re-working (Table 7.1). However, micro-sedimentological features preserved within the FMAZ II suggest the operation of post-depositional loading. A sudden influx of high tephra concentrations is identified by the sharp contact between units one and two in thin section. The discrete tephra lenses and lobate structures in unit one suggest that glass shards have loaded into the sediment (Fig 7.1b). Gravitational loading and the vertical movement of dense tephra shards down into less dense underlying sediment may have occurred due to the rapid influx of tephra to the sediment water interface at the seabed. Low shard concentrations beneath the main concentration peak at 304-305 cm may reflect the presence of these lenses and lobate structures (Fig 7.1). These observations are corroborated with 3D evidence where the lobate structures seen in unit one are the same as the loading structures seen in thin-section. 3D evidence additionally reveals the presence of bioturbation structures that were not originally detected in thin-section as they likely represent a 2D slice through some of these tubes (Table 7.2).

Bioturbation burrows seen in unit one in 3D reveal the mixing of tephra through sediment and vice versa (Fig 7.3c). This suggests that bioturbation may have been active during tephra deposition as Wheatcroft (1992) and Bromley (1996) suggest that burrows become filled with material that differs from the surrounding sediment in most endobenthic communities. It is suggested that tephra deposition was rapid and as a consequence the bioturbation mixing layer shifted upwards at a similar rate. This would result in the preservation of burrows as seen in unit one, as the sediment

below the tephra layer was quickly isolated from the influence of bioturbation. Ash deposits >1 cm thick, similar to the FMAZ II, typically smother the benthos (Carter et al.. 1995) and McCave (1995) note that a consequence of rapid ash deposition is the enhanced preservation of burrows beneath an ash horizon. This supports the interpretation that the blocky structure was deposited rapidly, either via primary airfall or sea-ice deposition (Table 7.1). It is possible that the burrowing features may have been superimposed on the sediment fabric following post-depositional re-colonisation, but there is no strong evidence to support this scenario.

No visible burrows are evident within unit three (Fig 7.2). Given the gradual decline in shard concentration in this unit (Fig 7.1) it is likely that bioturbation continued to be active. The absence of preserved burrows may reflect a higher bioturbation rate, resulting in the complete homogenisation of the tephra and sediment. This may be due to a slow-down in the upward migration of the mixing layer after tephra deposition. It is also possible that additional post-depositional processes such as current re-working may have altered the ichnofabric of the sediment and prevented the preservation of burrows.

The use of 2D and 3D imaging has revealed a range of depositional processes, i.e. bioturbation and loading, previously undetected using traditional tephrostratigraphic techniques (Table 7.1). This highlights the potential for combining a range of tephrostratigraphic and visualisation techniques to fully unravel the sedimentary history of deposits. In this instance, the new depositional evidence has not affected the integrity of the isochron and the FMAZ II continues to represent a well-resolved primary deposit.

7.3.3.2 Isochron placement

The 2D and 3D reconstruction of this deposit supports the isochron placement defined in chapter 4 and provides a more comprehensive analysis of the processes operating. The high concentration of tephra in unit two (between ~304-304.5 cm) has a dense appearance in all planes and a sharp contact with the underlying material suggests rapid influx of a high tephra volume. As such, sedimentological

visualisations additionally confirm that the position at ~304.5 cm equates to the correct stratigraphical placement of the isochron (Table 7.2) (Fig 7.1b, 6.2c).

7.3.4 2D and 3D analysis of the FMAZ IV

7.3.4.1 2D

There are two distinct units in this section based upon the 2D micro-sedimentology. The first occurs between 549 and 543.3 cm and is composed of a massive, moderately-sorted coarse silt with a low concentration of tephra shards, ~50 μm in diameter, distributed randomly within the matrix (Fig 7.4c). The second unit identified between 543.3 and 540 cm is composed of moderately-sorted, abundant 25-80 μm tephra shards within a coarse silt host sediment (Fig 7.4b). This second unit has a diffuse contact with the underlying sediment and there are occasional horizontally aligned lenses (~1.5 mm) of well-sorted tephra grains up to ~140 μm in size (Fig 7.4b). The visible tephra component has a similar shard size (25-80 μm) throughout the second unit. The tephra is highly concentrated but poorly mixed within the host sediment (Fig 7.4a). The isochron position was placed between 542-543 cm to coincide with the peak in shard concentration. This stratigraphic interval is characterised by horizontally aligned tephra lenses of well-sorted and concentrated glass shards (Fig 7.4c). The contact between the designated isochron position at 542-543 cm (Table 7.1) and the underlying sediment is diffuse.

7.3.4.2 3D

Based upon the 3D architecture there are three units within this deposit. The first occurs between ~545.4-548.0 cm and is characterised by discontinuous tephra packages that vary in concentration and appear across all planes of the core (Fig 7.5d).

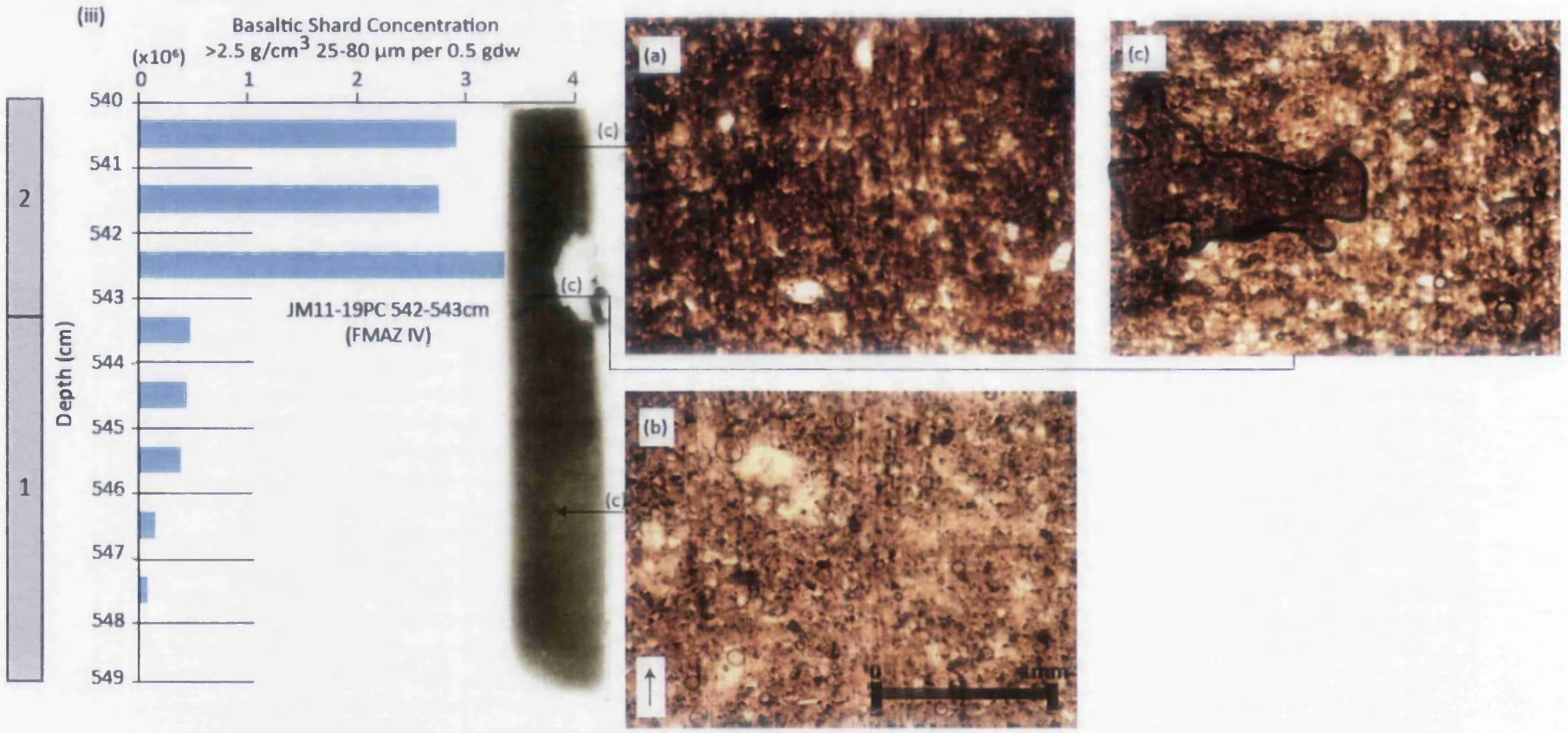

Figure 7.4 Thin-section micromorphology photomicrographs aligned to high-resolution shard concentration profiles (25-80 cm) for the FMAZ IV. (a) Moderately-sorted coarse silts with glass-shards distributed randomly in low concentrations throughout unit one (549.0-543.3 cm). (b) Unit two (543.3-540 cm) composed of moderately-sorted, abundant glass shards within a coarse silt host sediment. (h) Isochron position with occasional horizontally aligned lenses of well-sorted and concentrated glass shards. The contact between the two units is diffuse.

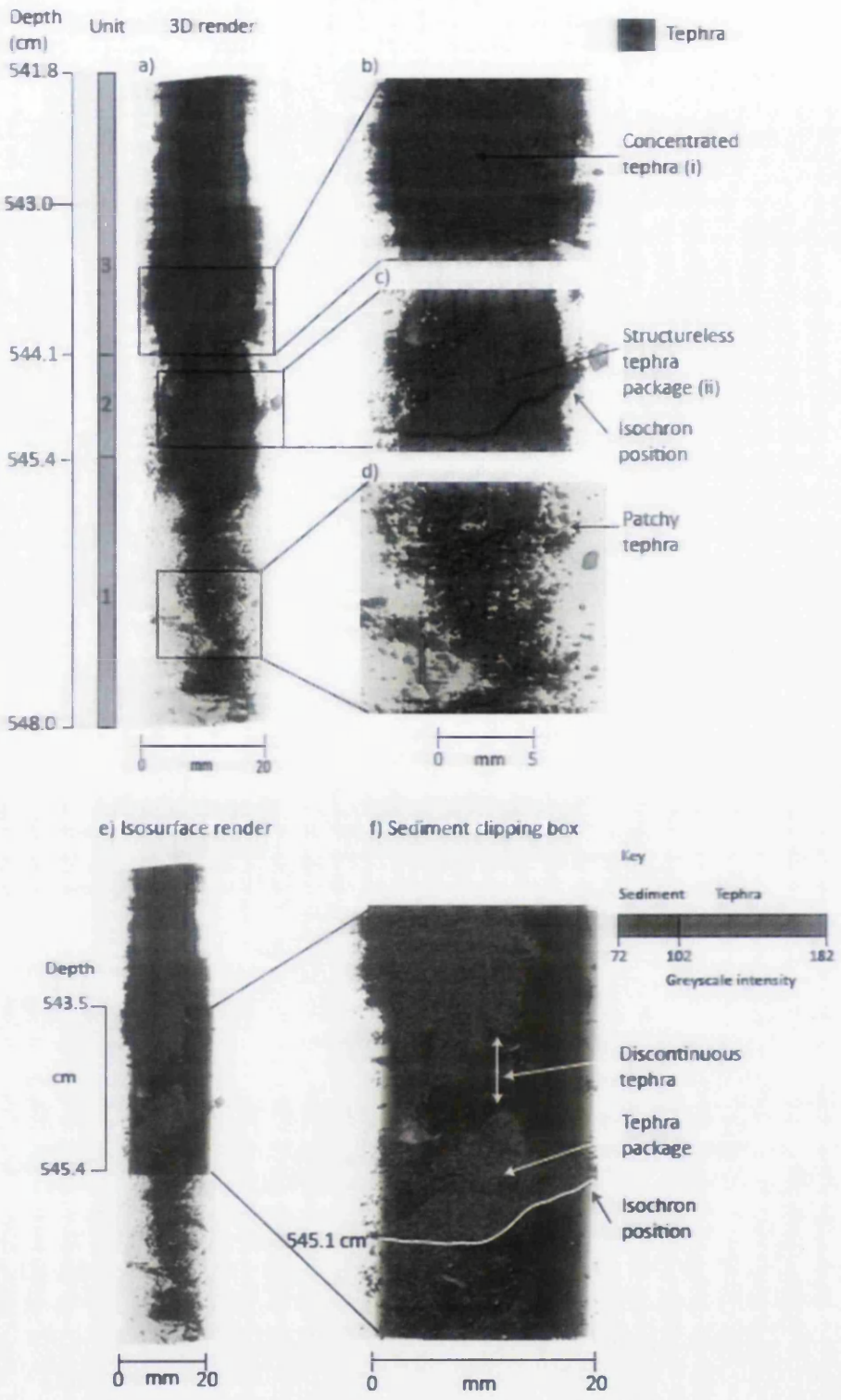

Figure 7.5 3D μCT isosurface render of the FMAZ IV deposit. a) Render of the whole resin block, displaying only the tephra phase. Structures have been magnified to highlight the indicative sedimentological features in b), c) and d). The isochron position has also been highlighted and is defined according to features observed in Figure 7.4. e) Render of the whole resin block, displaying the tephra phase with the addition of region of interest between 543.5-545.4 cm which displays both sediment and tephra phases. f) Magnification of the region of interest to illustrate the planar discontinuity between the tephra packages. The isochron position has been illustrated.

The overall appearance of this unit is a dispersed zone of tephra. The second unit, between ~544.1-545.4 cm, consists of a large structureless, concentrated unit of tephra, with variable concentrations through different planes of the 3D render (Fig 7.5f). A diffuse contact is observed between unit two and the underlying sediment of unit one. There is ~10 mm of sediment separating unit two from the highly concentrated and structureless tephra deposit in unit three ~541.8-544.1 cm (Fig 7.5f and 7.5b).

7.3.5 Re-interpretation of depositional processes

7.3.5.1 Sedimentation rate

Similar to the FMAZ II, the presence of a geochemically homogeneous deposit and a shard concentration profile with a clearly discernible peak were the main indicators used to interpret primary deposition (Table 7.1). The comparative absence of distinct micro-sedimentological features in the microfacies of the FMAZ IV deposit suggests differing depositional controls to the FMAZ II. The presence of horizontally aligned tephra lenses at the previously defined isochron position of 542-543 cm provide additional evidence for enhanced concentrations of tephra delivery into the sequence (Fig 7.4c). The absence of distinct structures provides an insight into the nature of tephra deposition at the site. It is suggested that this style of sedimentation may reflect primary airfall onto the ocean surface and subsequent deposition through the water column. The absence of load structrues may reflect a more gradual rate of sedimentation in comparison to the FMAZ II. A lack of structure may be an additional consequence of post-depositional modification through bottom current re-working and bioturbation. This interpretation has been previously suggested in response to the distinctive upward tail reflected in the shard concentration profile for this deposit (section 3.2.2).

A key contrast between this deposit and FMAZ II is the absence of bioturbation burrows detected in 3D (Fig 7.5a). This may be a result of enhanced bioturbative activity and slow upward migration of the bioturbation mixing layer (Table 7.2). It is suggested that bioturbation may have completely homogenised the sediment and

tephra, destroying any diagnostic sedimentological features such as tubular burrows. Deposition of this ash zone occurred during the interstadial of DO-14, which may have provided favourable conditions for a diverse range of ocean-dwelling organisms. The increase in fauna may have been an additional factor that promoted bioturbative activity. Furthermore, in comparison to the FMAZ II, there are no distinct loading structures which indicates that tephra deposition was not of the same rapidity. Greyscale renders of the FMAZ IV suggest there is a significant amount of sedimentary matrix within the tephra deposit (Fig 3.6), which may reflect a slower rate of tephra sedimentation.

7.3.5.2 Isochron placement

3D evidence from this deposit suggests the operation of more complex sedimentological processes than those deduced in chapter four and that the isochron position should be realigned accordingly (Table 7.2). The concentrated tephra package seen in unit two of the μCT-derived reconstruction is not observed in thin-section or in the shard concentration profile (Fig 7.5f), which highlights lateral variability within this core. The tephra package in unit two (Fig 7.5f) may represent the initial influx of ash into the sequence as a result of primary airfall and subsequent deposition through the water column. The highest concentration of tephra is seen in unit three, which may reflect subsequent input of tephra from bottom current redistribution during a period of intensified deep water formation (Ezat et al., 2014). Major element analysis indicates that the shards from unit two and three have identical geochemical signatures, as demonstrated on FeO/MgO vs TiO_2 and TiO_2 vs CaO biplots (Fig 7.6) (see appendix). No Grímsvötn sourced basalts have been detected in the Greenland ice-core framework for this period and no correlative events have been found in the ice-core records (Bourne et al., 2015). Consequently, it is not possible to determine whether the significant upward tail is a reflection of upward mixing of a deposit from a single eruption, an amalgamation of tephra deposits sourced from several closely spaced eruptions or continuous tephra delivery to the core site.

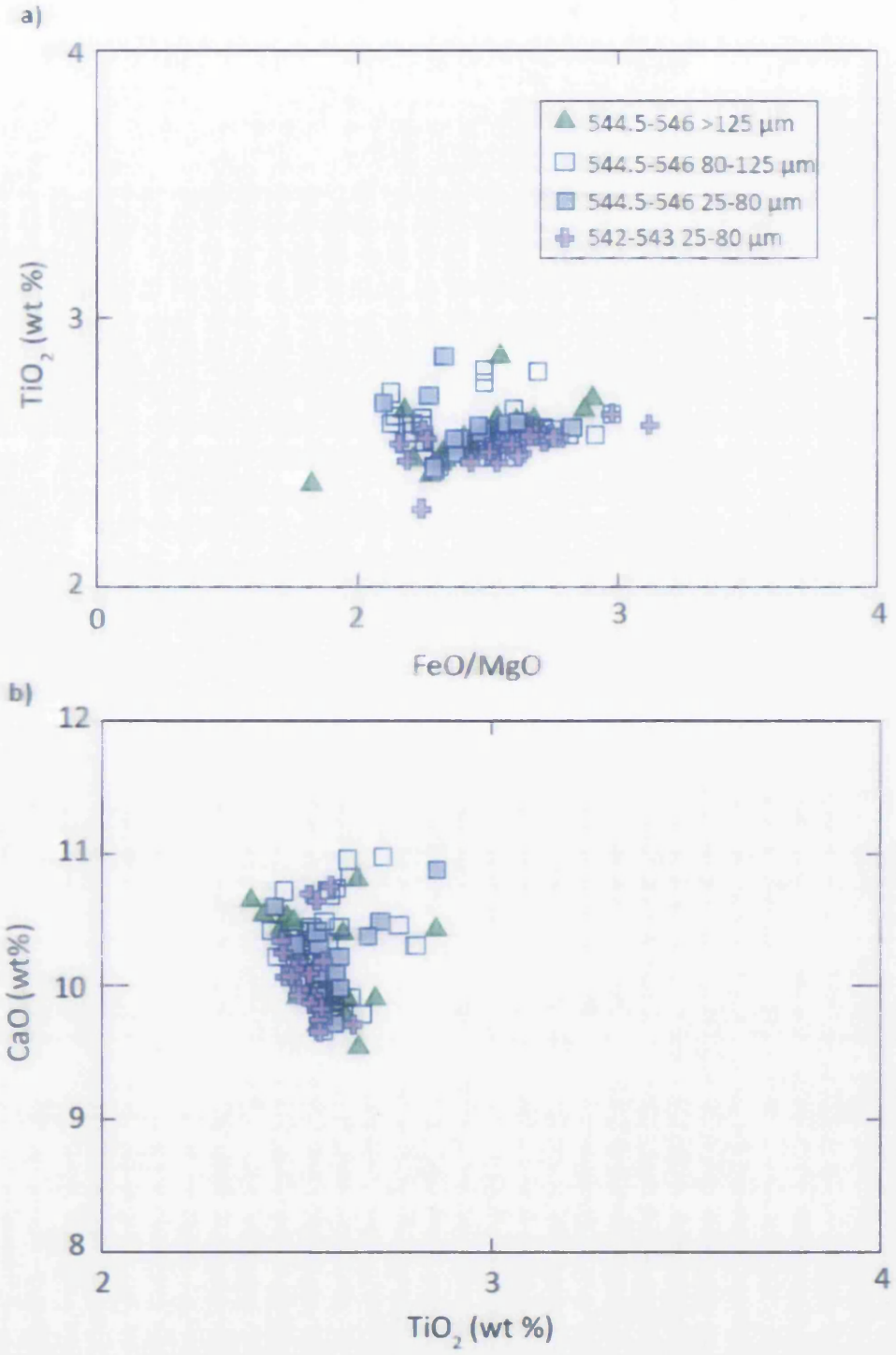

Figure 7.6 Major oxide results (wt %) for glass-shards extracted from 544.5-546 cm. The JM11-19PC 542-543 cm (FMAZ IV) compositions are derived from shard analyses obtained from all grain size fractions present in chapter three. Data have all been normalised to 100% total oxide concentrations. Outliers have been omitted.

Table 7.2 Summary of re-evaluated depositional processes and isochron position based upon 2D and 3D evidence presented throughout.

Tephra Layer	Shard profile	IRD signal?	Geochemistry	Sedimentary features	Deposition process	Modification mechanism	Isochron position (cm)	Isochron change?
FMAZ II	Peak with tails	No	Homogeneous	Burrows/lobes	Primary airfall/sea-ice	Bioturbation /loading	304-305	No
FMAZ IV	Peak with upward tail	No	Moderately homogeneous	Massive	Primary airfall	Bioturbation/ bottom currents	544.3-545.3	Yes

Alternatively, bioturbation may have acted as a mixing agent and dragged sediment down into the tephra horizon, subsequently diluting the concentration through the mixing. It is suggested that the isochron should be placed at the initial primary influx of tephra at ~544.3-545.3 cm. This is 2.3 cm below the isochron placement defined using traditional shard concentration profiles in chapter four (Fig 7.5f) (Table 7.2). This realignment highlights the importance of employing 3D reconstruction to aid correct stratigraphical placement of the isochron.

7.4 Advantages of sedimentological visualisation and future recommendations

Two and three-dimensional visualisations of tephra deposits have provided an exceptional insight into sedimentation processes within the marine environment, and highlighted the structures and distribution of tephra material within a sedimentary record. The micro-structural features observed highlight the complexity and variability of tephra concentration within a sedimentary core. Uneven distribution of tephra is a cause for concern when seeking isochrons, but this visualisation tool can be used to enhance confidence in the stratigraphic placement of isochrons. In relation to the FMAZ II, bioturbation was clearly an active process, but this has had limited impact on the position of the tephra isochron which is clearly discerned by a thick, densely-packed tephra deposit. In the same way, it is proposed that vertical mixing has had very little impact on the integrity of other proxies within this record. This observation would be difficult without sedimentological visualisation. No direct evidence for bioturbation processes were observed in the down-core shard concentration profile (Table 7.1). This demonstrates that traditional techniques will not always fully capture the complexity of tephra distribution that has been demonstrated in the 3D visualisations, but in this context the isochron and its stratigraphic position are intact (Table 7.2).

For the FMAZ IV, lateral variability across the core was a prominent feature that only became apparent from the 3D visualisations.

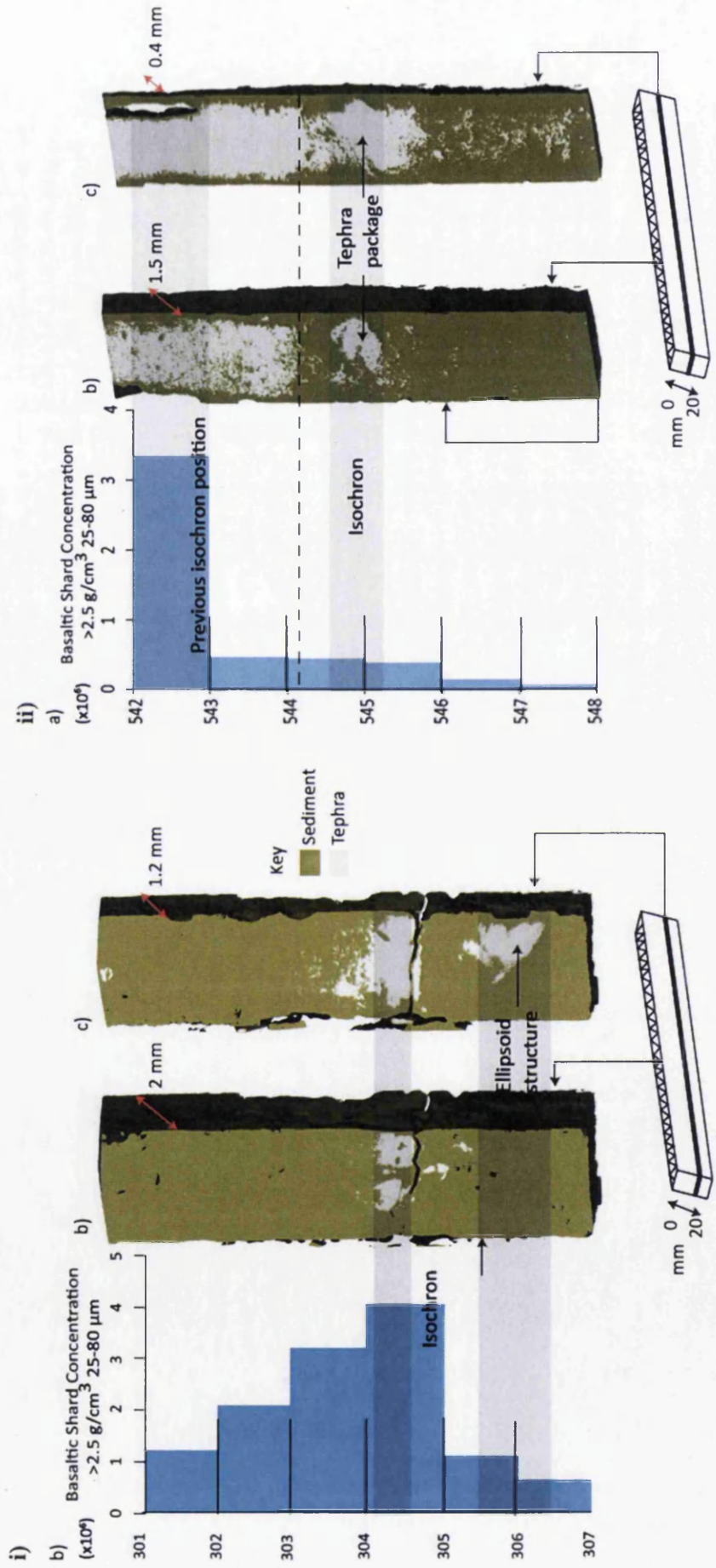

Figure 7.7 3D visualisation with clipping plane revealing subsurface structure. i) FMAZ II and ii) FMAZ IV deposits of different cutting planes (i.e. face of the resin block and middle plane) through the resin blocks. a) High-resolution shard-concentration profile (25-80 cm). b) and c) different cutting planes.

Figure 7.7 shows different clipping planes through the FMAZ IV deposit and highlights the lateral variability of the subsurface structure. During extraction of sediment for shard counting, a small sub-sample of ~1 g is taken from one side of a core. The internal lateral variability observed from the μCT scan clearly highlights that this type of sampling may not capture, or even over-represent, areas of concentrated tephra packages. This may produce a biased concentration profile and potentially affect the correct stratigraphical placement of the isochron (Fig 7.7), explaining the change required in the position of the FMAZ IV isochron (Fig 7.7ii) (Table 7.2).

Due to the spatial complexity and variability observed within these samples, multiple sub-samples across several parallel vertical profiles may provide a better constraint on shard concentrations and the lateral and horizontal continuity of a horizon. This is potentially important for cryptotephra deposits that exhibit a diffuse distribution and lower concentration peaks of <100 shards. Where higher tephra concentrations permit the use of μCT, analysis can be used to corroborate the position of the isochron. For the successful application of μCT analysis, thin-sections are crucial to permit an assessment of; a) composition, grading and sorting of sediments; b) contacts between sediment layers; c) micro-fabrics and textures to determine any imposed stresses to the sediment and; d) mineralogy (Bendle et al., 2015; Meer and Menzies 2011). These analyses represent important diagnostic sedimentological information that provide crucial building blocks for interpreting depositional processes that cannot be obtained using μCT. Each time a new core is investigated it may be necessary to create a thin-section for greyscale threshold validation, i.e. to check that segmentation corresponds with tephra shards. The μCT scan can help guide the optimal position of thin-sectioning based on the 3D structures. Bendle et al. (2015) recommend that μCT scanning be performed prior to sediment impregnation. Micromorphological analysis and μCT offer complementary approaches to understanding the micro-sedimentological characteristics of tephra deposits. A protocol for applying sedimentological analysis to sedimentary deposits is presented in Figure 7.8.

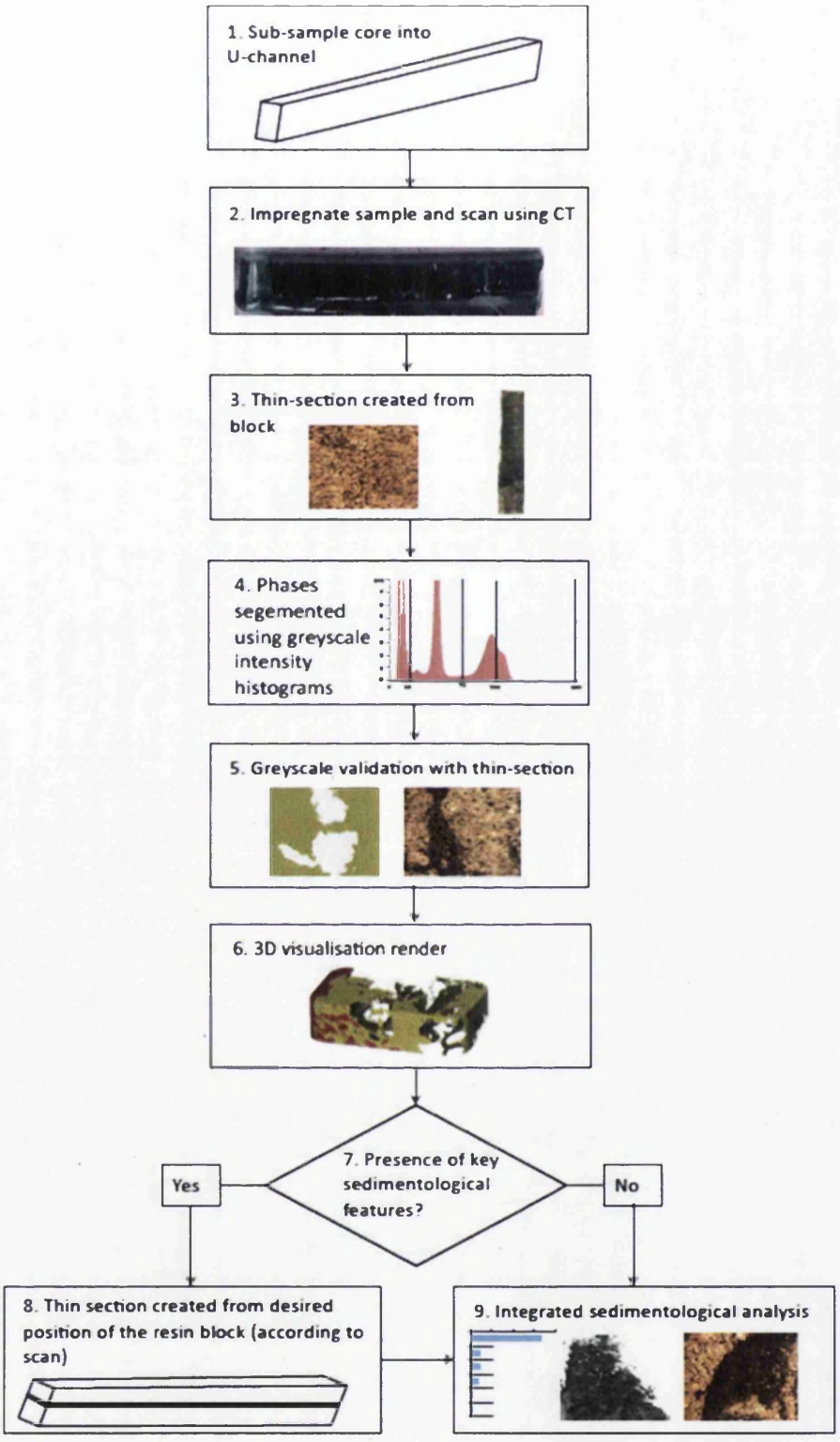

Figure 7.8 A protocol for 3D reconstruction of tephra deposits

While μCT and thin-section analysis have been successfully employed to examine high concentration tephra deposits with a visible expression, it is unclear whether it can be used to visualise tephra deposits in low concentrations (i.e. cryptotephras). It may be possible to detect cryptotephras within host sediments that exhibit a significantly different absorption coefficient to tephra than marine sediments, e.g. peat sediments. This may increase the attenuation contrasts and reduce overlap between tephra and host sediments on the greyscale histograms, which would make threshold definition clearer. This study has solely focused on visualising basaltic tephra deposits that have a small density contrast to marine sediments. Less dense rhyolitic material may show a greater density contrast to the host sediment which could aid intensity segmentation.

If the size of the scanned block is reduced, or if the scan is more focused on a section of the block, it may be possible to increase the scanning resolution of the deposit. This would permit the employment of edge detection, gradients, or local variance to provide a more robust method of phase segmentation (Landis and Keane, 2010). It is likely that targeted scanning of specific intervals within sequences would increase the μCT detection limits suitable for cryptotephra identification. The proportion of tephra relative to sediment should increase and improve segmentation with the different phases more clearly defined on the histograms.

7.5 Conclusions

• The application of 2D analysis was applied to the FMAZ II and IV to identify the presence of micro-sedimentological structures. This permitted a further assessment of the processes governing the taphonomic history of the deposits.

• Load structures were identified in thin-section for the FMAZ II deposit and suggest deposition via primary airfall or sea-ice. 3D visualisation of the FMAZ II is spatially complex and the presence of a large blocky structure confirms the correct stratigraphical placement of the isochron.

• The absence of burrows in the FMAZ IV has been linked to a more uniform sedimentary input that is less severe and subsequently conducive to enhanced levels of bioturbation. The identification of a package of tephra ~2.3 cm beneath the isochron, previously positioned using shard concentration profiles, resulted in realignment of the isochron.

• The correct stratigraphical placement of the isochron is not always represented by a peak in shard concentration, likely due to post depositional modification. Shard concentration profiles may fail to capture discontinuous tephra packages and create a biased profile that influences incorrect isochron placement.

• Thin-section analysis and μCT offer complementary approaches to understanding the micro-sedimentological characteristics of tephra deposits and subsequently, their depositional contexts. A protocol has been developed to assist in the application of 2D and 3D analysis.

Chapter 8 Synthesis and Discussion

8.1 Introduction

The following discussion outlines the main implications and findings of results presented in the previous four chapters. The initial focus presents a taphonomic assessment of contrasting tephrostratigraphical profiles from the network of North Atlantic cores. An inventory of shard distribution profiles together with diagnostic geochemical and sedimentological information underpins a robust protocol for assessing the integrity of marine tephra deposits. This facilitates the construction of a marine tephra framework for the NE Atlantic between 16 and 55 ka. Potential correlations between this framework and others reported in the literature e.g. Greenland ice-cores, are considered to assess phasing relationships within the climate system. Finally, issues preventing robust comparisons are discussed and suggestions are made for locating the most valuable isochrons in the marine environment.

8.2 Unraveling taphonomic processes in the marine environment

Shard concentration profiles and key diagnostic indicators including geochemical homogeneity, grain-size distributions and IRD co-variance are synthesised from each record to define indicative types of cryptotephra profiles with similar characteristics and features (see Table 8.1). These are examined to assess the relative value of accompanying diagnostic indicators (see Table 8.1).

Table 8.1 Synthesis of shard concentration profiles and associated indicators derived from cores analysed within the network. These have been utilised to interpret the depositional controls for each deposit and their potential for integration within a tephrochronological framework. Shard concentrations are based upon peak occurrences in the 25-80 μm fraction. IRD = high influx of ice-rafted debris at the corresponding depth interval. Heterogeneous = multiple geochemical populations with wide variations in element composition. Homogeneous = unimodal or bimodal populations containing a narrow range of geochemistries. Fine-grained = shards <80 μm. Coarse grained = shards predominantly >80 μm. Primary deposits are associated with airfall and/or sea ice deposition. Secondary deposits are associated with iceberg calving and where intensive post-depositional modification has occurred i.e. bottom currents. In this study, diffuse deposits that are predominantly airfall deposits have been compromised by the frequency of eruptions and are also considered secondary.

Profile type	No. of deposits	Core/depth	Shard concent-rations	Associated indicators	2D and 3D features	Deposition controls	Primary deposit?
Single-discrete peak (Fig 8.1a)	3	MD04-2829CQ 800-801 cm	187	Homogeneous, IRD, coarse grained	N/A	Airfall	Primary
		MD04-2829CQ 930-931 cm	32	Homogeneous, fine grained	N/A	Airfall	Primary
		MD04-2829CQ 934-935 cm	31	Homogeneous, fine grained	N/A	Airfall	Primary
Peak with upward and downward tails (Fig 8.1b)	4	JM11-19PC 196-197 cm	~21,000	Heterogeneous, IRD, fine grained	N/A	Ice-rafted	Secondary
		JM11-19PC 304-305 cm	>3 million	Homogenous, fine-grained	Loading/burrows	Airfall, bioturbation	Primary
		JM11-19PC 357-358 cm	~28,000	Homogenous, fine-grained	N/A	Airfall	Primary
		JM11-19PC 618-623 cm	29,000 RHY 450,000 BAS	Homogeneous, fine-grained	N/A	Airfall	Primary

Table 1 continued

Peak with extensive upward tail (Fig 8.1c)	1	JM11-19PC 544.3-545.3 cm	>3 million	Homogeneous, fine-grained	Massive	Airfall, bioturbation	Primary
Diffuse distribution (Fig 8.1d)	2	MD99-2281 1869-1890 cm	~900	Heterogeneous, IRD, mixture grain-sizes	N/A	Airfall, bottom currents	Secondary
		JM11-19PC 423-443 cm	~750,000	Heterogeneous, fine-grained	Massive	Airfall, bottom currents	Secondary
No peak/low background (Fig 8.e)	2	MD95-2010 793-794 cm	~14	Heterogeneous, IRD, coarse-grained	N/A	Sea-ice/Bottom currents	Secondary
		MD04-2829CQ colourless shards	~51	Heterogeneous, fine-grained	N/A	Bottom currents	Secondary

This permits the development of a marine protocol to assess depositional pathways and ultimately to explore the integrity of each tephra horizon as an isochron for inclusion within a tephrochronological framework.

8.2.1 Shard concentration profiles and related diagnostics

Twelve tephra deposits have been detected within the network and form five distinct shard concentration profile types. Schematic representations of concentration profiles have been illustrated in Fig 8.1 and summarised in Table 8.1. The following section provides a summary of each profile and their occurrence across the NE Atlantic network.

8.2.1.1 Single discrete peak

Single-discrete peaks are only found in one core and are quite rare amongst marine deposits (Table 8.1). This type of profile is characterised by a discrete peak in shard concentration, often constrained to 1 cm (Fig 8.1a). The clear peak represents the likely stratigraphical placement of the isochron and is a common profile exhibited by basaltic deposits in MD04-2829CQ (Table 8.1). Shard concentrations represented by each peak are <200 shards per 0.5 gdw and are manifested as cryptotephra horizons with varying degrees of lateral continuity (Fig 8.2). In each occurrence, a distinct homogeneous or two homogenous populations are observed. In deposits where a single geochemical population exists (MD04-2829CQ 930-931 cm, MD04-2829CQ 934-935 cm), IRD input and the percentage of coarse-grained shards is low. These are typical diagnostic features of primary airfall (Abbott et al., 2011). In contrast, the geochemically bimodal deposit 800-801 cm in MD04-2829CQ coincides with high IRD influx, which is not a common feature of primary deposits. An additional characteristic of the bimodal deposit is the predominance of coarse-grained shards >80 μm. Based upon initial deduction of geochemical homogeneity, the deposit is likely to have been affected by sea-ice deposition and highlights the potential of utilising grain-sizes to decipher transport processes.

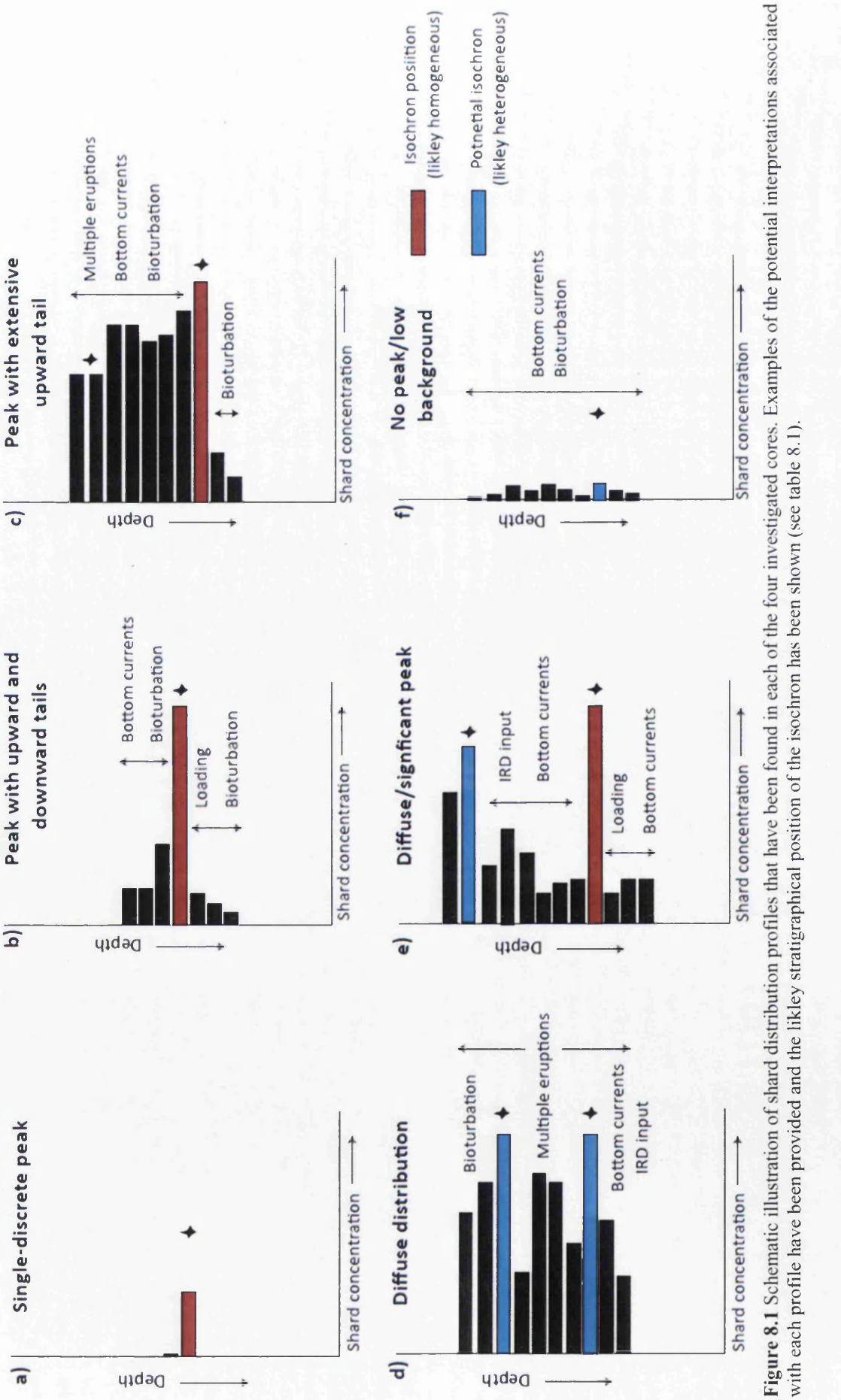

Figure 8.1 Schematic illustration of shard distribution profiles that have been found in each of the four investigated cores. Examples of the potential interpretations associated with each profile have been provided and the likley stratigraphical position of the isochron has been shown (see table 8.1).

Each discrete profile is characterised by a clearly defined primary isochron, likely to be derived from primary airfall or sea-ice, which can be securely integrated within a framework (Table 8.1).

8.2.1.2 Peak with upward and downward gradational tails

Profiles of this nature are the most commonly observed within marine and lacustrine environments, but in this network are detected exclusively within JM11-19PC (Table 8.1). These deposits are characterised by a clearly discernible peak with exponentially decreasing shard dispersion above and below (Fig 8.1b). Four JM11-19PC deposits (196-197 cm, 304-305 cm, 357-358 cm, 618-623 cm) exhibit a concentration profile of this kind and three of these contain homogeneous geochemical populations (Table 8.1). Peak shard concentrations vary according to composition of the tephra (Fig 8.2). Peaks at 196-197 cm and 357-358 cm are rhyolitic and exhibit concentrations of <30,000 shards. In contrast, basaltic peaks at 304-305 cm and 618-623 cm exhibit shard concentrations >450,000 (Fig 8.2) and the peak at 304-305 cm manifests as a macrotephra horizon. In each homogeneous deposit, there is no associated IRD input and fine-grained shards dominate the grain-size distribution; both of which are characteristic of primary airfall deposits (Abbott et al., 2011) (Table 8.1).

Upward and downward tails in each instance are likely to represent bioturbation and/or bottom current re-working, both of which are not features of singular peak profiles. These dispersed profiles may be indicative of slower site-specific sedimentation rates. As a consequence, the peak, as opposed to the position of first influx, is suggested to represent the correct stratigraphical placement of the isochron. In some instances these profile types reveal a heterogeneous tephra geochemistry and coincide with an increase or peak in IRD e.g. 196-197 cm (Fig 4.3). These are typically interpreted as ice-rafting signatures and suggest a significant temporal delay between the timing of eruption and deposition at the core site. As such, the deposit is not isochronous and is unsuitable for integration within the framework. In most instances, profiles of this kind are likely to represent primary airfall with post depositional re-working, but may also be a consequence of secondary deposition.

Co-variance with IRD is a key indicator to assess the role of iceberg rafting in this instance.

8.2.1.3 Peak with significant upward tail

Peaks with distinctive upward tails, where high shard concentrations are apparent several centimeters above the peak, are infrequently detected and only one marine deposit of this nature was found within the network (Table 8.1). The profile is characterised by a peak with a sharp lower contact and a significant upward tail of vertical tephra dispersion (Fig 8.1c). Although these profiles are similar to the peaks with gradational tails outlined above, the distinction is made to emphasise the extensive upward tail in relation to the downward tail i.e. high concentrations over several cm's and no exponential decrease. JM11-19PC 544.3-545.3 cm exhibits these properties, and in this instance the peak and position of first main influx occur at the same stratigraphic depth. There is minimal dispersion below the peak in shard concentration. Shards extracted from several depth intervals within the upward tail were found to have the same homogeneous geochemical composition as the lowermost peak. An assessment of the palaeoceanographic regime suggests the deposit occurs within a period of increased bottom water formation that favours bottom current re-working (Ezat et al., 2014). It is therefore advantageous to assess whether deposition occurred during stadial or interstadial climates, which exert a control upon bottom currents and subsequently the ability to re-mobilise previously deposited material. Additionally, there is no evidence of high IRD input and fine-grained shards dominate the grain-size distribution, both of which are common diagnostic features of primary airfall deposition (Table 8.1).

Davies et al. (2014) observed a similar shard concentration profile in MD99-2253, which yielded two unrelated homogeneous populations to the main peak within the declining tail of the deposit. This highlights the importance of exploring the geochemical composition of glass shards from multiple depths in this type of profile. This will assess whether the shards were derived from secondary re-working or determine the presence of additional primary tephras hidden within the declining tail (Davies et al., 2014).

8.2.1.4 Diffuse distribution with multiple peaks

Distributions of this type have been detected in two deposits from JM11-19PC (423-443 cm) and MD99-2281 (1869-1890 cm), both of which represent the FMAZ III complex (Table 8.1). The deposits are characterised by a high background of glass shards over a notable core interval (~20-30 cm) with numerous indistinct peaks (Fig 8.1d). Although the distributions in both cores are similar, the concentrations of shards in each core are contrasting. JM11-19PC peaks exhibit concentrations of ~750,000, compared to ~500 in MD99-2281 (Fig 8.2). Both deposits exhibit heterogeneous geochemical signatures derived from multiple depths and peaks. IRD input in association with these deposits show some contrasting features, with moderate covariance associated with MD99-2281 and low IRD input in JM11-19PC (Table 8.1). This suggests an ice-rafting component may have assisted in tephra delivery in MD99-2281. Assigning a precise isochron position is challenging and generally not possible due to the heterogeneity of shards and diffuse nature of the deposit. In light of these observations, these diffuse deposits may only be useful as low-resolution markers in the marine environment i.e. where the same geochemical composites occur at corresponding stratigraphical intervals. It is suggested that these diffuse profiles have been compromised by secondary re-working, but may be used as a marker for the same prolonged ice-rafting event seen in different marine cores. However, in MD99-2281 1883-1884 cm, a distinct peak occurs in association with a moderate heterogeneous geochemistry, which may represent primary airfall imprinted upon a dispersed profile i.e. (Fig 8.1e).

8.2.1.5 Diffuse distribution with no discernible peaks

Shard profiles of this kind do not usually reveal the presence of isochrons and are characterised by very low tephra concentrations with minor fluctuations and no definitive peaks (Fig 8.1f). This profile typically reflects a low background of shard concentrations, e.g. rhyolitic material in MD04-2829CQ and a period of minor influx in MD95-2010 793-794 cm (Table 8.1). In both examples, the deposits exhibit a heterogeneous geochemical signature and IRD input is low. In MD04-2829CQ, a

background of rhyolitic material is characterised by fine-grained shards. In conjunction with geochemical heterogeneity, the background signal is interpreted to reflect post-depositional re-working. Similar geochemically heterogeneous compositions indicate a continuous input of similar shards into the system and may highlight a memory effect at the site. In MD95-2010, the shards are predominantly coarse and likely to be deposited by a range of primary and secondary depositional processes (Table 8.1). These profiles are useful for understanding the depositional history at the core site but their use as isochrons is limited.

8.2.2 Visualising sedimentological features to assess post-depositional modification

After combining diagnostic information outlined in the previous section, it may be crucial in some instances to utilise sedimentological analysis to confirm the correct stratigraphical position of the isochron. This can also be used to pinpoint modification mechanisms that may not always be captured using traditional techniques. Two deposits, JM11-19PC 304-305 cm (FMAZ II) and 544.3-545.3 cm (FMAZ IV), exhibit peaks with gradational tails and a homogenous composition (Fig 8.1b). These were explored using 2D and 3D techniques to test sedimentation interpretations (see chapter 7) (Table 8.1).

The FMAZ II and FMAZ IV deposits provide contrasting examples of tephra depositional structures. Evidence of several bioturbation burrows can be seen in unit one of the FMAZ II penetrating ~20 mm below the initial primary input of the sediment (Fig 7.2c). However, these structures are not visible in the FMAZ IV and several lines of evidence are presented that suggest this is due the nature of sedimentation. The presence of a dense blocky structure in the FMAZ II and sedimentary loading below indicates rapid, high volume tephra delivery to the seabed. The severity of this ash fall is interpreted to have been sufficient to disrupt normal sedimentation processes and cease the operation of bioturbation. Therefore, in intervals where there is serious disturbance to the sedimentary system i.e. a catastrophic tephra input event or a turbidite, stratigraphical dispersion may be

limited. Such disturbances to the system may be highly beneficial for marine tephrochronology, preserving the deposit as an intact isochron and retaining its stratigraphic integrity. The absence of structures in the FMAZ IV suggests bioturbation may be enhanced in core sections where there is relatively uniform sedimentation. However, this may not apply in situations where stratigraphic dispersion is not a feature of the concentration profile i.e. in MD04-2829CQ. In these cases, the sedimentation rate may be of sufficient rapidity to consistently shift the biological mixing layer and preserve the integrity of the deposit. It may also be due to the exceptionally low tephra concentrations that prevent tephra from acting as a bioturbation tracer.

The application of sedimentological analysis provides new insight into estimating the extent of bioturbation processes and operation of other marine depositional processes, particularly in deposits that exhibit shard dispersion. Although not exhaustive, the identification of similar sedimentary structures, i.e. burrows, may be pivotal for assessing the true robustness of isochrons being employed in high precision correlations. Sedimentological analysis may be particularly useful for deposits requiring precise and secure isochron placement i.e. those that bracket a climate transition and traceable in ice-cores. It may be useful in circumstances where the isochron is not clearly discernible, such as profiles with gradational tails either side of the peak.

8.2.3 Dispersal and depositional controls at each core site

Each investigated core has revealed different cryptotephra profile types and absolute shard concentrations (Table 8.1, Fig 8.1). This section builds on the depositional controls for individual cryptotephra deposits and explores how atmospheric dispersal and oceanic transport may have affected the distribution and concentration of glass shards at each core site.

8.2.3.1 JM11-19PC

This core contains three different types of shard concentration profile (Fig 8.1 b,c,d). In each instance, the shard concentrations represent the highest detected within the network (Fig 8.2). This is likely to be a consequence of its proximity to Iceland and the main southeasterly trajectory of ash plumes within the east-flowing polar jet stream (Jennings et al., 2014). Others suggest the Faroe Shetland-Channel provides a detailed history of Icelandic volcanism due its proximity to Iceland (Wastegård et al., 2001, Wastegård and Rasmussen, 2014). On one hand, this is a great opportunity for detecting numerous tephra layers, but on the other, it provides significant glass shard input into the system. In periods of closely spaced eruptions e.g. FMAZ III, glass shards of varying geochemistry are deposited to form a heterogeneous amalgamation of tephra at the core site.

Benthic foraminifera abundances in the Nordic Seas suggest deep-water conditions during interstadials were very similar to present-day circulation patterns; dominated by bottom currents generated by thermohaline convection (Rasmussen et al., 1996). Bottom water formation in the Faroe-Shetland gateway may have focused material towards the site and enhanced re-working during interstadials (Rasmussen et al., 1996). As such, periods of bottom water formation may be responsible for enhanced gradational upper tails i.e. 544.3-545.3 cm. The presence of an ice-rafted deposit is likely due to the proximity to ice-rafting pathways during intense cold periods i.e. 196-197 cm. It is suggested that bottom currents, proximity to Iceland and ice-rafting pathways impart a strong control on tephra deposition and preservation in JM11-19PC. These controls have varied temporally and can partly be related to the overall climatic regime.

8.2.3.2 MD99-2281

MD99-2281 contains only one type of shard distribution profile (Fig 8.1c), although the absence of additional types may be a consequence of the targeted sampling window. The site is located ~300 km southwest of JM11-19PC (Fig 8.2) and is likely to be in an area susceptible to delivery from atmospherically derived tephra, reflected in moderate shard concentrations (Table 8.1).

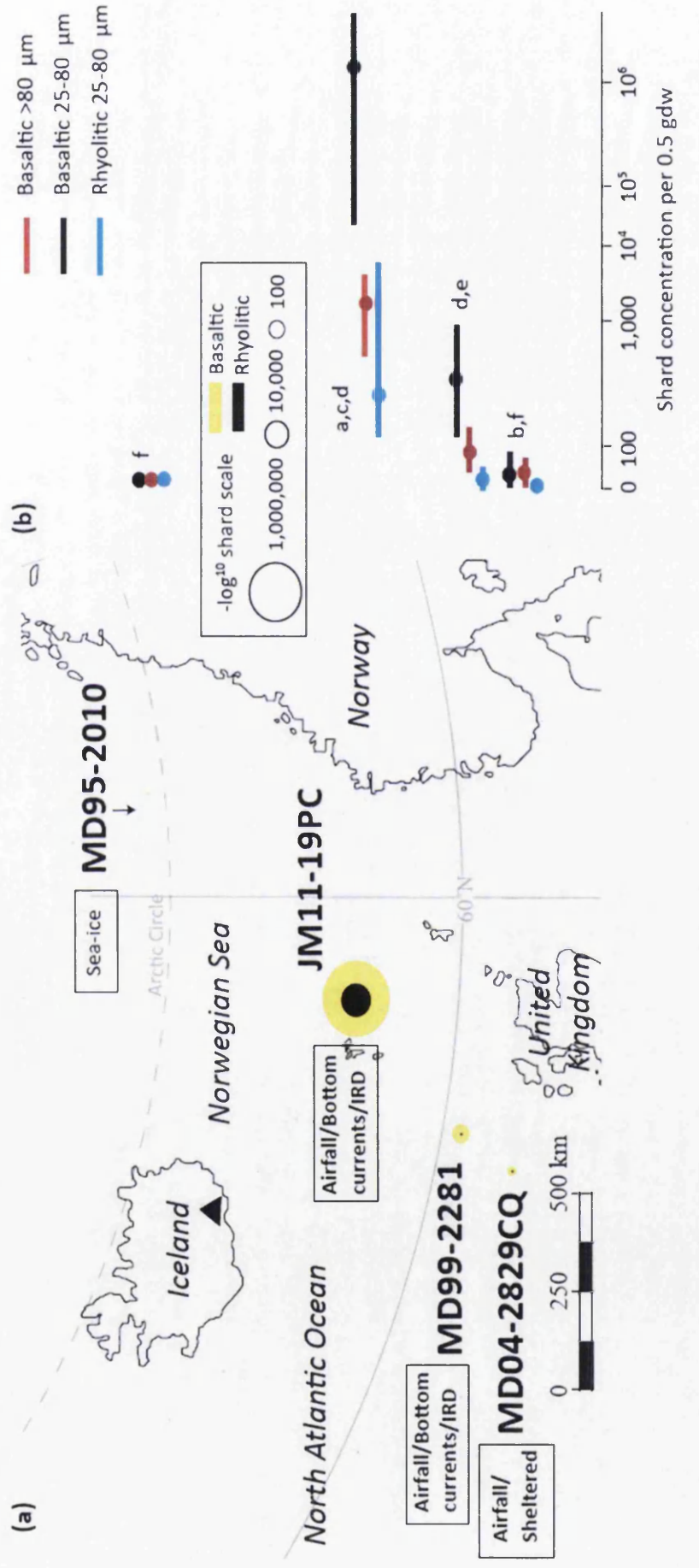

Figure 8.2 Schematic illustration of shard concentrations that have been found in each of the four investigated cores in relation to their location in the North Atlantic. The size of circle is based upon a -$\log^{10}$ scale to reflect the concentration of basaltic and rhyolitic shards found at each site. The lines represent the range of concentrations observed within each core and the dot represents the average shard concentration. Depositional processes affecting each site have also been indicated.

Bottom currents affecting MD99-2281 are influenced from circulation around the Faroe Islands and are likely to have followed the same pathway as currents affecting JM11-19PC. Geomorphological evidence suggests interglacial/interstadial sedimentation in the Faroe Bank is almost entirely controlled by bottom currents (Kuijpers et al., 1998). Hence, it is likely that deep-sea circulation has influenced tephra sedimentation and re-working (Kuijpers et al., 2002). Lower tephra concentrations in comparison to JM11-19PC may be due to depletion in the number of tephra particles entrained in suspension when overflowing the site.

An additional factor controlling deposition at MD99-2281 is the potential of tephra delivery through ice-rafting. During the last glacial period, southern parts of the Faroe Islands were under direct influence of the proximal Fennoscandian and BIIS ice-sheets. High concentrations of IRD grains in the record suggest the site may have been susceptible to iceberg calving. However, Hall et al. (2011) suggest the greatest contribution of IRD influx in the region is sourced from the BIIS. This is likely to reflect local ice-rafting signals, as opposed to ice-rafting sourced from proximal Icelandic and/or Laurentide ice sheets. As such, the icebergs are much less likely to contain tephra sourced from multiple eruptions and deposits may reflect a short delay between the eruption and subsequent deposition from calving.

8.2.3.3 MD04-2829CQ

MD04-2829CQ is situated ~100 km south east of MD99-2281 (Fig 8.2) and exhibits significantly lower tephra concentrations manifested as single discrete peaks (Fig 8.1a). This may be due to increasing distance from the main dispersal axis and local topographic controls. Specifically, sedimentation in MD04-2829CQ is likely be influenced by the Rosemary Bank, a seamount in close proximity to the site. The surrounding area exhibits a complex bathymetry and a peak vertical relief of 2000 m, with topographic depressions related to erosion between the seamount and the flanking contourite drift deposits, on which MD04-2829CQ is located (Howe et al., 2006). As a result, sedimentation around the seamount and surrounding basin is complex, a combination of the highly variable nature of seabed morphology,

sediment supply and the downslope process operating (Howe et al., 2006). These controls enhance bottom current velocities and keep particles in suspension for longer periods, potentially affecting the lateral transport of tephra particles. This may explain the memory effect/background of rhyolitic material at the site. Circulation around the Rosemary Bank is affected by eddies and gyres superimposed upon the net transport, inducing turbulence and potentially stopping tephra particles reaching the sea-bed. Thus, physical conditions may have reduced deposition of glass shards in this location.

The absence of tailed shard distributions in contrast to other sequences may be a consequence of high sedimentation and short pulses of tephra input, limiting the opportunity for re-working and preserving isochronous integrity. The presence of a continuous background of rhyolitic material in the record may reflect rhyolitic deposits that have remained mobile in the marine system and constitute the matrix of sedimentary influx to the site (Fig 8.1f).

8.2.3.4 MD95-2010

MD95-2010 represents the most distal core to Iceland (~1300 km) and is predominantly devoid of tephra (Fig 8.2). The presence of a diffuse, somewhat tenuous basaltic deposit (Fig 8.1d) may be the consequence of sea-ice rafting. The site is located on the northern limit of the North Atlantic Drift and is close to the former limits of the Fennoscandian ice-sheet, which completely covered the Vøring Plateau during the last glaciation (Mangerud et al., 1991). This affected glaciomarine controlled sedimentation and is likely to have had a significant impact upon tephra deposition. Additionally, dinocyst assemblages have been used by Eynaud et al. (2002) to establish the persistence of sea-ice cover at the site during interstadials in comparison to the rest of the Atlantic. As such, perennial sea-ice may have permanently capped the northern Norwegian Sea during the last glacial period and prevented tephra from reaching the sea-bed.

Exceptionally low concentrations of IRD throughout the record suggest that ice-rafting is unlikely to have contributed towards tephra deposition. This is in contrast to the high IRD influxes recorded in the other Atlantic cores within the study. Enhanced sea-ice cover duration and infrequent ice-rafting episodes are likely to account for the predominant absence of tephra.

8.2.4 Marine tephrochronological protocol

Given the diagnostic indicators identified in this study and an understanding of their local depositional controls, a stepped analytical protocol for resolving depositional pathways in the marine realm is proposed (Fig 8.3). The protocol highlights the importance of employing contiguous shard concentration profiles, comprehensive geochemical characterisation, IRD co-variance and where appropriate, micro-sedimentological features to unravel potential depositional mechanisms.

The protocol places strong emphasis on the geochemical characteristics of tephra deposits and more specifically the level of geochemical homogeneity. Previously, high IRD co-variance was automatically equated to tephra delivery from ice-rafting and integrity of the deposit was thought to be compromised. However, a number of examples of high IRD covariance with homogenous populations suggest that primary deposition may have occurred contemporaneously with ice-rafting. The bimodal deposit 800-801 cm in MD04-2829CQ coincides with high IRD influx yet the homogeneity of the two components is not a common feature of ice-rafted deposits. This suggests that IRD co-variance is not always a diagnostic indicator of secondary deposition and that emphasis should initially be placed on geochemical homogeneity. As a consequence, IRD indicators are included to corroborate ice-rafting following initial deductions of geochemical heterogeneity. If low IRD indicators are associated with geochemical heterogeneity, it is likely the deposit has been compromised by the frequency of eruptions or significant post-depositional re-working (Fig 8.3).

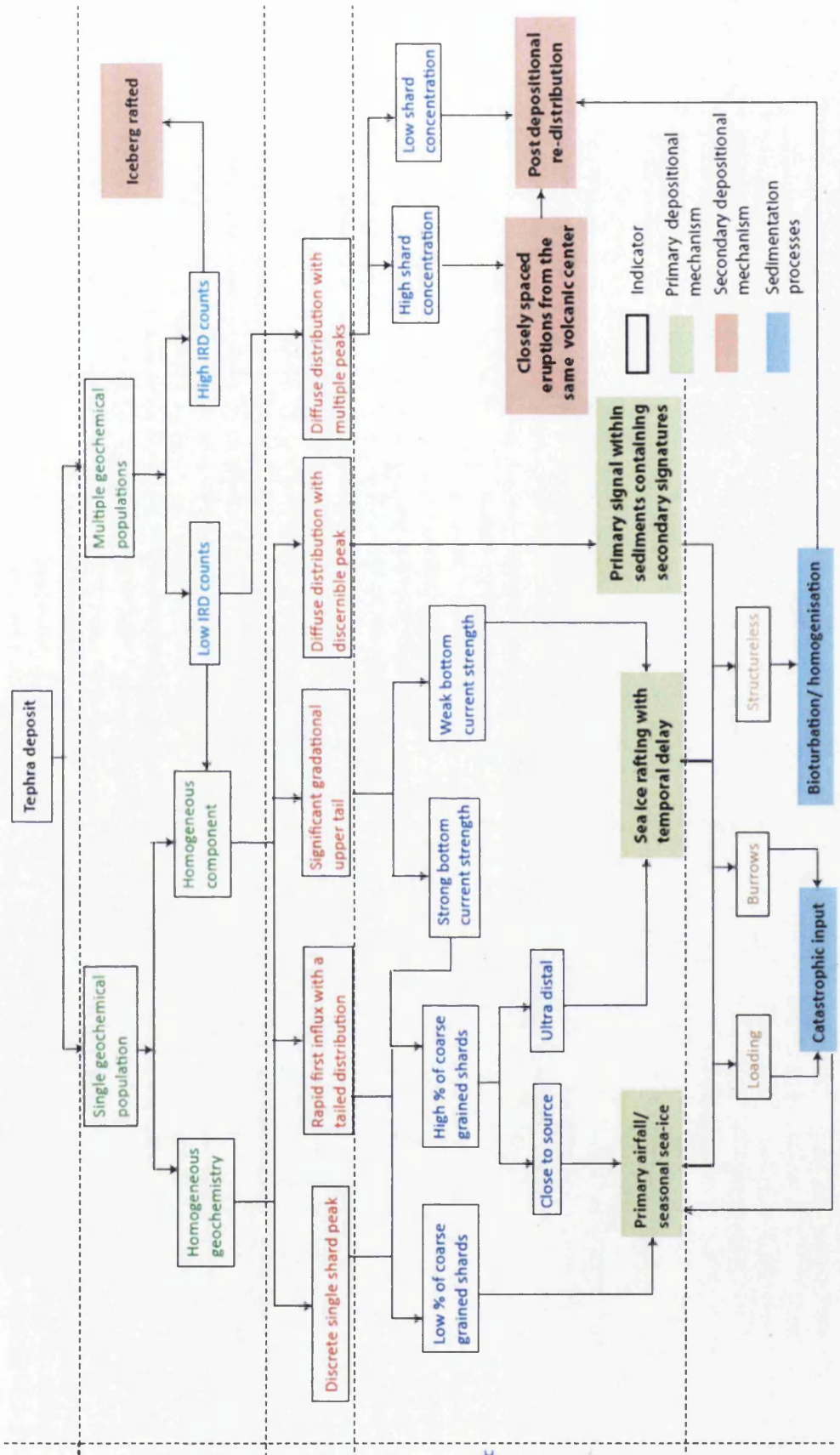

Figure 8.3 Protocol for the investigation of primary and secondary depositional processes in marine tephrochronological studies.

High-resolution concentration profiles represent the next critical diagnostic indicator within the protocol. Providing a homogeneous geochemical signature is observed, it is likely these profiles represent primary input and their stratigraphical expression is related to local sedimentation and sensitivity to re-working. A predominance of fine-grained shards is typically associated with primary airfall or seasonal sea-ice. If coarser shards are found within the deposit, it is likely that sea-ice rafting caused greater transport of shards away from the source. This would likely induce a limited temporal delay between the eruption and subsequent deposition, irresolvable within the resolution of the marine sequences. An understanding of the climatic regime and associated palaeoceaongraphic processes may provide additional information regarding the potential for sea-ice deposition. It is stressed this is unlikely to affect the temporal integrity of the isochron. The application of dinocyst assemblages and IP25 biomarkers may additionally assist in deciphering the presence of sea-ice (Belt et al, 2013). The final section of the protocol utilises sedimentology to validate the process mechanisms interpreted from other indicators and potentially refine the position of the tephra isochron (Fig 8.3).

The protocol highlights the importance of using a range of indicators in order to unravel the operation of different depositional mechanisms. It is accepted that the protocol is not exhaustive and further iterations and refinements are envisaged due to the complex interplay of processes that are spatially and temporally dependent across the North Atlantic. A key section of the protocol that is likely to be subject to future revision is the application of sedimentological techniques, currently in their infancy. The identification of structures i.e. burrows, within the micro-facies of a deposit provide a valuable starting point for substantiating the modes of tephra delivery to the sea-floor. As more structures are observed, this should permit greater understanding of the range of diagnostic sedimentological signatures of primary and secondary deposits.

As the number of investigations employing a range of diagnostic indicators increases, a catalogue of shard concentration profiles and their associated depositional processes can be compiled. It is anticipated that an inventory, outlined here, should permit a deduction of the deposits that should be pursued further as they are likely to reflect primary deposition. This study has revealed that discrete peaks

have been found ubiquitously in association with homogeneous geochemistry and consequently reflect primary deposition. In contrast, a diffuse distribution is unlikely to be homogeneous and its value as an isochronous marker is limited. As such, profiles of this type may not be worth pursuing further.

8.3 Updating the tephrochronological framework for the North Atlantic

The marine toolkit and an understanding of spatially dependent sedimentation controls have been used to assess which deposits are suitable for integration within the North Atlantic framework. Specifically, eight cryptotephra and two macro tephra deposits have been identified as potential isochrons within marine cores spanning MIS 2 and 3. Eight are basaltic in composition, and two are rhyolitic; these have been deemed isochronous deposits of varying potential (Fig 8.4). Two of these horizons, JM11-19PC 304-305 cm (FMAZ II) and JM11-19PC 618-623 cm (NAAZ II) are previously known tephra deposits and represent ice-marine tie-points. MD04-2829CQ 800-801 cm represents a previously unidentified tephra deposit within the framework and may act tentatively as an ice-marine tie-line (Fig 8.5, 8.6). The emerging framework forms a basis for the identification of coeval cryptotephra deposits and assessments of climatic phasing (Fig 8.5). For clarity, tephra deposits that exhibit ice-marine correlations and occur in more than one record are considered first, followed by single tephra occurrences detected exclusively in a single core.

8.3.1 FMAZ II

A basaltic macrotephra, JM11-19PC 304-305 cm (FMAZ II), exhibits a homogeneous peak sourced from the Kverkfjöll system and correlates with NGRIP 1848.0 m, forming a strong ice-marine correlation (Fig 8.5, 8.6). The integrity of this deposit has been tested rigorously through the use of sedimentological analysis to corroborate primary deposition and refine the position of the tephra isochron (Table 8.1).

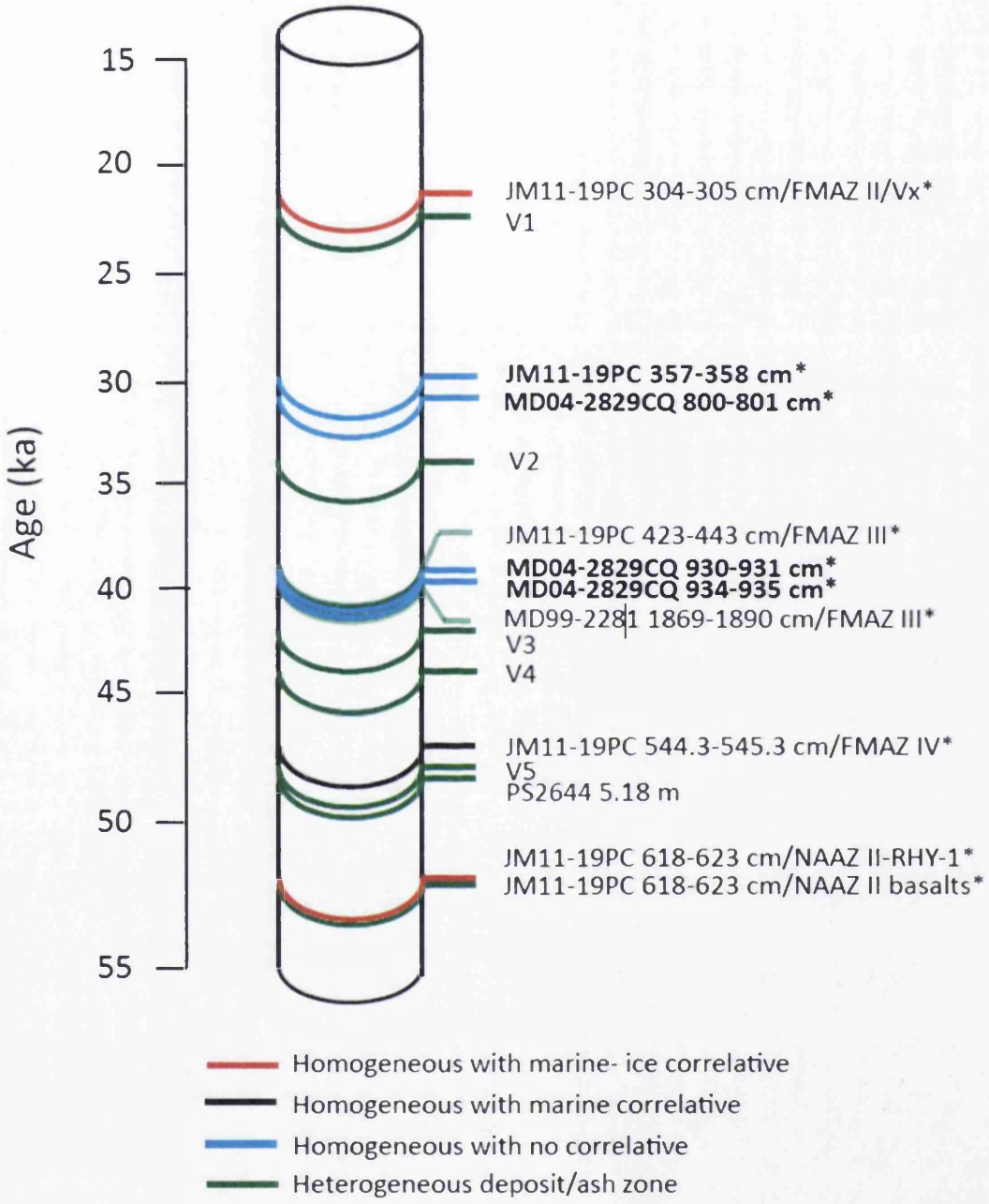

Figure 8.4 North Atlantic marine tephrochronological framework. Tephra deposits detected within the study have been added to the existing framework and their geochemical correlatives have been indicated. JM11-19PC 304-305 cm and JM11-19PC 544.3-545.3 cm are macrotephras. The integrity of the deposit has been shown in a colour system, dependent upon their geochemical characteristics and taphonomical expressions within sequences. Deposits highlighted in bold represent previously unknown tephras and * indicate additions to the framework presented in this study.

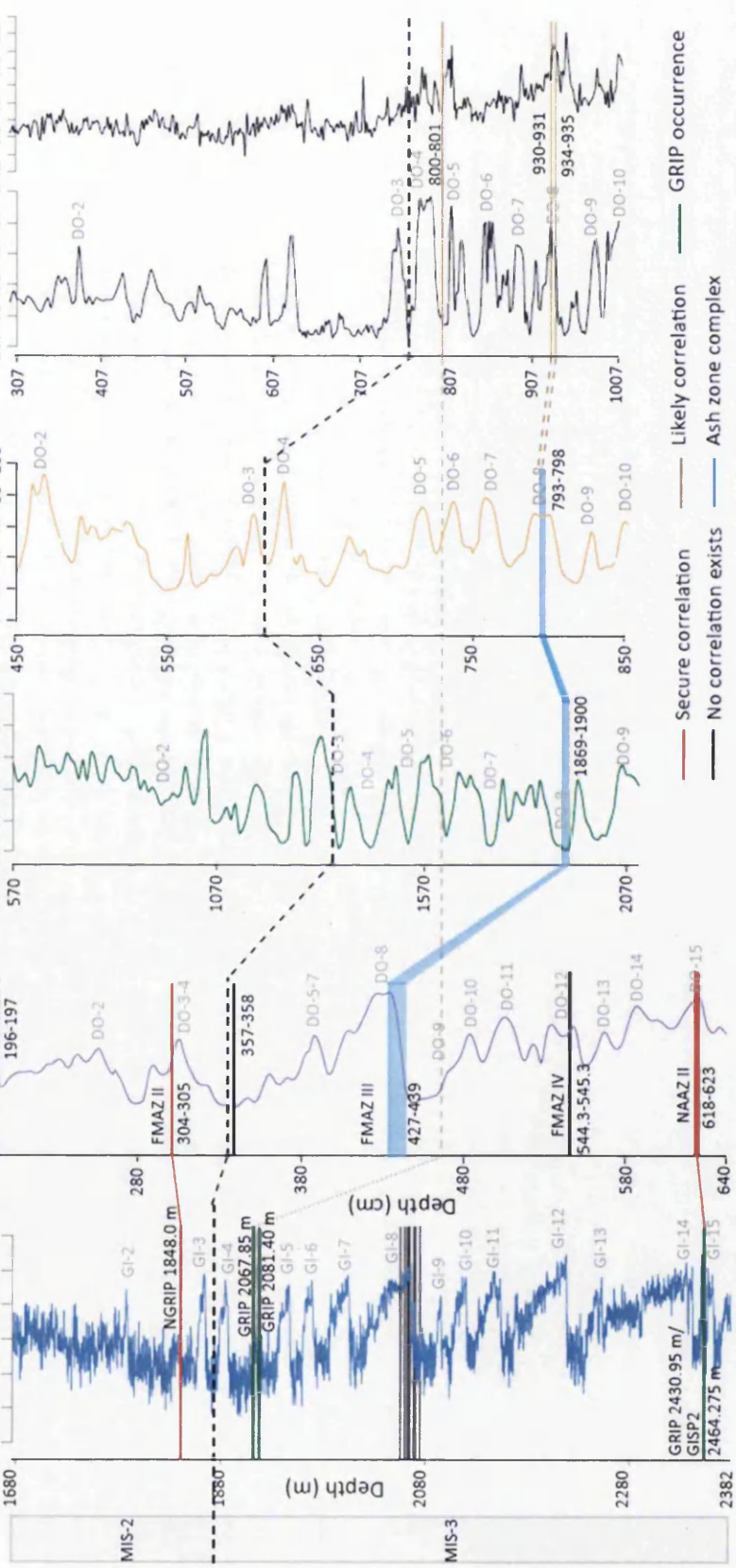

Figure 8.5 Tephra based marine and ice-core correlations between each core analysed within the thesis. The thickness of the bars represent the stratigraphic dispersion according to shard concentrations. Corresponding proxy information is derived from Ezat et al. (2014), Zumaque et al. (2012), Eynaud et al. (2002) and Hall et al. (2011). The strength of the isochron has been determined using diagnostic indicators presented within the marine tephrochronological protocol and shown visually by the colours described within the key. Approximate D-O positions have been presented. GRIP tephra occurrences are highlighted in green. It is noted that MD99-2281 has only been analysed between 1869-1900 cm.

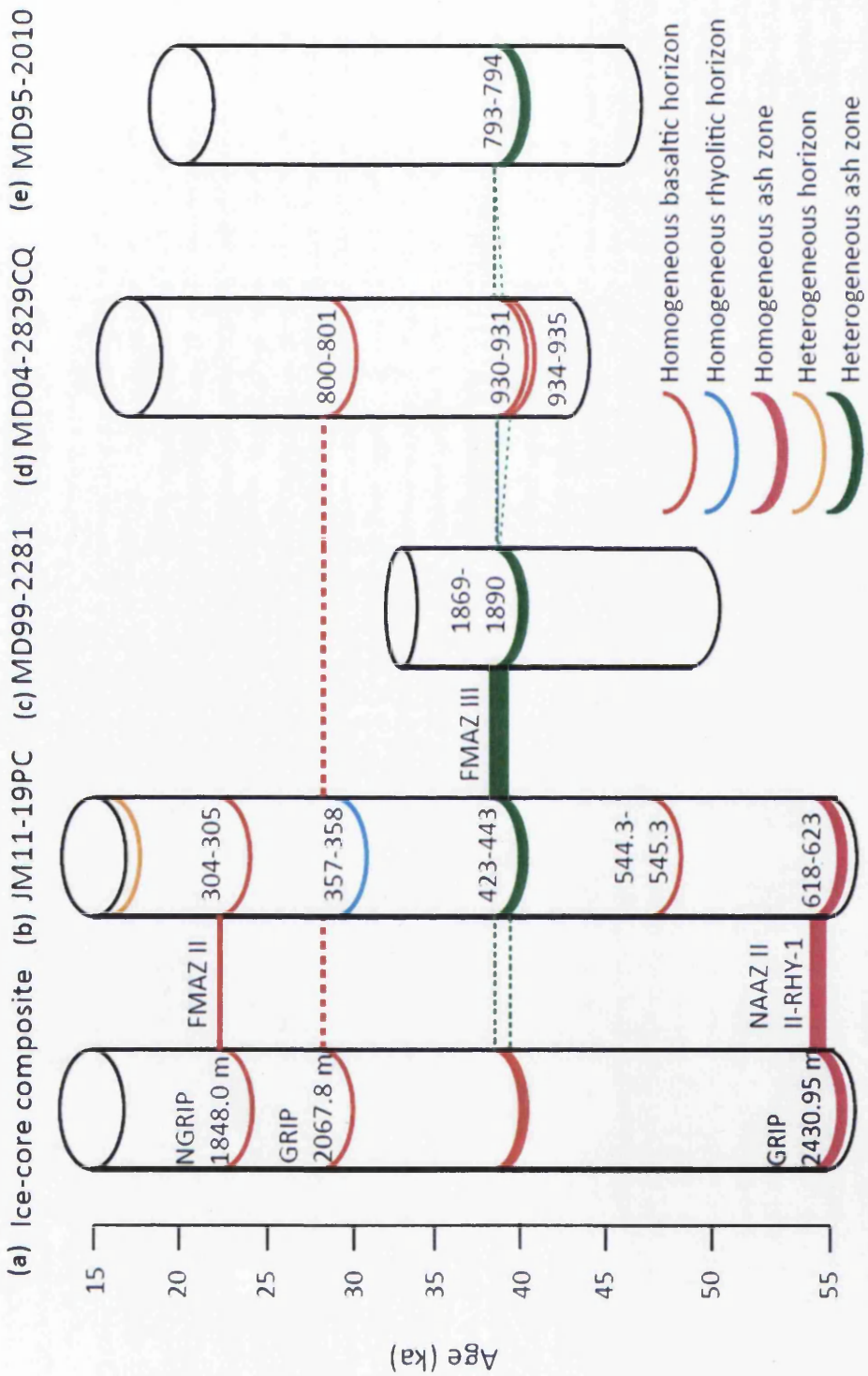

Figure 8.6 Schematic tephra framework for marine cores analysed within the study and correlations with those found in the Greenland ice-cores. The age scale is approximate and is for stratigraphic purposes only. The integrity of the isochron has been determined using diagnostic indicators presented within the marine tephrochronological protocol and shown visually by the colours described within the key. It is noted that MD99-2281 has only been analysed between 1869-1900 cm. The red line at ~38 k in the ice-cores represents the stratigraphically equivalent horizons to the FMAZ III.

Although this horizon has not been detected in other cores within this investigation, this deposit is widespread in other Faroese records (Rasmussen et al., 2003), the Labrador Sea (Wastegård et al., 2006) and a single Reykjanes Ridge record (Lackschewitz and Wallrabe-Adams, 1997) (Fig 8.4).

According to the stratigraphic position of 304-305 cm, the tephra was deposited in a cold period above the warmest phase of DO-3, as inferred from the magnetic susceptibility record in JM11-19PC (Fig 8.5). The FMAZ II has additionally been detected in association with low magnetic susceptibility values, after the warmth of DO-3, in nearby Faroese cores (Fig 8.7). Similarly, the tephra falls stratigraphically in a prolonged cold period after GI-3 within NGRIP, which permits an assessment of climatic phasing (Fig 8.4, 8.7). The FMAZ II is located on the falling limb of DO-3 in JM11-19PC, LINK15 and ENAM93-21, which may reflect a slight delay in cooling recorded in the North Atlantic (Fig 8.7). However, this may reflect a lag in the deposition of magnetic particles into the local system. Although the tephra fell within a cold period, precluding an assessment of abrupt climate transitions, the correlation can be used to suggest a coupling between the oceans and atmosphere at this point (Fig 8.4, 8.7). Therefore, the deposit represents a well-defined isochronous marker that can be used for high-resolution correlations.

8.3.2 NAAZ II

A bimodal homogeneous deposit, JM11-19PC 618-623 cm, exhibits a significant peak of basaltic (II-THOL-2) and rhyolitic (II-RHY-1) geochemistries. In the absence of high-resolution shard concentration profiles, it is difficult to assess whether these populations exhibit a stratigraphic separation or occur contemporaneously. Nonetheless, the II-RHY-1 component exhibits an ice-core correlative (GRIP 2430.95 m) and is detected in a number of North Atlantic records and nearby Faroese sequences (Fig 8.5, 8.6, 8.7). The stratigraphic position of the II-RHY-1 component in JM11-19PC, LINK 16 and ENAM 93-21 falls on the peak warmth according to the magnetic susceptibility record (Fig 8.6).

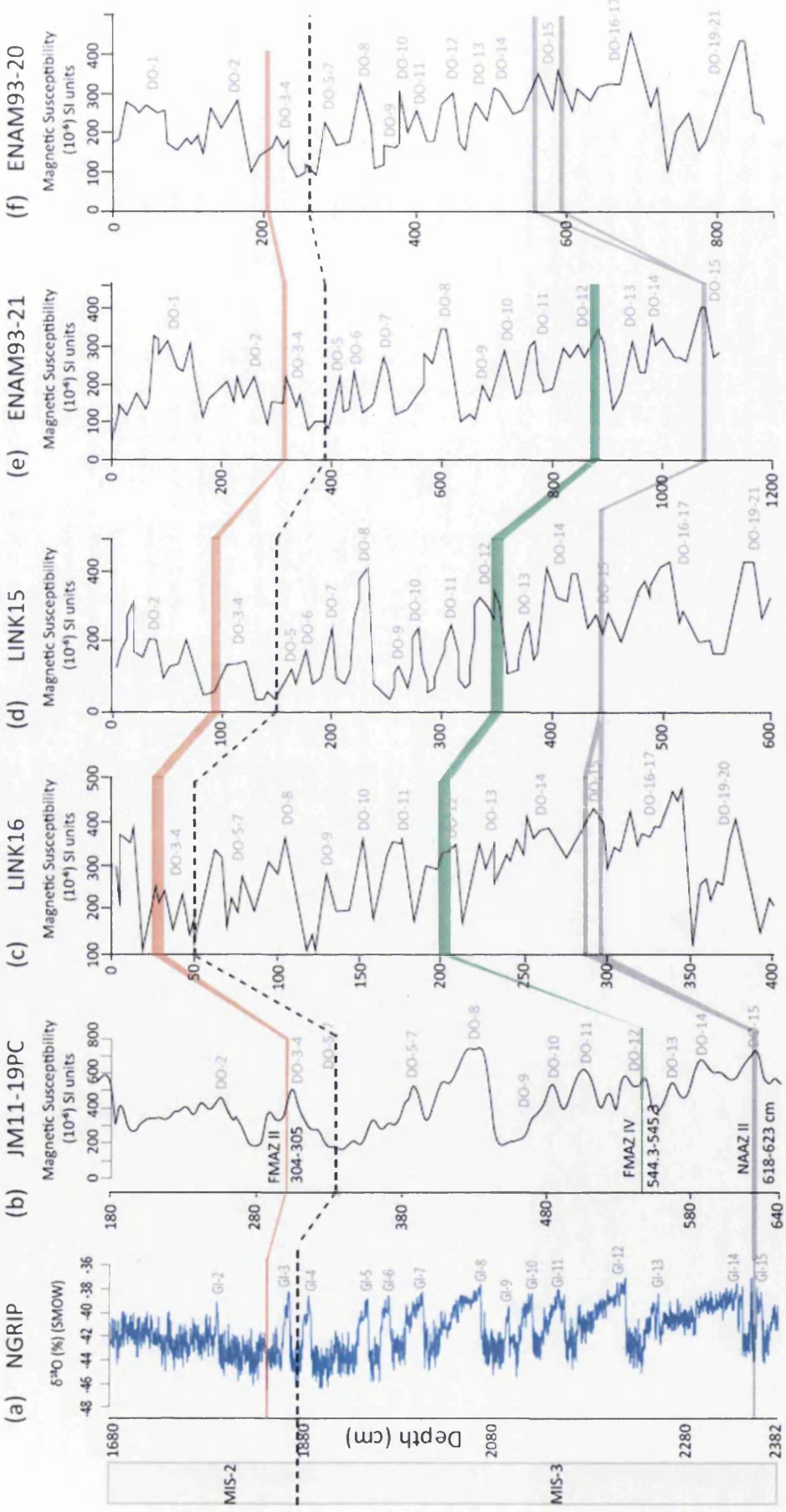

Figure 8.7 Magnetic susceptibility and positions of the FMAZ II, IV and NAAZ II within the (a) Greenland ice-cores, (b) JM11-19PC and (c-f) additional cores from the Faroes region (Wastegård and Rasmussen, 2014). Horizontal bars indicate the position of the tephra deposits. Approximate DO positions have additionally been defined after Wastegård and Rasmussen (2014).

However, II-RHY-1 falls on the rapid transition between GI-15 and GS-15 in the ice-core records, indicating cooling may have been initiated in the atmosphere prior to cooling in the marine realm (Fig 8.7). This may indicate an atmospheric driver of climatic events during GI-15. This is in contrast to previous studies by Austin et al. (2004) and Brendryen et al. (2011), who suggest the rapid climate transitions between GI-15 and GS-15 occurred synchronously between the ice and oceanic realms. These investigations utilise other paleoceanographic proxies i.e. *N. pachyderma* sin., which do not record the same changes as magnetic susceptibility. As such, the proxy used within each study affects these interpretations. DO-15 is not as pronounced in the magnetic susceptibility record of LINK15 in comparison to nearby records and appears to fall in the peak cooling associated with DO-15 (Fig 8.7). The initial II-RHY-1 occurrence in ENAM93-21 falls on the warming limb of DO-15 (Fig 8.7). Despite the close geographical location of Faroese cores, their corresponding magnetic susceptibility record is variable and suggests local depositional controls have affected the magnetic signal. As a consequence, this affects the reliability of the climatic signal recorded in the magnetic record and plagues judgment on the phasing of rapid climatic changes.

The widespread distribution of the NAAZ II across the North Atlantic provides a viable means to correlate between distal marine records. This will be particularly useful for deciphering the presence of other geochemical components of this ash zone and regional dispersal mechanisms. NAAZ II is additionally useful for comparing paleoclimate signals in a time period where chronological control is rare and models are largely constructed by direct synchronisation of $\delta^{18}O$ stratigraphies.

8.3.3 FMAZ III

A composite of cryptotephra deposits and shards, defined as the FMAZ III in the marine environment, have been identified straddling DO-8 within JM11-19PC, MD99-2281 and tentatively in MD95-2010 (Fig 8.5, 8.6). Rigorous geochemical analyses reveal significant heterogeneity in JM11-19PC, MD99-2281 and MD95-2010. It has been suggested that the frequency of Grímsvötn-sourced eruptions during this period, as observed in the Greenland ice-core framework, has contributed

towards the observed heterogeneity. There is disparity identified within the heterogeneous distributions between cores. JM11-19PC exhibits a greater concentration of shards with higher TiO_2 and lower CaO contents, whereas MD99-2281 exhibits a greater number of shards with lower TiO_2 and higher CaO contents (Fig 8.8a). This suggests differing depositional controls and may be related to shifts in the dominant wind dispersal trajectories following individual eruptions. Even within heterogeneous deposits, a different suite of eruptions may be represented.

The presence of two homogeneous populations in MD04-2829CQ and the absence of additional populations associated with the FMAZ III composite are unique, and likely related to both air dispersal and site-specific sedimentation processes (Fig 8.6). One of the distinct populations, MD04-2829CQ 930-931 cm, appears to be unrelated to glass shards from other marine cores as demonstrated on TiO_2 vs CaO biplots, but falls within the general FMAZ III envelope (Fig 8.8a). A greater number of shards from this population overlap with other element oxides on TiO_2 vs FeO/MgO biplots, but these geochemical compositions are generally low in other records (Fig 8.8b). There is minimal overlap of this population with stratigraphically equivalent ice-core horizons, but the composition falls within the general Grímsvötn evolutionary trend for this period. It is likely that this horizon represents an eruption that is currently undetected in the Greenland records and other marine records.

The second homogeneous horizon, 934-935 cm, was initially thought to represent a strong correlation to NGRIP 2071.50 m and NEEM 1759.85 m. If a correlation were to exist, the stratigraphic position of this horizon indicates warming in the oceans preceded warming in the atmosphere. This implies that the ocean was the primary driver of abrupt climate changes (Fig 8.4). However, significant differences in barium and niobium concentrations between 934-935 cm and NEEM 1759.85 m highlight discrepancies in trace element composition. This suggests that these two deposits have been derived from a separate magma chamber and are therefore likely to represent two separate eruptions. It is likely that more eruptions may have occurred in DO-8 than are documented in the Greenland ice-core framework.

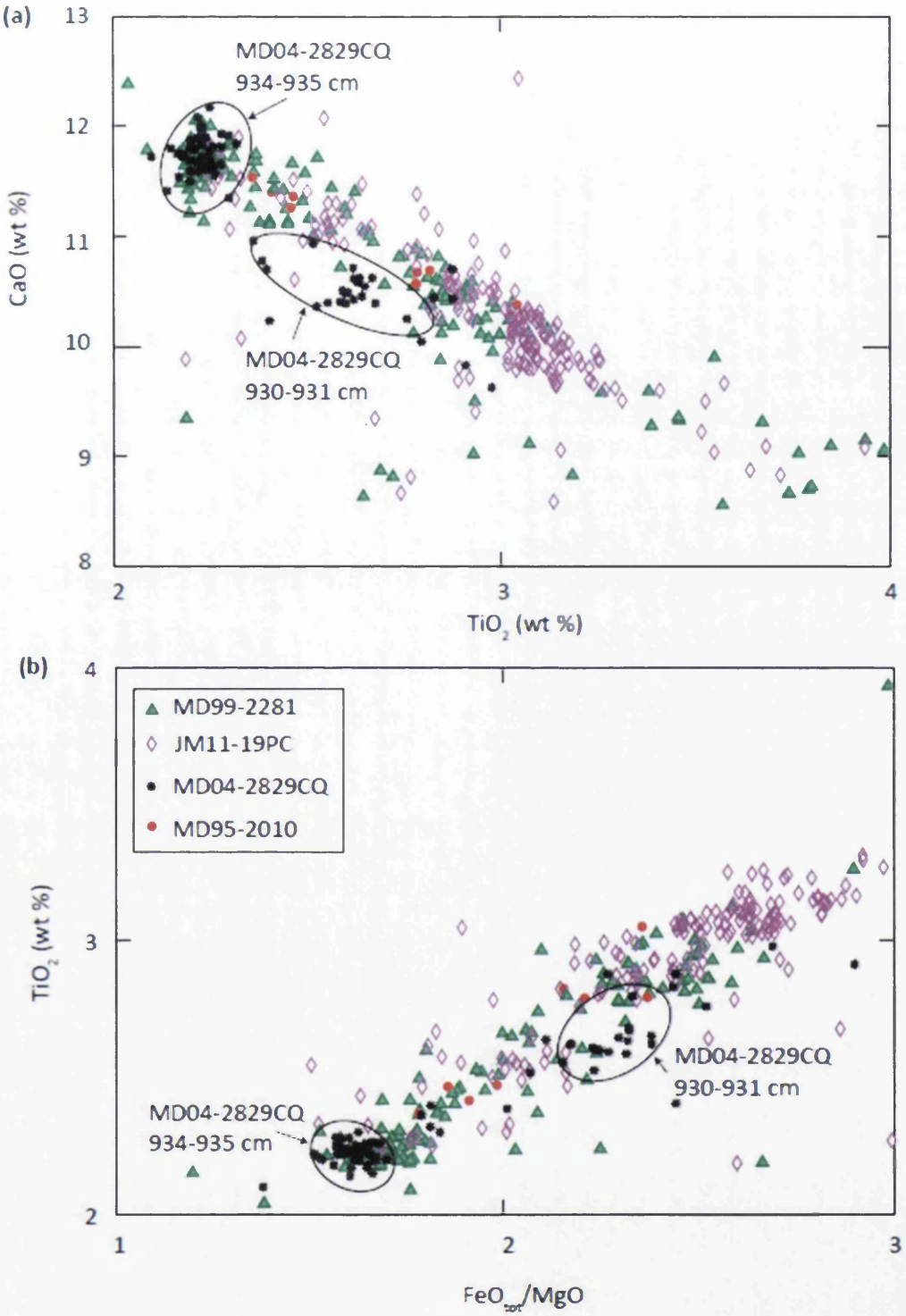

Figure 8.8 Major oxide results for FMAZ III deposits found within each of the four investigated marine cores. All data have been normalised to 100% total oxide concentration. Individual populations in MD04-2829CQ have been highlighted (outliers have been included).

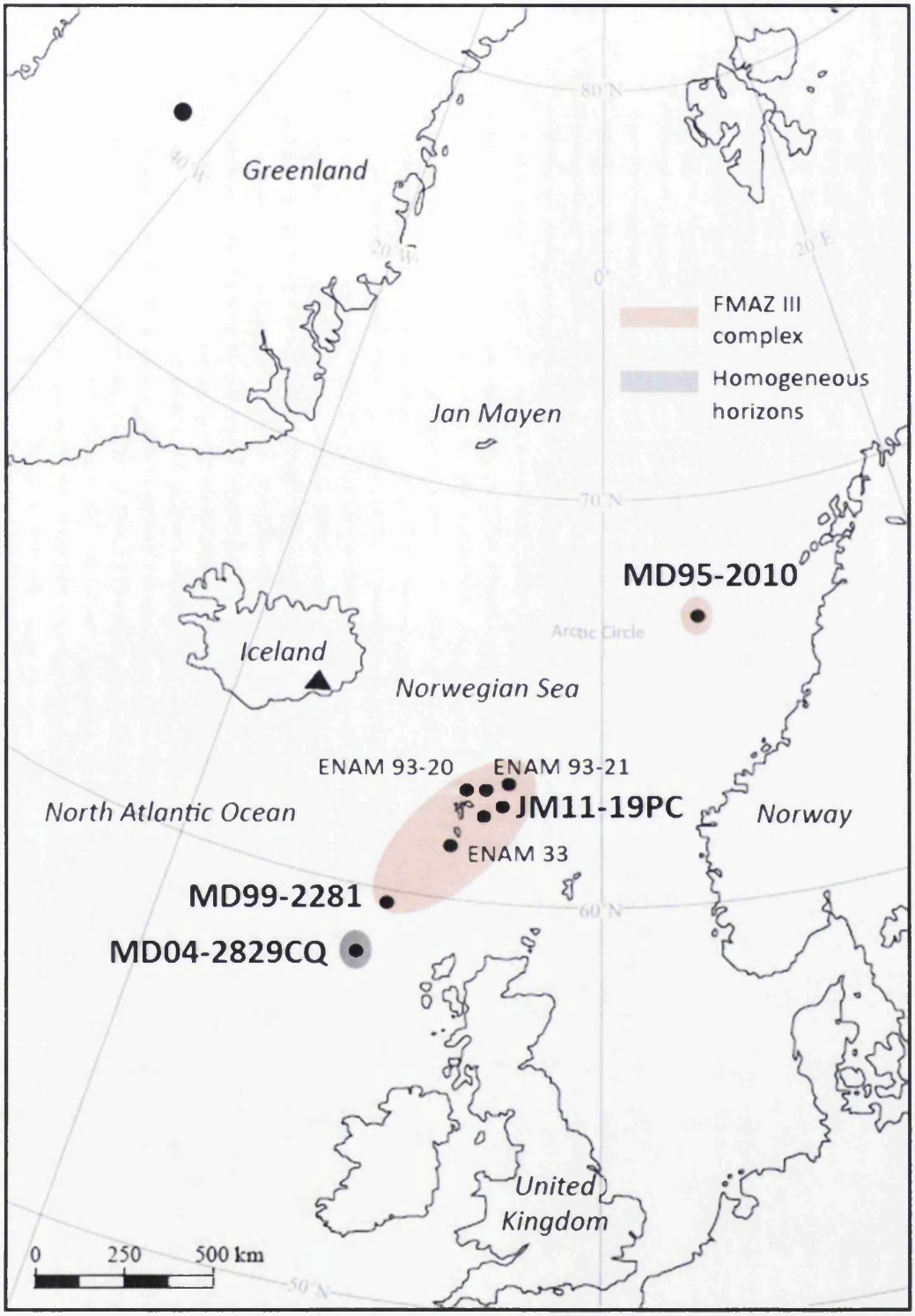

Figure 8.9 Distribution of the FMAZ III in the North Atlantic. Marine occurrences in the Faroes region consist of a heterogeneous complex of multiple eruptions (Rasmussen et al., 2003; Wastegård et al., 2006; this study). MD04-2829CQ consists of two stratigraphically separated homogenous horizons that may not be related to the FMAZ III. MD95-2010 consists of shards that share geochemical similarity to the FMAZ III but cannot be confidently be considered of sufficient quantity to constitute an isochron.

As a consequence, correlations between cores that exhibit similar major element geochemistries may also contain composites of glass shards sourced from different magma chambers within the Grímsvötn system and may not be genetically related. MD04-2829CQ is located outside of the Faroes region and the two homogeneous horizons may be unrelated to the FMAZ III complex detected in Faroese records, despite exhibiting similar major element geochemistry. As such, there is no unambiguous geochemical evidence to provide a correlative link between the FMAZ III and stratigraphically equivalent ice-core horizons. Tephra preserved in the ice may be sourced from eruptions that exhibit different dispersal pathways compared to those recorded in the marine environment. In light of this information, marine-marine correlations of the FMAZ III are to be exercised with care. More work is needed to characterise trace-element compositions of the FMAZ III and ice-core horizons in DO-8 to assess genetic similarities between different occurrences in the North Atlantic.

A fundamental perquisite for synchronising records between the marine and cryospheric realms relies on the completeness of the Greenland ice-core records for documenting eruption histories and the preservation of common tephra horizons. An incomplete volcanic event stratigraphy reduces the likelihood for locating a stratigraphically distinct horizon in the oceans that exhibits the same geochemical composition as an ice-core horizon. Generally, geochemical heterogeneity is a common feature of marine sequences during DO-8 and this plagues the integration of records. Despite the stratigraphic importance of the FMAZ III and stratigraphically equivalent ice-core horizons, there may be more important isochrons to focus on tracing in the marine environment. Ideally, these will bracket rapid climate transitions, be geochemically distinctive and occur during a period of relative volcanic quiescence. These characteristics should increase the likelihood of stratigraphic separation in the marine environment, coupled with a diagnostic geochemical fingerprint. Essentially, it may be advantageous to focus on tephras sourced from volcanic centres other than Grímsvötn to increase the likelihood of tracing a geochemically distinct deposit.

Nonetheless, a rigorous investigation into the FMAZ III has revealed a wealth of complexity associated with eruption frequency, geochemical subtleties and marine

deposition. By its very nature, the FMAZ III forms a diachronous surface in the marine environment and may be useful exclusively as a low-resolution marker in marine studies for DO-8 (Fig 8.5, 8.6). The deposit has been traced in the Rockall Trough, the Faeroes Region and tentatively to the Norwegian seas, which provides a means to link records together in DO-8, similarly to the way the NAAZ II is used as a marker for DO-15.

8.3.4 FMAZ IV

A basaltic macrotephra, JM11-19PC 544.3-545.3 cm (FMAZ IV), exhibits a homogeneous peak with a significant upward tail sourced from Grímsvötn. Despite the stratigraphic dispersion, the integrity has been tested rigorously using 2D and 3D analysis to realign the position of the isochron to best reflect the initial input of primary deposition (Table 8.1). No Grímsvötn-sourced deposits exist within the ice-core framework for this period and it is difficult to assess whether the upward tail is a reflection of re-working or several closely spaced eruptions. However, FMAZ IV has been found in numerous other Faroese records and provides a useful marine-marine correlation (Fig 8.7) (Wastegård and Rasmussen, 2014). High magnetic susceptibility values suggest deposition occurred during peak interstadial conditions associated with DO-12 in JM11-19PC, LINK16 and ENAM93-21 (Fig 8.7). However, the initial FMAZ IV input falls on the warming limb of LINK15 (Fig 8.7d). This may be a consequence of post-depositional modification and incorrect isochron placement. If other marine occurrences of this deposit can be traced outside the Faroes region, it may facilitate the piecing together of a reconstruction of oceanic responses in the marine realm during DO-12.

A potential caveat with FMAZ IV is the diffuse nature of the deposit. Without the addition of 3D analysis, isochron placement would be challenging and this may have implications for similar FMAZ IV deposits detected in other cores. Nonetheless, FMAZ IV in JM11-19PC has been well constrained, and caution is encouraged when linking this deposit to other FMAZ IV records.

8.3.5 MD04-2829CQ 800-801 cm

A homogeneous horizon, MD04-2829CQ 800-801 cm is a new discovery and exhibits a well-resolved discrete peak and represents a tentative ice-marine correlation (Fig 8.5). Although no similar correlatives have been detected in the marine environment, there are numerous ice-core horizons that exhibit a similar tholeiitic basalt composition of Kverkfjöll origin. Subtle differences in TiO_2 indicate a strong geochemical overlap with GRIP 2067.85 m and GRIP 2081.40 m but cannot be distinguished using major element signatures in isolation. Stratigraphically, GRIP 2067.85 m falls on the cooling transition of GI-5.1 and is more likely to be related to the 800-801 cm horizon, which is located during peak stadial conditions following DO-5 (Fig 8.5). As this horizon brackets a rapid climatic transition, future trace element geochemistry is necessary to facilitate potential synchronisation and permit an assessment of phasing relationships. The presence of a secondary Grímsvötn population in 800-801 cm is highlighted, due to the absence of Grímsvötn-sourced basalts in the ice-core framework during this period. It is likely this represents a contemporaneous eruption with a dispersal pathway south of Greenland. This deposit may hold considerable potential for use as a high-resolution isochronous marker horizon.

8.3.6 JM11-19PC 357-358 cm

A homogeneous rhyolitic horizon, JM11-19PC 357-358 cm, is a new addition to the tephrochronological framework. The horizon exhibits a well-resolved peak that is likely to be sourced from the Katla system and shows no affinity to any horizons present within the Greenland ice-cores (Fig 3.5). The predominant absence of rhyolitic material in the ice may be a reflection of eruption dynamics and preferential transport pathways south of Iceland. Additionally, no homogeneous rhyolitic deposits have been previously discovered within the North Atlantic during MIS 3 (Fig 8.4). Homogeneous rhyolitic tephras are rare, although numerous rhyolitic deposits have been detected in marine sequences spanning MIS 4 and 5 (Brendryen et al., 2010; Abbott et al., 2013; Davies et al., 2014). This may be a consequence of

limited cryptotephra investigations conducted during MIS 3, or the use of different methods employed to isolate rhyolitic cryptotephra shards. The tight homogeneity indicates it may be useful for high-resolution correlations. However, Katla sourced rhyolites appear to exhibit very similar geochemical compositions throughout Pleistocene and Holocene records, and distinguishing between individual eruptions may be problematic (Lane et al., 2012). Indeed, rigorous trace element characterisation may not offer sufficient diagnostic capabilities (Lane et al., 2012). Careful stratigraphic scrutinisation may aid correlations between sequences, but it is currently unclear how many Katla eruptions occurred during this period and therefore any future correlations are to be exercised with care.

8.4 How valuable is the framework? Potential and future challenges

The identification of twelve tephra deposits during MIS 2 and 3 within four cores makes a significant contribution to the tephrochronological framework for the North Atlantic region (Fig 8.6). The emerging framework contributes to previous low-resolution tephra frameworks for the North Atlantic and forms the basis for identification of coeval cryptotephra deposits in other disparate archives. Successful framework development has resulted from the fulfillment of key criteria such as robust geochemical characterisation and rigorous taphonomic assessments to successfully pinpoint the correct stratigraphical placement of the isochron.

Key functions of the framework include the ability to facilitate synchronisation between the ice and marine realms to assess climate phasing. JM11-19PC 304-305 cm is constrained to a 1 cm interval and exhibits a homogeneous geochemical population, with a unique geochemical signature directly comparable to an ice correlative. Tephras of this nature satisfy stringent criteria to demonstrate the utmost integrity of the deposit. An insight into phasing associated with abrupt climate events is prevented due of the timing of deposition during stable climatic conditions, although it still has value for constraining time-slices. In contrast, ice-core horizons deposited during DO-8 bracket an abrupt transition but, as yet, there has been a failure to detect a common stratigraphically equivalent horizon in the marine

environment that is well-constrained and exhibits a distinct geochemical composition. It is essential that a distinction is made to determine whether a valuable isochron is defined by; a) a primary deposit with secure isochron placement, or; b) important stratigraphic placement facilitating an assessment of abrupt climate phasing. There is little value in a geochemically heterogeneous deposit or one where an isochron position cannot be confidently discerned, even if it falls on a rapid event. In essence, primary deposition must first be discerned before evaluating its stratigraphic placement. This has important ramifications for targeting future core locations and stratigraphic sampling windows.

The fundamental purpose of a secure isochron is the ability to trace coeval deposits with confidence, precision and to successfully integrate unique proxy evidence. This study set out to test phasing relationships over abrupt transitions, however it has become clear that a variety of complex challenges must be addressed before this can be achieved. Given the complexity associated with atmospheric dispersal patterns and processes operating internally with the marine environment, targeting site locations that are likely to produce well-constrained primary isochrons represents an integral task. Marine cryptotephra investigations are still in their infancy and much is to be gained from future examinations of shard distributions and taphonomy. When this information is used in conjunction with ongoing tephra searches in the Greenland ice-cores, it should permit a deduction of tephras that have the potential to fulfil a pivotal role in testing climatic phasing relationships. Primary isochrons also have a clear role in augmenting volcanic histories and dispersal compilations where proximal and medial evidence is limited. Additional uses include an assessment of marine reservoir offsets when used in tandem with radiocarbon dating.

This study has additionally demonstrated that a unique set of depositional parameters are required to produce well-resolved primary deposits with diagnostic chemical signatures. Fundamentally, these are dependent upon the diagnostic chemistry of the eruptive source and are compromised by the eruptive frequency, oceanographic regime and site-specific sedimentation. Recent cryptotephra studies have encouraged investigations of deposits in high-sedimentation areas of the North Atlantic in order to increase the chances of tephras preserved as discrete deposits (Bourne et al., 2013, Davies et al., 2014). However, as demonstrated in MD99-2281, even in records of

high-sedimentation, intervals characterised by numerous closely spaced eruptions have provided significant tephra input into the ocean system. As a consequence, in tandem with bottom current reworking, eruptive frequency has prevented a clear stratigraphic separation of the tephra deposit. This indicates that in locations sensitive to bottom current circulations, cores may be composed of tephra-rich material that produces a high background of glass shards. It may be more fruitful to target areas outside of the Faroes region or specific intervals unaffected by intense bottom current circulations, irrespective of sedimentation rate. Areas of sheltered bathymetry i.e. south of MD04-2829CQ in the Rockall Trough, may provide ideal conditions for preserving discrete tephra horizons. Conversely, JM11-19PC 304-305 cm represents a strong primary isochron, despite influence from the above aforementioned factors. This is attributed to a catastrophic input event that preserved the deposit. Indeed, even in unfavorable locations, unique input events may be crucial for seeking isochrons.

It is clear that a variety of complex challenges are associated with North Atlantic marine tephrochronology. Correlating deposits to the Greenland ice-cores has been more difficult than previously envisaged. This is due to subtle geochemical differences between equivalent horizons and a potentially incomplete volcanic event stratigraphy that might not preserve common horizons due to different transport pathways. Nonetheless, the comprehensive geochemical dataset of deposits presented are of great importance for tracing these into other sequences. Each building block in the framework has the potential to widen the geographical area over which precise correlations are achievable. Future success in this approach is dependent upon rigorous assessments of marine taphonomy and robust geochemical fingerprinting. Undoubtedly, cryptotephrochronology is a powerful tool that has the potential to test climatic synchroneity. This requires a concerted effort to reconstruct the full tephra distribution in the North Atlantic region and subsequent construction of a more complete volcanic event stratigraphy.

Chapter 9 Conclusions

9.1 Summary of the main findings

The overall aim of this work was to develop a framework of isochronous tephras in North Atlantic marine sequences during MIS 2-3 that could act as tie-points to the Greenland ice-cores. A key premise of this work was the development of a protocol that facilitated an assessment of the isochronous nature of tephra deposits in the marine environment with a particular focus on those present in cryptotephra form. To achieve this goal, the potential of utilising innovative sedimentological techniques was explored to fully unravel the transport and depositional processes operating in the marine environment. This multi-faceted approach has resulted in the development of a considered framework of volcanic events that represent the most valuable deposits for the correlation of disparate records of Late Pleistocene age. Two ice-marine tie-lines demonstrate the future potential of assessing the relative timing of rapid climatic changes. The main findings are outlined as follows:

(a) Twelve tephra deposits are identified in four North Atlantic marine records using a combination of density and magnetic separation techniques. Methodological procedures for the latter technique were optimised to successfully extract basaltic cryptotephra from mineral-rich marine sediments. Ten deposits are determined to be primary isochrons based on diagnostic indicators such as geochemical homogeneity and dominance of fine-grained shards (<80 μm). Eight of these are cryptotephra deposits and single-shard geochemical analyses together with stratigraphic positions are employed to develop a tephrochronological framework for the North East Atlantic. Basaltic deposits from the Grímsvötn system dominate the framework and highlight the eruptive frequency of this system during the last glacial period. Four deposits (one rhyolitic and three basaltic deposits) have not been detected in the ice-

core framework and expand the volcanic event stratigraphy. Six deposits extend previously known tephra horizons into other marine records. Rhyolitic isochrons in marine sequences are rare during MIS 3 and may reflect differing air dispersal trajectories or relative infrequency of silicic eruptions. Only two of the tephras in this framework, FMAZ II and NAAZ II, represent ice-marine tie-lines. The remaining tephras in this framework, however, are considered the most valuable as potential tie-points that remain to be identified in the ice-core records or may well be present in other marine or terrestrial deposits.

(b) Geochemical, stratigraphical and sedimentological indicators are embedded within a new protocol to help assess the depositional integrity of tephra deposits. Only deposits considered to represent primary events are included within the tephrochronological framework. Diagnostic signs of secondary transported cryptotephra deposits include a heterogenous geochemical population that may straddle several rock suites, an associated peak in IRD and a diffuse shard concentration profile. Such characteristics may indicate an ice-rafted origin. This range of indicators was used in conjunction with a variety of climatic and palaeoceanographic information to help determine the dominant method of tephra delivery to the sea-floor. A key condition of this protocol is that the indicators are considered collectively and an assessment of depositional integrity cannot be founded solely on a single indicator. The development of this protocol represents a significant step for optimising the application of marine-based isochrons for both the TRACE project and future work. What is more, this marine tephra protocol has potential applications for palaeoceaongraphers for estimating bioturbation processes and provides the foundation for taphonomic tephra toolkits for terrestrial environments.

(c) The application of thin-section and μCT analysis to visualise tephra deposits offers new insight into the processes controlling transportation and deposition. These techniques have revealed post-depositional processes that were not fully captured using conventional stratigraphic methods. Micro-sedimentological analysis represents a new addition to the protocol and enables refinement and correct

stratigraphical placement of the isochron. Indeed, these techniques have suggested the tephra isochron is not always laterally continuous or represented by the peak in shard concentration.

(d) Cryptotephra records from the different marine records are spatially and temporally variable particularly in relation to: a) the presence/absence of marine tephra deposits; b) the concentration of glass shards within a tephra deposit; c) their stratigraphic dispersion and shard concentration profiles, and d) the depositional processes operating at the site. These characteristics may reflect different air dispersal trajectories, internal dynamics of the ocean environment, sedimentation rate and proximity to ice-rafting pathways.

(e) The two ice-marine correlatives facilitate an exploration of the relative timing of climatic transitions. JM11-19PC 304-305 cm (FMAZ II) is located in association with low magnetic susceptibility values during DO-3 and within NGRIP the horizon falls stratigraphically in a prolonged cold period after GI-3. This suggests a close coupling between the oceans and atmosphere at this point. In contrast, JM11-19PC 618-623 cm (II-RHY-I) falls on the peak warmth of GI-15 according to the magnetic susceptibility record but falls on the rapid transition between GI-15 and GS-15 in the ice-core. This may indicate that cooling may have been initiated in the atmosphere prior to cooling in the oceans. However, this may also be a consequence of local controls on the magnetic signal and limited understanding of the sensitivity and response of this proxy.

(f) One of the disappointing outcomes of this work is the difficulty of establishing an ice-marine tie-line during GI-8. The FMAZ III is a key marker horizon in the marine environment during this interval and the geochemical range of this deposit exhibits a broad compositional overlap with fourteen cryptotephra deposits preserved within the Greenland ice-cores. This is thought to indicate that the FMAZ III is an amalgamation of several closely spaced Grímsvötn eruptions that cannot be stratigraphically separated within the marine records investigated here.

One homogenous horizon detected in the Rockall Trough, however, exhibits exceptional major element overlap with a single equivalent ice-core horizon dating to 38.3 b2k. This was considered a significant finding and a potential ice-marine tie-line that would replace the compromised FMAZ III deposit. Differences in trace-element composition, however, suggest that the ice and marine deposits do not relate to the same volcanic event and hence no tie-line can be established. It seems that some eruptions may not be documented in the ice-core records during GI-8 and that this interval is characterized by an exceptionally complex period of volcanic activity. The FMAZ III, therefore, may only be used as a stratigraphic marker for the marine environment during DO-8 just as the NAAZ II is utilised as a marker for DO-15.

9.2 Recommendations for future work

(a) A concerted effort is necessary to explore whether the tephras in this framework can be traced into other records of last glacial age. Favourable locations include sequences retrieved from high sedimentation areas that are sheltered from intensive bottom currents. These are most likely to contain stratigraphically well-resolved, primary tephra deposits. MD04-2829CQ satisfied these criteria and therefore future searches may prove fruitful in locations to the south of this core site. What is more, there is much to be gained from targeting time-intervals that are characterised by tephras with unique and diagnostic geochemical signatures. Grímsvötn basalts have confounded the DO-8 interval and distinguishing between them has provided many challenges.

(b) A key component of any marine tephra study will require a full characterisation of geochemical fingerprint. Trace element analysis provides additional information for differentiating between deposits exhibiting similar major element compositions. Further trace element work, however, will also require a full consideration of magmatic evolution and characterisation of proximal deposits from different source volcanoes for data comparison exercises with distal deposits. Further

trace element analysis on deposits in this study includes characterisation of FMAZ III complexes from different sequences in the North Atlantic. Trace element analysis of stratigraphically equivalent ice-core horizons may provide an evaluation of compositional similarities with FMAZ III. These analyses are crucial to assess the synchronising potential of Grímsvötn tephras straddling DO-8.

(c) Together with rigorous characterisation procedures, the marine tephra protocol requires a careful consideration of a range of sedimentological indicators. It is imperative that the full range of indicators are considered and dependence on one characteristic is avoided. Following this protocol, it is crucial to ensure that the integrity of a deposit is assessed before being incorporated within the regional tephra framework.

(d) Each cryptotephra deposit and macrotephra deposit, where the basal contact is blurred, requires careful assessment of where to place the isochron. Given the spatial complexity and variability observed within small core sub-samples analysed using μCT, multiple sub-samples across several parallel vertical profiles should be extracted (where possible) to better constrain shard concentration profiles. This will hopefully identify and explore the lateral and horizontal continuity of tephra deposits in future tephra investigations. Further work is also required to test the viability of μCT for detecting cryptotephras.

References

Abbott, P.M., Davies, S.M., Austin, W.E.N., Pearce, N.J.G., Hibbert, F.D., 2011. Identification of cryptotephra horizons in a North East Atlantic marine recording spanning marine isotope stages 4 and 5a (similar to 60,000-82,000 a b2k). Quaternary International, 246, 177-189.

Abbott, P.M., Davies, S.M., Steffensen, J.P., Pearce, N.J.G., Bigler, M., Johnsen, S.J., Seierstad, I.K., Svensson, A., Wastegård, S., 2012. A Detailed Framework of Marine Isotope Stage 4 and 5 Volcanic Events recorded in two Greenland ice-cores. Quaternary Science Reviews. 36, 59-77.

Abbott, P.M., Austin, W.E.N., Davies, S.M., Pearce, N.J.G., Hibbert, F.D., 2013. Cryptotephrochronology of the Eemian and the last interglacial-glacial transition in the North East Atlantic. Journal of Quaternary Science. 28, 501-524.

Abbott, P.M., Austin, W.E.N., Davies, S.M., Pearce, N.J.G., Rasmussen, T.L., Wastegård, S., 2014. Re-evaluation and extension of the Marine Isotope Stage 5 tephrostratigraphy of the Faroe Islands Region: the cryptotephra record. Palaeogeography, Palaeoclimatology, Palaeoecology, 409, 153-168.

Abbott, P.M., Davies, S.M., 2012. Volcanism and the Greenland ice-cores: the tephra record. Earth-Science Reviews, 115, 173-191.

Alley, R.B., Meese, D.A., Shuman, C.A., Gow, A.J., Taylor, K.C., Grootes, P.M., White, J.W.C., Ram, M., Waddington, E.D., Mayewski, P.A., Zielinski, G.A., 1993. Abrupt increase in Greenland snow accumulation at the end of the Younger Dryas event. Nature, 362, 527-529.

Alley, R. B., Clark, P. U., Keigwin, L. D., Webb, R. S., 1999. Making sense of millennial-scale climate change, in: Mechanisms of global climate change at millennial time scales, edited by: Clark, P. U., Webb, R. S., Keigwin, L. D,. Geophysics Monograph, 385– 394.

Atkins, C.B., 2004. Photographic Atlas of striations from selected glacial and non-glacial environments. Antarctic Data Series No. 28. Antarctic Research Centre, Victoria, University of Wellington.

Austin, W.E.N., Wilson, L.J., Hunt, J.B., 2004. The age and chronostratigraphical significance of North Atlantic Ash Zone II. Journal of Quaternary Science. 19, 137-146.

Austin W.E.N., Hibbert, F.D., 2012. Tracing time in the ocean: a brief review of chronological constraints (60-8 kyr) on North Atlantic marine event-based stratigraphies. Quaternary Science Reviews, 36, 28-37.

Austin, W.E.N., Hibbert, F.D., Rasmussen, S.O., Peters, C., Abbott, P.M., Bryant, C.L., 2012. The synchronization of palaeoclimatic events in the North Atlantic region during Greenland Stadial 3 (ca 27.5 to 23.3 kyr b2k). Quaternary Science Reviews, 36, 154-163.

Austin, W.E., Abbott, P. A., 2010. Comment: Were last glacial climate events simultaneous between Greenland and France? A quantitative comparison using non-tuned chronologies. Blaauw, M., Wohlfarth, B., Christen, J.A., Ampel, D., Veres, K., Hughen, F., Preusser, Svensson, A., 2009. Journal of Quaternary Science, 25, 6.

Bard, E., 1998. Geochemical and geophysical implications of the radiocarbon calibration. Geochimica Cosmochimica Acta, 62, 2025–2038.

Barker, S., Chen, J., Gong, X., Jonkers, L., Knorr, G., Thornalley, D., 2015. Icebergs not the trigger for North Atlantic cold events. Nature, 520, 333-336

Begét, J., Mason, O., Anderson, P., 1992. Age, extent and climatic significance of the c. 3400 BP Aniakchak tephra, western Alaska, USA. The Holocene, 2, 51-56.

Belt, S.T., Muller, J., 2013. The Arctic sea ice biomarker IP25: a review of current understanding, recommendations for future research and applications in palaeo sea-ice reconstructions. Quaternary Science Reviews, 79, 9-25.

Bender, M., Sowers, T., Dickinson, M.L., Orchado, J., Grootes, P., Mayweski, P.A., Meese, D.A., 1994. Climate correlations between Greenland and Antarctica during the past 100,000 years. Nature, 372, 663-666.

Bendle, J.M., Palmer, A.P., Carr, S.J., 2015. A comparison of micro-CT and thin section analysis of Lateglacial glaciolacustrine varves from Glen Roy, Scotland. Quaternary Science Reviews, 114, 61-77.

Birks, H.H., Gulliksen, S., Haflidason, H., Mangerud, J., Possnert, G., 1996. New radiocarbon dates for the Vedde Ash and the Saksunarvatn Ash from Western Norway. Quaternary Research, 45, 119-127.

Blaauw, M., 2012. Out of tune: the dangers of aligning proxy archives. Quaternary Science Reviews, 36, 38-49.

Blaauw, M., Wohlfarth, B., Christen, J.A., Ampel, L., Veres, D., Hughen, K.A., Preusser, F., Svensson, A., 2009. Were last glacial climate events simulataneous between Greenland and France? A quantitative comparison using non-tuned chronologies. Journal of Quaternary Science, 24, 0, 1-8.

Blockley, S.P.E., Pyne-O'Donnell, S.D.F., Lowe, J.J., Matthews, I.P., Stone, A., Pollard, A.M., Turney, C.S.M., Molyneux, E.G., 2005. A new and less destructive laboratory procedure for the separation of distal glass shards from sediments. Quaternary Science Reviews, 24, 1952-1960.

Blockley, S.P.E., Lane, C.S., Lotter, A.F., Pollard, A.M., 2007. Evidence for the presence of the Vedde Ash in Central Europe. Quaternary Science Reviews, 26, 3030-3036.

Blockley, S.P.E., Lane, C.S., Hardiman, M., Rasmussen, S.O., Seierstad, I.K., Steffensen, J.P., Svensson, A., Lotter, A.F., Turney, C.S.M., Bronk Ramsey, C., 2012. Synchronisation of palaeoenvironmental records over the last 60,000 years, and an extended INTIMATE event stratigraphy to 48,000 b2k. Quaternary Science Reviews, 36, 2-10.

Blockley, S.P.E., Bourne, S.P.E., Bourne, A.J., Brauer, A., Davies, S.M., Hardiman, M., Harding, P.R., Lane, C.S., MacLeod, A., Matthews, I.P., Pyne-O'Donnell, S.D.F., Rasmussen, S.O., Wulf, S., Zanchetta, G., 2014. Tephrochronology and the extended INTIMATE event stratigraphy 8-128 ka b2k. Quaternary Science Reviews, 106, 1-13.

Bond, G., Heinrich, H., Broecker, W., Labeyrie, L., McManus, J., Andrews, J., Huon, S., Jantschik, R., Clasen, S., Simet, C., Tedesco, K., Klas, M., Bonani, G., Ivy, S., 1992. Evidence for massive discharges of icebergs into the North Atlantic ocean during the last glacial period. Nature 360, 245-249.

Bond, G., Showers, W., Cheseby, M., Lotti, R., Almasi, P., deMenocal, P., Priore, P., Cullen, H., Hadjas, I., Bonani, G., 1997. A pervasive millennial-scale cycle in North Atlantic Holocene and Glacial climates. Science, 278, 5341, 1257-1266.

Borchardt, G.A., Aruscavage, P.J., Millard Jr., H., 1972. Correlation of the Bishop ash, a Pleistocene marker bed, using instrumental neutron activation analysis. Journal of Sedimentary Petrology, 42, 201-206.

Boulay, S., 2000. Variabilité climatique rapide en atlantique nord - un potentiel de réponses: La carotte MD99-2281 (sud des îles faeroes), MASTER Université Paris-Sud, Orsay.

Bourne, A.J., 2012. The late Quaternary tephrochronology of the Adriatic region; implications for the synchronization of marine records. Unpublished PhD thesis, Royal Holloway, University of London, UK.

Bourne, A.J., Davies, S.M., Abbott, P.M., Rasmussen, S.O., Steffensen, J.P., Svensson, A., 2013. Revisiting the Faroe Marine Ash Zone III in two Greenland Ice Cores: implications for marine-ice-core correlations. Journal of Quaternary Science, 28, 641-646.

Bourne, A., Cook, E., Abbott, P.M., Seierstad, I., Steffensen, J., Svensson, A., Fischer, H., Schüpbach, S., Davies, S.M., 2015. A tephra lattice for Greenland and a reconstruction of volcanic events spanning 25–45 ka b2k. Quaternary Science Reviews 118, 122-141.

Boygle, J.E., 1994. Tephra in lake sediments: An unambiguous geochronological marker? PhD Thesis, University of Edinburgh.

Bramham-Law, C.W.F., Theuekauf, M., Lane, C.S., Mangerud, J., 2013. New findings regarding the Saksurnavatn Ash in Germany. Journal of Quaternary Science, 28, 248-257.

Bramlette, M.N., Bradley, W.H., 1941. Geology and biology of North Atlantic deep-sea cores between Newfoundland and Ireland: I. Lithology and geologic interpretation. U.S. Geological Survey Professional Paper. 196-A, 1–34.

Brauer, A., Haug, G.H., Dulski, P., Sigman, D.M., Negendank, J.F.W., 2008. An abrupt wind shift in Western Europe at the onset of the Younger Dryas period. Nature Geoscience, 1, 520-523.

Brauer, A., Hajdas, I., Blockley, S.P.E., Bronk Ramsey, C., Christl, M., Ivy-Ochs, S., Moseley, G.E., Nowaczyk, N.N., Rasmussen, S.O., Roberts, H.M., Spotl, C., Staff, R.A., Svensson, A., 2014. The importance of independent chronology in

integrating records of past climate change for the 60-8 ka INTIMATE time interval. Quaternary Science Reviews, 106, 47-66.

Brendryen, J., Haflidason, H., Sejrup, H.P., 2010. Norwegian Sea tephrostratigraphy of marine isotope stages 4 and 5: Prospects and problems for tephrochronology in the North Atlantic region. Quaternary Science Reviews. 29, 847-864.

Brendryen, J., Haflidason, H., Serjup, P., 2011. Non-synchronous deposition of North Atlantic Ash Zone II in Greenland ice cores, and North Atlantic and Norwegian Sea sediments: an example of complex glacial-stage tephra transport. Journal of Quaternary Science, 26, 7, 739-745.

Broecker, W.S., 2003. Does the trigger for abrupt climate change reside in the ocean or the atmosphere? Science, 300, 5625, 1519-1522.

Bromley, R.G., 1996. Trace fossils: biology, taphonomy and applications (second edition). Chapman and Hall, London.

Bromley, R.G., Ekdale, A.A., 1986. Composite ichnofabrics and tiering of burrows. Geological Magazine, 123, 59-65.

Cane, M. A., Clement, A.C., 1999. A role for the tropical Pacific coupled ocean-atmosphere system on Milankovitch and millennial timescales. Part II: Global impacts, in Mechanisms of Global Climate Change at Millennial Time Scales, Geophysiscs Monograph, 112, edited by P. U. Clark, R. S. Webb., Keigwin, L.D., 373–383, AGU, Washington, D. C.

Carey, S., 1997. Influence of convective sedimentation on the formation of wide-spread tephra fall layers in the deep sea. Geology, 25, 839-842.

Carter, L., Nelson, C.S., Neil, H.L., Froggatt, P.C., 1995. Correlation, dispersal and preservation of the Kawakawa tephra and other late Quaternary tephra layers in the Southwest Pacific Ocean. New Zealand Journal of Geology and Geophysics, 38, 29-46.

Cassidy, M., Watt, S.F.L., Palmer, M.R., Trofimovs, J., Symons, W., Maclachlan, S.E., Stinton, A.J., 2014. Construction of volcanic records from marine sediment cores: a review and caste study (Montserrat, West Indies). Earth-Science Reviews, 138, 137-155.

Clement, A.C., Peterson, L.C., 2008. Mechanisms of abrupt climate change of the last glacial period. Reviews of Geophysics, 46, RG4002.

Cnudde, V., Boone, M.N., 2013. High-resolution X-ray computed tomography in geosciences: a review of the current technology and applications. Earth-Science Reviews, 123, 1-17.

Cook, E., 2015. Tracing and constraining cryptotephra deposits in the Greenland ice-core records between GS-5.1 and the Early Holocene. Unpublished PhD thesis, Swansea University, UK.

Coulter, S.E., Pilcher, J.R., Plunkett, G., Baillie, M., Hall, V.A., Steffensen, J.P., Vinther, B.M., Clausen, H.B., Johnsen, S.J., 2012. Holocene tephras highlight complexity of volcanic signals in Greenland ice cores. Journal of Geophysical Research: Atmospheres, 117, D21.

Dansgaard, W., Clausen, H.B., Gundestrup, N., Hammer, C.U., Johnsen, S.J., Kristinsdóttir, P.M., Reeh, N., 1982. A new Greenland deep ice core. Science 218, 1273-1277.

Davies, S.M., 2015. Cryptotephras: the revolution in correlation and precision dating. Journal of Quaternary Science, 30, 2, 114-130.

Davies, S.M., Wohlfarth, B., Wastegård, S., Andersson, M., Blockley, S., Possnert, G., 2004. Were there two Borrobol Tephras during the early Lateglacial period: implications for tephrochronology? Quaternary Science Reviews, 23, 581-589.

Davies, S.M., Hoek, W.Z., Bohncke, J.P., Lowe, J.J., Pyne-O'Donnell, S., Turney, C.S.M., 2005. Detection of Lateglacial distal tephra layers in the Netherlands. Boreas, 34, 123-135.

Davies, S.M., Wastegård, S., Rasmussen, T.L., Svensson, A., Johnsen, S.J., Steffensen, J.P., Andersen K.K., 2008. Identification of the Fugloyarbanki tephra in the NGRIP ice core: a key tie-point for marine and ice-core sequences during the last glacial period. Journal of Quaternary Science. 23, 409-414.

Davies, S.M., Wastegaard, S., Abbott, P.M., Barbante, C., Bigler, M., Johnsen, S.J., Rasmussen, T.L., Steffensen, J.P., Svensson, A., 2010. Tracing volcanic events in the NGRIP ice-core and synchronising North Atlantic marine records during the last glacial period. Earth and Planetary Science Letters. 294 (1-2), 69-79.

Davies, S.M., Abbott, P.M., Pearce, N.J.G., Wastegård, S., Blockley, S.P., 2012. Integrating the INTIMATE records using tephrochronology: rising to the challenge. Quaternary Science Reviews, 36, 11-27.

Davies, S.M., Abbott, P.M., Meara, R.H., Pearce, N.J.G., Austin, W.E.N., Chapman, M.R., Svensson, A., Bigler, M., Rasmussen, T.L., Rasmussen, S.O., Farmer, E.J., 2014. A North Atlantic tephrostratigraphical framework for 130-60 ka b2k: new tephra discoveries, marine-based correlations, and future challenges. Quaternary Science Reviews, 1-21.

Dickson, R.R., Meincke, J., Malmberg, S.A., Lee, A.J., 1988. The 'great salinity anomoly' in the northern north Atlantic 1968-1982. Progress in Oceanography, 20, 103-151.

Dugmore, A.J., 1989. Icelandic volcanic ash in Scotland. Scottish Geographical Magazine, 105, 168-172.

Dugmore, A.J., Larsen, G., Newton, A.J., Sugden, D.E., 1992. Geochemical stability of fine-grained silicic Holocene tephras in Iceland and Scotland. Journal of Quaternary Science, 7, 173-183.

Dugmore, A., Newton, A., 2012. Isochrons and beyond- maximising the use of tephrochronology. Jökull 62, 39–52.

Eiríksson, J., Knudsen, K.L., Haflidason, H., Henriksen, P., 2000. Late-glacial and Holocene palaeoceanography of the North Icelandic shelf. Journal of Quaternary Science, 15, 23-42.

Enache, M.D., Cumming, B.F., 2006. The morphological and optical properties of volcanic glass: a tool to assess density-induced vertical migration of tephra sediment in cores. Journal of Paleolimnology, 35, 661-667.

Eynaud, F., Turon, J.L., Matthiessen, J., Kissel, C., Peypouquet, J.P., De Vernal, A., Henry, M., 2002. Norwegian sea-surface palaeoenvironments of marine oxygen-isotope stage 3: the paradoxical response of dinoflagellate cysts. Journal of Quaternary Science, 17, 349–359.

Ezat, M.M., Rasmussen, T.L., Groeneveld, J., 2014. Persistent intermediate water warming during cold stadials in the southeastern Nordic seas during the past 65 k.y. Geology, 663–666.

Fisher, R.V., 1961. Proposed classification of volcanoclastic sediments and rocks. Geological Society of America Bulletin, 72, 1409-1414.

Froggatt, P.C., Gosson, G.J., 1982. Techniques for the preparation of tephra samples for mineral or chemical analysis and radiometric dating. Geology Department, Victoria University of Wellington Publication. 23, 1-12.

Fronval, T., Jansen, E., Haflidason, H., Sejrup, H.P., 1998. Variability in surface and deep water conditions in the Nordic Seas during the Last Interglacial Period. Quaternary Science Reviews, 17, 963–985.

Gehrels, M.J., Lowe, D.J., Hazell, Z.J., Newnham, R.M., 2006. A continuous 5300-yr Holocene cyrptotephrostratigraphic record from northern New Zealand and implications for tephrochronology and volcanic hazard assessment. The Holocene, 16, 173-187.

Gonzalez, R.C., Woods, R.E., 2008. Digital image processing, Addison-Wesley, Third edition.

Griggs, A.J., Davies, S.M., Abbott, P.M., Rasmussen, T.L., Palmer, A.P., 2014. Optimising the use of marine tephrochronology in the North Atlantic: a detailed investigation of the Faroe Marine Ash Zones II, III and IV. Quaternary Science Reviews, 106, 122-139

.

Grönvold, K., Óskarsson, N., Johnsen, S.J., Clausen, H.B., Hammer, C.U., Bond, G., Bard, E., 1995. Ash layers from Iceland in the Greenland GRIP ice core correlated with oceanic and land sediments. Earth Planetary Science Letters, 135, 149-155.

Guðmundsdóttir, E.R., Eiríksson, J., Larsen, G., 2011. Identification and definition of primary and reworked tephra in Late Glacial and Holocene marine shelf sediments off North Iceland. Journal of Quaternary Science, 26, 589-602.

Haflidason, H., Eiríksson, J., van Kreveld, S., 2000. The tephrochronology of Iceland and the North Atlantic region during the Middle and Late Quaternary: a review. Journal of Quaternary Science, 15, 2-22.

Hall, I.R., Colmenero-Hidalgo, E., Zahn, R., Peck, V.L., Hemming, S.R., 2011. Centennial- to millennial-scale ice-ocean interactions in the subpolar northeast Atlantic 18–41 kyr ago. Paleoceanography, 26, PA2224.

Harris, C., 1998. The micromorphology of paraglacial and periglacial slope deposits: a case study from Morfa Bychan, west Wales UK. Journal of Quaternary Science, 13, 73-84.

Hayward, C., 2012. High spatial resolution electron probe microanalysis of tephras and melt inclusions without beam-induced chemical modification. The Holocene. 22, 119-125.

Heiken, G., Wohletz, K., 1985. Volcanic Ash. University of California Press, Berkeley, 246.

Heinrich, H., 1988. Origin and consequences of cyclic ice rafting in the northeast Atlantic Ocean during the past 130,000 years. Quaternary Research, 29, 142-152.

Hemming, S.R., 2004. Heinrich events: massive late Pleistocene detritus layers of the North Atlantic and their global climate imprint. Reviews of Geophysics, 42, RG1005.

Hibbert, F. D., Austin, W. E. N., Leng, M. J., Gatliff, R. W., 2010. British ice sheet dynamics inferred from north Atlantic ice-rafted debris records spanning the last 175 000 years. Journal of Quaternary Science, 25, 461–482.

Hibbert, F.D., Wastegård, S., Gwynn, R., Austin, W.E., 2014. Identification of a MIS 6 age (c. 180 ka) Icelandic tephra within NE Atlantic sediments: a new potential chronostratigraphic marker. Geological Society, London, Special Publications, 398.

Holliday, N. P., Pollard, R. T., Read, J. F., Leach, H., 2000. Water mass properties and fluxes in the Rockall trough, 1975–1998. Deep- Sea Research, 47, 1303–1332.

Howe, J.A., Stoker, M.S., Masson, D.G., Pudsey, C.J., Morris, P., Larter, J., Bulat, J., 2006. Seabed morphology and the bottom-current pathways around the Rosemary Bank seamount, northern Rockall Trough, North Atlantic. Marine and Petroleum Geology, 23, 2, 165-181.

Huber, C., Leuenberger, M., Spahni, R., Flückiger, J., Schwander, J., Stocker, T.F., Johnsen, S., Landais, A., Jouzel, J., 2006. Isotope calibrated Greenland tempera- ture record over Marine Isotope Stage 3 and its relation to CH_4. Earth Planetary Science Letters, 243, 504-519.

Hunt, J.B., Hill, P.G., 1993. Tephra geochemistry: a discussion of some persistent analytical problems. The Holocene, 3, 271-278.

Ivanochko, T. S., Ganeshram, R.S., G. J. A. Brummer, G. Ganssen, S. J. A. Jung, S. G. Moreton, D., Kroon., 2005. Variations in tropical convection as an amplifier of global climate change at the millennial scale. Earth Planetary Science Letters, 253, 302–314.

Jennings, A., Thordason, T., Zalzal, K., Stoner, J., Hayward, C., Geirsdóttir, A., Miller, G., 2014. Holocene tephra from Iceland and Alaska in SE Greenland Shelf Sediments. . In: Austin, W.E.N., Abbott, P.M., Davies, S.M., Pearce, N.J.G., Wastegård, S. (Eds.), Marine Tephrochronology, Geological Society of London Special Publication, vol. 398.

Jakobsson, S.P., 1979. Petrology of recent basalts of the Eastern Volcanic Zone, Iceland. Acta Nat. Island. 26, 1–103.

Jakobsson, S.P., Jónasson, K., Sigurdsson, I.A., 2008. The three igneous rock suites of Iceland. Jökull, 58, 117-38.

Jónasson, K., 2007. Silicic volcanism in Iceland: composition and distribution within the active volcanic zones. Journal of Geodynamics, 43, 101-117.

Jumars, P.A., Wheatcroft, R.A., 1989. Responses of benthos to changing food quality and quantity, with a focus on deposit feeding and bioturbation. In Berger WH, Smetacek VS, Wefer G. (Eds) Productivity of the Ocean: Present and Past, Wiley, New York. 235-253.

Kemp, R.A., 1999. Micrmorphology of loess-palaeosol sequences: a record of palaeoenvironmental change. Catena, 35, 179-196.

Ketcham, R.A., Carlson, W.D., 2001. Acquisition, optimization and interpretation of X-ray computed tomographic imagery: applications to the geosciences. Computers and Geosciences, 27, 381-400.

Kilfeather, A.A., van der Meer, J.J.M., 2008. Pore size, shape and connectivity in tills and their relationship to deformation processes. Quaternary Science Reviews, 27, 250-266.

Kindler, P., Guillevic, M., Baumgartner, M., Schwander, J., Landais, A., Leuenberger, M., 2014. Temperature reconstruction from 10 to 120 kyr b2k from the NGRIP ice core. Climate of the Past, 10, 887-902.

Kissel, C., Laj, C., Labeyrie, L., Dokken, T., Voelker, A., Blamart, D., 1999. Rapid climatic variations during marine isotopic stage 3: Magnetic analysis of sediments from Nordic seas and north Atlantic. Earth and Planetary Science Letters, 171, 489–502.

Knutti, R., Fluckiger, J., Stocker, T.F., Timmerman, A., 2004. Strong hemispheric coupling of glacial climate through freshwater discharge and ocean circulation. Nature, 430, 851-856.

Knutz, P. C., Austin, W. E. N., Jones, E. J. W., 2001. Millennial- scale depositional cycles related to British ice sheet variability and north Atlantic paleocirculation since 45 kyr B.P., Barra fan, U.K. Margin. Paleoceanography, 16, 53–64.

Kooistra, M.J., Pulleman, M.M., 2010. Features related to Faunal activity. In: Stoops, G., Mcarcelino, V., Mees, F. Interpretation of micromorphological features of soils and regoliths. Elsevier, Amsterdam, 397-418.

Kuehn, S.C., Froese, D.G., Shane, P.A.R., 2011. The INTAV inter comparison of electron-beam microanalysis of glass by tephrochronology laboratories: results and recommendations. Quaternary International, 246, 19-47.

Kuhs, M., Austin, W.E.N., Abbott, P.M., Hodell, D.A., 2014. Iceberg-rafted tephra as a potential tool for the reconstruction of ice-sheet processes and ocean surface circulation in the glacial North Atlantic. In: Austin, W.E.N., Abbott, P.M., Davies, S.M., Pearce, N.J.G., Wastegård, S. (Eds.), Marine Tephrochronology. Geological Society of London Special Publication, 398.

Kuijpers, A., Andersen, M. S., Kenyon, N. H., Kunzendorf, H., van Weering, T. C. E., 1998. Quaternary sedimentation and Norwegian Sea overflow pathways around Bill Bailey Bank, northeastern Atlantic. Marine Geology, 152, 101–127.

Kuijpers, A., Hansen, B., Huhnerbach, V., Larsen, B., Nielsen, T., Werner, F., 2002. Norwegian sea overflow through the Faroe-Shetland gateway as documented by its bedforms. Marine Geology, 188, 147–164.

Kvamme, T., Mangerud, J., Furnes, H., Ruddiman, W., 1989. Geochemistry of Pleistocene ash zones in cores from the North Atlantic. Norsk Geologisk Tidskrift. 69, 251-272.

Labeyrie, L., Cortijo, E., Jansen, E. 1999. Rapport scientifique de la mission INTERPOLE MD99-114/812 IMAGES V, Brest.

Lacasse, C., Paterne, M., Werner, R., Wallrabe-Adams, H.-J., Sigurdsson, H., Carey, S., Pinte, G., 1996. Geochemistry and Origin of Pliocene and Pleistocene Ash Layers from the Iceland Plateau, Site 907. In Thiede, J., Myhre, A.M., Firth, J.V., Johnson, G.L. and Ruddiman, W.F. (eds) Proceedings of the Ocean Drilling Program, Scientific Results, 151, 309-331.

Lackschewitz, K.S., Wallrabe-Adams, H.J., 1997. Composition and origin of volcanic ash zones in Late Quaternary sediments from the Reykjanes ridge: evidence for ash fallout and ice-rafting. Marine Geology, 136, 209-224.

Landais, A., Barnola, J.M., Masson-Delmotte, V., Jouzel, J., Chappellaz, J., Caillon, N., Huber, C., Leuenberger, M., Johnsen, S.J., 2004. A continuous record of temperature evolution over a sequence of Dansgaard-Oeschger events during Marine Isotopic Stage 4 (76 to 62 kyr BP). Geophysical Research Letters, 31, L22211.

Landis, E.N., Keane, D.T., 2010. X-ray microtomography. Materials characterization, 61, 1305-1316.

Lane, C.S., Andric, M., Cullen, V.L., Blockley, S.P.E., 2011. The occurrence of distal Icelandic and Italian tephra in the Late-glacial of Lake Bled, Slovenia. Quaternary Science Reviews. 30, 1013-1018.

Lane, C.S., Blockley, S.P.E., Mangerud, J., Smith, V.C., Lohne, O.S., Tomlinson, E.L., Matthews, I.P., Lotter, A.F., 2012. Was the 12.1 ka Icelandic Vedde Ash one of a kind? Quaternary Science Reviews, 33, 87-99.

Lane, C.S., Brauer, A., Blockley, S.P.E., Dulski, P., 2013. Volcanic ash reveals time-transgressive abrupt climate change during the Younger Dryas. Geology, 41, 1251-1254.

Lane, C.S., Cullen, V.L., White, D., Bramham-Law, C.W.F., Smith, V.C., 2014. Cryptotephra as a dating and correlation tool in archaeology. Journal of Archaeological Science, 42, 42-50.

Larsen, G., 1981. Tephrochronology by microprobe glass analysis. In Tephra Studies as a Tool in Quaternary Research, Self S, Sparks RSJ (eds). 95–102.

Larsen, G., Eiríksson, J., 2008. Late Quaternary terrestrial tephrochronology of Iceland- frequency of explosive eruptions, type and volume of tephra deposits. Journal of Quaternary Science, 23, 2, 109-120.

Larsen, G., Dugmore, A., Newton, A., 1999. Geochemistry of historical-age silicic tephras in Iceland. The Holocene, 9, 463-471.

Larsen, G., Newton, A.J., Dugmore, A.J., Vilmundardóttir, E.G., 2001. Geochemistry, dispersal, volumes and chronology of Holocene silicic tephra layers from the Katla volcanic system, Iceland. Journal of Quaternary Science, 16, 119-132.

Larsen, G., Eiríksson, J., Knudsen, K.L., Heinemeier, J., 2002. Correlation of late Holocene terrestrial and marine tephra markers, north Iceland: implications for reservoir age changes. Polar Research. 21, 283-290.

Le Maître, R.W., Bateman, P., Dudek, A., Keller, J., Lameyre, Le Bas, M.J., Sabine, P.A., Schmid, R., Sorensen, H., Streckeisen, A., Woolley, A.R., Zanettin, B., 1989. A Classification of Igneous Rocks and Glossary of Terms, Blackwell, Oxford.

Lowe, D.J., 2011. Tephrochronology and its application: a review. Quaternary Geochronology. 6, 107-153.

Lowe, J.J., Turney, C.S.M., 1997. Vedde Ash layer discovered in a small lake basin on the Scottish mainland. Journal of the Geological Society, 154, 605–612.

Lowe, J.J., Hoek, W.Z., 2001. Inter-regional correlation of palaeoclimatic records for the Last Glacial-Interglacial Transition: a protocol for improved precision recommended by the INTIMATE project group. Quaternary Science Reviews, 20, 1175-1187.

Lowe, J.J., 2001. Abrupt climate changes in Europe during the last glacial-interglacial transition: the potential for testing hypotheses on the synchroneity of climate events using tephrochronology. Global and Planetary Change, 30, 73-4.

Lowe, J.J., Rasmussen, S.O., Björck, S., Hoek, W.Z., Steffensen, J.P., Walker, M.J.C., Yu, Z.C., 2008. Synchronisation of palaeoenvironmental events in the North Atlantic region during the Last Termination: a revised protocol recommended by the INTIMATE group. Quaternary Science Reviews. 27, 6-17.

MacDonald, G.A., Katsura, T., 1964. Chemical composition of Hawaiian lavas. Journal of Petrology, 5, 83-133

Mackie, E., Davies, S.M., Turney, C.S.M., Dobbyn, K., Lowe, J.J., 2002. The use of magnetic separation techniques to detect basaltic microtephra in glacialeinterglacial transition (LGIT; 15-10 ka cal. BP) sediment sequences in Scotland. Scottish Journal of Geology. 38, 21-30.

Mangerud, J., 1991. The last interglacial/glacial cycle in northern Europe. In Quaternary Landscapes, Shane LCK, Cushing EJ (eds). University of Minnesota Press: Minneapolis; 38-75.

Mangerud, J., Lie, S.E., Furnes, H., Kristiansen, I.L., Lømo, L., 1984. A Younger Dryas ash bed in western Norway, and its possible correlations with tephra in cores from the Norwegian Sea and the North Atlantic. Quaternary Research, 21, 85-104.

Manville, V., Wilson, C.J.N., 2004. Vertical density currents: a review of their potential role in the deposition and interpretation of deep-sea ash layers. Journal of the Geological Society. 161, 947-958.

Matthews, I.P., Palmer, A.P., Folkes, H., Trincardi, F., 2011a. Understanding tephra layers in marine sediments, the potential of thin section micromorphology to investigate depositional and taphonomic processes. Marine Tephrochronology Meeting, Geological Society London, UK, 26 October, 2011.

Matthews, I.P., Birks, H.H., Bourne, A.J., Brooks, S.J., Lowe, J.J., MacLeod, A., Pyne-O'Donnell, S.D.F., 2011b. New age estimates and climostratigraphic correlations for the Borrobol and Penifiler tephras: evidence from the Abernethy Forest, Scotland. Journal of Quaternary Science, 26, 3, 247-252.

McCave, I.N., 1988. Biological pumping upwards of the coarse fraction of deep-sea sediments. Journal of Sedimentology and Petrology, 58, 148-158.

McCave, I.N., Manighetti, B., Robinson, S.G., 1995. Sortable silt and fine sediment size/composition slicing: Parameters for paleocurrent speed and palaeoceanography. Palaeoceanography, 10, 3, 593-610.

Menzies, J., Brand, U., 2007. The internal sediment architecture of a drumlin, Port Byron, New York State, U.S.A. Quaternary Science Reviews, 26, 322-355.

Meyer, P.S., Sigurdsson, H., Schilling, J.G., 1985. Petrological and Geochemical Variations along Iceland's Neovolcanic Zones. Journal of Geophysical Research, 90, 10,043-10,072.

Michels, K.H., 2000. Inferring maximum geostrophic current velocities in the Norwegian-Greenland Sea from settling velocity measurements of sediment surface samples: methods, application, and results. Journal of Sedimentary Research, 70, 1036-1050.

Mortensen, A.K., Bigler, M., Grönvold, K., Steffensen, J.P., Johnsen, S.J., 2005. Volcanic ash layers from the Last Glacial Termination in the NGRIP ice core. Journal of Quaternary Science, 20, 209-219.

Muscheler, R., Kromer, B., Bjork, S., Svensson, A., Friedrich, M., Kaiser, K.F., Southon, J., 2008. Tree rings and ice-cores reveal ^{14}C calibration uncertainties during the Younger Dryas. Nature Geoscience, 1, 263-267.

Muscheler, R., Adolphi, F., Svensson, A., 2014. Challenges in ^{14}C dating towards the limit of the method inferred from anchoring a floating tree ring radiocarbon chronology to ice core records around the Laschamp geomagnetic field minimum. Earth and Planetary Science Letters, 394, 209-215.

Nakagawa, T., Gotanda, K., Haraguchi, T., Danhara, T., Yonenobu, H., Brauer, A., Yokoyama, Y., Tada, R., Takemura, K., Staff, R.A., Payne, R., Bronk Ramsey, C., Bryant, C., Brock, F., Schlolaut, G., Marshall, M., Tarasov, P., Lamb, H., 2012. SG06, a fully continuous and varved sediment core from Lake Suigetsu, Japan: stratigraphy and potential for improving the radiocarbon calibration model and understanding of late Quaternary climate changes. Quaternary Science Reviews, 36, 164-176.

NGRIP members, 2004. High-resolution record of Northern Hemisphere climate extending into the last interglacial period. Nature, 431, 147-151.

Óladóttir, B.A, Sigmarsson, O., Larsen, G., Thordarson, T., 2008. Katla volcano, Iceland: magma composition, dynamics and eruption frequency as recorded by Holocene tephra layers. Bulletin of Volcanology 70: 475–493.

Óladóttir, B.A., Sigmarsson, O., Larsen, G., Devidal, J.L., 2011. Provenance of basaltic tephra from Vatnajökull subglacial volcanoes, Iceland, as determined by major and trace element analyses. The Holocene, 21, 7, 1037-1048.

Óskarsson, N., Sigvaldason, G.E., Steinthórsson, S. 1982. A Dynamic Model of Rift Zone Petrogenesis and the Regional Petrology of Iceland, Journal of Petrology, 23, 28-74.

Palmer, A.P., Lee, J.A., Kemp, R.A., Carr, S.J., 2008. Revised laboratory procedures for the preparation of thin sections from unconsolidated material. Unpublished Internal Report, Royal Holloway, University of London.

Paulsen, D.E., Li, H.C., Ku, T.L., 2003. Climate variability in central China over the last 1270 years revealed by high-resolution stalagmite records. Quaternary Science Reviews, 22, 691-701.

Payne R.J., Kilfeather, A.A., van der Meer, J.J.M., Blackford, J.J., 2006. Experiments on the taphonomy of tephra in peat. Suo 56, 147-156.

Pearce, N.J.G., Westgate, J.A., Perkins, W.T., Eastwood, W.J., Shane, P., 1999. The application of laser ablation ICP-MS to the analysis of volcanic glass shards from tephra deposits: bulk glass and single shard analysis. Global and Planetary Change, 21, 151-171.

Pearce, N.J.G., Denton, J.S., Perkins, W.T., Westgate, J.A., Alloway, B.V., 2007. Correlation and characterisation of individual glass shards from tephra deposits using trace element laser ablation ICP-MS analyses: current status and future potential. Journal of Quaternary Science, 22, 721-736.

Pearce, N.J.G., Perkins, W.T., Westgate, J.A., Wade, S.C., 2010. Trace-element micro-analysis by LA-ICP-MS: the quest for comprehensive chemical

characterisation of single, sub-10 mm volcanic glass shards. In: Abstracts, International Field Conference on Tephrochronology, Volcanism, and Human Activity, Kirishima, Japan (9-17 May). INQUA International Focus Group on Tephrochronology and Volcanism (INTAV), 77-78.

Pearce, N.J.G., Abbott, P.M., Martin-Jones, C., 2014. Microbeam methods for the analysis of glass in fine-grained tephra deposits: a SMART perspective on current and future trends. In: Austin, W.E.N., Abbott, P.M., Davies, S.M., Pearce, N.J.G., Wastegård, S. (Eds.), Marine Tephrochronology, Geological Society of London Special Publication, vol. 398.

Persson C. 1966. Försök till tefrokronologisk datering av några svenska torvmossar. Geologiska Foereningan i Stockholm Föerhandlingar 88: 361–395.

Polacci, M., Baker, D.R., Mancini, L., Tromba, G., Zanini, F., 2006. Three-dimensional investigation of volcanic textures by x-ray microtomography and implications for conduit processes. Geophysical Research Letters, 33.

Purcell, C., Harbert, W., Soong, Y., McLendon, T.R., Haljasmaa, I.V., McIntyre, D., JiKich, J., 2009. Velocity measurements in reservoir rock samples from the SAROC unit using various pore fluids, and integration into a seismic survey taken before and after CO2 sequestration flood. In: Gale, J., Herzog, H., Braitsch, J., Greenhouse Gas Control Technologies 9. Energy Procedia. Elsevier Science Bv, Amsterdam, 2323-2331.

Pyne-O'Donnell, S.D.F., Blockley, S.P.E., Turney, C.S.M., Lowe, J.J., 2008. Distal volcanic ash layers in the Lateglacial Interstadial (GI-1): problems of stratigraphic discrimination. Quaternary Science Reviews, 27, 72-84.

Pyne-O'Donnell, S.D.F., Hughes, P.D.M., Froese, D.G., Jensen, B.J.L., Kuehn, S.C., Mallon, G., Amesbury, M.J., Charman, D.J., Daley, T.J., Loader, N.J., Mauquoy, D., Street-Perrott, F.A., Woodman-Ralph, J., 2012. High-precision ultra-distal Holocene tephrochronology in North America. Quaternary Science Reviews. 52, 6-11.

Rach, O., Brauer, A., Wilkes, H., Sachse, D., 2014. Delayed hydrological response to Greenland cooling at the onset of the Younger Dryas in western Europe. Nature Geosciences. 7, 109-112.

Rasmussen, S.O., Seierstad, I.K., Andersen, K.K., Bigler, M., Dahl-Jensen, D., Johnsen, S.J., 2008. Synchronization of the NGRIP, GRIP, and GISP2 ice cores across MIS 2 and palaeoclimatic implications. Quaternary Science Reviews, 27, 18-28.

Rasmussen, S.O., Abbott, P.M., Blunier, T., Bourne, A.J., Brook, E.J., Buchardt, S.L., Buizert, C., Chappellaz, J., Clausen, H.B., Cook, E., Dahl-Jensen, D., Davies, S.M., Guillevic, M., Kipfstuhl, S., Laepple, T., Seierstad, I., Severinghaus, J.P., Steffensen, J.P., Stowasser, C., Svensson, A., Vallelonga, P., Vinther, B.M., Willhelms, F., Winstrup, M., 2013. A first chronology for the North Greenland Eemian Ice drilling ice core. Climate of the Past, 9, 2713-2730.

Rasmussen, S.O., Bigler, M., Blockley, S.P.E., Blunier, T., Buchardt, S.L., Clausen, H.B., Cvijanovic, I., Dahl-Jensen, D., Johnsen, S.J., Fischer, H., Gkinis, V., Guillevic, M., Hoek, W.Z., Lowe, J.J., Pedro, J., Popp, T., Seierstad, I.K., Steffensen, J.P., Svensson, A.M., Vallelonga, P., Vinther, B.M., Walker, M.J.C., Wheatley, J.J., Winstrup, M., 2014. A stratigraphic framework for abrupt climatic changes during the last glacial period based on three synchronized Greenland ice-core records: refining and extending the INTIMATE event stratigraphy. Quaternary Science Reviews, 106, 14-28.

Rasmussen, T.L., Thomsen, E., Tjeerd, C.E., Weering, V., Labeyrie, L., 1996. Rapid changes in surface and deep water conditions at the Faroe Margin during the last 58,000 years. Palaeoceanography. 11, 757-771.

Rasmussen, T.L., Wastegard, S., Kuijpers, E., van Weering, T.C.E., Heinemeier, Thornsen, E., 2003. Stratigraphy and distribution of tephra layers in marine sediment cores from the Faroe Islands, North Atlantic. Marine Geology, 199, 263-277.

Reimer, P.J., Bard, E., Bayliss, A., Beck, J.W., Blackwell, P.G., Bronk Ramsey, C., Buck, C.E., Cheng, H., Edwards, R.L., Friedrich, M., Grootes, P.M., Guilderson, T.P., Haflidason,H., Hajdas,I., Hatte, C., Heaton, T.J., Hoffmann, D.L., Hogg, A.G., Hughen, K.A., Kaiser, K.F., Kromer, B., Manning, S.W., Niu, M., Reimer, R.W., Richards, D.A., Scott, E.M., Southon, J.R., Staff, R.A., Turney, C.S.M., van der Plicht, J., 2013. IntCal13 and Marine13 radiocarbon age calibration curves 0-50,000 years cal BP. Radiocarbon 55, 1869-1887.

Rohling, E.J., Liu, Q.S., Roberts, A.P., Stanford, J.D., Rasmussen, S.O., Langen, P.L., Siddall, M., 2009. Controls on the East Asian monsoon during the last glacial cycle, based on comparison between Hulu Cave and polar ice-core records. Quaternary Science Reviews, 28, 3291-3302.

Ruddiman, W.F., Glover, L.K., 1972. Vertical mixing of ice rafted volcanic ash in north Atlantic sediments. Geological Society of America Bulletin. 83, 2817-2836.

Seierstad, I.K., Abbott, P.M., Bigler, M., Blunier, T., Bourne, A., Brook, E., Buchardt, S.L., Buizert, C., Clausen, H.B., Cook, E., Dahl-Jensen, D., Davies, S., Guillevic, M., Johnsen, S.J., Pedersen, D.S., Popp, T.J., Rasmussen, S.O., Severinghaus, J., Svensson, A., Vinther, B.M., 2014. Consistently dated records from the Greenland GRIP, GISP2 and NGRIP ice cores for the past 104 ka reveal

regional millennial-scale $\delta^{18}O$ gradients with possible Heinrich event imprint. Quaternary Science Reviews. 106, 29-46.

Shackleton, N.J., Hall, M.A., Vincent, E., 2000. Phase relationships between millennial-scale events 64,000-24,000 years ago. Paleoceanography, 15, 565-569.

Skinner, L.C., 2008. Revisiting the absolute calibration of the Greenland ice-core age-scales. Climate of the Past, 4, 295-302.

Sparks, R., 1981. Triggering of volcanic eruptions by earth tides. Nature. 290, 448.

Stanford, J.D., Rohling, E.J., Bacon, S., Roberts, A.P., Grousset, F.E., Bolshaw, M., 2011. A new concept for the paleoceanographic evolution of Heinrich event 1 in the North Atlantic. Quaternary Science Reviews, 30, 1047-1066.

Stärz, M., Gong, X., Stein, R., Darby, D.A., Kauker, F., Lohmann, G., 2012. Glacial shortcut of Arctic sea-ice transport. Earth and Planetary Science Letters, 257- 358, 257 -267.

Steffensen, J.P., Andersen, K.K., Bigler, M., Clausen, H.B., Dahl-Jensen, D., Fischer, H., Goto-Azuma, K., Hansson, M., Johnsen, S.J., Jouzel, J., Masson-Delmotte, V., Popp,T., Rasmussen, S. O., Roethlisberger, R., Ruth, U., Stauffer, B., Siggaard-Andersen, M.-L., Sveinbjornsdóttir, A.E., Svensson, A., White, J.W.C., 2008. High-resolution Greenland ice core data show abrupt climate change happens in few years. Science 321, 680-684.

Stevenson, J.A., Millington, S.C., Beckett, F.M., Swindles, G.T., Thordason, T., 2015. Big grains go far: understanding the discrepancy between tephrochronology and satellite infrared measurements of volcanic ash. Atmospheric Measurement Techniques, 8, 2069-2091.

Storey, M., Stecher, O., 2009. $^{40}Ar/^{39}Ar$ age calibration against counted annual layers. Geophysical research Abstracts, 10, 1.

Sun, S.S., McDonough, W.F., 1989. Chemical and isotopic systematics of oceanic basalts; implications for mantle composition and processes. In: Magmatism in the ocean basins. Saunders, A.D. and Norry, M.J. (Editors), Geological Society of London, London. 42, 313-345.

Svensson, A., Andersen, K.K., Bigler, M., Clausen, H.B., Dahl-Jensen, D., Davies, S.M., Johnsen, S.J., Muscheler, R., Rasmussen, S.O., Röthlisberger, R., Steffensen, J.P., Vinther, B.M., 2006. The Greenland Ice Core Chronology 2005, 15-42ka. Part 2: comparison to other records. Quaternary Science Reviews, 25, 3258-3267.

Svensson, A., Andersen, K. K., Bigler, M., Clausen, H. B., Dahl- Jensen, D., Davies, S. M., Johnsen, S. J., Muscheler, R., Parrenin, F., Rasmussen, S. O., Rothlisberger, R., Seierstad, I., Steffensen, J. P., Vinther, B. M., 2008. A 60 000 year Greenland stratigraphic ice core chronology, Climate of the Past, 4, 47–57.

Tarplee, M.F.V., van der Meer, J.J.M., Davis, G.R., 2011. The 3D microscopic signature of strain within glacial sediments revealed using X-ray computed microtomography. Quaternary Science Reviews, 30, 3501-3532.

Thomas, E.R., Wolff, E.W., Mulvaney, R., Johnsen, S.J., Steffensen, J.P., Arrowsmith, C., 2009. Anatomy of a Dansgaard-Oeschger warming transition: high-resolution analysis of the North Greenland Ice Core Project ice core. Journal of Geophysical Research: Atmospheres, 114, D08102.

Thorarinsson, S., 1944. Tefrokronologiska studier på Island. Geografiska Annaler, 26, 1-217.

Thornalley, D.J.,R, McCave, I.N., Elderfield, H., 2011. Tephra in deglacial ocean sediments south of Iceland: stratigraphy, geochemistry and oceanic reservoir ages. Journal of Quaternary Science 26: 190– 198.

Todd, J.A., Austin, W.E.N., Abbott, P.M., 2014. Quantiying bioturbation in a simulated ash fall event. In: Austin, W.E.N., Abbott, P.M., Davies, S.M., Pearce, N.J.G., Wastegard, S. (Eds), Marine Tephrochronology. Geological Society, London, Special Publications, 398.

Turney, C.S.M., Harkness, D.D., Lowe, J.J., 1997. The use of microtephra horizons to correlate Late-glacial lake sediment successions in Scotland. Journal of Quaternary Science, 12, 6, 525-531.

Turney, C.S.M., 1998. Extraction of rhyolitic ash from minerogenic lake sediments. Journal of Paleolimnology. 19, 199-206.

Turney, C.S.M., Lowe, J.J., Davies, S.M., Hall, V., Lowe, D.J., Wastegård, S., Hoek, W.Z., Alloway, B. and SCOTAV and INTIMATE Members, 2004. Tephrochronology of Last Termination Sequences in Europe: a protocol for

improved analytical precision and robust correlation procedures (a joint SCOTAV-INTIMATE proposal). Journal of Quaternary Science, 19, 111-120.

Turney, C.S.M., van den Burg, K., Wastegård, S., Davies, S.M., Whitehouse, N.J., Pilcher, J.R., Callaghan, C., 2006. North European last glacial-interglacial transition (LGIT; 15-9 ka) tephrochronology: Extended limits and new events. Journal of Quaternary Science, 21, 4, 335-345.

Van Andel, T.H., 2005. The ownership of time: approved radiocarbon calibration or freedom of choice? Antiquity 79, 944-948.

van der Meer, J.M., Menzies, J., 2011. The micromorphology of unconsolidated sediments. Sedimentary Geology. 238, 213-232.

Voelker, A.H.L., Workshop participants, 2002. Global distribution of centennial-scale records for Marine Isotope Stage (MIS) 3: a database. Quaternary Science Reviews, 21, 1185-1212.

Voelker, A.H.L., Haflidason, H., 2015. Refining the Icelandic tephrachronology of the last glacial period- The deep-sea core PS2644 record from the Southern Greenland Sea. Global and Planetary Change, 131, 35-62.

Voelker, A.H.L., Grootes, P.M., Nadeau, M.J., Sarnthein, M., 2000. Radiocarbon levels in the Iceland Sea from 25-53 kyr and their link to the Earth's magnetic field intensity. Radiocarbon. 42, 437-452.

Walden, J., Oldfield, F., Smith, J., 1999. Environmental Magnetism: a Practical Guide. Quaternary Research Association, Technical Guide No. 6.

Wallrabe-Adams, H.J., Lackschewitz, K.S., 2003. Chemical composition, distribution, and origin of silicic volcanic ash layers in the Greenland-Iceland-Norwegian Sea: explosive volcanism from 10 to 300ka as recorded in deep sea sediments. Marine Geology. 19, 273-293.

Wang, Y.J., Cheng, H., Edwards, R.L., An, Z.S., Wu, J.Y., Shen-C, C., Dorale, J.A., 2001. A high-resolution absolute dated Late Pleistocene monsoon record from Hulu Cave. Nature, 294, 5550, 2345-2348.

Wastegård, S., Rasmussen, T.L., 2014. Faroe Marine Ash Zone IV, a new MIS 3 ash zone of the Faroe Islands margin. In: Austin, W.E.N., Abbott, P.M., Davies, S.M., Pearce, N.J.G., Wastegard, S., Marine Tephrochronology, Geological Society of London Special Publication, vol. 398.

Wastegård, S., Wohlfarth, B., Subetto, D.A. & Sapelko, T.V., 2000. Extending the known distribution of the Younger Dryas Vedde Ash into north-western Russia. Journal of Quaternary Science, 15, 581-586.

Wastegård, S., Björck, S., Grauert, M., Hannon, G.E., 2001. The Mjauvotn tephra and other Holocene tephra horizons from the Faroe Islands: a link between the Icelandic source region, the Nordic Seas, and the European continent. The Holocene, 11, 101-109.

Wastegård, S., 2002. Early to middle Holocene silicic tephra horizons from the Katla volcanic system, Iceland: new results from the Faroe Islands. Journal of Quaternary Science, 17, 8 723-730.

Wastegård, S., Björck, S., Greve, C., Rasmussen, T.L., 2005. A tephra based correlation between the Faroe Islands and the Norwegian Sea raises questions about chronological relationships during the last interglacial. Terra Nova, 17, 7-12.

Wastegård, S., Rasmussen, T.L., Kuijipers, A., Nielsen, T., van Weering, T.C.E., 2006. Composition and origin of ash zones from Marine Isotope Stages 3 and 2 in the North Atlantic. Quaternary Science Reviews, 25, 2409-2419.

Wastegård, S., Rundgren, M., Schoning, K., Andersson, S., Björk, S., Borgmark, A., Possnert, G., 2008. Age, geochemistry and distribution of the mid-Holocene Hekla-S/Kebister tephra. The Holocene, 18, 4, 539-549.

Wennberg, O.P., Rennan, L., Basquet, R., 2009. Computed tomography scan imaging of natural open fractures in a porous rock; geometry and fluid flow. Geophysical Prospecting, 57, 239-249.

Wheatcroft, R.A., 1992. Experimental tests for particle-size dependent bioturbation in the deep ocean. Limnology and Oceanography, 37, 90-104.

White, J.D.L., Houghton, B.F., 2006. Primary volcaniclastic rocks. Geology, 34, 677-680.

Wiesner, M.G., Wang, Y., Zheng, L., 1995. Fallout of volcanic ash to the deep South China Sea induced by the 1991 eruption of Mount Pinatubo (Philippines). Geology 23, 885-888.

Wulf, S., Kraml, M., Brauer, A., Keller, J., Negendank, J.F.W., 2004. Tephrochronology of the 100 ka lacustrine sediment record of Lago Grande di Monticchio (southern Italy). Quaternary International, 122, 7-30.

Wulf, S., Keller, J., Paterne, M., Mingram, J., Lauterbach, S., Opitz, S., Sottili, G., Giaccio, B., Albert, P.G., Satow, C., Tomlinson, E.L., Viccaro, M., Brauer, A., 2012. The 100-133 ka record of Italian explosive volcanism and revised tephrochronology of Lago Grande di Monticchio. Quaternary Science Reviews, 58, 104-123.

Zielinski, G.A., Mayewski, P.A., Meeker, L.D., Whitlow, S., Twickler, M.S., 1996. A 110,000 year record of explosive volcanism from the GISP2 (Greenland) ice core. Quaternary Research, 45, 109-118.

Zumaque, J., Eynaud, F., Zaragosi, S., Marret, F., Matsuzaki K.M., Kissel, C., Roche, D., Malaize, B., Michel, E., Billy, I., Richter, T., Palis, E., 2012. An ocean-ice coupled response during the last glacial: a view from a marine isotopic stage 3 record south of the Faroe Shetland Gateway. Climate of the Past, 8, 1997-2017.

Quaternary Science Reviews 106 (2014) 122–139

Contents lists available at ScienceDirect

Quaternary Science Reviews

journal homepage: www.elsevier.com/locate/quascirev

Optimising the use of marine tephrochronology in the North Atlantic: a detailed investigation of the Faroe Marine Ash Zones II, III and IV

Adam J. Griggs [a,*], Siwan M. Davies [a], Peter M. Abbott [a], Tine L. Rasmussen [b], Adrian P. Palmer [c]

[a] Department of Geography, College of Science, Swansea University, Singleton Park, Swansea SA2 8PP, UK
[b] Centre for Arctic Gas Hydrate, Environment and Climate (CAGE), Department of Geology, University of Tromso, NO9037 Tromso, Norway
[c] Department of Geography, Royal Holloway, Egham Hill, Egham TW20 0EX, UK

ARTICLE INFO

Article history:
Received 10 November 2013
Received in revised form
23 April 2014
Accepted 28 April 2014
Available online 10 June 2014

Keywords:
North Atlantic
Tephra
Taphonomy
Synchronisation
Micromorphology

ABSTRACT

Tephrochronology is central to the INTIMATE[1] goals for testing the degree of climatic synchroneity during abrupt climatic events that punctuated the last glacial period. Since their identification in North Atlantic marine sequences, the Faroe Marine Ash Zone II (FMAZ II), FMAZ III and FMAZ IV have received considerable attention due to their potential for high-precision synchronisation with the Greenland ice-cores. In order to optimise the use of these horizons as isochronous markers, a detailed re-investigation of their geochemical composition, sedimentology and the processes that deposited each ash zone is presented. Shard concentration profiles, geochemical homogeneity and micro-sedimentological structures are investigated for each ash zone preserved within core JM11-19PC, retrieved from the south-eastern Norwegian Sea on the central North Faroe Slope. This approach allows a thorough assessment of primary ash-fall preservation and secondary depositional features and demonstrates its value for assessing depositional integrity in the marine environment. Results indicate that the FMAZ II and IV are well-resolved primary deposits that can be used as isochrons for high-precision correlation studies. We outline key recommendations for future marine tephra studies and provide a protocol for optimising the application of tephrochronology to meet the INTIMATE synchronisation goals.

1. Introduction

1.1. Synchronisation of disparate climatic archives

Tephrochronology is regarded as one of the key techniques for providing time-synchronous marker horizons which can be used to establish independent and precise tie-points between disparate palaeoarchives (e.g. Haflidason et al., 2000; Lowe et al., 2008; Davies et al., 2010; Abbott and Davies, 2012). Establishing precise correlation between proxy records is crucial for assessing the degree of climatic synchroneity between different components of the climate system during abrupt climatic shifts of the last glacial period (Austin and Hibbert, 2012; Davies et al., 2012). The geographical range over which tephra can be traced has been extended following the identification of cryptotephra deposits in ultra-distal locations and as such has increased the number of tie-lines between widely separated archives (e.g. Blockley et al., 2007; Lane et al., 2011; Pyne-O'Donnell et al., 2012). A number of horizons currently exist which enable direct synchronisation between the oceanic and cryospheric realms in the North Atlantic region during the last glacial period (Austin et al., 2004; Davies et al., 2008). However, in order to fully exploit these tie-lines, it is essential to assess the depositional integrity of the tephra horizons in the marine environment – an issue which is currently confounded by the complexity of processes that control deposition in the oceans (e.g. Austin et al., 2004; Brendryen et al., 2010; Abbott et al., 2011). Here we present a detailed geochemical and sedimentological analysis of Marine Isotope Stage (MIS) 2 and 3 (26–50 ka BP) age tephra deposits found in a single North Atlantic marine core (JM11-19PC). We explore the potential depositional processes in order to refine and assess the stratigraphic position of each tephra isochron. This core was selected because of the excellent tephra preservation with ample core material available for the preparation of thin sections.

* Corresponding author. Tel.: +44 1792 295233.
E-mail addresses: 607416@swansea.ac.uk, lake_tahoe4@hotmail.com (A.J. Griggs).

[1] INTIMATE: INTegrating Ice core, MArine and TErrestrial records 60,000–8000 yrs b2k (EU COST Action ES0907 http://cost-es0907.geoenvi.org/.)

http://dx.doi.org/10.1016/j.quascirev.2014.04.031

1.2. Understanding depositional processes in the marine environment: primary vs secondary mixing and taphonomical considerations

The regional dispersal and localised deposition of tephra in North Atlantic marine sequences is the product of several processes occurring aerially and internally within the ocean system, which in turn influences their applicability as isochronous horizons (Brendryen et al., 2010). One of the fundamental prerequisites of tephrochronology is that tephra is deposited and preserved in a sequence rapidly, i.e. geologically instantaneously, following an eruption (Lowe, 2011). However, tephra shards in the marine realm are subject to both secondary transport and depositional processes (Fig. 1), which potentially introduces stratigraphic and, therefore, chronological uncertainties. These are particularly relevant for cryptotephra deposits that are comprised of a low concentration of glass particles and are thus invisible to the naked eye. Direct sedimentological analysis of tephra and cryptotephra deposits, allied to rigorous geochemical fingerprinting and down-core shard concentration profiles can provide important evidence for the mode of tephra delivery to the seabed. The main modes of tephra delivery from the eruption to the ocean water surface and then through the water column are presented below.

1.2.1. Primary airfall

Following an eruption, tephra is ejected into the atmosphere and primary ash fall deposits are expected to contain a well-sorted distribution, determined by size and density-related processes during the transport of ash through the atmosphere (Sparks, 1981). Thus, a primary airfall deposit will most likely contain a greater concentration of fine-grained tephra particles as the distance from source increases. Primary airfall deposits are also characterised by a homogeneous geochemical population, representing a single eruption, or potentially a couple of homogeneous populations, from very closely-timed eruptions (Brendryen et al., 2010).

1.2.2. Iceberg rafting

Following an eruptive event, an important transport pathway is the proximal deposition of tephra onto ice-sheets which then subsequently undergo calving and rafting to distal locations (Fig. 1) (Brendryen et al., 2010). This process can deliver larger material to a distal depositional site than would typically be associated with primary atmospheric fallout. Iceberg rafting is also dependant on the time taken for the iceberg to calve from the ice-sheet into the ocean; hence it is likely to contain an amalgamation of material sourced from a number of eruptions and different volcanic centres (Ruddiman and Glover, 1972; Lackschewitz and Wallrabe-Adams, 1997; Brendryen et al., 2010). Thus, it is expected that tephra delivered via iceberg rafting would be characterised by a poorly-sorted size distribution and a heterogeneous geochemical signature (Brendryen et al., 2010; Abbott et al., 2011). The identification of co-varying IRD in the succession is a further criterion for identifying iceberg rafting events (Lackschewitz and Wallrabe-Adams, 1997; Davies et al. 2014). Iceberg rafting is likely to compromise the integrity of a tephra horizon by causing a significant temporal delay between the eruption and subsequent deposition into a sedimentary sequence, possibly by up to several millennia (Brendryen et al., 2010). However, it has been suggested that the study of iceberg rafted tephra deposits could aid in the reconstruction of glacial ocean surface circulation patterns (Kuhs et al., 2014).

1.2.3. Sea-ice rafting

Another potentially important transport mechanism is the deposition of tephra onto sea-ice, which can cause time lags of years to decades (Brendryen et al., 2010). Although sea-ice persisted permanently in some areas of the North Atlantic during the last glacial, modelling estimates suggest that this was limited to the central Arctic Ocean and areas under the influence of the East Greenland Current, and that sea-ice production was typically seasonal, particularly in the Nordic Seas (Stärz et al., 2012). This prevents the accumulation of multiple eruptions and thus sea-ice rafted deposits are likely to have a homogenous geochemical signature (e.g. Austin et al., 2004). For example, Austin et al. (2004) interpreted that the homogeneous geochemistry and coarser shard sizes of the North Atlantic Ash Zone II (NAAZ II) in MD95-2006, was indicative of initial airfall deposition and subsequent transport to the core site by sea-ice. However, coarser shard sizes are not always a diagnostic indicator of sea-ice rafting, as fine-grained glass shards can also be transported long distances on sea-ice. Whilst this mechanism can increase the regional dispersal of tephra, it is unlikely to affect a deposits integrity as an isochron because the temporal lag is far less than the sampling resolution of marine sequences. As this mechanism does not involve calving from ice sheets, the deposit is unlikely to be associated with a coeval IRD signal.

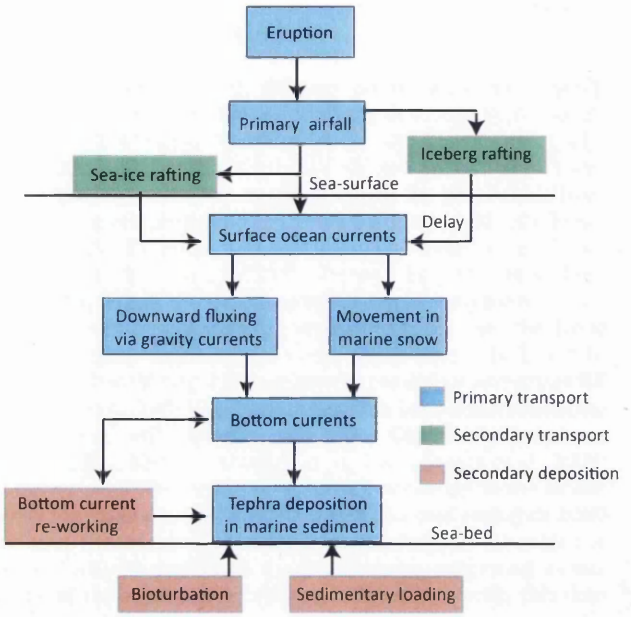

Fig. 1. Schematic summary of the main processes that can influence the transport and deposition of tephra in the marine environment.

1.2.4. Ocean currents

Following tephra deposition onto the ocean surface by means of wind, iceberg rafting or sea-ice rafting, the glass shards will move from the surface down to the seabed (Wallrabe-Adams and Lackschewitz, 2003). Laboratory experiments demonstrate that vertical density currents generated by ash loading allow the movement of particles to overcome strong density gradients in the ocean and transport ash one to three orders of magnitude faster than is possible by Stokes settling Law (Manville and Wilson, 2004). Wallrabe-Adams and Lackschewitz (2003) hypothesised that glass particles could be transported laterally over a relatively large distance (20–55 km) during the sinking process. However, rapid settling of ash particles implies that the transport through the water column would not affect the chronological integrity of the deposit. Although residence time in

the water column can be affected by turbulence and salinity boundaries (Manville and Wilson, 2004), this is unlikely to keep a shard in suspension for more than a few days to weeks, since tephra is likely to fall through the water column within marine snow (Fig. 1). For example, Wiesner et al. (1995) demonstrated that the vertical oceanic settling velocities into deep-water sediment traps in the South China Sea were >2 cm/s following the paroxysmal phase of the Pinatubo eruption in 1991.

One process that may disturb this signal, however, is redistribution and erosion by bottom currents. Michels (2000) calculated that geostrophic bottom current velocities may range from 25 to 36 cm/s in the Nordic Seas during storm events, which may influence the spatial distribution of tephra, resulting in distinct variations in horizon thickness and glass shard concentration in nearby cores (Wallrabe-Adams and Lackschewitz, 2003). Thus, an increase in bottom currents during interstadials and storm events may remobilise material from previously deposited eruptions. Any bottom-current induced erosion is likely to mobilise tephra material and produce an upward gradational distribution or tail-off in shard concentration (e.g. Abbott et al., 2013, 2014). Thus, for cryptotephra deposits, an upward tail in concentration from a main peak would be expected to have a corresponding homogeneous geochemical signature throughout the deposit. However, material from older eruptions may become remobilised and transported from one site to another, resulting in the deposition of material sourced from a number of different events. This reinforces the need for careful scrutinisation of cryptotephra shard concentration profiles together with an assessment of geochemical results from several intervals within these deposits (Abbott et al. 2014; Davies et al., 2014).

1.2.5. *Post-depositional reworking of material*

Following deposition of tephra onto the seabed, as well as being reworked by bottom currents, tephra is also susceptible to bioturbation (Abbott et al., 2011). Characteristic sedimentological evidence of bioturbation includes a gradational upper contact that is spread over several centimetres which introduces a number of stratigraphical uncertainties (Manville and Wilson, 2004; Lowe, 2011). Low concentrations of shards below the peak are also considered to be a signature of bioturbation, although this is unlikely to affect the position of the peak in shard concentration (Ruddiman and Glover, 1972). Remobilisation of material can also occur as a result of turbidity currents, and present-day tephrostratigraphic techniques are not sufficient to isolate the complex interplay of post-depositional processes and pinpoint the modification mechanisms at work.

However, recent investigations by Matthews et al. (2011) examined the potential of micromorphology to identify microsedimentological structures within tephra deposits from a marine core in the Southern Adriatic. This work identified features associated with turbidite deposition, bioturbation and additional micro-scale evidence of gravitational loading and resedimentation. Micro-morphological analysis of sediment structures has the potential to provide additional supporting evidence for understanding the taphonomic processes associated with tephra deposition. When combined with the detailed analysis of the tephra geochemistry, shard distribution and particle size analysis, this approach provides a more precise assignment of tephra and in the marine environment. We adopt this approach to investigate three ash zones in one marine core and assess its potential value for the examination of tephra and cryptotephra deposits in this sedimentary environment.

1.3. *The Faroe Marine Ash Zones: optimising their employment as time-stratigraphic marker horizons*

Tephra deposits in North Atlantic marine sediments, mainly retrieved from the IRD belt, were originally described by Bramlette and Bradley (1941) and later by Ruddiman and Glover (1972), who named these horizons the 'North Atlantic Ash Zones' (NAAZ I and II). Investigations in the Faroes region during the past decade have identified 4 new tephra deposits, 'Faroe Marine Ash Zones' (FMAZ) I, II, III and IV (Rasmussen et al., 2003; Wastegård et al., 2006; Wastegård and Rasmussen, 2014), although only the latter three horizons, fall within the time-interval of this investigation.

FMAZ II was first discovered in marine cores near the Faroe Islands as a black visible horizon that varied from 2 to 10 cm in thickness and was thought to have been deposited via primary airfall (Rasmussen et al., 2003). This tephra has since been discovered in the Labrador Sea, NE Atlantic, and the Greenland ice cores (26,740 ± 390 a b2k[2]) (Wastegård et al., 2006; Davies et al., 2008; Svensson et al., 2008; Austin et al., 2012). According to the NGRIP stratigraphic position, the tephra falls within a cold period *ca.* 1000 years after the onset of Greenland Interstadial (GI) −3 which is consistent with its position in the marine cores, suggesting a close coupling of the atmospheric and oceanic systems during this time (Davies et al., 2008).

FMAZ III was originally described in the Faroes region as the '33 ka tephra', where it forms a visible scattered tephra zone spanning the transition into the peak warmth of Dansgaard-Oeschger (DO) event 8, identified in the ratio between planktonic to benthic foraminfera abundances (Rasmussen et al., 2003; Wastegård et al., 2006). Davies et al. (2010) proposed the correlation of a NGRIP tephra at 2066.95 m (38,122 ± 723 a b2k[2]) to the FMAZ III, which suggested deposition ca 100 years after the onset of the GI-8 warming. However, Bourne et al. (2013) have subsequently discovered a suite of tephra layers in the NGRIP and NEEM ice-cores that represent 14 volcanic events between Greenland Stadial (GS) 9 and GI-8 – all of which fall within the compositional range of the FMAZ III found within the Faroes region. As such, Bourne et al. (2013) suggest that the FMAZ III most likely represents a complex ash zone in the marine environment made up of material from several closely-timed eruptions. This has major implications for establishing tephra correlations between ice core and marine records at this time and a re-evaluation of this deposit is required to assess whether individual stratigraphic horizons seen in the ice can be resolved in the marine realm.

The FMAZ IV is a recent discovery and appears as a thick black horizon in a number of marine cores in the Faroe Shetland Channel (Wastegård and Rasmussen, 2014). The horizon is thought to have been deposited during DO-12 and dates to *ca.* 47,000 years BP according to age model estimates (Wastegård and Rasmussen, 2014).

Initial work on the FMAZs focused on shards >150 μm in diameter (Rasmussen et al., 2003; Wastegård et al., 2006). Our study builds upon these investigations and employs cryptotephra extraction techniques to additionally explore the fine-grained fraction (25–150 μm) and present a contiguous shard concentration profile within a single marine core from the Faroes region. These profiles are considered alongside detailed geochemical results obtained from three separate grain-size fractions to capture the full compositional range of these tephra deposits. Microsedimentological structures across the depositional contacts are also investigated to refine the stratigraphical placement of the tephra isochron.

[2] Age uncertainties are reported as 1-sigma corresponding errors for the GICC05 chronology following Svensson et al. (2008).

2. Methodology

2.1. Core recovery and measurements

The JM11-19PC core was retrieved onboard the R-V Jan Mayen in May 2011 from 1179 m water depth on the central North Faroe Slope in the Southeastern Norwegian Sea (62°48′98″ N 03°52′04″ E) (Fig. 2). The core is ~11 m long and penetrates into MIS 6 sediments at the base. In this investigation we examine the depth interval between 183 and 558 cm, covering MIS 2 and part of MIS 3. Whole core magnetic susceptibility was measured onboard using a Geotek MSCL core loop sensor following procedures outlined in Rasmussen et al. (1996).

2.2. Density separation and identification of tephra shards

The tephra content of the core sequence between 183 and 558 cm depth was initially investigated at a 5 cm contiguous resolution and then intervals of elevated shard concentrations were further analysed at a 1 cm resolution. The samples were prepared and quantified according to the methodology outlined in Turney (1998) and Blockley et al. (2005) and modified for marine tephras by Abbott et al. (2011, 2013). Sediment samples were freeze dried and 0.5 g of dry weight sediment for each sample was weighed for tephra analysis. The sediment was then immersed in dilute HCl (10%) overnight to remove carbonate material. Each sample was subsequently wet-sieved into three separate grain-size fractions (>125 μm, 80–125 μm and 25–80 μm). The 25–80 μm fraction was density separated into three fractions using the heavy liquid sodium polytungstate to aid the isolation of rhyolitic (2.3–2.5 g/cm^3) and basaltic grains (>2.5 g/cm^3). Material from the >125 μm, 80–125 μm and 25–80 μm (2.3–2.5 g/cm^3) fractions was mounted in Canada Balsam on microscope slides and inspected for tephra content using optical microscopy. Material with a density of >2.5 g cm^3 was magnetically separated to purify the basaltic material.

2.3. Magnetic separation and spiking of basaltic tephra shards

Basaltic tephra exhibits ferromagnetic properties, mainly due to the high Fe content and through the influence of paramagnetic elements such as Al, Mg and Na (Walden et al., 1999). This allows tephra shards to be separated when a magnetic current is applied. Such separation significantly reduces the amount of non-magnetic particles, particularly quartz, in the sample of interest, improving efficiency during optical identification of basaltic tephra (Froggatt and Gosson, 1982). Previous use of magnetic separation to aid the isolation of basaltic material from other mineral components has demonstrated the efficiency that this technique can achieve by alteration of the magnetic field strength and the forward/sideway tilt of the apparatus (Froggatt and Gosson, 1982; Mackie et al., 2002).

With the use of a Frantz IsoDynamic Magnetic Separator, a series of experiments were conducted on ten different marine samples from a nearby Faroe Islands core (LINK 16) with previously quantified shard counts (Abbott et al., 2014). The magnetic current, tilt and slope were altered at intervals of 0.05 nA between 0.60 and 1.00 nA and five degrees between −15° and 25° respectively and the total number of separated basaltic shards in the magnetic fraction was determined. Two replicates of each sample were processed. The parameters that delivered the most effective recovery of tephra were identified as a current of 0.85 nA, tilt of −15° and a slope of 22.5° (Fig. 3). These parameters were then used to quantify the number of basaltic glass shards present within the JM11-19PC sequence.

A palynological quantification technique, previously applied to the study of tephra by Gehrels et al. (2006) and Bourne (2012) was employed due to the exceptionally high number of basaltic glass shards in the >2.5 g/cm^3 fraction. A Lycopodium spore tablet was added to the magnetically-separated residue and dissolved in 5 ml of distilled water in a centrifuge tube. These samples were placed in a water bath at 50 °C for two hours to ensure complete dissolution of the tablet. A dilute (10%) solution of HCl (2 ml) was then added to the

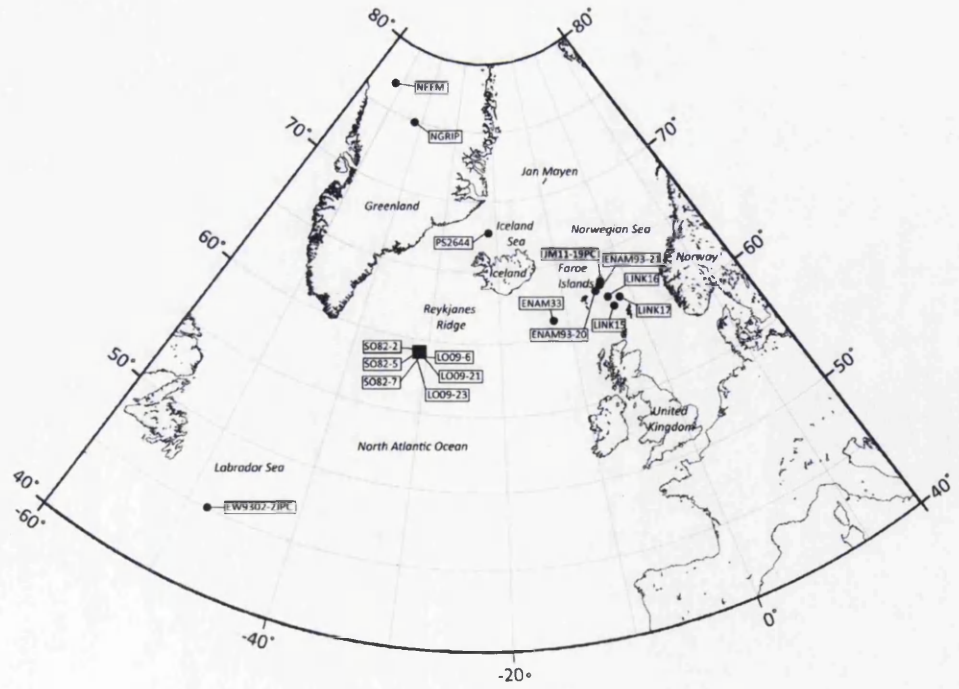

Fig. 2. Location map of the coring sites for JM11-19PC and Greenland ice and North Atlantic marine cores referred to in the text.

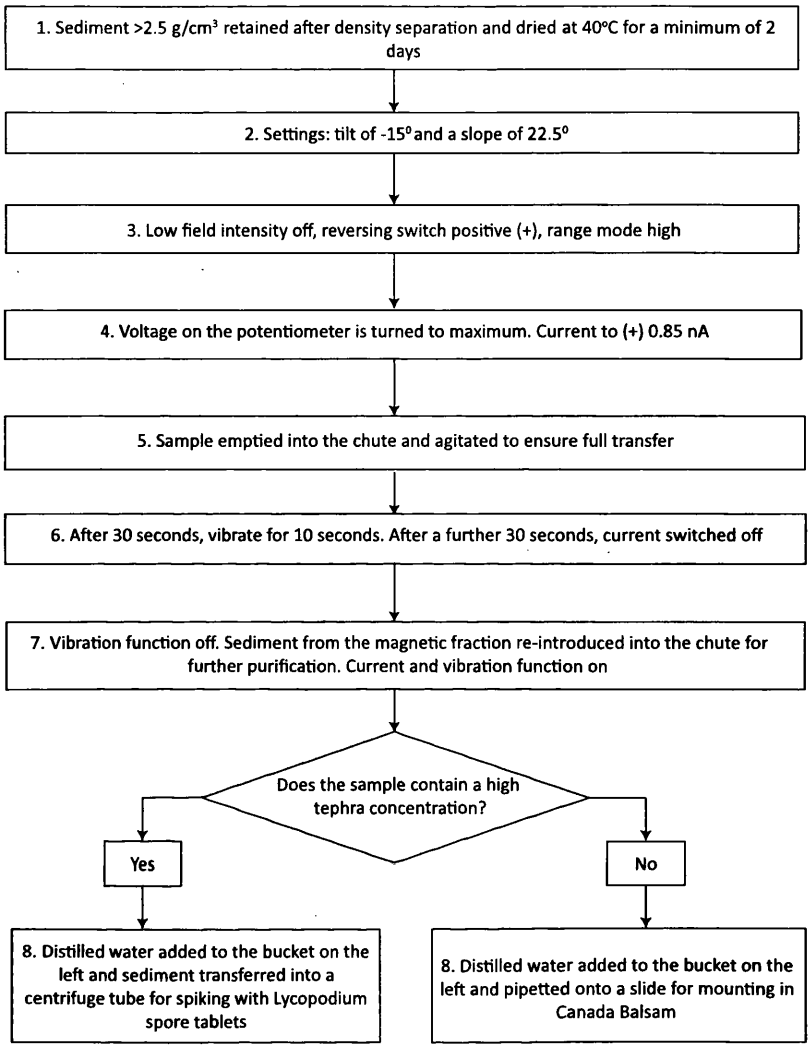

Fig. 3. Summary of protocol for the magnetic separation of basaltic shards from mineral-rich sediments.

solution to remove any remaining sodium bicarbonate. The spiked sample was washed three times with distilled water by centrifugation and finally 5 ml of distilled water was added to the centrifuge tube. The solution was shaken vigorously to mix the sample and eight drops of the mixture were pipetted onto a microscope slide and mounted in Canada Balsam. This amount was deemed to be the optimum volume to cover the slide beneath the cover slip, similar to the 500 µl recommended by Gehrels et al. (2006). Glass shards were counted alongside Lycopodium spores in each sample across three vertically-defined transects per slide. The concentration of tephra shards, *C*, was calculated using (Eq. (1)):

$$C = l \times \left(\frac{a}{bd}\right) \quad (1)$$

Where *a*) is the glass shard count, *b*) is the Lycopodium spore count, *d*) is the sample dry weight and *l*) is the number of Lycopodium spores in each tablet ($n = 20{,}848$) according to the manufacturer estimate determined using an electronic particle counter. This methodology was adapted for the high-resolution sampling intervals, where three tablets (i.e. 62,544 spores) were added to the magnetically-separated residue due to the exceptionally high glass shard concentrations.

2.4. Geochemical characterisation of glass shards

Glass shards were extracted for major element geochemical analysis from each grain-size fraction. Samples were processed according to the methodology outlined above and then mounted in epoxy resin on glass slides. The slides were then ground using silicon carbide paper and polished using 9, 6 and 1 µm diamond suspension to expose polished glass shard surfaces for electron-probe microanalysis (EPMA). The oxide concentrations of ten major and minor elements were analysed using wavelength-dispersive EPMA at the Tephrochronological Analytical Unit at the University of Edinburgh, using a Cameca SX100 electron microprobe equipped with five vertical WD spectrometers. The operating conditions are modified from Hayward (2012) and are outlined in the Supplementary information. Pure metals, simple silicate minerals and synthetic oxides, including andradite were used for calibration, and the secondary standards Lipari and BCR2g were analysed regularly to monitor elemental drift and to assess the accuracy of the shard analyses. Glass shards preserved in the marine realm are susceptible to variable levels of post-depositional hydration (Wallrabe-Adams and Lackschewitz, 2003; Abbott et al., 2011). As such the results of the EPMA analysis were normalised to 100% total oxide values (i.e. an anhydrous basis) to

remove any variability that may be apparent when comparing datasets from different depositional environments that have not experienced comparable levels of post-depositional hydration (Abbott et al., 2011; Pearce et al., 2014). All analyses with total oxide values < 94% were rejected. All raw data values are provided in the Supplementary information (see Tables 1–3). Similarity coefficient (SC) comparisons were employed using the methods outlined in Borchardt et al. (1972) and Begét et al. (1992).

2.5. Thin-section preparation

Undisturbed sediment samples were extracted in U-channels (20 × 20 mm) spanning the onset of tephra deposition and the decline in tephra shard deposition associated with each of the three ash zones. Thin-sections were prepared following the procedures outlined in Palmer et al. (2008), including the application of acetone replacement methods to limit cracking of silty clay sediment during drying (van der Meer and Menzies, 2011). Each thin-section was polished to a thickness of between 25 and 35 μm.

3. Results

3.1. Tephrostratigraphy, geochemistry and micromorphology

The tephrostratigraphy for JM11-19PC is presented in Fig. 4. Three distinct tephra deposits, composed of brown shards, were observed in the >2.5 g/cm^3 (25–80 μm), 80–125 μm and >125 μm fractions, spanning the position of the visible tephra horizons. Each deposit exhibits distinct peaks in shard concentration relative to background values. Geochemical results reveal that each major peak is made up of material with a basaltic composition (Fig. 5, Table 1).

3.2. FMAZ II

3.2.1. Tephrostratigraphy: JM11-19PC 298–308 cm

A visible black macrotephra forms a distinct 1 cm-thick horizon between 304 and 305 cm depth and coincides with the highest shard concentration (>4 million shards gdw in the 25–80 μm fraction and 147 in the >125 μm fraction). A sharp increase and decrease in shard concentration profile over 6 cm suggests a rapid pulse of tephra with limited post-depositional re-working. The shards have a dark brown colour, dense blocky morphology and some are slightly vesicular in appearance.

3.2.2. Micro-sedimentology

There are two distinct units in this section. The first occurs between 307 and 304.5 cm and consists of a poorly-sorted silty clay with occasional tephra shards (~55 μm in diameter; n = 20), distributed within the matrix (Fig. 6a). Toward the top of this unit, there are occasional (~1–3 mm) lenses of well-sorted tephra grains up to ~200 μm in size within the host sediment. These lenses are irregular, aligned horizontally or vertically within the host sediment (Fig. 6b) and generally composed of sediment from Unit 2. The second unit identified between 304.5 cm and 298 cm is composed of well-sorted, abundant tephra shards dominated by the size fraction of 25–80 μm (Fig. 6d). The unit has a sub-horizontal, sharp contact at 304–304.5 cm depth (Fig. 6c). There is evidence of discrete lobate structures below this level. Here, below the contact, material from unit 2 has penetrated into unit 1.

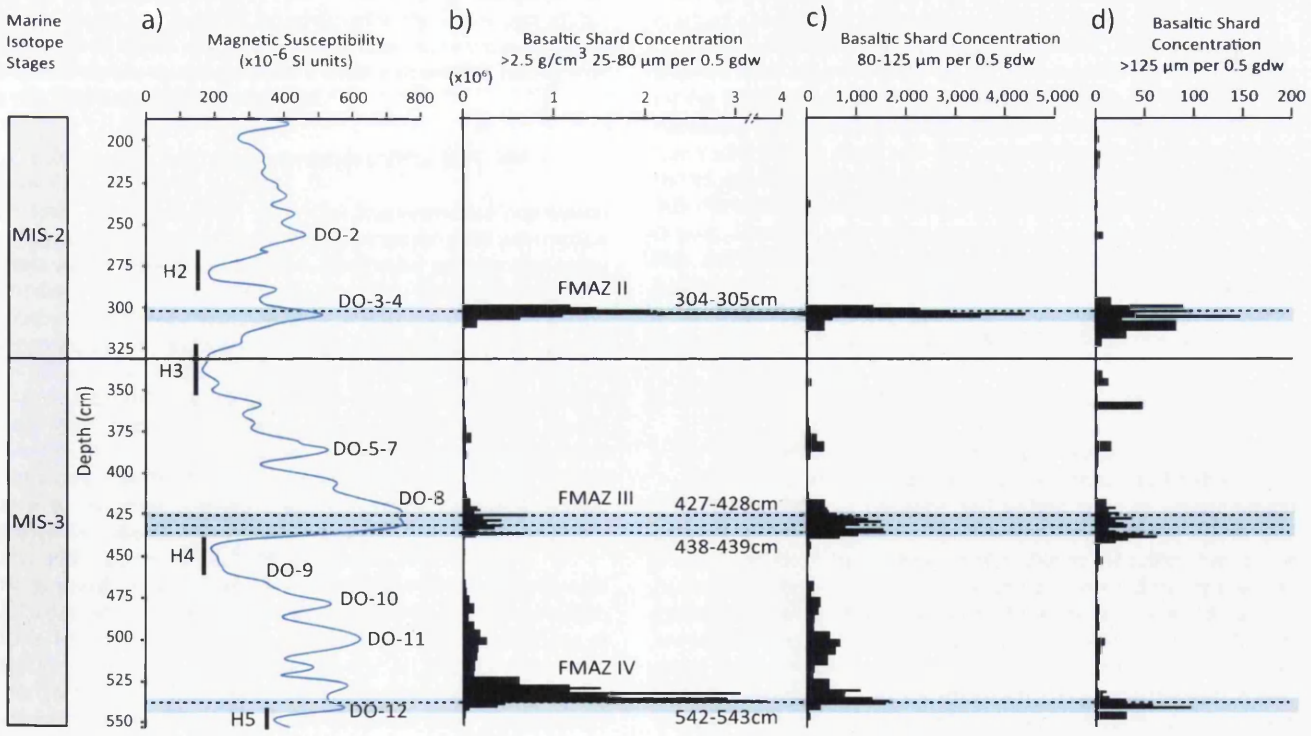

Fig. 4. Tephra stratigraphy for MIS 2 and late MIS 3 section from the JM11-19PC core. a) Magnetic susceptibility b) Number of basaltic shards with a density >2.5 g/cm^3 within the 25–80 μm fraction. c) Number of basaltic shards within the 80–125 μm fraction. d) Number of basaltic shards within the >125 μm fraction. Grey dotted lines denote samples for which glass shards were extracted for geochemical analysis. The shaded blue area denotes the depth intervals sampled for thin section analysis (see Fig. 6). H = Heinrich event approximate positions. DO = Dansgaard-Oeschger event and the number denotes the associated Greenland Interstadial event following the recommendations of Rasmussen et al. (2014). gdw = grams dry weight sediment. (For interpretation of the references to colour in this figure legend, the reader is referred to the web version of this article.)

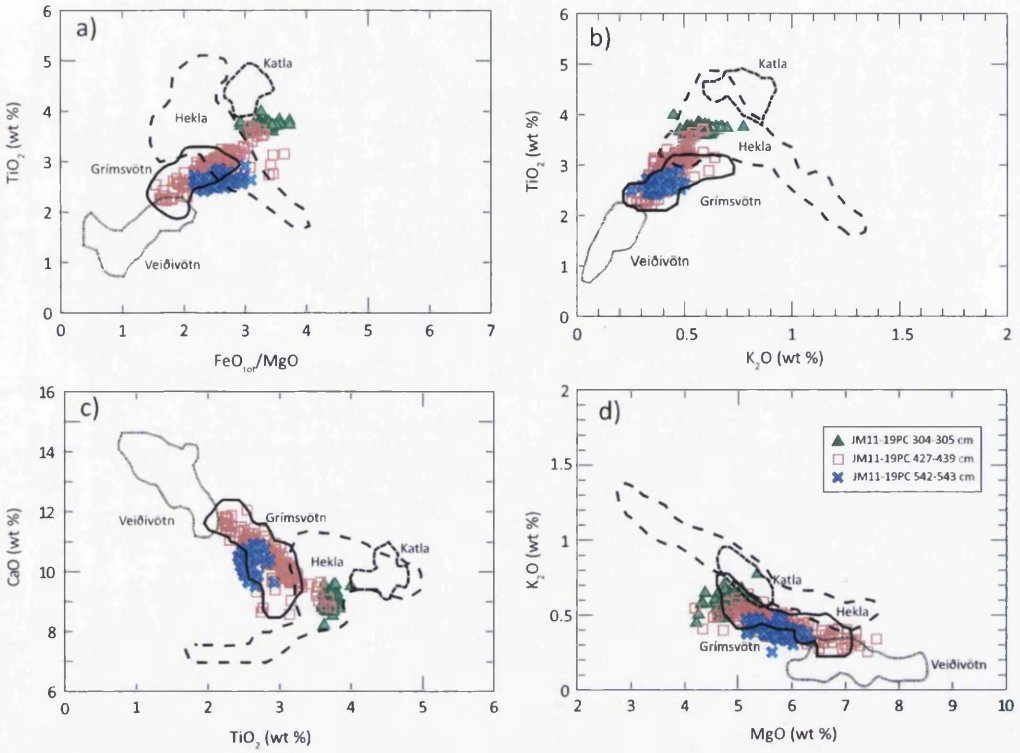

Fig. 5. Glass shard analyses for the 3 FMAZs in JM11-19PC compared to geochemical envelopes for different source volcanoes based on individual whole rock analyses presented in Jakobsson (1979), Boygle (1994), Larsen et al. (2002), Óladóttir et al. (2008) and Jakobsson et al. (2008). Data have all been normalised to 100% total oxide concentrations.

These features are most easily explained as loading structures. The tephra becomes less densely concentrated in the upper part of this unit and more mixed within the coarse-silty clay matrix (Fig. 6d). The visible tephra component has a similar shard size throughout this unit and no grading is observed.

3.2.3. Geochemistry and wider correlations; JM11-19PC 304–305 cm

In total, 85 shards form a distinct homogeneous population (Fig. 7), with only four clear outliers in the coarser >125 μm fraction and one in the 25–80 μm fraction. Distinctive geochemical characteristics include SiO_2 concentrations of ~47.7–51.0 wt%, TiO_2 concentrations of ~3.7 wt%, CaO concentrations of ~8.2–9.6 wt%, K_2O concentrations between ~0.4 and 0.8 wt% and FeO_{tot}/MgO ratios between ~2.8 and 3.7 (see Table 1). These characteristics are typical of a transitional alkali basaltic composition, suggesting a source from the Eastern or Southern Icelandic flank zones (Jakobsson, 1979). Comparisons with proximal Icelandic material demonstrate that the distinct geochemical population has a close affinity to material sourced from the Hekla/Vatnafjöll system (Fig. 5) (Jakobsson, 1979; Larsen, 1981; Lackschewitz and Wallrabe-Adams, 1997; Davies et al., 2008; Jakobsson et al., 2008).

Glass shard analyses from JM11-19PC show strong affinity with FMAZ II preserved in five other marine cores from the Faroes region and the NGRIP ice-core with an average similarity coefficient of 0.98 (Rasmussen et al., 2003; Wastegård et al., 2006; Davies et al., 2008). JM11-19PC and the NGRIP data-set exhibit a tighter geochemical population than observed for the other marine cores (Fig. 7). The wider geochemical scatter of shards from previously published Faroese cores and EW 9302-JPC in the Labrador Sea potentially extends the full compositional range of this eruption. Alternatively, this scatter may be the result of bottom current reworking (see Discussion 4.1.1 below). We also note that no shards investigated in this study fall within the FMAZ II-2 sub-population originally identified by Wastegård et al. (2006) (Fig. 7).

The geochemical population of JM11-19PC 304–305 cm also displays some affinities to the V1 ash zone deposited in marine cores on the Reykjanes Ridge (Lackschewitz and Wallrabe-Adams, 1997). According to the magnetic susceptibility record from JM11-19PC and a few radiocarbon dates and IRD record from the Reykjanes Ridge, the V1 ash zone falls in a similar stratigraphic position to the 304–305 cm horizon (Lackschewitz and Wallrabe-Adams, 1997). The V1 deposit, however, is heterogeneous (Fig. 7) and co-varies with high IRD, a diagnostic features of iceberg rafted deposits. However, a notable sub-peak, SO82-5-V1x-KAL, contains a homogenous population with no coeval IRD signal and exhibits a high similarity coefficient value of 0.95 with JM11-19PC 304–305 cm (Fig. 7).

3.3. FMAZ III

3.3.1. Tephrostratigraphy: JM11-19PC 423–443 cm

This deposit straddles the warming transition of DO-8 (Fig. 4). The deposit forms a complex and diffuse zone of tephra which exhibits 2 minor peaks in shard concentration in the 25–80 μm fraction, although the tephra is not visible to the naked eye. These peaks in the fine-grained fraction are not mirrored in the coarser-grained fractions, which contain multiple peaks across 13 cm and are offset from the 25–80 μm peaks in concentrations (Fig. 4). Total shard concentrations per 0.5 gdw do not exceed ~700,000 in the fine fraction and 62 shards in the coarse (>125 μm) fraction, which is significantly less than the other deposits examined within this study. Glass shards from each of the peaks at 438–439 cm and 427–428 cm in all grain-size fractions and the mid-point at 434 cm (25–80 μm fraction only) were extracted and prepared for geochemical analysis. In total, 173 glass shards were analysed for geochemistry. A correlation of the JM11-19PC tephra record with

Table 1
Mean and 1σ major element results of glass shards extracted from the main populations for the FMAZ II, III and IV. Total oxide values are raw values prior to normalisation. All major elements are expressed as percentage weight. Total iron is expressed as FeO. n = number of shards analysed. Two different EPMA operating setups were used. For the first setup, three sets of column conditions were employed. Firstly, NaO_2 and Al_2O_3 were determined using an accelerating voltage of 15 kV and a beam current of 0.5 nA. Secondly, MgO, K_2O, CaO, FeO and SiO_2 were determined using an accelerating voltage of 15 kV and a beam current of 2 nA. Thirdly, P_2O_5, TiO_2 and MnO were determined using accelerating voltage of 15 kV and a beam current of 60 nA. A 4 μm beam diameter was used throughout. Counting times were 20 s at the peak position and 10 s for background for all elements except MnO (60 and 60 s). For the second EPMA setup two column conditions were used. Na_2O, MgO, Al_2O_3, SiO_2, K_2O, CaO, and FeO were determined using an accelerating voltage of 15 kV and a beam current of 2 nA and P_2O_5, TiO_2, and MnO were determined using an accelerating voltage of 15 kV and a beam current of 60 nA. A 5 μm beam diameter was used throughout. Counting times were 20 s at the peak position and 10 s for background for all elements except TiO_2 (30 and 15 s), MnO (50 and 40 s) and FeO (40 and 20 s). The full data-set and reference values are given in the Supplementary file.

Tephra layer	Depth (cm)	Grain size (μm)	n	SiO_2	TiO_2	Al_2O3	FeO	MnO	MgO	CaO	Na_2O	K_2O	P_2O_5	Total
FMAZ II	304–305	25–80	22	50.13	3.71	12.77	15.35	0.24	4.78	8.92	3.05	0.56	0.48	97.68
				0.44	0.09	0.30	0.51	0.01	0.27	0.26	0.33	0.06	0.04	1.18
FMAZ II	304–305	80–125	41	49.49	3.70	13.15	15.33	0.25	4.83	9.15	3.13	0.57	0.41	97.34
				0.64	0.05	0.38	0.50	0.01	0.19	0.20	0.25	0.05	0.02	1.37
FMAZ II	304–305	>125	22	50.14	3.70	12.70	15.34	0.24	4.75	9.10	3.06	0.59	0.39	98.05
				0.30	0.04	0.36	0.34	0.01	0.19	0.21	0.12	0.05	0.02	0.80
FMAZ II Average	304–305	25–80, 80–125, >125	85	49.82	3.70	12.93	15.34	0.24	4.80	9.08	3.09	0.57	0.42	97.61
				0.61	0.06	0.41	0.46	0.01	0.21	0.23	0.25	0.05	0.04	1.22
FMAZ III	427–428	25–80	25	49.94	2.99	13.16	14.18	0.23	5.68	10.38	2.75	0.43	0.26	98.54
				0.43	0.30	0.42	0.97	0.01	0.56	0.70	0.26	0.08	0.04	0.75
FMAZ III	427–428	80–125	28	49.46	2.86	13.40	13.87	0.22	6.01	10.56	2.91	0.42	0.27	97.78
				0.51	0.40	0.64	1.09	0.02	0.72	0.80	0.27	0.10	0.06	1.55
FMAZ III	427–428	>125	8	49.62	2.61	13.66	13.00	0.21	6.43	11.13	2.73	0.37	0.23	98.05
				0.30	0.28	0.28	0.71	0.01	0.54	0.47	0.16	0.06	0.04	0.86
FMAZ III	434–435	25–80	23	49.96	3.02	12.98	14.49	0.23	5.54	10.15	2.89	0.46	0.27	98.36
				0.43	0.28	0.37	0.74	0.02	0.52	0.55	0.19	0.07	0.03	1.07
FMAZ III	438–439	25–80	24	49.97	3.03	13.06	14.24	0.23	5.66	10.18	2.91	0.46	0.26	98.76
				0.37	0.26	0.37	0.71	0.01	0.47	0.51	0.21	0.06	0.03	0.89
FMAZ III	438–439	80–125	25	49.89	2.95	13.12	14.08	0.22	5.83	10.38	2.86	0.42	0.26	98.89
				0.40	0.21	0.28	0.79	0.01	0.49	0.51	0.17	0.06	0.02	0.97
FMAZ III	438–439	>125	23	49.73	2.90	13.26	13.98	0.22	6.00	10.38	2.85	0.42	0.27	98.31
				0.32	0.30	0.47	1.02	0.02	0.53	0.62	0.13	0.05	0.04	0.70
FMAZ III Average	427–439	25–80, 80–125, >125	156	49.81	2.94	13.20	14.07	0.23	5.83	10.38	2.85	0.43	0.26	98.42
				0.44	0.31	0.47	0.93	0.02	0.59	0.65	0.22	0.07	0.04	1.09
FMAZ IV	542–543	25–80	25	50.58	2.56	13.26	14.17	0.23	5.67	10.09	2.80	0.39	0.23	98.18
				0.36	0.09	0.23	0.47	0.01	0.27	0.28	0.12	0.05	0.01	0.78
FMAZ IV	542–543	80–125	32	50.11	2.59	13.30	14.24	0.23	5.76	10.30	2.84	0.40	0.23	97.83
				0.46	0.09	0.24	0.57	0.01	0.33	0.35	0.23	0.04	0.02	1.08
FMAZ IV	542–543	>125	14	50.34	2.63	13.23	13.93	0.23	5.84	10.46	2.71	0.40	0.23	98.24
				0.38	0.12	0.28	0.49	0.01	0.27	0.36	0.18	0.06	0.02	0.86
FMAZ IV Average	542–543	25–80, 80–125, >125	71	50.32	2.59	13.27	14.15	0.23	5.75	10.26	2.80	0.39	0.23	98.03
				0.46	0.10	0.24	0.53	0.01	0.30	0.36	0.19	0.04	0.02	0.95

that of a neighbouring core (ENAM93-21) suggests that no coeval IRD signal is associated with the FMAZ III deposit (Fig. 8).

3.3.2. *Micro-sedimentology*

This deposit is composed of a single unit from 443 to 423 cm and contains massive, poorly-sorted coarse silty clay (Fig. 6ii). Tephra shards, ~45 μm in diameter (n = 20), are randomly distributed within the host sediment, although there are occasional small (~1 mm) sub-horizontal and irregular lenses of tephra concentrated within the unit (Fig. 6e). There are no distinct micro-sedimentological features that coincide with the peaks in shard concentration (Fig. 6ii).

3.3.3. *Geochemistry and wider correlations JM11-19PC 427–439 cm*

Distinctive geochemical characteristics of this deposit include SiO_2 contents of ~48.5–51.1 wt%, K_2O concentrations of ~0.4 wt %, TiO_2 concentrations of ~2.3–3.7 wt%, CaO concentrations of ~8.8–12.1 wt% and MgO concentrations between ~4.7 and 7.6 wt% (Fig. 9). These characteristics are typical of a tholeiitic basaltic composition, with the TiO_2 and K_2O concentrations implying an origin from the Grímsvötn system (Jakobsson, 1979) (Fig. 5). Although a volcanic source can be determined for the deposit, glass shards from each individual depth sample occupy the full range of Grímsvötn-sourced material. Each grain-size fraction from 438 to 439 cm appears to exhibit a relatively tight population, although no other distinct populations can be observed for the other depth-intervals that have been analysed. Moreover, biplots of TiO_2 vs CaO and FeO_{tot}/MgO vs TiO_2 highlight the heterogeneity and wide range of values for these oxides (Fig. 9d).

Seventeen outlier shards are found in this deposit and appear unrelated to the main FMAZ III population and cannot be regarded as additional sub-populations (Fig. 9a). Although six of these shards fall within the FMAZ III-2 envelope, previously defined by Wastegård et al. (2006), we do not believe that this sub-population is present within JM11-19PC due to the low number of analyses that fall within this envelope.

Glass shard analyses from the main geochemical population show strong similarities and a similarity coefficient of 0.98 with FMAZ III deposits from three other marine cores in the Faroes region (Rasmussen et al., 2003; Wastegård et al., 2006) (Fig. 9). The geochemical composition of these previously published deposits exhibit a near-identical spread to the JM11-19PC 427–439 cm deposit. This can be clearly observed on TiO_2 vs CaO and FeO_{tot}/MgO vs K_2O geochemical biplots (Fig. 9a and b).

Wastegård et al. (2006) proposed that a correlation may exist between the V2 ash zone and the FMAZ III. The V2 ash zone has

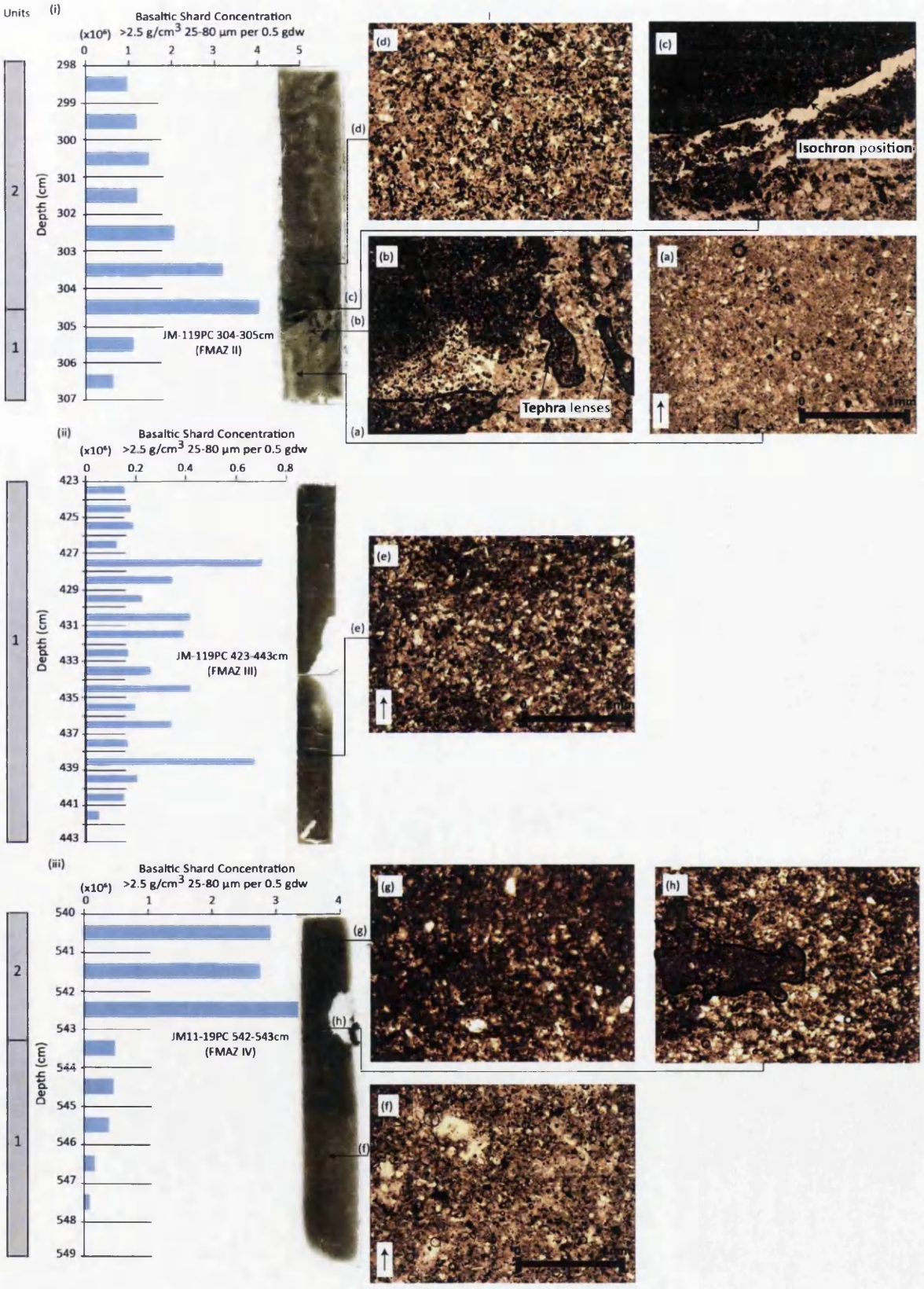

Fig. 6. Thin-section micromorphology images aligned to high-resolution shard concentration profiles (25–80 µm fraction) across each ash zone. Indicative microfacies features observed throughout each of the FMAZ deposits are presented. Units 1 and 2 are defined according to the micro-sedimentological features observed. (i) FMAZ II deposit (a) unit 1 (307–304.5 cm) with a massive, relatively poorly-sorted matrix of silty clay. Light and dark brown glass shards are dispersed in relatively low concentrations. (b) Irregular

been dated to 36.5–29.8 ^{14}C ka BP in five cores on the Reykjanes Ridge (Lackschewitz and Wallrabe-Adams, 1997). The V2 ash zone exhibits a heterogeneous geochemical signature and coincides with a high input of IRD, sourced from active erosion on the Icelandic ice sheet (Lackschewitz and Wallrabe-Adams, 1997). A number of shards fall within the JM11-19PC 427–439 cm compositional envelope (Fig. 9c), although the wide geochemical spread across all elemental oxides prevents a correlation between the two deposits.

Fig. 9d highlights how the wide geochemical range of the FMAZ III deposit in JM11-19PC straddles the compositional fields for ten of the cryptotephra deposits identified in NGRIP during this time period (between 38,048 ± 721 a b2k and 38,826 ± 740 a b2k) (Bourne et al., 2013). Thus, none of the glass shard populations from the individual depth intervals between 427 and 439 cm can be exclusively correlated to a single ice-core horizon.

3.4. FMAZ IV

3.4.1. Tephrostratigraphy; JM11-19PC 533–548 cm

A visible thick black macrotephra (6 cm) was deposited during the early stages of DO-12 and after H5, according to the high magnetic susceptibility values (Fig. 4). A rapid increase in shard concentration is evident in the 25–80 μm fraction at 542–543 cm, increasing to ~2.9 million shards per 0.5 gdw. Thus, 542–543 cm represents the peak in shard concentration and is suggested to equate to the correct stratigraphical placement of the isochron. The initial major influx in the 80–125 μm fraction is 1 cm below this peak. This slight depth offset could be due to different settling velocities through the ocean, or the movement of heavier material through soft sediment (Enache and Cumming, 2006). Shards at 542–543 cm are yellowish-brown in colour, have a vesicular appearance and display a variety of platy morphologies. In general, the shard concentration profile forms a similar upward tail to that of the 298–303 cm deposit, although the decline in concentration is far more gradual in this horizon; forming a tailed, gradational distribution that covers a ~40 cm interval. This can be seen visibly in the core and is reflected in the 25–80 μm fraction, which maintains shard concentrations >1 million per 0.5 g (gdw) at the end of the 10 cm high-resolution sampling interval.

3.4.2. Micro-sedimentology

There are two distinct units in this section. The first occurs between 549 and 543.3 cm and is composed of a massive, moderately-sorted coarse silt with a low concentration of tephra shards, ~50 μm in diameter (n = 20), distributed randomly within the matrix (Fig. 6f). The second unit identified between 543.3 and 540 cm is composed of moderately-sorted, abundant tephra shards dominated by the 25–80 μm size fraction within a coarse silt host sediment. This second unit has a diffuse contact with the underlying sediment and there are occasional horizontally aligned lenses (~1.5 mm) of well-sorted tephra grains up to ~140 μm in size (Fig. 6h). The visible tephra component has a similar shard size (25–80 μm) throughout the second unit. The tephra is highly concentrated but poorly mixed within the host sediment (Fig. 6g).

3.4.3. Geochemistry and wider correlations: JM11-19PC 542–543 cm

In total, 71 shard analyses form a homogeneous population (Fig. 10), with 1 clear outlier in the 25–80 μm fraction and two clear outliers in the 80–125 μm fraction. Distinctive geochemical characteristics of the main population are SiO_2 concentrations of ~49.0–51.4 wt%, K_2O concentrations of ~0.4 wt% and TiO_2 and MgO concentrations of ~2.6 wt% and ~5.8 wt% respectively (Fig. 10). These geochemistries are characteristic of the tholeiitic rock suite, and the latter two oxides suggest a strong affinity to the Grímsvötn system in the Eastern Volcanic Zone of Iceland (Jakobsson et al., 2008) (Fig. 5).

A comparison of the glass shard analyses with deposits from four other marine cores in the Faroes region suggests a strong statistical similarity (SC = 0.98) with the recently discovered 'FMAZ IV' tephra (Wastegård and Rasmussen, 2014). This can be clearly observed on FeO_{tot}/MgO vs TiO_2 and CaO vs MgO biplots (Fig. 10a). JM11-19PC exhibits a tighter distribution of geochemistries in comparison to other cores analysed in the Faroes region, and only glass shards isolated in LINK 15 have a sub-population with a Katla affinity.

Wastegård and Rasmussen (2014) suggest that a potential correlation exists between the FMAZ IV and the V5 ash zone found in two cores on the Reykjanes Ridge, with an age estimate of 46.2–52.5 ^{14}C ka BP (Lackschewitz and Wallrabe-Adams, 1997). The deposit has no coeval IRD signal, but exhibits a heterogeneous geochemical distribution (Lackschewitz and Wallrabe-Adams, 1997). One of the populations from the V5 ash zone in core SO82-7-KAL includes a number of shards which fall within the JM11-19PC 542–543 cm compositional envelope (Fig. 10b). A statistical similarity coefficient of 0.95 suggests a correlation may exist between the two deposits, although the absence of shard concentration profiles prevents a full correlation as the stratigraphic position of the isochron within the Reykjanes Ridge record is uncertain.

A number of basaltic horizons deposited during MIS 3 have also been reported in core PS-2644 in the Iceland Sea, NW of Iceland (Voelker et al., 2000). Two horizons lie in a similar stratigraphic position to JM11-19PC 542–543 cm, based upon the planktonic foraminifera $\delta^{18}O$ record (Voelker et al., 2000; Wastegård and Rasmussen, 2014). The horizon at 5.18 m within PS-2644 has a relatively homogenous population but exhibits higher TiO_2, FeO_{tot} and K_2O concentrations than JM11-19PC 542–543 cm. The horizon at 5.22 m is heterogeneous with multiple geochemical populations, although some shards display affinity to the JM11-19PC 542–543 cm compositional envelope (Fig. 10b). The heterogeneity of this deposit, however, makes it difficult to provide a correlative link between the Faroes region and the Iceland Sea.

4. Discussion

4.1. Determining transport and depositional processes

4.1.1. FMAZ II

A striking feature of the FMAZ II deposit is the strong geochemical homogeneity reflected in the JM11-19PC data-set.

horizontally and vertically aligned tephra lenses, composed of abundant, well-sorted glass shards. (c) Isochron position of JM11-19PC at 304–305 cm with a sharp contact of abundant well-sorted tephra. (d) Unit 2 (304.5–298.0 cm) of the FMAZ II deposit; the glass shards are less densely concentrated in the upper part of this unit and more mixed within the host sediment. (ii) FMAZ III deposit (e) Indicative microfacies features with structureless/massive, relatively poorly-sorted matrix of coarse clays and coarse silts, with glass shards distributed in lenses randomly throughout. A high number of mineral grains are also present. (iii) FMAZ IV deposit (f) Moderately-sorted coarse silts with glass shards distributed randomly in low concentrations throughout unit 1 (549.0–543.3 cm) (g) Unit 2 (543.3–540 cm) of the FMAZ IV composed of moderately-sorted, abundant glass shards within a coarse silt host sediment. (h) Isochron position of JM11-19PC 542–543 cm with occasional horizontally aligned lenses of well-sorted and concentrated glass shards (highlighted). The contact between unit 1 and unit 2 is diffuse. (For interpretation of the references to colour in this figure legend, the reader is referred to the web version of this article.)

Glass shard analyses from other cores in the Faroes region reveal a wider scatter (Fig. 7) which has been suggested to represent different phases of the same eruption, although an eruption closely separated in time cannot be excluded (Wastegård et al., 2006). Alternatively, this scatter may result from the operation of bottom currents and the transportation of material from older eruptions to these sites. Glass shards analysed from the JM11-19PC and LINK17 cores exhibit the tightest geochemical populations and plot consistently within the NGRIP 1848.0 m (FMAZ II) compositional envelope. This suggests that deposition was likely controlled by one dominant primary process in the Faroes region and several lines of evidence suggest that this tephra was deposited isochronously, most likely via sea-ice rafting. Firstly, the concentration of coarse-grained shards (>125 μm) is very low in this deposit and the dominant grain size (i.e. 25–80 μm) is typical for primary-airfall or sea-ice rafted deposits. Secondly, the absence of a strong coeval IRD signal suggests that iceberg rafting was not responsible for deposition (Fig. 8). Thirdly, micro-sedimentological features within JM11-19PC suggest the operation of sediment loading. A sudden influx of high tephra concentrations is identified by the sharp contact between units one and two, and the discrete tephra lenses in unit one suggest that glass shards have loaded into the sediment (Fig. 6b). This may result from the rapid influx of tephra to the sediment/water interface at the seabed and the vertical movement of denser tephra shards into the less dense underlying sediment. Thus, the discrete packages of tephra beneath the isochron are interpreted to be the result of gravitational loading. This feature is also apparent in the low shard concentrations beneath the main distribution peak at 304–305 cm (Fig. 4). We postulate that this may be evidence for sea-ice deposition, as we suggest tephra is likely to have fallen to the ocean floor rapidly, following the high accumulation of primary airfall deposits onto seasonal sea-ice. High concentrations of visible tephra occur ~2 cm above the load structure at 302–303 cm and although the sedimentary matrix is structureless, this suggests the density contrast was no longer sufficient for the sediment to become unstable and deform. This could represent the diminishing input of tephra into the succession. Importantly, the isochron is placed at 304–305 cm in the JM11-19PC core, marking the sharp contact between the two sedimentary units and the loading of high tephra delivery into the sequence, which is further re-inforced by a peak in shard concentration at this depth interval.

The correlation of this horizon to the SO82-5-V1x-KAL horizon on the Reykjanes Ridge provides further evidence for the operation of sea-ice rafting. The high number of coarse-grained shards (up to 500 μm in diameter) within the V1x horizon suggests that primary airfall is unlikely. Although Lackschewitz and Wallrabe-Adams (1997) propose that the horizon is a product of local sediment gravity flows, the evidence presented here cannot rule out the possibility of sea-ice rafting which was particularly prevalent during the stadial conditions at the time of tephra deposition.

4.1.2. FMAZ IV

The geochemical homogeneity of the FMAZ IV deposit in JM11-19PC and other cores in the Faroes region strongly implies primary deposition. Several lines of evidence suggest that this tephra was deposited isochronously, most likely via primary airfall. Firstly, the concentration of coarse-grained shards (>80 μm) is very low and the dominant grain size (i.e. <80 μm) is typical for atmospherically-derived deposits. Secondly, geochemical similarities between this deposit and the V5 ash zone in core SO82-5, which exhibits no coeval IRD signal, suggests iceberg rafting was not responsible for its deposition. Thirdly, unlike the FMAZ II, the absence of load structures in the microfacies of this deposit suggests a sea-ice component did not assist in tephra delivery to the site. In addition, a distinct feature of this tephra deposit is an upward tail on the shard concentration profile (Fig. 4). This evidence may suggest greater rates of bioturbation during this period and upward mixing (e.g. Jumars and Wheatcroft, 1989; Abbott et al., 2013; Todd et al., 2014) or re-working by stronger bottom currents during interstadial conditions following primary deposition onto the seafloor. There is also a possibility that material from this one eruption may have been repeatedly overlain at the site following deposition in other regions. Implicit in this interpretation is that movement of particles through the ocean was not as aggregated or as rapid as when it was deposited from the melting of sea-ice and was of insufficient concentration to cause gravitational loading. We believe that these processes are unlikely to have affected the depth and value of the isochron.

The presence of glass shards of Katla composition in the nearby LINK 15 implies that the processes controlling deposition at this particular site were different to those operating at other core locations. Given the absence of loading at JM11-19PC, there is unlikely to be a sea-ice component and thus, the heterogeneity within the LINK 15 deposit may be a reflection of different bottom current transport pathways. Importantly, the isochron is placed at 542–543 cm in the JM11-19PC core, marking the peak in shard concentration and the initial presence of tephra lenses identified within the microfacies. The isochron position also falls within high magnetic susceptibility values in the JM11-19PC core, suggested to equate to the warmth of DO-12, providing further evidence that a sea-ice component is unlikely to have assisted in the deposition of this tephra deposit.

4.1.3. FMAZ III

The diffuse nature of the FMAZ III deposit, which contains multiple peaks in shard concentration, combined with geochemical heterogeneity, suggests either the operation of iceberg rafting and/or post-depositional processes. Iceberg rafting is unlikely due to the absence of a coeval IRD signal (Fig. 8) and low concentrations of coarse-grained shards (>125 μm) (Fig. 4). Instead, the evidence suggests that primary airfall is the dominant transport process, but implies that another process may have operated to modify this depositional signal.

The diagnostic tailed shard distribution and homogeneous geochemistry exhibited by the FMAZ IV has been interpreted to be a signature of bottom current remobilisation and/or bioturbation of material from a single eruption, which implies that these processes alone were insufficient to produce the heterogeneous composition of the FMAZ III deposit. However, the geochemical similarities between this deposit and ten separate volcanic events identified in NGRIP over this time period (Bourne et al., 2013) suggests that the FMAZ III is a tephra zone made up of an amalgamation of glass shards sourced from several closely-timed Grímsvötn eruptions. The sedimentary accumulation rate in the marine environment is most likely insufficient to isolate and stratigraphically separate glass shards from each closely-timed individual eruption as preserved in the ice-core record (Bourne et al., 2013). We postulate that bottom currents and bioturbation further contributed to form the amalgamation of this tephra deposit, following deposition via primary airfall. This is further supported by the microfacies of JM11-19PC, which consists of a structureless mass of sediment with sporadic tephra packages dispersed randomly throughout the sequence, reflecting frequent input into the system and/or remobilisation of shards (Fig. 6). In this instance, the microfacies analysis for FMAZ III cannot help to assign the position of the isochron. Furthermore, this deposit demonstrates that the integrity of the isochron, despite being a product of primary airfall, is compromised by the frequency of eruptions during this period of deposition.

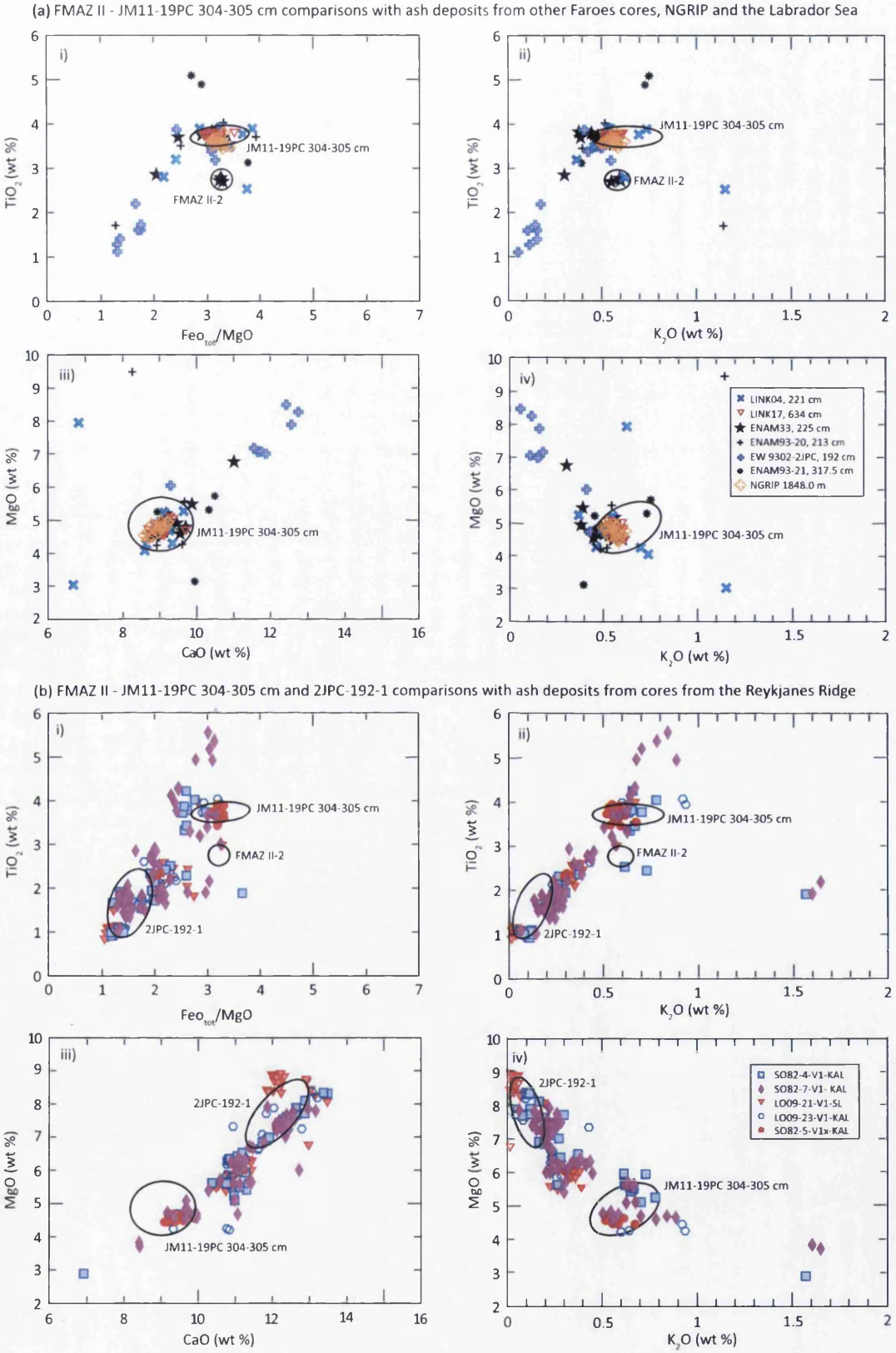

Fig. 7. Major oxide results (wt %) for glass shards from the FMAZ II deposit. (a) (i–iv) The JM11-19PC 304–305 cm compositional envelope is derived from shard analyses obtained from all grain size fractions investigated in this study. An envelope rather than the individual data points are shown for clarity. Geochemical results for other reported FMAZ II deposits in the North Atlantic are shown for comparison and the FMAZ II-2 compositional envelope is defined by Wastegård et al. (2006). Glass shard analyses from six marine cores from the Faroes region and EW9302-2JPC in the Labrador Sea are from Wastegård et al. (2006). Data for NGRIP 1848.0 m from Davies et al. (2008). (b) (i–iv) Geochemical envelopes for the 2JPC-192-1 (a geochemical population present in EW9302-2JPC) and JM11-19PC 304–305 cm deposits compared to V1 and V1-x glass shard analyses derived from five marine cores on the Reykjanes Ridge (Lackschewitz and Wallrabe-Adams, 1997). Data have all been normalised to 100% total oxide concentrations. Outliers from JM11-19PC have been omitted.

The FMAZ III forms a diachronous surface and whilst the deposit can be useful for marine correlations, its use as a high-precision isochronous tie-point is limited. High sedimentation areas may well preserve well-defined shard concentration peaks with distinct geochemical populations. We refer to this deposit as an 'ash zone' and suggest that this term be used solely as a descriptive term to depict the presence of tephra within a core, without any preconceived notions of geochemical characteristics and depositional processes. If horizons can be resolved within the ash zone using techniques outlined above, then the deposit could well reveal discrete isochrons. Implicit in this definition is that the FMAZ II and FMAZ IV are ash zones that form well-defined isochronous horizons.

4.2. The development of a protocol for assessing tephra deposition in the marine environment

Using existing knowledge from previous marine tephra investigations (e.g. Haflidason et al., 2000; Rasmussen et al., 2003; Wastegård et al., 2006; Brendryen et al., 2010; Abbott et al., 2011, 2013) and the diagnostic signatures of the FMAZs outlined here, we are able to recommend a stepped analytical protocol for resolving tephra depositional pathways in the marine realm (Fig. 11). This procedure highlights the importance of employing contiguous shard concentration profiles, geochemical characteristics and IRD indicators. Micromorphological analysis provides important additional sedimentological evidence for the dominant processes of tephra delivery to the sea floor and supports the correct stratigraphical placement of the isochron. The occurrence of sedimentary loading has been suggested here to potentially reflect the delivery of tephra to the site via sea-ice. However, distinguishing between sea-ice rafting and primary-airfall is not essential, as sea-ice transportation is unlikely to have affected the position or integrity of the tephra horizon for use as an isochronous marker. Identification of tephra deposits transported by iceberg rafting, however, is crucial.

This protocol also encourages an understanding of ocean currents and the climatic regime associated with tephra deposition. The tephrostratigraphic record from the Faroe-Shetland Channel provides some of the highest concentrations of tephra presently found in the North Atlantic (Wastegård and Rasmussen, 2014). This may be due to its proximity to Iceland and/or due to elevated bottom current transport pathways concentrating material following eruptions. Thus, it is essential to assess whether deposition occurred during stadial or interstadial climates, which exert a control on the strength of bottom currents and subsequently the ability to remobilise previously deposited material. This protocol highlights the importance of using a range of indicators in order to unravel the operation of different depositional mechanisms. We also stress that this protocol is not exhaustive and envisage further iterations and additions based on further work at a network of sites in the North Atlantic to refine the complex interplay of processes that are spatially dependant. Nonetheless, we believe that the protocol outlined in Fig. 11 provides a robust framework and a suite of indicators that will aid in the assessment of depositional processes influencing both tephra and cryptotephra deposits in the marine environment.

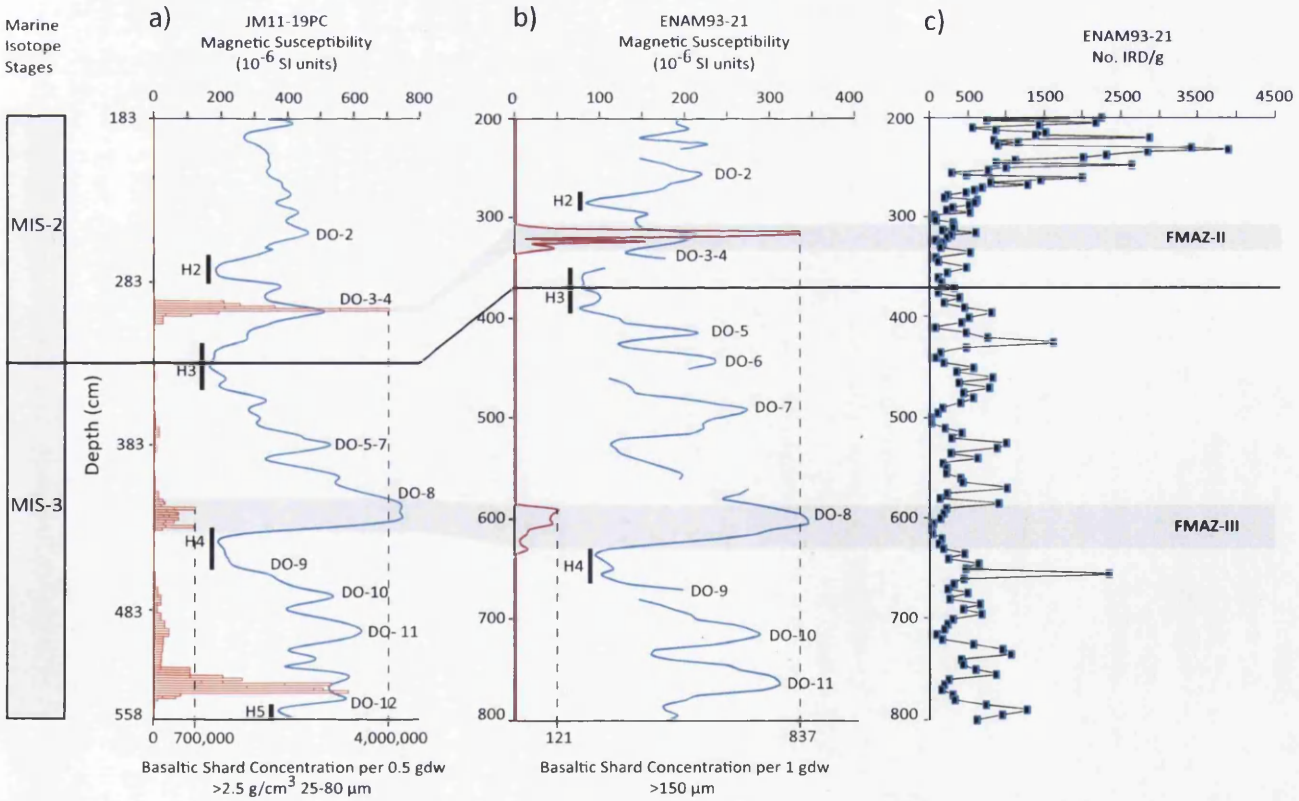

Fig. 8. Comparison of JM11-19PC and ENAM93-21 magnetic susceptibility and tephrostratigraphies to ascertain a corresponding IRD signal. a) Magnetic susceptibility for JM11-19PC with corresponding tephra counts with a density >2.5 g/cm^3 within the 25–80 µm fraction (gdw = grams dry weight sediment) b) Magnetic susceptibility for ENAM93-21 (Rasmussen et al., 1996) with corresponding tephra counts from the >150 µm fraction (Rasmussen et al., 2003). c) Number of ice-rafted grains >500 µm per gdw (IRD) in ENAM93-21 (Rasmussen et al., 1996). The grey bars represent correlation between records based upon the position of the FMAZ II and FMAZ III horizons in both sequences. H = Heinrich event approximate positions. DO = Dansgaard-Oeschger event following the recommendations in Rasmussen et al. (2014).

(a) JM11-19PC geochemical distribution of all grain size fractions between 427-439 cm

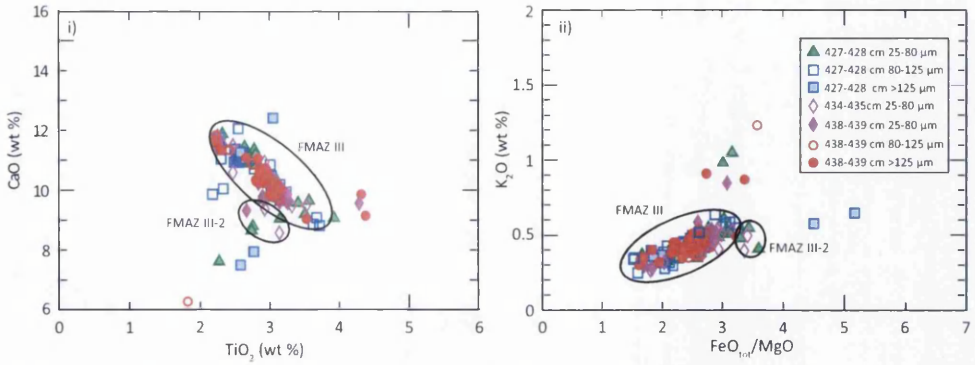

(b) Comparison of the geochemical populations from JM11-19PC 427-439 cm with ash deposits from marine cores from the Faroes region

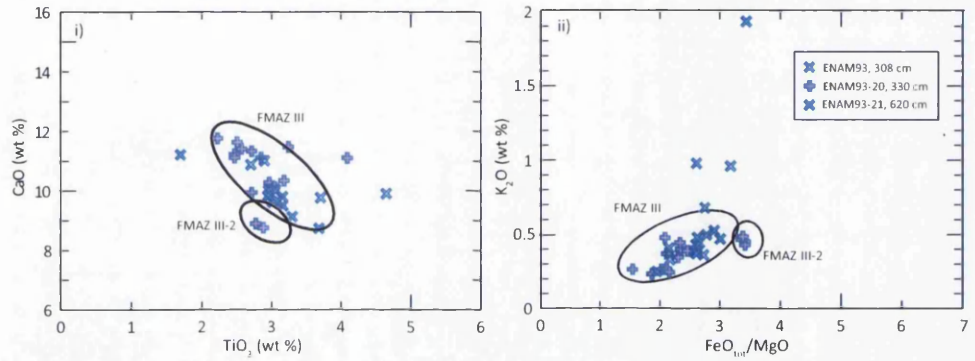

(c) Comparison of the geochemical populations from JM11-19PC 427-439 cm with ash deposits from marine cores from the Reykjanes Ridge

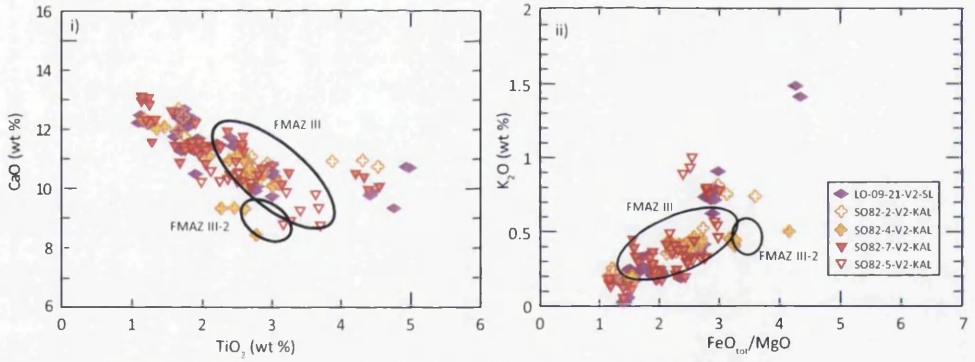

(d) Comparison of all grains sizes from JM11-19PC 427-439 cm with 10 horizons from NGRIP

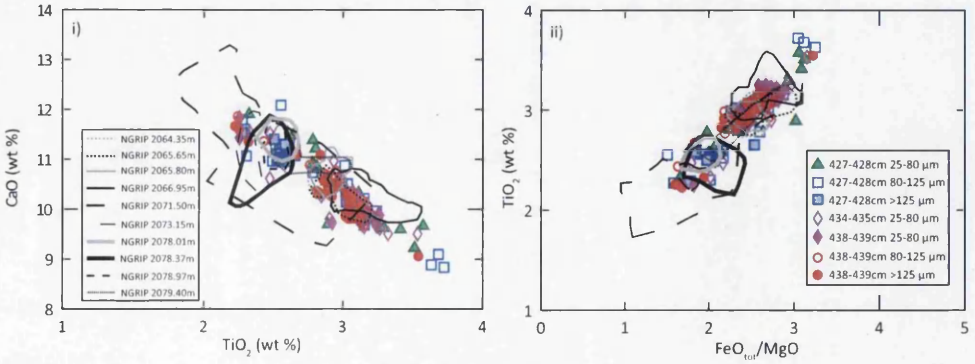

Fig. 9. Major oxide results (wt %) for the FMAZ III deposit identified in JM11-19PC. (a) (i & ii) The FMAZ III compositional envelope is derived from the main geochemical population from 427 to 439 cm in JM11-19PC and the FMAZ III-2 envelope is a sub-population defined by Wastegård et al. (2006). (b) (i & ii) JM11-19PC FMAZ III and FMAZ III-2 envelopes compared to glass shard analyses from three marine cores in the Faroes region (Wastegård et al., 2006). (c) (i & ii) JM11-19PC FMAZ III and FMAZ III-2 envelopes compared to the V2 ash zone identified in four marine cores on the Reykjanes Ridge (Lackschewitz and Wallrabe-Adams, 1997). (d) (i & ii) Glass shard analyses from JM11-19PC 427–439 cm compared to ten geochemical compositional envelopes for cryptotephra deposits identified in NGRIP between 38,048 ± 721 a b2k and 38,826 ± 740 a b2k (Bourne et al., 2013). The data have all been normalised to 100% total oxide concentrations.

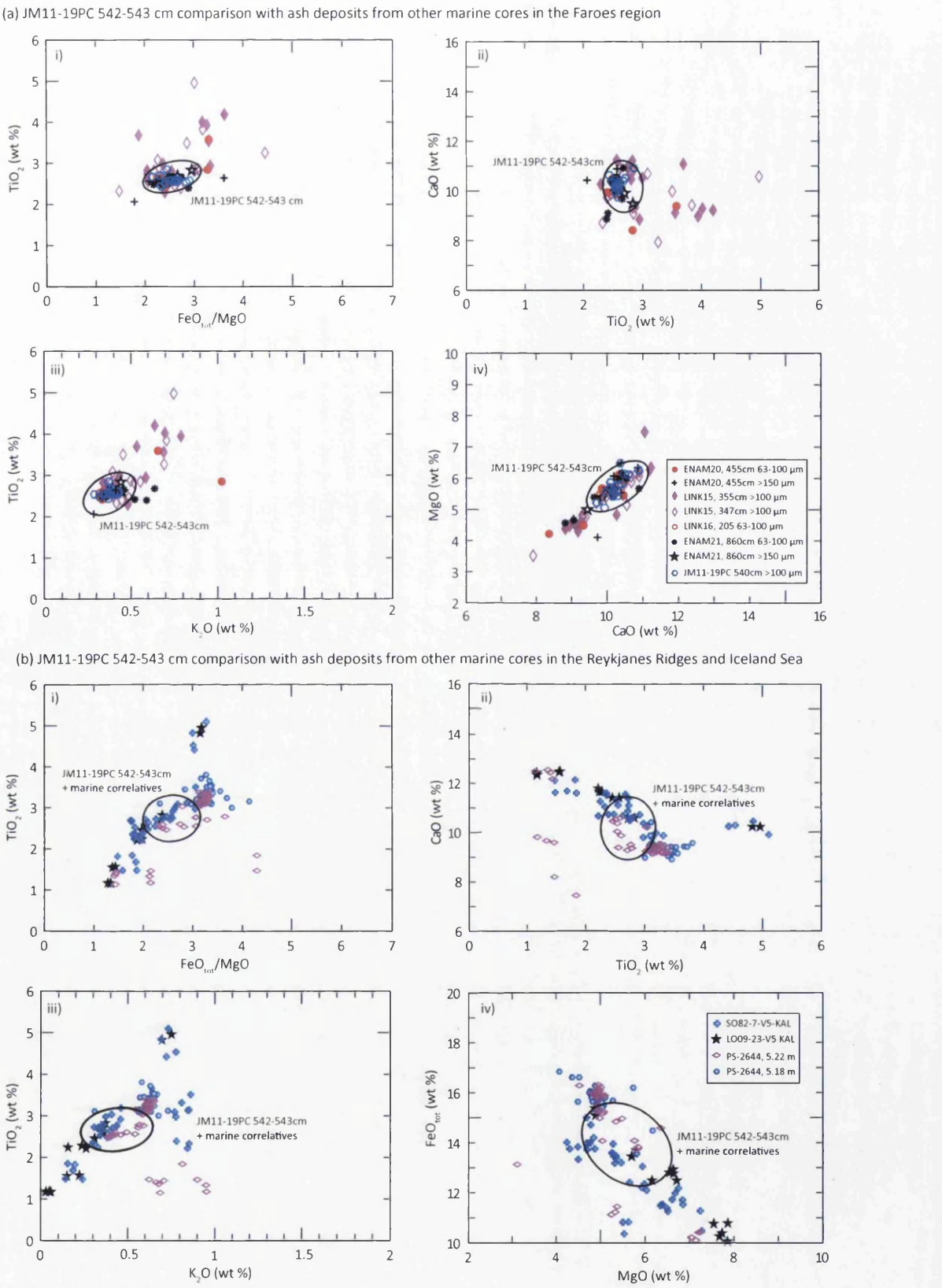

Fig. 10. Major oxide biplots (wt %) for the FMAZ IV deposit in JM11-19PC. a) JM11-19PC 542–543 cm compositional envelope derived from glass shard analyses extracted from all grain-size fractions. (a) (i–iv) This envelope is compared to tephra deposits from four other marine cores from the Faroes region and additional JM11-19PC glass shard analyses reported by Wastegård and Rasmussen (2014). b) Glass shard analyses from JM11-19PC and ENAM93-21 are combined to create a separate compositional envelope named 'JM11-19PC 542–543 cm + marine correlatives'. (b) (i–iv) This envelope is plotted alongside glass shard analyses from the V5 ash zone compiled from two marine cores on the Reykjanes Ridge (Lackschewitz and Wallrabe-Adams, 1997) and two horizons derived from one marine core in the Iceland Sea (Voelker et al., 2000). Data have all been normalised to 100% total oxide concentrations. Outliers from JM11-19PC have been omitted.

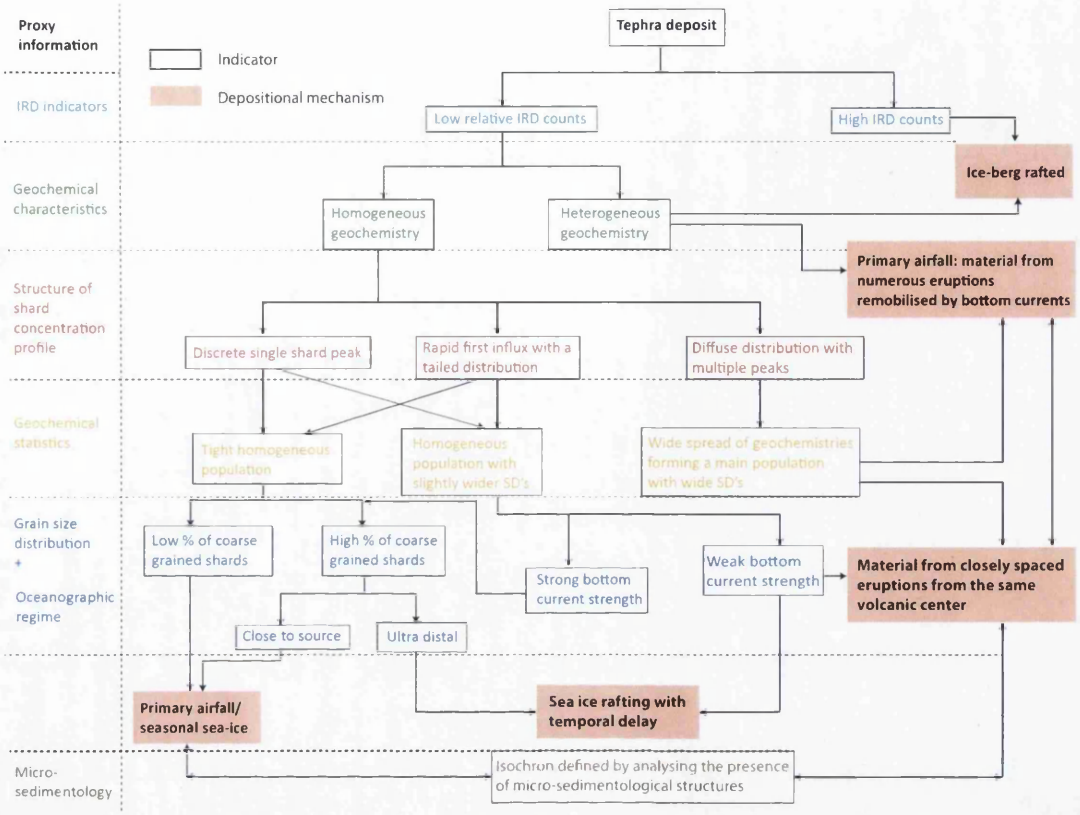

Fig. 11. Protocol for the investigation of primary and secondary depositional processes in marine tephrochronological studies. SD = Standard Deviation.

5. Conclusions

The tephrostratigraphy of a North Atlantic marine core from the southeastern Norwegian Sea has been presented, focussing on three basaltic tephra horizons, referred to as the Faroe Marine Ash Zones. High-resolution contiguous shard concentration profiles, rigorous geochemical characterisation of three separate grain-size fractions and micromorphological techniques are employed to successfully decouple secondary depositional signals. Correlation to previously obtained geochemical data from marine and ice-core archives indicate that i.) the FMAZ III cannot be used as a marine-ice isochron in high-precision studies, unless individual homogeneous horizons can be resolved in cores from high sedimentation areas, and ii) the FMAZ II and IV are well-resolved primary deposits that can be used as isochrons for high-precision correlation studies. Key primary features of these two horizons are a well-defined shard concentration peak, homogeneous geochemical signatures, a high percentage of fine-grained shards and an absence of a coeval IRD signal. The diagnostic features of each of the three tephra deposits have enabled the development of a protocol to assess depositional pathways for future marine tephrochronological studies in the North Atlantic. This protocol highlights the need for adopting a rigorous stratigraphic investigation with intensive geochemical acquisition. When these techniques are combined with an understanding of site specific palaeoceanographic processes, this enables the decoupling of the complex interplay of processes that operated in the North Atlantic during the last glacial period. Where sufficient material exists, we recommend the use of micromorphology to provide further discriminatory evidence for the dominant method of tephra delivery to the sea floor. However, as yet, it is uncertain how useful this technique will be for cryptotephra deposits comprised of low concentrations of glass shards. Moreover, this study reinforces the importance of employing down-core high-resolution shard concentration profiles for resolving transport and depositional mechanisms and we recommend routine use of this technique in tephrochronological studies. The protocol outlined in this study represents an important step towards optimising the application of marine-based tephra and cryptotephra isochrons for correlating to coeval deposits in the Greenland ice-cores and other disparate records.

Acknowledgements

This study forms part of the Tephra constraints on Rapid Climate Events (TRACE) project which aims to correlate tephra found in the Greenland Ice Cores and North Atlantic marine cores in order to understand mechanisms of abrupt climate change during the last glacial period. The research leading to these results has received funding from the European Research Council under the European Union's Seventh Framework Programme (FP7/2007-2013)/ERC grant agreement n° [259253]. AJG, SMD and PMA acknowledge the support of the Climate Change Consortium of Wales (C3W). AJG acknowledges the QRA for the Postgraduate Research Award for thin-section preparation at Royal Holloway, University of London. We thank the captain and crew of the R-V Jan Mayen for their assistance in the retrieval of core JM11-19PC. We are grateful for the assistance of Dr Chris Hayward with the use of the electron microprobe at the Tephrochronology Analytical Unit, University of Edinburgh. We are grateful to Professor Stefan Wastegård for providing geochemical data for the FMAZ IV and Dr Hans-Joachim Wallrabe-Adams for providing geochemical data for the V ash zones. Sune Rasmussen, Sean Pyne-O'Donnell and Sabine Wulf are

thanked for their constructive reviews of this manuscript. This paper contributes to the EU-funded COST ACTION INTIMATE (ES0907) (http://cost-es0907.geoenvi.org/) and to the INTREPID (Enhancing tephrochronology as a global research tool through improved fingerprinting and correlation techniques and uncertainty modelling) – an INQUA INTAV-led project (International Focus Group on Tephrochronology and Volcanism, project no. 0907).

Appendix A. Supplementary data

Supplementary data related to this article can be found at http://dx.doi.org/10.1016/j.quascirev.2014.04.031.

References

Abbott, P.M., Davies, S.M., 2012. Volcanism and the Greenland ice-cores: the tephra record. Earth Sci. Rev. 115, 173–191.

Abbott, P.M., Davies, S.M., Austin, W.E.N., Pearce, N.J.G., Hibbert, F.D., 2011. Identification of cryptotephra horizons in a North East Atlantic marine record spanning marine isotope stages 4 and 5a (~60,000-82,000 a b2k). Quat. Int. 246, 177–189.

Abbott, P.M., Austin, W.E.N., Davies, S.M., Pearce, N.J.G., Hibbert, F.D., 2013. Cryptotephrochronology of the Eemian and the Last Interglacial-glacial transition in the North East Atlantic. J. Quat. Sci. 28, 501–524.

Abbott, P.M., Austin, W.E.N., Davies, S.M., Pearce, N.J.G., Rasmussen, T.L., Wastegard, S., Brendryen, J., 2014. Re-evaluation and extension of the Marine Isotope Stage 5 tephrostratigraphy of the Faroe Islands region: the cryptotephra record. Palaeogeogr. Palaeoclimatol. Palaeoecol. (in press).

Austin, W.E.N., Hibbert, F.D., 2012. Tracing time in the ocean: a brief review of chronological constraints (60-8 kyr) on North Atlantic marine event-based stratigraphies. Quat. Sci. Rev. 36, 28–37.

Austin, W.E.N., Wilson, L.J., Hunt, J.B., 2004. The age and chronostratigraphical significance of North Atlantic Ash Zone II. J. Quat. Sci. 19, 137–146.

Austin, W.E.N., Hibbert, F.D., Rasmussen, S.O., Peters, C., Abbott, P.M., Bryant, C.L., 2012. The synchronization of palaeoclimatic events in the North Atlantic region during Greenland Stadial 3 (ca 27.5 to 23.3 kyr b2k). Quat. Sci. Rev. 36, 154–163.

Begét, J., Mason, O., Anderson, P., 1992. Age, extent and climatic significance of the c. 3400 BP Aniakchak tephra, western Alaska, USA. Holocene 2, 51–56.

Blockley, S.P.E., Lane, C.S., Lotter, A.F., Pollard, A.M., 2007. Evidence for the presence of the Vedde Ash in Central Europe. Quat. Sci. Rev. 26, 3030–3036.

Blockley, S.P.E., Pyne-O'Donnell, S.D.F., Lowe, J.J., Matthews, I.P., Stone, A., Pollard, A.M., Turney, C.S.M., Molyneux, E.G., 2005. A new and less destructive laboratory procedure for the physical separation of distal glass tephra shards from sediments. Quat. Sci. Rev. 16–17, 1952–1960.

Borchardt, G.A., Aruscavage, P.J., Millard Jr., H., 1972. Correlation of the Bishop ash, a Pleistocene marker bed, using instrumental neutron activation analysis. J. Sediment. Petrol. 42, 201–206.

Bourne, A.J., 2012. The Late Quaternary Tephrochronology of the Adriatic Region: Implications for the Synchronization of Marine Records (Unpublished PhD thesis). Royal Holloway, University of London, UK.

Bourne, A.J., Davies, S.M., Abbott, P.M., Rasmussen, S.O., Steffensen, J.P., Svensson, A., 2013. Revisiting the Faroe Marine Ash Zone III in two Greenland ice Cores: implications for marine-ice-core correlations. J. Quat. Sci. 28, 641–646.

Boygle, J.E., 1994. Tephra in Lake Sediments: an Unambiguous Geochronological Marker? (Ph.D. thesis) University of Edinburgh.

Bramlette, M.N., Bradley, W.H., 1941. Geology and Biology of North Atlantic Deep-sea Cores Between Newfoundland and Ireland: I. Lithology and Geologic Interpretation. U.S. Geological Survey Professional Paper. 196-A, pp. 1–34.

Brendryen, J., Haflidason, H., Sejrup, H.P., 2010. Norwegian Sea tephrostratigraphy of marine isotope stages 4 and 5: prospects and problems for tephrochronology in the North Atlantic region. Quat. Sci. Rev. 29, 847–864.

Davies, S.M., Wastegård, S., Rasmussen, T.L., Svensson, A., Johnsen, S.J., Steffensen, J.P., Andersen, K.K., 2008. Identification of the Fugloyarbanki tephra in the NGRIP ice core: a key tie-point for marine and ice-core sequences during the Last Glacial period. J. Quat. Sci. 23, 409–414.

Davies, S.M., Wastegård, S., Abbott, P.M., Barbante, C., Bigler, M., Johnsen, S.J., Rasmussen, T.L., Steffensen, J.P., Svensson, A., 2010. Tracing volcanic events in the NGRIP ice-core and synchronising North Atlantic marine records during the Last Glacial period. Earth Planet. Sci. Lett. 294 (1–2), 69–79.

Davies, S.M., Abbott, P.M., Pearce, N.J.G., Wastegård, S., Blockley, S.P.E., 2012. Integrating the INTIMATE records using tephrochronology: rising to the challenge. Quat. Sci. Rev. 36, 11–27.

Davies, S.M., Abbott, P.M., Meara, R.H., Pearce, N.J.G., Austin, W.E.N., Chapman, M.R., Svensson, A., Bigler, M., Rasmussen, 2014. A North Atlantic tephra framework for 130,000–60,000 years b2k: new tephra discoveries, marine based-correlations and future challenges. Quat. Sci. Rev. 106, 101–121.

Enache, M.D., Cumming, B.F., 2006. The morphological and optical properties of volcanic glass: a tool to assess density-induced vertical migration of tephra in sediment cores. J. Paleolimnol. 35, 661–667.

Froggatt, P.C., Gosson, G.J., 1982. Techniques for the Preparation of Tephra Samples for Mineral or Chemical Analysis and Radiometric Dating, vol. 23. Geology Department, Victoria University of Wellington Publication, pp. 1–12.

Gehrels, M.J., Lowe, D.J., Hazell, Z.J., Newnham, R.M., 2006. A continuous 5300-yr Holocene cyrptotephrostratigraphic record from northern New Zealand and implications for tephrochronology and volcanic hazard assessment. Holocene 16, 173–187.

Haflidason, H., Eiríksson, J., van Kreveld, S., 2000. The tephrochronology of Iceland and the North Atlantic region during the Middle and Late Quaternary: a review. J. Quat. Sci. 15, 3–22.

Hayward, C., 2012. High spatial resolution electron probe microanalysis of tephras and melt inclusions without beam-induced chemical modification. Holocene 22, 119–125.

Jakobsson, S.P., 1979. Petrology of recent basalts of the Eastern Volcanic Zone, Iceland. Acta Nat. Isl. 26, 1–103.

Jakobsson, S.P., Jónasson, K., Sigurdsson, I.A., 2008. The three igneous rock suites of Iceland. Jökull 58, 117–138.

Jumars, P.A., Wheatcroft, R.A., 1989. Responses of benthos to changing food quality and quantity, with a focus on deposit feeding and bioturbation. In: Berger, W.H., Smetacek, V.S., Wefer, G. (Eds.), Productivity of the Ocean: Present and Past. Wiley, New York, pp. 235–253.

Kuhs, M., Austin, W.E.N., Abbott, P.M., Hodell, D.A., 2014. Iceberg-rafted tephra as a potential tool for the reconstruction of ice-sheet processes and ocean surface circulation in the glacial North Atlantic. In: Austin, W.E.N., Abbott, P.M., Davies, S.M., Pearce, N.J.G., Wastegård, S. (Eds.), Marine Tephrochronology, Geological Society of London Special Publication, vol. 398.

Lackschewitz, K.S., Wallrabe-Adams, H.J., 1997. Composition and origin of volcanic ash zones in Late Quaternary sediments from the Reykjanes Ridge: evidence for ash fallout and ice rafting. Mar. Geol. 136, 209–224.

Lane, C.S., Andric, M., Cullen, V.L., Blockley, S.P.E., 2011. The occurrence of distal Icelandic and Italian tephra in the Lateglacial of Lake Bled, Slovenia. Quat. Sci. Rev. 30, 1013–1018.

Larsen, G., 1981. Tephrochronology by microprobe glass analysis. In: Self, S., Sparks, R.S.J. (Eds.), Tephra Studies as a Tool in Quaternary Research, pp. 95–102.

Larsen, G., Eiríksson, J., Knudsen, K.L., Heinemeier, J., 2002. Correlation of late Holocene terrestrial and marine tephra markers, north Iceland: implications for reservoir age changes. Polar Res. 21, 283–290.

Lowe, D.J., 2011. Tephrochronology and its application: a review. Quat. Geochronol. 6, 107–153.

Lowe, J.J., Rasmussen, S.O., Björck, S., Hoek, W.Z., Steffensen, J.P., Walker, M.J.C., Yu, Z.C., 2008. Synchronisation of palaeoenvironmental events in the North Atlantic region during the last termination: a revised protocol recommended by the INTIMATE group. Quat. Sci. Rev. 27, 6–17.

Mackie, E., Davies, S.M., Turney, C.S.M., Dobbyn, K., Lowe, J.J., 2002. The use of magnetic separation techniques to detect basaltic microtephra in glacial-interglacial transition (LGIT; 15-10 ka cal. BP) sediment sequences in Scotland. Scott. J. Geol. 38, 21–30.

Manville, V., Wilson, C.J.N., 2004. Vertical density currents: a review of their potential role in the deposition and interpretation of deep-sea ash layers. J. Geol. Soc. 161, 947–958.

Matthews, I.P., Palmer, A.P., Folkes, H., Trincardi, F., 2011. Understanding tephra layers in marine sediments, the potential of thin section micromorphology to investigate depositional and taphonomic processes. In: Marine Tephrochronology Meeting. Geological Society London. UK, 26 October, 2011.

van der Meer, J.M., Menzies, J., 2011. The micromorphology of unconsolidated sediments. Sediment. Geol. 238, 213–232.

Michels, K.H., 2000. Inferring maximum geostrophic current velocities in the Norwegian-Greenland Sea from settling velocity measurements of sediment surface samples: methods, application, and results. J. Sediment. Res. 70, 1036–1050.

Óladóttir, B.A., Sigmarsson, O., Larsen, G., Thordarson, T., 2008. Katla volcano, Iceland: magma composition, dynamics and eruption frequency as recorded by Holocene tephra layers. Bull. Volcanol. 70, 475–493.

Palmer, A.P., Lee, J.A., Kemp, R.A., Carr, S.J., 2008. Revised Laboratory Procedures for the Preparation of Thin Sections from Unconsolidated Material. Unpublished Internal Report. Royal Holloway, University of London.

Pearce, N.J.G., Abbott, P.M., Martin-Jones, C., 2014. Microbeam methods for the analysis of glass in fine-grained tephra deposits: a SMART perspective on current and future trends. In: Austin, W.E.N., Abbott, P.M., Davies, S.M., Pearce, N.J.G., Wastegård, S. (Eds.), Marine Tephrochronology, Geological Society of London Special Publication, vol. 398.

Pyne-O'Donnell, S.D.F., Hughes, P.D.M., Froese, D.G., Jensen, B.J.L., Kuehn, S.C., Mallon, G., Amesbury, M.J., Charman, D.J., Daley, T.J., Loader, N.J., Mauquoy, D., Street-Perrott, F.A., Woodman-Ralph, J., 2012. High-precision ultra-distal Holocene tephrochronology in North America. Quat. Sci. Rev. 52, 6–11.

Rasmussen, S.O., Bigler, M., Blockley, S.P.E., Blunier, T., Buchardt, S.L., Clausen, H.B., Cvijanovic, I., Dahl-Jensen, D., Johnsen, S.J., Fischer, H., Gkinis, V., Guillevic, M., Hoek, W.Z., Lowe, J.J., Pedro, J., Popp, T., Seierstad, I., Steffensen, J.P., Svensson, A.M., Vallelonga, P., Vinther, B.M., Walker, M.J.C., Wheatley, J.J., Winstrup, M., 2014. A framework for robust naming and correlation of past abrupt climatic changes during the recent glacial period based on three synchronised Greenland ice-cores. Quat. Sci. Rev. 106, 14–28.

Rasmussen, T.L., Thomsen, E., Tjeerd, C.E., Weering, V., Labeyrie, L., 1996. Rapid changes in surface and deep water conditions at the Faroe Margin during the last 58,000 years. Palaeoceanography 11, 757–771.

Rasmussen, T.L., Wastegard, S., Kuijpers, A., van Weering, T.C.E., Heinemeier, J., Thomsen, E., 2003. Stratigraphy and distribution of tephra layers in marine sediment cores from the Faeroe Islands, North Atlantic. Mar. Geol. 199, 263–277.

Ruddiman, W.F., Glover, L.K., 1972. Vertical mixing of ice rafted volcanic ash in north Atlantic sediments. Geol. Soc. Am. Bull. 83, 2817–2836.

Sparks, R., 1981. Triggering of volcanic eruptions by earth tides. Nature 290, 448.

Stärz, M., Gong, X., Stein, R., Darby, D.A., Kauker, F., Lohmann, G., 2012. Glacial shortcut of Arctic sea-ice transport. Earth Planet. Sci. Lett. 257–358, 257–267.

Svensson, A., Andersen, K.K., Bigler, M., Clausen, H.B., Dahl-Jensen, D., Davies, S.M., Johnsen, S.J., Muscheler, R., Parrenin, F., Rasmussen, S.O., Röthlisberger, R., Seierstad, I., Steffensen, J.P., Vinther, B.M., 2008. A 60 000 year Greenland stratigraphic ice core chronology. Clim. Past 4, 47–57.

Todd, J.A., Austin, W.E.N., Abbott, P.M., 2014. Quantifying bioturbation of a simulated ash fall event. In: Austin, W.E.N., Abbott, P.M., Davies, S.M., Pearce, N.J.G., Wastegård, S. (Eds.), Marine Tephrochronology, Geological Society of London Special Publication, vol. 398.

Turney, C.S.M., 1998. Extraction of rhyolitic ash from minerogenic lake sediments. J. Paleolimnol. 19, 199–206.

Voelker, A.H.L., Grootes, P.M., Nadeau, M.J., Sarnthein, M., 2000. Radiocarbon levels in the Iceland Sea from 25–53 kyr and their link to the Earth's magnetic field intensity. Radiocarbon 42, 437–452.

Walden, J., Oldfield, F., Smith, J., 1999. Environmental Magnetism: a Practical Guide. Quaternary Research Association. Technical Guide No. 6.

Wallrabe-Adams, H.J., Lackschewitz, K.S., 2003. Chemical composition, distribution, and origin of silicic volcanic ash layers in the Greenland-Iceland-Norwegian Sea: explosive volcanism from 10 to 300 ka as recorded in deep sea sediments. Mar. Geol. 19, 273–293.

Wastegård, S., Rasmussen, T.L., Kuijpers, A., Nielsen, T., van Weering, T.C.E., 2006. Composition and origin of ash zones from Marine Isotope Stages 3 and 2 in the North Atlantic. Quat. Sci. Rev. 25, 2409–2419.

Wastegård, S., Rasmussen, T.L., 2014. Faroe Marine Ash Zone IV – a new MIS3 ash zone of the Faroe Islands margin. In: Austin, W.E.N., Abbott, P.M., Davies, S.M., Pearce, N.J.G., Wastegård, S. (Eds.), Marine Tephrochronology, Geological Society of London Special Publication, vol. 398.

Wiesner, M.G., Wang, Y., Zheng, L., 1995. Fallout of volcanic ash to the deep South China Sea induced by the 1991 eruption of Mount Pinatubo (Philippines). Geology 23, 885–888.